frontiers | Research Topics

Planning and operation of hybrid renewable energy systems, volume II

Edited by
Weihao Hu, Amjad Anvari-Moghaddam, Liansong Xiong, Haoran Zhao, Yuefang Du, Di Cao and Sayed Abulanwar

Published in
Frontiers in Energy Research

ISSN 1664-8714
ISBN 978-2-8325-2517-3
DOI 10.3389/978-2-8325-2517-3

About Frontiers

Frontiers is more than just an open access publisher of scholarly articles: it is a pioneering approach to the world of academia, radically improving the way scholarly research is managed. The grand vision of Frontiers is a world where all people have an equal opportunity to seek, share and generate knowledge. Frontiers provides immediate and permanent online open access to all its publications, but this alone is not enough to realize our grand goals.

Frontiers journal series

The Frontiers journal series is a multi-tier and interdisciplinary set of open-access, online journals, promising a paradigm shift from the current review, selection and dissemination processes in academic publishing. All Frontiers journals are driven by researchers for researchers; therefore, they constitute a service to the scholarly community. At the same time, the *Frontiers journal series* operates on a revolutionary invention, the tiered publishing system, initially addressing specific communities of scholars, and gradually climbing up to broader public understanding, thus serving the interests of the lay society, too.

Dedication to quality

Each Frontiers article is a landmark of the highest quality, thanks to genuinely collaborative interactions between authors and review editors, who include some of the world's best academicians. Research must be certified by peers before entering a stream of knowledge that may eventually reach the public - and shape society; therefore, Frontiers only applies the most rigorous and unbiased reviews. Frontiers revolutionizes research publishing by freely delivering the most outstanding research, evaluated with no bias from both the academic and social point of view. By applying the most advanced information technologies, Frontiers is catapulting scholarly publishing into a new generation.

What are Frontiers Research Topics?

Frontiers Research Topics are very popular trademarks of the *Frontiers journals series*: they are collections of at least ten articles, all centered on a particular subject. With their unique mix of varied contributions from Original Research to Review Articles, Frontiers Research Topics unify the most influential researchers, the latest key findings and historical advances in a hot research area.

Find out more on how to host your own Frontiers Research Topic or contribute to one as an author by contacting the Frontiers editorial office: frontiersin.org/about/contact

Planning and operation of hybrid renewable energy systems, volume II

Topic editors

Weihao Hu — University of Electronic Science and Technology of China, China
Amjad Anvari-Moghaddam — Aalborg University, Denmark
Liansong Xiong — Xi'an Jiaotong University, China
Haoran Zhao — Shandong University, China
Yuefang Du — University of Electronic Science and Technology of China, China
Di Cao — University of Electronic Science and Technology of China, China
Sayed Abulanwar — Mansoura University, Egypt

Citation

Hu, W., Anvari-Moghaddam, A., Xiong, L., Zhao, H., Du, Y., Cao, D., Abulanwar, S., eds. (2023). *Planning and operation of hybrid renewable energy systems, volume II*. Lausanne: Frontiers Media SA. doi: 10.3389/978-2-8325-2517-3

Table of contents

frontiers | Frontiers in Energy Research

TYPE Editorial
PUBLISHED 09 May 2023
DOI 10.3389/fenrg.2023.1212394

OPEN ACCESS

EDITED AND REVIEWED BY
Alfonso Chinnici,
University of Adelaide, Australia

*CORRESPONDENCE
Weihao Hu,
whu@uestc.edu.cn

RECEIVED 26 April 2023
ACCEPTED 02 May 2023
PUBLISHED 09 May 2023

CITATION
Hu W, Anvari-Moghaddam A, Xiong L, Zhao H, Du Y, Cao D and Abulanwar S (2023), Editorial: Planning and operation of hybrid renewable energy systems, Volume II.
Front. Energy Res. 11:1212394.
doi: 10.3389/fenrg.2023.1212394

Editorial: Planning and operation of hybrid renewable energy systems, Volume II

Weihao Hu[1]*, Amjad Anvari-Moghaddam[2], Liansong Xiong[3], Haoran Zhao[4], Yuefang Du[1], Di Cao[1] and Sayed Abulanwar[5]

[1]University of Electronic Science and Technology of China, Chengdu, Sichuan Province, China, [2]Department of Energy Technology, Aalborg University, Aalborg, Denmark, [3]School of Electrical Engineering, Xi'an Jiaotong University, Xi'an, Shaanxi Province, China, [4]School of Electrical Engineering, Shandong University, Jinan, Shandong Province, China, [5]Department of Electrical Engineering, Mansoura University, Mansoura, Dakahlia, Egypt

KEYWORDS

current control, voltage control, frequency stability, harmonic analysis, operation with renewable energy

Editorial on the Research Topic
Planning and operation of hybrid renewable Energy systems, Volume II

Renewable energy contributes to clean and economic energy systems. However, it also poses a great challenge to the operation of energy systems in terms of current, voltage, and frequency problems in power systems due to the intermittency and uncertainty of renewable energy. This Frontiers Research Topic aims to present state-of-the-art studies on solving these problems. There are in total 11 articles accepted for this Research Topic after careful peer-to-peer review, and they cover the following three categories.

Current, voltage control, and harmonic analysis

To deal with the poor active modulation of the working mode of converters and the large current stress in the Buck circuit of DC-DC converters, Li et al. propose an improved frequency/amplitude modulation control strategy. To improve the efficiency of dual active bridge converters, including a reduction of the effective value of current and a widening of the soft switching area, Shi et al. propose an optimized extended phase-shift modulation strategy. Voltage stability is greatly influenced by the doubly-fed induction generator at the point of common coupling, where wind farms are integrated into the bulk power grid. Liu et al. propose a reactive power compensation strategy to achieve the expected voltage quality of the power grid via a minimum amount of control actions in emergencies. The triggering of the Tokamak power supply in nuclear fusion energy provides spectrum-rich harmonics to the DC side of the power supply and threatens the operational safety of the Tokamak device; thus, He et al. propose a harmonic analysis method to examine the DC side. Zhang explore the influence of driving and parasitic parameters on the switching behaviors of a SiC MOSFET since its behaviors affect the efficiency and power density of converters.

Frequency control

You et al. suggest a dynamic power-based stepwise inertial control scheme for a wind power plant to minimize secondary frequency dip and reduce the maximum frequency deviation. Wei et al. propose a frequency control scheme for the LCC-HVDC sending end system based on the concept of rapid power compensation to improve the frequency characteristics of the renewable energy sending end grid. Bi et al. propose a coordinated active/reactive power-control strategy for the VSC-HVDC system based on the rapid power compensation mode to suppress grid electromechanical and frequency oscillations.

Operation with renewable energy

Zhang et al. determine a feasible region model for an integrated energy system, according to the capacity of key equipment and its pipeline capacity, using the multi-energy balance equation. Dong et al. propose a two-stage, robust optimization operation model of a hybrid AC-DC distribution network to handle the stochastic uncertainty of the distributed renewable energy output and to minimize the total system operational cost. With batteries largely integrated in energy systems, it is important to estimate their state of charge. Yang et al. propose an optimized state of charge estimation algorithm based on an extended kalman filter.

Overall, energy systems face great challenges regarding the integration of renewable energy, including voltage, current, and frequency problems. Further study is still required to better address the problems in hybrid renewable energy systems.

Author contributions

HW wrote the article and other authors gave suggestions and did the proof reading. All authors contributed to the article and approved the submitted version.

Conflict of interest

The authors declare that the research was conducted in the absence of any commercial or financial relationships that could be construed as a potential conflict of interest.

Publisher's note

frontiers | Frontiers in Energy Research

TYPE Original Research
PUBLISHED 21 September 2022
DOI 10.3389/fenrg.2022.1027439

OPEN ACCESS

EDITED BY
Liansong Xiong,
Xi'an Jiaotong University, China

REVIEWED BY
Da Xu,
China University of Geosciences Wuhan, China
Jilei Ye,
Nanjing Tech University, China
Rui Li,
Shanghai Jiao Tong University, China

*CORRESPONDENCE
Bo Yang,
yangbo@epri.sgcc.com.cn

SPECIALTY SECTION
This article was submitted to Process and Energy Systems Engineering, a section of the journal Frontiers in Energy Research

RECEIVED 25 August 2022
ACCEPTED 06 September 2022
PUBLISHED 21 September 2022

CITATION
Yang B, Li G, Tang W and Li H (2022), Research on optimized SOC estimation algorithm based on extended kalman filter.
Front. Energy Res. 10:1027439.
doi: 10.3389/fenrg.2022.1027439

Research on optimized SOC estimation algorithm based on extended kalman filter

Bo Yang[1,2]*, Guanjun Li[3,2], Wencheng Tang[1] and Haoyuan Li[2]

[1]School of Mechanical Engineering, Southeast University, Nanjing, China, [2]China Electric Power Research Institute Co, Ltd., Nanjing, China, [3]School of Automation, Southeast University, Nanjing, China

The paper studies the estimation of state of charge (SOC) of batteries. Firstly, the research status of battery management system, battery equivalent model and SOC estimation algorithm is introduced, and the performance of common equivalent circuit model and SOC estimation algorithm in complexity and accuracy is compared and analyzed. On this basis, this paper proposes an extended Kalman filter (EKF) algorithm based on the first-order RC model, and optimizes it by piecewise fitting. The accuracy of the optimized EKF algorithm is greatly improved. Finally, the modeling and simulation are completed through MATLAB/SIMULINK, and the experimental platform is designed and built to test the SOC estimation algorithm based on EKF. The simulation and experimental results verify the accuracy of the estimation algorithm.

KEYWORDS

state of charge, estimation algorithm, extended kalman filter nomenclature: simulink (RRID:SCR_014744), matlab (RRID:SCR_001622), kalman filter

Introduction

The energy situation in today's world is facing a core contradiction, that is, the contradiction between growing demand and increasingly tight supply. In the traditional energy, the reserves of non-renewable energy represented by coal and fossil fuels are limited, and it is more and more difficult to explore. With the emission of carbon dioxide and various harmful gases, it seriously endangers the safety of the earth's environment. Facing the disharmonious development of global climate caused by energy problems, as of 12 June 2020, 125 countries in the world have promised to achieve the goal of carbon neutrality by the middle of the 21st century (Chenic et al., 2022). Therefore, streamlining the energy structure and improving energy utilization have become the joint efforts of scholars and researchers all over the world. The research on renewable clean energy such as photovoltaic and wind energy has objectivity and inevitability, and electrochemical power supply has become the focus of research because of its high energy conversion and storage efficiency.

As a key technology, energy storage technology not only promotes the intelligence of large-scale distributed power grid (Yan et al., 2021; Sridhar and Salkuti, 2022), but also relates to the large-scale grid connection of renewable energy. It is of great significance to improve the efficiency of clean energy power generation. It is a key research object of

countries all over the world, especially developed countries (Luo et al., 2015). At present, pumped storage is still the main energy storage means in the world, with the largest installed capacity, accounting for 98% of the total global energy storage capacity by 2015. However, at the same time, energy storage technologies such as compressed air, flywheel, superconductivity, lead-acid battery and lithium-ion battery are also developing rapidly. Different energy storage technologies have different characteristics.

Among them, lithium battery energy storage has become a research hotspot because of its safety and efficiency, short energy storage cycle and high energy density. The voltage and capacity of a single lithium-ion battery are limited, so that multiple batteries need to be cascaded to form a battery module to adapt to the application in the scenario of high voltage and high power level. Therefore, the management system for battery module has been further developed.

The core function of battery management system (BMS) is to reasonably estimate the battery parameters and give different solutions for different situations, so as to ensure the safe and stable operation of battery energy storage system. The technology development of BMS has been paid attention by more and more manufacturers. General Motors Corporation of the United States has developed a BMS serving EV1 of electric vehicle, which has the functions of live monitoring, shunt adoption, thermal management and so on. It can realize the power-off protection of abnormal voltage, and support the application on the battery module cascaded with up to 26 batteries (Lee and Cheng, 2005). Germany has also independently developed BADICHE system and BATTMAN system (Garcia et al., 2010); Toyota Motor Corporation of Japan has developed Prius system for hybrid electric vehicles; Tesla Motors has independently developed the corresponding battery management system for pure electric vehicles. It is a general trend that traditional vehicles are constantly replaced by new energy vehicles.

Lithium-ion battery is the main energy storage element in the energy storage system. Its various parameters usually change in actual working conditions, and need to be measured indirectly by certain means. At present, the commonly used method is to establish the equivalent model of the battery, and then determine the various states of the battery at a certain time through the study of the equivalent model. At present, the equivalent models of batteries are roughly divided into three categories: electrochemical model, mathematical model and equivalent circuit model. In this paper, the equivalent circuit model is used to study, and its accuracy is between electrochemical model and mathematical model. It is easy to model the equivalent circuit model and predict the SOC, so it is widely used in all kinds of automotive BMS.

It is the key and difficult point of BMS system to realize the accurate estimation of battery SOC based on equivalent model and corresponding estimation algorithm. At present, the commonly used SOC estimation algorithms mainly include traditional algorithm, filtering algorithm, learning algorithm and hybrid algorithm.

Two typical traditional algorithms are ampere hour integration method (Liu et al., 2019) and open circuit voltage method (Zhang et al., 2016). The ampere hour integration method is calculated by adding the initial value of SOC and the integral value of current during charging and discharging process. This method is simple and easy to understand, but there are obvious shortcomings. Before SOC estimation, the initial value of SOC is usually unknown. Moreover, this method has high requirements for the accuracy of current sampling, and SOC estimation is easily affected by the inaccurate initial value and cumulative error of integration (LI et al., 2013; Xiong et al., 2020). As an open-loop estimation method (Caumont et al., 2000; Zhu et al., 2004), its estimation accuracy is difficult to ensure.

The open circuit voltage method establishes the corresponding relationship between SOC and open circuit voltage (OCV) by measuring the OCV of the battery, and then determines the SOC by looking up the table (Xiong et al., 2018). This method also has high requirements for the accuracy of voltage sampling, and the battery needs to stand for several hours before OCV measurement which is difficult to meet the requirements of on-line calculation which means SOC cannot be estimated in real time (Li et al., 2017).

Common filtering algorithms include Kalman filtering algorithm (KF) (Rakhmatov et al., 2003; Xing et al., 2011), particle filtering (PF)algorithm (Zhou et al., 2016) and synovial observer (Chen et al., 2016; Chen et al., 2017) algorithm. Among several filtering algorithms, KF can give consideration to both computational complexity and estimation accuracy, so it is widely used in automobile, energy storage, navigation and other fields.

In 1960, Rudolph E. Kalman proposed the concept of standard Kalman filter (SKF). This method is widely used in discrete linear systems because of its recursive iteration of predicted and measured values and continuous convergence to obtain accurate results. Moreover, it needs less computing space and has rapidity and accuracy which make it suitable for online computing. The accuracy of Kalman filter depends on the accuracy of modeling. When the model is inaccurate, the accuracy of the algorithm will be greatly affected (Zhang et al., 2017).However, linear Kalman filter can only be used in linear battery model. Because it sacrifices part of the accuracy, the estimation is not accurate enough. On this basis, an extended Kalman filter suitable for nonlinear systems is proposed. This method linearizes the nonlinear system by ignoring the higher-order term through the Taylor expansion of the function, which greatly improves the application scope of the algorithm and improves the accuracy to a certain extent. In order to further improve convergence and robustness, scholars have proposed a series of derivative algorithms, such as adaptive extended Kalman filter (AEKF) (Dong et al., 2018), unscented Kalman

filter (UKF) (He et al., 2013) and cubature Kalman filter (CKF) (Arasaratnam et al., 2010).

Neural network (NN) (Wang and Zhou, 2018) and fuzzy logic (FL) (Zheng et al., 2019) are typical learning algorithms. NN is a mathematical model that analyzes the system by simulating the synaptic connection of human brain. By training NN with a large amount of data, the relationship between input and output of nonlinear system can be simulated with high accuracy. When the training data is sufficient, the output accuracy is high. However, when the amount of data is too large, it will also lead to overfitting. At this time, the estimation accuracy of NN will decline. The disadvantage of NN is that it relies on a large number of training data, and different training strategies will have a great impact on the estimation results. FL refers to a mathematical method that simulates the thinking mode of the human brain for judging uncertain things with the help of the concept of membership function, so as to deal with nonlinear and large lag objects. Common FL algorithms include mean blur and Gaussian blur.

Hybrid algorithm combines two or more algorithms. Literature (Guo et al., 2016) combines the least square method and adaptive unscented Kalman filter (AUKF). Through simulation experiments, it is verified that the proposed algorithm has higher SOC estimation accuracy and convergence than the single AUKF. Literature (Xu et al., 2020) proposes a hybrid algorithm PF-CKF that combines PF and CKF. This hybrid algorithm significantly improves the SOC estimation accuracy by updating the battery model parameters in real time. Although the hybrid algorithm can achieve better results, its computational complexity is greatly increased, which is higher than the single algorithm.

The paper uses the extended Kalman filter algorithm based on equivalent circuit model to estimate the battery SOC and optimizes it by piecewise fitting which improves the accuracy and stability of the estimation.

Equivalent model of lithium-ion battery

As an energy storage element, lithium-ion battery has precise internal structure and complex working principle. Due to the influence of its own service state and external environment, the internal characteristics of the battery often change. These factors mainly include the internal discharge depth, charge and discharge rate, life aging degree and external environment temperature. In the process of predicting the battery state of charge, the battery management system needs to monitor and collect the changing internal parameters of the battery in real time, so as to analyze and calculate the internal characteristics of the battery in different states and realize the real-time estimation of the battery state of charge.

The packaging of lithium-ion battery is highly integrated, so the lithium-ion battery looks like a black box system. For the external monitoring system, only the two battery parameters of battery port voltage and load current can be obtained directly through detection. However, the relevant parameters characterizing the battery characteristics inside the battery cannot be obtained intuitively through monitoring, which makes it difficult for the battery management system to estimate the battery SOC. Therefore, it is necessary to establish the equivalent circuit model inside the battery and realize the quantitative description of the actual circuit characteristics inside the battery through modeling, so as to meet the needs of BMS for reliable estimation of battery SOC. Modeling battery is difficult as it is actually a non-linear model depending on various changing variables like temperature, discharging, and charging states (Sher and Addoweesh, 2012). The establishment of the internal equivalent circuit model of the battery needs to be able to accurately simulate the actual working characteristics of the battery, including static and dynamic characteristics. At the same time, the amount of calculation and complexity should be moderate to ensure the response speed of the estimation process. The establishment of accurate battery internal equivalent model is the basis of the accuracy and rapidity of the subsequent estimation algorithm in this paper.

When the battery is in an open circuit state, the potential value on the electrode is called the equilibrium electrode potential. When the battery is in a dynamic state and there is current flowing in the closed circuit, the potential value on the electrode is called the actual electrode potential. The actual electrode potential is not invariable. With the current passing through the battery, its value will gradually deviate from the equilibrium potential. This phenomenon is the polarization phenomenon of the battery. The difference between the equilibrium electrode potential and the actual electrode potential is called the overvoltage difference, and the magnitude of the overvoltage difference reflects the degree of polarization of the battery. Generally speaking, the deviation degree of electrode potential is positively correlated with the current flowing through the unit electrode, and large current will aggravate the polarization phenomenon. According to the different causes of polarization, battery polarization can be divided into three categories: ohmic polarization, electrochemical polarization and concentration polarization. The corresponding battery internal resistance are ohmic internal resistance, electrochemical polarization internal resistance and concentration polarization internal resistance. Therefore, the internal resistance of the battery can be divided into ohmic internal resistance and polarization internal resistance. The value of ohmic internal resistance is related to temperature, SOC and other variables (Zhongbao et al., 2017).

The polarization of the battery represents the offset of the battery port voltage to the open circuit voltage after power on. In order to simulate this phenomenon, a variety of internal

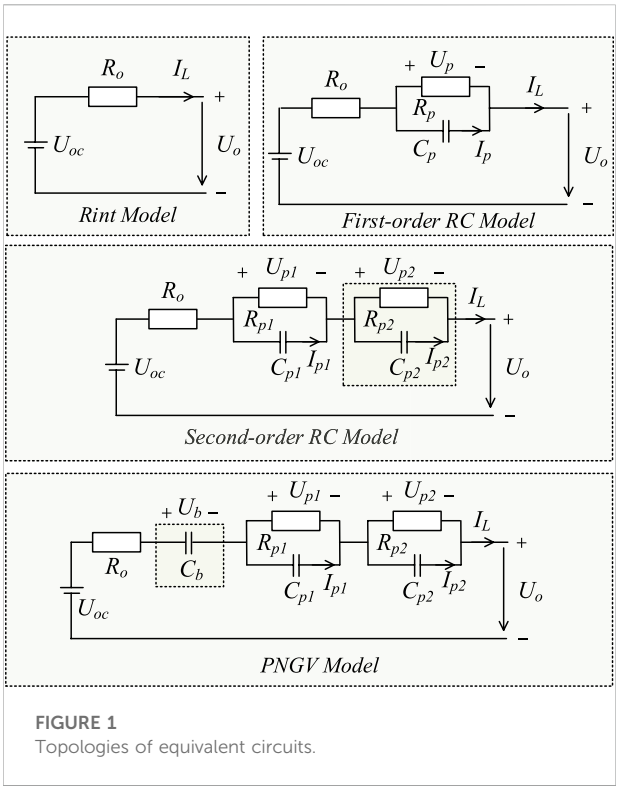

FIGURE 1
Topologies of equivalent circuits.

equivalent circuit models of the battery have appeared. At present, several common equivalent circuit topologies are Rint model, first-order RC model, second-order RC model and PNGV model, as shown in Figure 1.

The Rint model consists of an ideal voltage source and a resistor in series. Its advantages lie in simple topology, easy determination of parameter values and easy realization of modeling and simulation. However, this modeling method simply equates the internal resistance of the battery with a constant resistance. This is equivalent to assuming that the internal resistance of the battery is constant during charging and discharging which deviates from the actual situation. In practice, the internal structure and chemical mechanism of the battery are complex. Affected by the state of charge, working temperature, current and other factors, the internal resistance of the battery is in a dynamic state. Therefore, using an internal resistance with a constant resistance value for equivalence will produce large errors.

The first-order RC model, also known as Thevenin model, adds a first-order RC parallel circuit composed of polarization resistance and polarization capacitance to the topology of Rint model. This resistance-capacitance circuit can simulate the dynamic process of the generation and elimination of battery polarization effect (Rakhmatov et al., 2003). In the Rint equivalent circuit model, the polarization phenomenon is linearly simplified as a kind of instantaneous polarization, while in practical work, the battery usually has a more complex polarization process. For example, when the battery begins to have current, its port voltage will not change instantaneously, but change slowly with time. After the current path is disconnected, the polarization process will not stop instantaneously, but will decay slowly with time. Therefore, in order to more accurately simulate the polarization characteristics of the battery, an RC parallel circuit is added to the first-order RC circuit. By adjusting the value of RC, the nonlinear change process of voltage with time can be approximately simulated, so that the external characteristics of the battery port are more in line with the actual external characteristic curve. Due to the addition of resistance capacitance parallel circuit, the accuracy of the first-order RC model is improved. At the same time, the circuit is relatively simple and the parameters are easy to measure.

The second-order RC model consists of an ohmic resistor and two RC polarization circuits in series. A group of RC parallel circuits are added to the topology of the first-order RC model. This further improves the accuracy of the simulation. Similarly, connecting more RC parallel circuits in series in the circuit can continuously improve the accuracy of the equivalent model, but the complexity of the model also increases, the rapidity of the algorithm is difficult to guarantee, and there are high requirements for hardware.

PNGV model is formed by adding a capacitor on the basis of the second-order RC model to describe the cumulative effect of load current, that is, the change of open circuit voltage caused by external load. PNGV model can truly simulate the charge and discharge behavior of battery, and is widely used in transient analysis. However, PNGV is not suitable for long-time simulation, otherwise the current accumulation effect will cause a large change of open circuit voltage.

It should be noted that in the process of charge and discharge, the internal parameters of the battery are not constant, but constantly changing, and the specific value is related to the SOC in the current state. In order to make the prediction results more accurate, in the application process of the equivalent model, the parameter value of the equivalent model should be corrected in real time according to the estimated value of the current SOC, that is, the battery equivalent circuit model with dynamic parameters should be established.

Through the analysis of the above models, the relationship between the complexity and accuracy of the model is roughly positively correlated, that is, the higher the accuracy of the model, the higher the complexity, and the higher the complexity means the decrease of the calculation speed. Therefore, how to balance the relationship between calculation speed and calculation accuracy is the key point to be considered when selecting the equivalent model. As for SOC estimation algorithm, there are two aspects to consider. On the one hand, in order to reduce the error, the equivalent model is supposed to simulate the actual working state as much as possible. On the other hand, the algorithm based on the

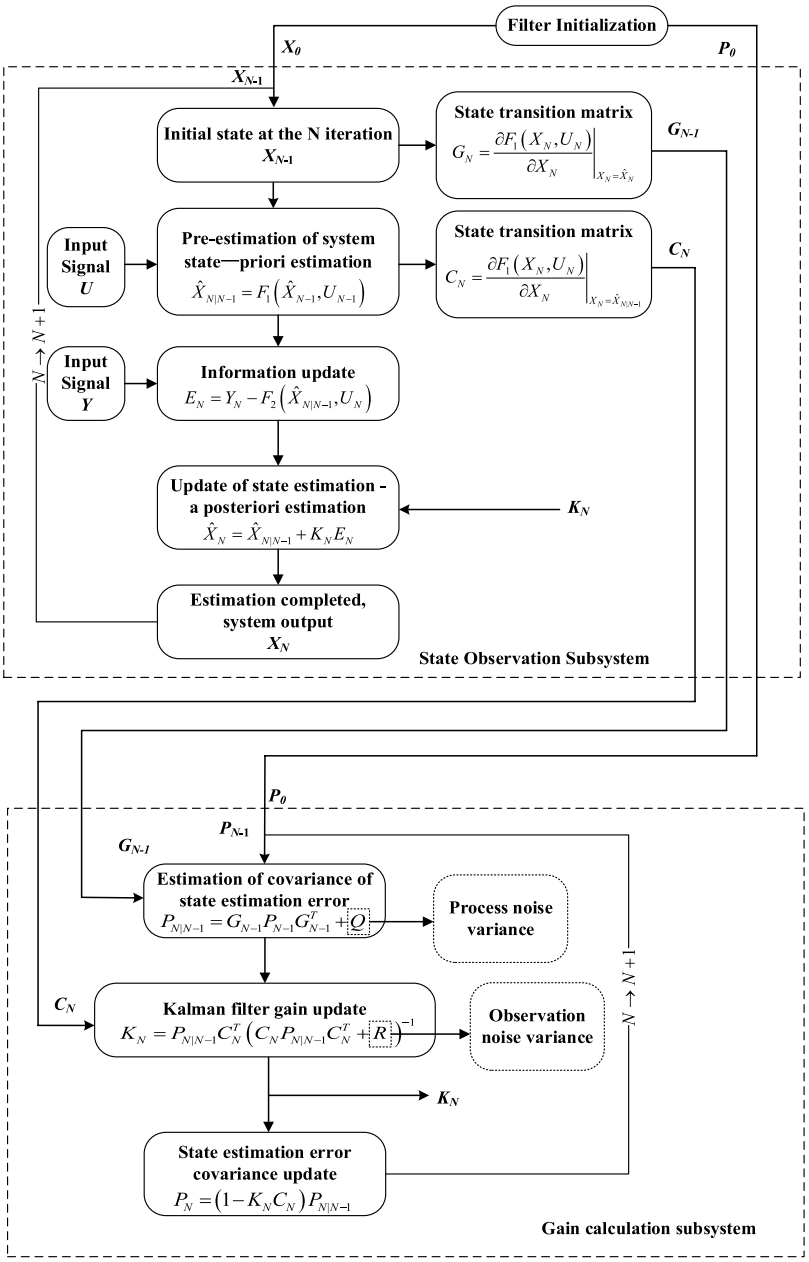

FIGURE 2
SOC calculation process based on EKF.

equivalent model will be embedded in the battery management system. Therefore, the equivalent model should not be too complex and the order should not be too high. It should occupy less memory and be easy to implement. After comprehensive consideration, the first-order RC model is selected as the equivalent model of EKF algorithm.

Combined with relevant circuit theoretical knowledge, the state equations of first-order RC model can be deduced. The state equations are listed based on the voltage current relationship of the complete circuit and the resistance-capacitance parallel circuit, as shown in Eq. 1.

$$U_o = U_{oc} - U_p - I_L R_o$$
$$U_p = \frac{I_p}{sC_p} = \frac{I_L - U_p / R_p}{sC_p} = \frac{I_L}{sC_p} - \frac{U_p}{sC_p R_p} \tag{1}$$

In the above formula, Uoc is the open circuit voltage of the battery in the static state, Uo is the port voltage, Up is the

voltage on the polarization resistance, Ro is the ohmic internal resistance, Rp is the polarization internal resistance, Cp is the polarization capacitance, Ip is the current flowing through the polarization capacitance and IL is the load current. The model is a nonlinear system which takes the load current IL as the input variable and the port voltage Uo as the output variable.

EKF modeling based on first-order RC model

SOC estimation is one of the important functions of battery management system. The accurate prediction of SOC is an important guarantee to realize the functions of battery monitoring and equalization. Kalman filter is an algorithm that uses the monitored data related to the predicted data to correct the estimated value of the predicted data, and finally realizes the accurate estimation of the predicted data through continuous iteration. Kalman filter can be divided into two parts: prediction and correction. It makes *a priori* estimation and a posteriori estimation on the predicted data respectively. The EKF method is more widely used in engineering because most systems are nonlinear in practical application, The basic idea of EKF is to linearize the nonlinear equation by using Taylor expansion. In this way, the nonlinear system is approximated as a linear time-varying system, so the EKF method can be used (Garcia et al., 2010). When the predicted object is a nonlinear system, its state space expression is shown in Eq. 2.

$$\begin{cases} X_N = F_1(X_{N-1}, U_{N-1}) + W \\ Y_N = F_2(X_N, U_N) + V \end{cases} \tag{2}$$

In the above equation, F1 (XN,UN) and F2 (XN,UN) are the state equation function and observation equation function of the system respectively.Expand F1 (XN,UN) and F2 (XN,UN) with first-order Taylor formula respectively:

$$F_1(X_N, U_N) \approx F_1(\hat{X}_N, U_N) + \left.\frac{\partial F_1(X_N, U_N)}{\partial X_N}\right|_{X_N=\hat{X}_N} (X_N - \hat{X}_N) \tag{3}$$

$$F_2(X_N, U_N) \approx F_2(\hat{X}_{N|N-1}, U_N) + \left.\frac{\partial F_2(X_N, U_N)}{\partial X_N}\right|_{X_N=\hat{X}_{N|N-1}} (X_N - \hat{X}_{N|N-1}) \tag{4}$$

The recurrence formula of EKF is shown in Eqs 5–8:
The state space expression of the predicted object:

$$\begin{cases} X_N = G_{N-1}X_{N-1} + [F_1(\hat{X}_{N-1}, U_{N-1}) - G_{N-1}\hat{X}_{N-1}] + W \\ Y_N = C_N X_N + [F_2(\hat{X}_N, U_N) - C_N\hat{X}_N] + V \end{cases}$$

$$\begin{cases} G_N = \left.\dfrac{\partial F_1(X_N, U_N)}{\partial X_N}\right|_{X_N=\hat{X}_N} \\ C_N = \left.\dfrac{\partial F_2(X_N, U_N)}{\partial X_N}\right|_{X_N=\hat{X}_{N|N-1}} \end{cases} \tag{5}$$

The priori estimate of state variables:

$$\hat{X}_{N|N-1} = F_1(\hat{X}_{N-1}, U_{N-1}) \tag{6}$$

The priori estimate of error covariance matrix:

$$P_{N|N-1} = G_{N-1}P_{N-1}G_{N-1}^T + Q \tag{7}$$

Gain matrix:

$$K_N = P_{N|N-1}C_N^T\left(C_N P_{N|N-1}C_N^T + R\right)^{-1} \tag{8}$$

The posteriori estimate of state variables:

$$\hat{X}_N = \hat{X}_{N|N-1} + K_N\left[Y_N - F_2\left(\hat{X}_{N|N-1}, U_N\right)\right] \tag{9}$$

The posteriori estimate of error covariance matrix:

$$P_N = (1 - K_N C_N)P_{N|N-1} \tag{10}$$

In the EKF method, Q and R are the variance of process noise and observation noise respectively. The state transition matrix GN and the observation matrix CN are the real-time first-order derivative of the state equation function and the observation equation function respectively to ensure the prediction accuracy.

The circuit relation equations of the first-order RC model are shown in Eq. 1. Taking SOC and up as state variables, combined with the state expression of EKF predicted system, the state space equation of first-order RC model based on EKF algorithm in discrete system can be deduced, as shown in Eq. 11.

$$\begin{cases} \begin{bmatrix} SOC \\ U_p \end{bmatrix} = \begin{bmatrix} 0 & 0 \\ 0 & -\dfrac{1}{R_p C_p} \end{bmatrix}\begin{bmatrix} SOC \\ U_p \end{bmatrix} + \begin{bmatrix} -\dfrac{1}{Q_{max}} \\ \dfrac{1}{C_p} \end{bmatrix} I_{LN} \\ U_o = F_{2-SOC-OCV}(SOC) - U_p - I_L R_o - V \end{cases} \tag{11}$$

Discretize (11) to obtain the discrete state space equation, as shown in Eq. 12.

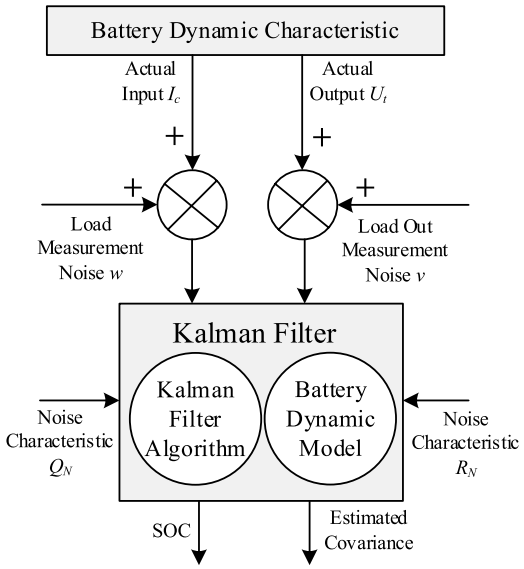

FIGURE 3
Connection block diagram of SOC estimation based on EKF.

$$\begin{cases} \begin{bmatrix} SOC_{N+1} \\ U_{pN+1} \end{bmatrix} = \begin{bmatrix} 1 & 0 \\ 0 & 1-\dfrac{\Delta t}{R_p C_p} \end{bmatrix} \begin{bmatrix} SOC_N \\ U_{pN} \end{bmatrix} + \begin{bmatrix} -\dfrac{\Delta t}{Q_{max}} \\ \dfrac{\Delta t}{C_p} \end{bmatrix} I_{LN} \\ U_{oN} = F_{2-SOC-OCV}(SOC_N) - U_{pN} - I_{LN} R_{oN} - V \end{cases} \tag{12}$$

In the formula, Δt represents the sampling period of the discrete system, and the system coefficient matrices GN、HN、CN、DN are respectively shown in Eq. 13.

$$\begin{aligned} G_N &= \begin{bmatrix} 1 & 0 \\ 0 & 1-\dfrac{\Delta t}{R_p C_p} \end{bmatrix} \\ H_N &= \begin{bmatrix} -\dfrac{\Delta t}{Q_{max}} \\ \dfrac{\Delta t}{C_p} \end{bmatrix} \\ C_N &= \begin{bmatrix} \left.\dfrac{\partial F_2(SOC)}{\partial SOC}\right|_{SOC_N = SOC_{N|N-1}} & 1 \end{bmatrix} \\ D_N &= R_{oN} \end{aligned} \tag{13}$$

It should be noted that Ro、Rp、Cp and other parameters in Eqs 12, 13 are functions of SOC, which means they have mapping relationship with SOC. Therefore, when using EKF algorithm to estimate SOC, it is necessary to make data table and linear

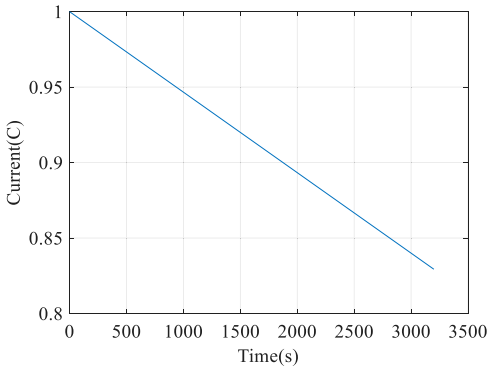

FIGURE 4
Non-constant discharge current.

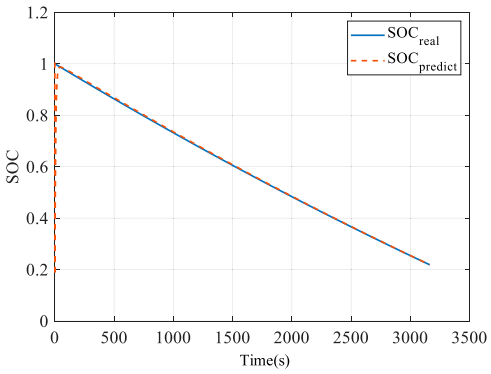

FIGURE 5
SOC estimation curve of EKF method under non-constant current source.

programming the corresponding relationship between Ro、Rp、Cp and SOC. During each iteration, update the equivalent circuit parameters of the first-order RC model according to the latest estimated value of SOC. The SOC calculation process based on EKF is shown in Figure 2.

The linear fitting method for the data table is ordinary least squares. According to the known data points in the data table, the one-to-one mapping curve of SOC and Ro、Rp、Cp is fitted. The slope and intercept of the curve are shown in Eq. 14.

$$\begin{aligned} k &= \frac{\sum_{i=1}^{n} x_i y_i - n\bar{x}\cdot\bar{y}}{\sum_{i=1}^{n} x_i^2 - n\bar{x}^2} \\ b &= \frac{\bar{y}\sum_{i=1}^{n} x_i^2 - \bar{x}\sum_{i=1}^{n} x_i y_i}{\sum_{i=1}^{n} x_i^2 - n\bar{x}^2} \end{aligned} \tag{14}$$

When SOC is at different levels, the variation degree of internal parameters such as internal resistance and capacitance varies greatly. If the data table is fitted as a whole,

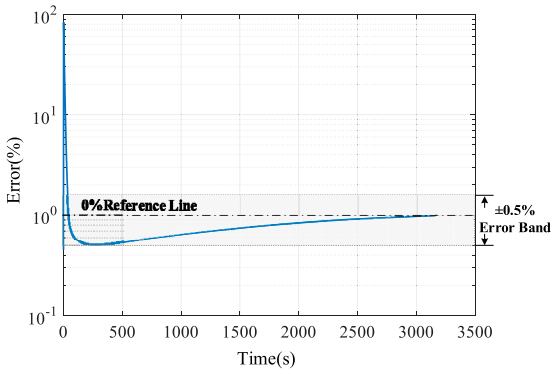

FIGURE 6
SOC estimation error of EKF method under non-constant current source.

TABLE 1 Parameter identification data of first-order RC model.

SOC	Uoc (V)	Ro (Ω)	Rp (Ω)	Cp (F)
0.1	3.4153	0.1243	0.0074	3980.7
0.2	3.5329	0.1222	0.0412	14101
0.3	3.5743	0.1162	0.0425	3500.2
0.4	3.6211	0.1080	0.0158	7500.9
0.5	3.6960	0.1118	0.0243	3432.8
0.6	3.7928	0.1215	0.0323	5535.8
0.7	3.8500	0.0936	0.0038	1928.9
0.8	3.9368	0.1143	0.0181	13468
0.9	4.0200	0.1108	0.0243	2622.6

it is easy to produce large errors and deviate from the real situation. Therefore, in the data processing of the data table, the original algorithm is optimized by piecewise fitting to improve the accuracy of estimation as shown in Figure 3.

Simulation verification

The simulation software used in this paper is Matlab/Simulink. The discharge current decreases as a linear function from 1C, as shown in Figure 4. The SOC estimation curve and the SOC estimation error is shown in Figure 5 and Figure 6 respectively. The simulation results show that EKF method still has good follow-up to SOC. The estimation error is within ±0.5%, and the estimation accuracy is high.

Experimental verification

The internal parameters of the battery will be affected by the changes of various environmental factors. Therefore, parameter identification is needed in SOC estimation. In this paper, in order to improve the accuracy of SOC estimation, the battery discharge state is tracked and corrected in real time by establishing a data table. NCR18650BF lithium-ion battery is selected for the experiment. In order to get the data table, HPPC tests was carried out on the battery. Conduct a charge and discharge pulse test on every SOC step and the SOC step is 0.1. The amplitude of charge and discharge pulses is 1C, lasting for 20s. The standing interval between charge and

TABLE 2 elements used in the experiment including and battery specifications.

Element	Battery	NCR18650BF
	Electronic Load	Chroma633200A
	Hall Current Sensor	HS01-50
Battery Specifications	Capacity	3400mAh
	Full Voltage	4.2V
	Termination Voltage	2.75V
	Standard Voltage	3.7V
	Operating Temperature	-20~60°C

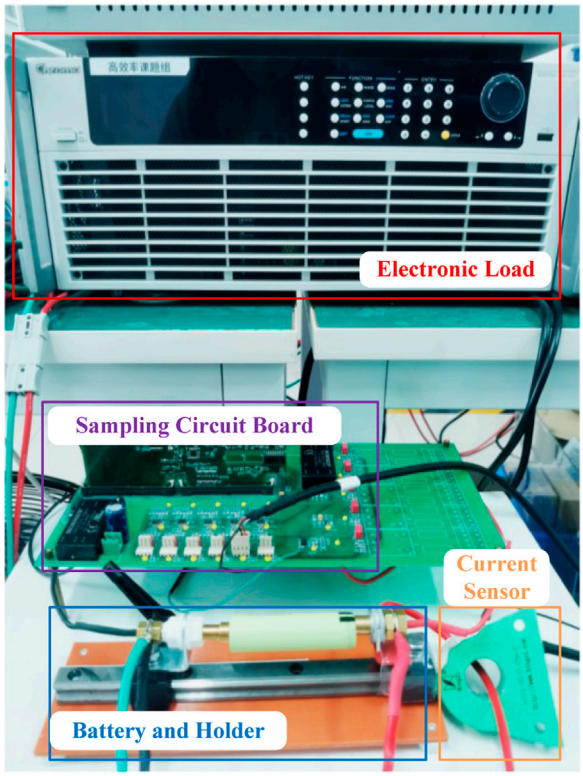

FIGURE 7
Appearance of experimental platform.

FIGURE 8
Electronic load display.

discharge pulses is 80s. After that, SOC is adjusted with a charge and discharge current of 0.2C. After standing for 1 hour, conduct the next charge and discharge pulse test and repeat this cycle. The experimental temperature is 25 ± 2°C. Through HPPC tests, the data table of internal parameters of lithium-ion battery can be obtained. It is shown in Tables 1 and 2.

NCR18650BF battery was used to build the experimental prototype, and the SOC estimation experiment was carried out in constant current discharge mode.

The experimental platform is shown in Figure 7. It mainly includes the battery discharge link, sampling link and calculation link. In the figure, from top to bottom, there are electronic load, sampling circuit board, battery, battery holder and Hall current sensor. The load used in the experiment is the 63200A series programmable electronic load of Chroma company, which has various modes such as constant current (CC), constant resistance (CR), constant voltage (CV), constant power (CP), etc. In the experiment, the constant current discharge of the battery can be controlled by adjusting the electronic load in the CC working mode. At the same time, the electronic load used in the experiment can measure the SOC of the battery and display it in real time as shown in Figure 8. The measured value is taken as the real-time actual value of SOC for reference.

The calculation link processes and calculates the sampled voltage and current data to obtain the real-time SOC prediction value. The program flow chart is shown in Figure 9.

In the program, timer interrupt and main loop are carried out in parallel. Timer interrupt is used to collect port voltage and load current to track the change of detectable value. The main cycle is responsible for EKF calculation according to the collected data to realize SOC prediction. Due to the large fluctuation range of the actually measured data table, if the overall linear programming of the data table is carried out, the prediction result error is very large. Therefore, it is decided to carry out the linear programming in sections, and the linear programming coefficient of each function is different. The SOC is divided into ten levels, and each level is stepped by 0.1. When the program is running, the specific linear programming coefficient should be judged according to the level where the SOC iteration value is located. It should be noted that the

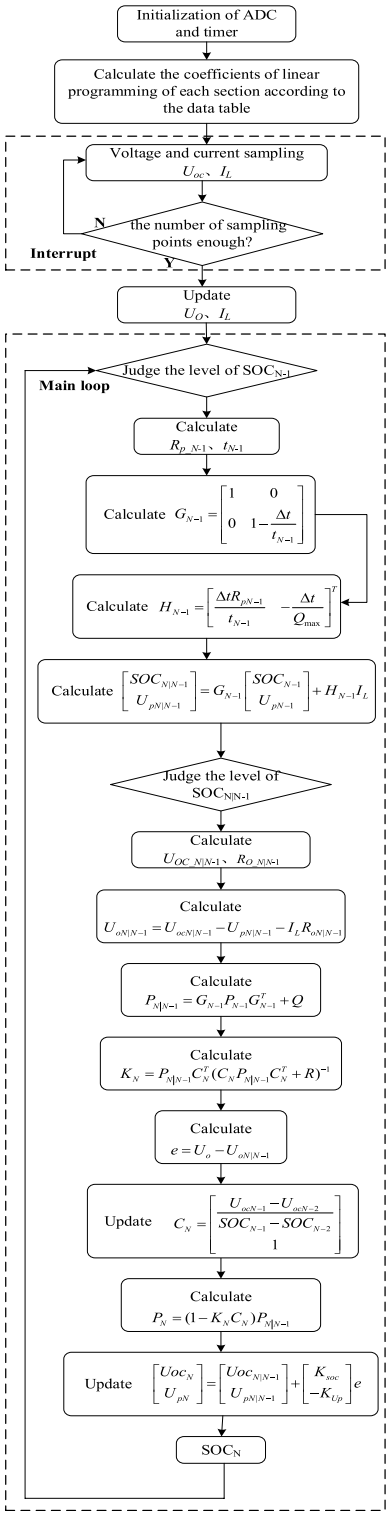

FIGURE 9
Procedure flow.

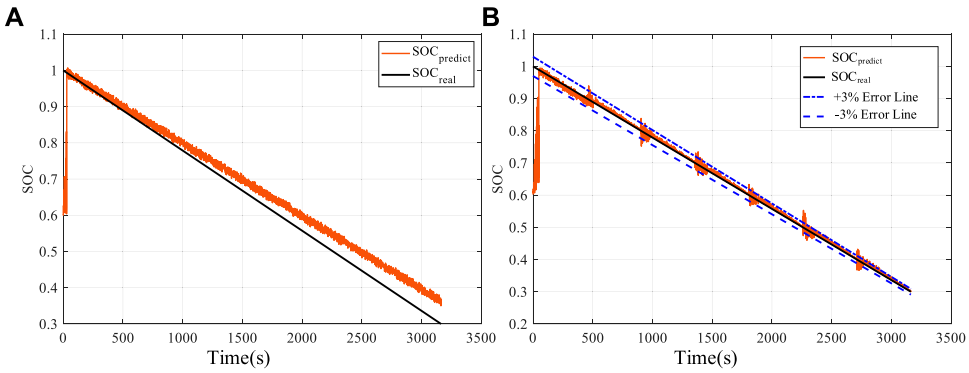

FIGURE 10
(A) Comparison between actual SOC curve and estimated SOC curve before optimization. **(B)** Comparison between actual SOC curve and estimated SOC curve after optimization.

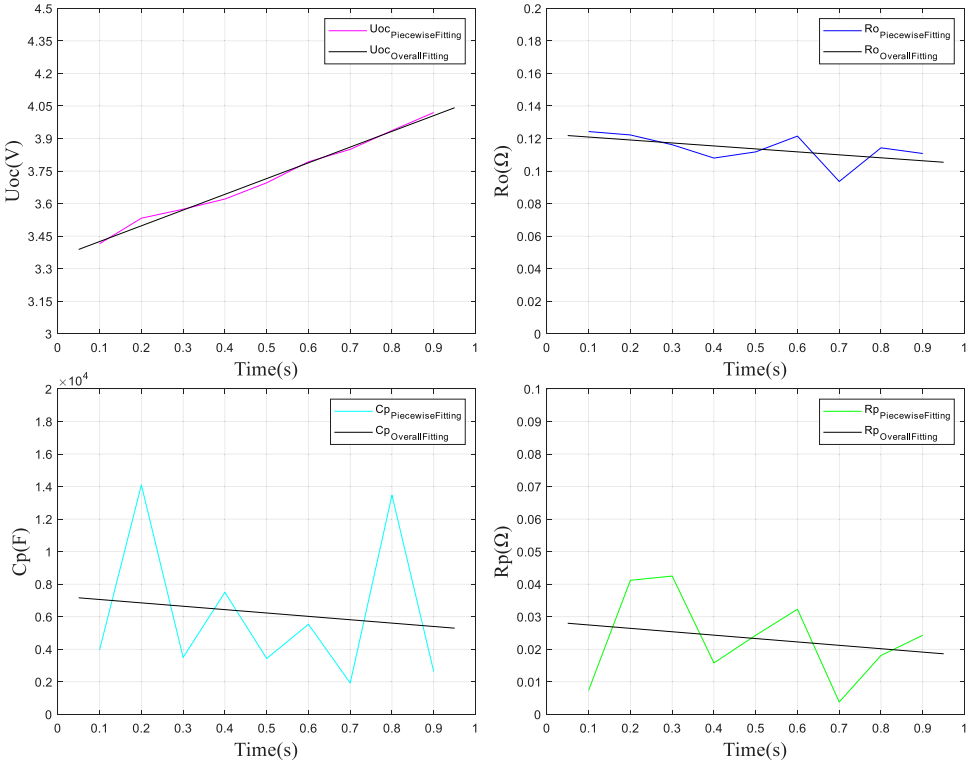

FIGURE 11
Comparison between overall fitting and piecewise fitting.

sampled data and the data used for EKF calculation should be stored separately, so as not to change the data used for calculation before the EKF calculation in the main cycle is completed. In this program, set the sampling frequency to 1 kHz and the frequency of parameter update to 5Hz.

Figure 10A shows the comparison between the SOC estimation curve measured in the experiment before optimization and the actual curve. At the beginning of the iteration, the SOC estimated value can quickly follow the real value in a short time. Then with the passage of time, the estimation error becomes larger and larger. And because of the disturbance and noise in the actual experiment, the estimation result has a small amplitude oscillation.

After analysis, this may be due to the deviation error caused by the overall linear fitting when identifying the data table in the

algorithm. Therefore, piecewise fitting is adopted for the data table instead of overall fitting. When SOC is at different levels, different calculation coefficients are used. Figure 11 shows the comparison of different fitting methods of the data table. The optimized experimental results are shown in Figure 10B. It can be seen that although there are still oscillations and offsets in the estimation results, a correction will be made whenever entering a new level. As time goes on, the estimated results will not deviate significantly from the true value. Compared with the results before optimization, the estimation accuracy is significantly improved.

Summary

Aiming at the problem of battery SOC estimation, this paper proposes an EKF estimation algorithm based on piecewise fitting. The traditional EKF algorithm directly fits various parameters based on the full SOC segment, which is easy to cause the problem of parameter overfitting and then lead to the deviation of estimation results. The proposed method can achieve SOC tracking in the whole SOC range, has strong self-correction ability, and the estimation error in actual working conditions is basically less than 3%. Subsequently, the author will further optimize the algorithm to optimize the oscillation of SOC estimation value caused by switching state matrix parameters in different SOC sections, so as to further reduce the maximum estimation error.

Data availability statement

The original contributions presented in the study are included in the article/supplementary materials, further inquiries can be directed to the corresponding author.

Author contributions

BY contributed to methodology and original draft. GJ organized the data curation. WC performed the visualization of the manuscript. HY contributed to review and editing. All authors contributed to manuscript revision, read, and approved the submitted version.

Funding

This work was supported in part by the Supported by the Open Fund of Jiangsu Engineering Technology Research Center for Energy Storage Conversion and Application (China Electric Power Research Institute) under Grant NY80-21-001.

Conflict of interest

Author BY, GL, and, HL were employed by the company China Electric Power Research Institute Co, Ltd.

The remaining author declares that the research was conducted in the absence of any commercial or financial relationships that could be construed as a potential conflict of interest.

Publisher's note

All claims expressed in this article are solely those of the authors and do not necessarily represent those of their affiliated organizations, or those of the publisher, the editors and the reviewers. Any product that may be evaluated in this article, or claim that may be made by its manufacturer, is not guaranteed or endorsed by the publisher.

References

Arasaratnam, I., Haykin, S., and Hurd, T. R. (2010). Cubature Kalman filtering for continuous-discrete systems: Theory and simulations. *IEEE Trans. Signal Process.* 58 (10), 4977–4993. doi:10.1109/tsp.2010.2056923

Caumont, O., Le Moigne, P., Rombaut, C., Muneret, X., and Lenain, P. (2000). Energy gauge for lead-acid batteries in electric vehicles. *IEEE Trans. energy Convers.* 15, 354–360. doi:10.1109/60.875503

Chen, Q., Jiang, J., Liu, S., and Zhang, C. (2016). A novel sliding mode observer for state of charge estimation of EV lithium batteries. *J. Power Electron.* 16 (3), 1131–1140. doi:10.6113/jpe.2016.16.3.1131

Chen, Q., Jiang, J., Ruan, H., and Zhang, C. (2017). Simply designed and universal sliding mode observer for the SOC estimation of lithium-ion batteries. *IET Power Electron.* 10 (6), 697–705. doi:10.1049/iet-pel.2016.0095

Chenic, A. Ş., Cretu, A. I., Burlacu, A., Moroianu, N., Vîrjan, D., Huru, D., et al. (2022). Logical analysis on the strategy for a sustainable transition of the world to green energy—2050. Smart cities and villages coupled to renewable energy sources with low carbon footprint. *Sustainability* 14, 8622. doi:10.3390/su14148622

Dong, X., Zhang, C., and Jiang, J. (2018). Evaluation of SOC estimation method based on EKF/AEKF under noise interference. *Energy Procedia* 152 (1), 520–525. doi:10.1016/j.egypro.2018.09.204

Garcia, P., Fernandez, L. M., Garcia, C. A., and Jurado, F. (2010). Energy management system of fuel-cell-battery hybrid tramway. *IEEE Trans. Ind. Electron.* 57 (12), 4013–4023. doi:10.1109/tie.2009.2034173

Guo, X., Kang, L., Yao, Y., Huang, Z., and Li, W. (2016). Joint estimation of the electric vehicle power battery state of charge based on the least squares method and the Kalman filter algorithm. *Energies* 9 (2), 100–116. doi:10.3390/en9020100

He, H., Qin, H., Sun, X., and Shui, Y. (2013). Comparison study on the battery so C estimation with EKF and UKF algorithms. *Energies* 6 (10), 5088–5100. doi:10.3390/en6105088

Lee, Y. S., and Cheng, M. W. (2005). Intelligent control battery equalization for series connected lithium-ion battery strings. *IEEE Trans. Ind. Electron.* 52 (5), 1297–1307. doi:10.1109/tie.2005.855673

Li, Jiahao, Barillas, J. K., Guenther, C., and Danzer, M. A. (2013). A comparative study of state of charge estimation algorithms for LiFePO4 batteries used in electric vehicles. *J. Power Sources* 230, 244–250. doi:10.1016/j.jpowsour.2012.12.057

Li, Z., Huang, J., Liaw, B. Y., and Zhang, J. (2017). On state-of-charge determination for lithium-ion batteries. *J. Power Sources* 348, 281–301. doi:10.1016/j.jpowsour.2017.03.001

Liu, Z., Li, Z., Zhang, J., Su, L., and Ge, H. (2019). Accurate and efficient estimation of lithium-ion battery state of charge with alternate adaptive extended kalman filter and ampere-hour counting methods. *Energies* 12, 757. doi:10.3390/en12040757

Luo, X., Wang, J., Dooner, M., and Clarke, J. (2015). Overview of current development in electrical energy storage technologies and the application potential in power system operation. *Appl. Energy* 137, 511–536. doi:10.1016/j.apenergy.2014.09.081

Rakhmatov, D., Vrudhula, S., and Wallach, D. A. (2003). A model for battery lifetime analysis for organizing applications on a pocket computer. *IEEE Trans. VLSI. Syst.* 11 (6), 1019–1030. doi:10.1109/tvlsi.2003.819320

Sher, H. A., and Addoweesh, K. E. (2012). Power storage options for hybrid electric vehicles—a survey. *J. Renew. Sustain. Energy* 4 (5), 1588–1593.

Sridhar, S., and Salkuti, S. R. (2022). Development and future scope of renewable energy and energy storage systems. *Smart Cities* 5, 668–699. doi:10.3390/smartcities5020035

Wang, H., and Zhou, G. (2018). State of charge prediction of supercapacitors via combination of Kalman filtering and backpropagation neural network. *IET Electr. Power Appl.* 12 (4), 588–594. doi:10.1049/iet-epa.2017.0242

Xing, Y., Ma, E., Tsui, K. L., and Pecht, M. (2011). Battery management systems in electric and hybrid vehicles. *Energies* 4 (12), 1840–1857. doi:10.3390/en4111840

Xiong, R., Cao, J., Yu, Q., He, H., and Sun, F. (2018). Critical review on the battery state of charge estimation methods for electric vehicles. *IEEE Access* 6, 1832–1843. doi:10.1109/access.2017.2780258

Xiong, X., Wang, S. L., Fernandez, C., Yu, C., Zou, C., and Jiang, C. (2020). A novel practical state of charge estimation method: An adaptive improved ampere-hour method based on composite correction factor. *Int. J. Energy Res.* 44 (14), 11385–11404. doi:10.1002/er.5758

Xu, W., Xu, J., and Yan, X. (2020). Lithium-ion battery state of charge and parameters joint estimation using cubature Kalman filter and particle filter. *J. Power Electron.* 20 (1), 292–307. doi:10.1007/s43236-019-00023-4

Yan, X., Wang, C., Wang, Z., Ma, H., Liang, B., and Wei, X. (2021). A united control strategy of photovoltaic-battery energy storage system based on voltage-frequency controlled VSG. *Electronics* 10, 2047. doi:10.3390/electronics10172047

Zhang, C., Jiang, J., Zhang, L., Liu, S., Wang, L., and Loh, P. (2016). A generalized SOC-OCV model for lithium-ion batteries and the SOC estimation for LNMCO battery. *Energies* 9 (11), 900. doi:10.3390/en9110900

Zhang, Y., Xiong, R., He, H., and Shen, W. (2017). Lithium-Ion battery pack state of charge and state of energy estimation algorithms using a hardware-in-the-loop validation. *IEEE Trans. Power Electron.* 32 (6), 4421–4431. doi:10.1109/tpel.2016.2603229

Zheng, W., Xia, B., Wang, W., Lai, Y., Wang, M., and Wang, H. (2019). State of charge estimation for power lithium-ion battery using a fuzzy logic sliding mode observer. *Energies* 12 (13), 2491. doi:10.3390/en12132491

Zhongbao, Wei, Meng, Shujuan, Tseng, K. J., Lim, T. M., Soong, B. H., and Skyllas-Kazacos, M. (2017). An adaptive model for vanadium redox flow battery and its application for online peak power estimation. *J. Power Sources* 344, 195–207. doi:10.1016/j.jpowsour.2017.01.102

Zhou, D., Zhang, K., Ravey, A., Gao, F., and Miraoui, A. (2016). Online estimation of lithium polymer batteries state-of-charge using particle filter-based data fusion with multimodels approach. *IEEE Trans. Ind. Appl.* 52 (3), 2582–2595. doi:10.1109/tia.2016.2524438

Zhu, C., Coleman, M., and Hurley, W. (2004). State of charge determination in a lead-acid battery: Combined EMF estimation and ah. Balance approach[C]//Power electronics specialists conference. *IEEE 35th Annu.* 3, 1908–1914. PESC 04. 2004.

frontiers | Frontiers in Energy Research

TYPE Original Research
PUBLISHED 29 September 2022
DOI 10.3389/fenrg.2022.1005796

OPEN ACCESS

EDITED BY
Liansong Xiong,
Nanjing Institute of Technology (NJIT), China

REVIEWED BY
Tingting Sun,
Hefei University of Technology, China
Bowen Wang,
Kashgar University, China
Zongbo Li,
Xi'an Jiaotong University, China

*CORRESPONDENCE
Jiangdong Cao,
caojd@jssc.edu.cn

SPECIALTY SECTION
This article was submitted to Process and Energy Systems Engineering, a section of the journal Frontiers in Energy Research

RECEIVED 28 July 2022
ACCEPTED 22 August 2022
PUBLISHED 29 September 2022

CITATION
You J, Xu D and Cao J (2022), Dynamic power-based temporary frequency support scheme for a wind farm. *Front. Energy Res.* 10:1005796. doi: 10.3389/fenrg.2022.1005796

Dynamic power-based temporary frequency support scheme for a wind farm

Jiahan You, Dan Xu and Jiangdong Cao*

School of Intelligent Manufacturing and Information, Jiangsu Shipping College, Nantong, China

Doubly fed induction generators can participate in frequency support following a disturbance by releasing their rotational energies. However, when regaining the rotor speed, a secondary frequency dip (SFD) tends to produce a sudden output drop. This study suggests a dynamic power-based stepwise inertial control (IC) scheme of a wind power plant for minimizing the SFD while reducing the maximum frequency deviation (MFD), considering the non-negligible wake. To this end, the reference of the output power increases to the torque limit. Afterward, the power reference smoothly decays with the dynamically decreasing incremental power and then automatically switches to the maximum power point tracking operation. The performance of the temporary frequency support with the suggested stepwise IC strategy is investigated with various penetration levels of wind power. Test results demonstrate that the suggested stepwise IC strategy can minimize the SFD and reduce mechanical stresses on the wind turbine during the recovery of the rotor speed while reducing the MFD. Therefore, the suggested stepwise IC strategy secures the dynamic frequency stability of an electric power system dominated by wind power generations.

KEYWORDS

stepwise inertial control, power system control, second frequency dip, mechanical stress, rotor speed recovery

Introduction

The electric power system faces challenges of system frequency stability with high-wind-power-penetrated power girds (Wang et al., 2020). The reasons for this phenomenon are explained as follows: doubly fed induction generators (DFIGs) are unable to sustain the system frequency since they decouple the speed of the rotor from the frequency (Xiong et al., 2020; Guo et al., 2022). This results in a reduction in the system inertia response and primary frequency response (Gevorgian et al., 2015; Yang et al., 2021). The range of operation of the DFIG is almost six times that of the conventional synchronous generators (SGs) due to the various characteristics of the DFIG and SG; therefore, the DFIG can be a strong choice to sustain the system frequency (Wang and Tomsovic, 2018). Thus, DFIGs are required to participate in inertial control (IC) to preserve the frequency stability of the power grid.

The IC strategies can be roughly divided into three classifications characterized by the definition of the shape of the power reference: *df/dt*-based IC, frequency deviation-based IC, and stepwise IC (Morren et al., 2006; Vyver et al., 2016; Li et al.,2017; Hu and WU, 2019; Wu et al., 2019; Kheshti et al., 2019; Peng et al., 2020). The *df/dt*-based IC can emulate the inertia response to support the reduced inertia response. Frequency deviation-based IC is capable of emulating the primary frequency response to reduce the maximum grid frequency deviation (MGFD). A stepwise IC scheme is determined by the preset power reference trajectories and not the measured grid frequency. The power reference trajectories can be a temporary frequency control trajectory (Yang et al., 2018) and a reliable power reference trajectory (Kheshti et al., 2019). The stepwise IC can boost the grid frequency at a high level owing to the rapid frequency support response (Yang et al., 2018; Kheshti et al., 2019). However, after performing the frequency support response, the rotor speed is required to be regained up to the optimal speed, such a process tends to cause a second frequency drop (SFD) (Lao et al., 2020).

A constant stepwise power reference is addressed to regain the rotor speed (Ullah et al., 2008), and due to the sudden output power drop, an SFD is inevitable. To mitigate the SFD, the authors (Hafiz and Abdennour, 2015) suggest that the power reference of the wind turbines decays in a ramp manner during the recovery period of the rotor speed. The authors (Kang et al., 2016; Xu and Xu, 2017) propose a fixed power reference scheme and a constantly accelerating power reference based on mechanical power to regain the rotor speed, however, the SFD still exists due to the sudden power reduction; furthermore, the output power reduction to counterbalance the SFD and the rotor speed recovery is difficult to determine. A two-level variable coefficient-based controller is designed for DFIG (Xiong et al., 2021). However, the effectiveness of the two-level scheme strongly depends on the predetermined training of the fuzzy controller.

This study addresses a dynamic power-based stepwise IC strategy of the wind power plant with the purpose of minimizing the SFD and mechanical stresses on the wind turbine during the recovery of the rotor speed while reducing the MGFD. To this end, the power reference increases to the torque limit. Afterward, the power reference smoothly decays with the dynamically decreasing incremental power and then automatically switches to the maximum power point tracking operation (MPPTO). The benefits of the proposed stepwise IC strategy are indicated with various penetration levels of wind power.

Doubly fed induction generator model

The mechanical power captured from the wind through the wind turbine can be defined as a nonlinear function of the rotor radius (R), air density (ρ), wind speed (vw), pitch angle (β), tip-speed ratio (λ), and power coefficient (c_p), as follows:

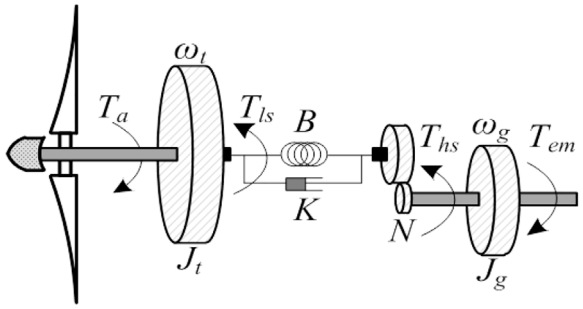

FIGURE 1
Two-mass model.

$$P_m = \frac{1}{2}\rho\pi R^2 v_{wind}^3 c_P(\lambda,\beta), \tag{1}$$

$$c_P(\lambda,\beta) = 0.645\left\{0.00912\lambda + \frac{-5 - 0.4(2.5+\beta) + 116\lambda_i}{e^{21\lambda_i}}\right\}, \tag{2}$$

$$\lambda_i = \frac{1}{\lambda + 0.08(2.5+\beta)} - \frac{0.035}{1 + (2.5+\beta)^3}, \tag{3}$$

$$\lambda = \frac{\omega_r R}{v_w}. \tag{4}$$

In (1), c_p has a maximum value ($c_{P,\,\max}$) at the optimal tip-speed ratio (λ_{opt}), where the DFIG can capture the maximum power from the wind. The formula of the MPPTO is as follows:

$$P_{MPPT} = \frac{1}{2}\rho\pi R^2\left(\frac{\omega_r R}{\lambda_{opt}}\right)^3 c_{P,\max} = k_g\omega_r^3, \tag{5}$$

where P_{MPPT} is the reference for the MPPTO and k_g is set to 0.512.

To model the mechanical dynamics, a two-mass shaft model, which is expressed in (6)–(8), is employed in this study (see Figure 1). T_{wt}, H_t, ω_t, T_m, H_g, and ω_r are the mechanical torques, inertia constants, and rotor speeds of the turbine and generator, respectively. T_e is the generator's electrical torque. K and B are the spring constant and damping constant, respectively. θ_t and θ_{ls} are the displacements of the angular of the turbine rotor and low-speed shaft, respectively. ω_{ls} is the low-speed shaft rotor speed, as shown in (Boukhezzar and Siguerdidjane, 2011).

$$2H_t\frac{d\omega_t}{dt} = T_m - T_{ls}, \tag{6}$$

$$2H_g\frac{d\omega_r}{dt} = T_{hs} - T_{em}, \tag{7}$$

$$T_{ls} = K(\theta_t - \theta_{ls}) + B(\omega_t - \omega_{ls}). \tag{8}$$

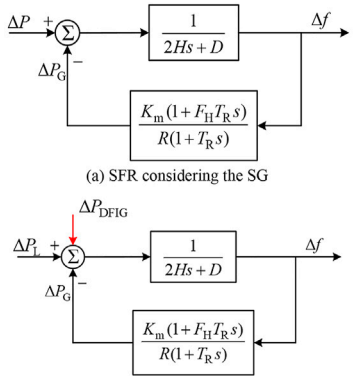

FIGURE 2
SFR of the single machine model.

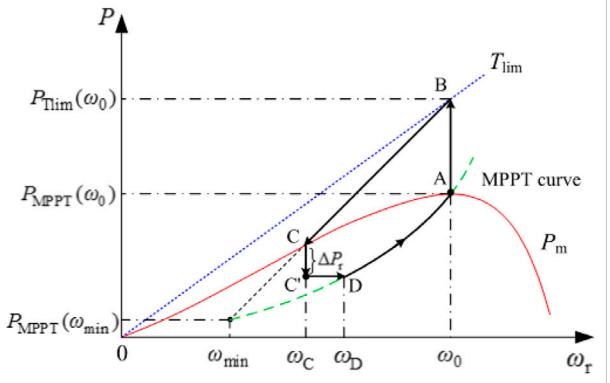

FIGURE 3
Operational concepts of the conventional stepwise IC scheme.

Stepwise inertial control of a wind power plant

During the frequency support phase (FSP), active power is injected into the grid by decreasing the rotor speed. When designing the stepwise IC scheme, more attention should be paid to the stalling of the rotor speed. During the rotor speed recovery phase (RSRP), the rotor speed is restored by absorbing the power from the grid; the degree of the SFD should be noticed when designing the control strategy.

As illustrated in Figure 2A, based on the low-order system frequency response model (shi et al., 2018), the system frequency deviation ($\Delta f\ (t)$) in the time domain can be represented as follows:

$$\Delta f\,(t) = \frac{\Delta P}{K_1 + D}\left[1 + \alpha e^{-\xi\omega_n t}\sin\left(\omega_d t + \beta\right)\right], \tag{9}$$

$$\omega_n = \sqrt{\frac{DR + K_m}{2HRT_R}}, \tag{10}$$

$$\xi = \left(\frac{2HR + (DR + K_m F_H)T_R}{2\,(DR + Km)}\right)\omega_n, \tag{11}$$

where ω_n, ξ, and ω_d are the natural oscillation frequency, damping ratio, and damped frequency, respectively. α and β are the derived coefficients from the SFR model. ΔP is the size of the disturbance.

The maximum frequency deviation and frequency nadir can be given as shown in Eqs 14 and 15, respectively, by deriving the occurrence time of the frequency nadir.

$$\Delta f_{\max} = \frac{\Delta P}{K_1 + D}\left(1 + \alpha_1 e^{-\xi\omega_n t_{nadir}}\right), \tag{12}$$

$$f_{nadir} = f_{nom} - \Delta f_{\max} = f_{nom} - \frac{\Delta P}{K_1 + D}\left(1 + \alpha_1 e^{-\xi\omega_n t_{nadir}}\right), \tag{13}$$

where K_1 is the setting value of the primary governor response. f_{nom}, $\Delta f_{\max}$, and f_{nadir} are the nominal system frequency, maximum frequency deviation, and frequency nadir, respectively.

As shown in (Yang et al., 2022), the improved SFR model is represented as shown in Figure 2B. The equivalent size of disturbance (ΔP) is calculated as follows:

$$\Delta P = \Delta P_L - \Delta P_{DFIG}, \tag{14}$$

where ΔP_{DFIG} indicates the additional power from the DFIG when performing temporary frequency support.

Thus, frequency nadir can be rearranged as follows:

$$f_{nadir} = f_{nom} - \frac{\Delta P_L - \Delta P_{DFIG}}{K_1 + D}\left(1 + \alpha_1 e^{-\xi\omega_n t_{nadir}}\right). \tag{15}$$

In (Eq. 15), it is evidenced that the DFIG supports system frequency after the system frequency changes. The instantaneous system frequency is higher, thereby reducing the maximum system frequency deviation with the larger ΔP_{DFIG}. Furthermore, in the RSRP, if a larger ΔP_{DFIG} instantly decreases from the power reference, a severe SFD tends to be produced. If ΔP_{DFIG} smoothly decreases, the depth of the SFD can be reduced.

Conventional stepwise inertial control scheme

Figure 3 displays the features of the conventional stepwise IC scheme, which includes two sequential stages highlighted in the black line: FSP (line A to C) and RSRP (line C to D). Prior to a severe disturbance, the DFIG operates in the MPPTO, which corresponds

to point A. Upon detecting a disturbance, to reduce Δf_{max}, the DFIG instantly increases its output power from P_0 to P_{Tlim} (ω_0), which is the torque limit at ω_0 and corresponds to point B, as shown in Figure 3. To avoid the stalling of the rotor speed, the power reference for stepwise IC (P_{set}) is defined as follows:

$$P_{set} = \frac{P_{Tlim}(\omega_0) - P_{MPPT}(\omega_{min})}{\omega_0 - \omega_{min}}(\omega_r - \omega_{min}) + P_{MPPT}(\omega_{min}), \tag{16}$$

where P_{MPPT} (ω_0) is the power reference of the MPPT operation prior to a disturbance. ω_{min} is the minimum rotor speed. P_{MPPT} (ω_{min}) is the value of P_{MPPT} at ω_{min}.

A conventional stepwise IC scheme can reduce the MFD since a certain amount of kinetic energy is rapidly released in the early stage of a frequency disturbance. The released kinetic energy (ΔE) during the FSP can be expressed as follows:

$$\Delta E = 0.5 J_{DFIG}(\omega_0^2 - \omega_C^2), \tag{17}$$

where J_{DFIG} represents the moment of inertia of the DFIG. ω_C is the rotor speed at operating point C, as shown in Figure 3.

According to the swing equation, since the output power of the DFIG is more than P_m, the rotor speed decreases so that P_{set} decreases with ω_r from operating point B to operating point C. It should be noticed that ω_r would converge to point C, which indicates the intersection of the P_m curve and (16). Thus, the conventional stepwise IC strategy avoids stalling of ω_r since ω_C is located in the stable operating region.

After ω_r convergence, the conventional stepwise IC scheme instantly reduces the reference of the output power from P_{set} (ω_C) to P_{set} (ω_C) $-\Delta P_r$, so as to restore ω_r, and then, is kept until P_{set} meets the MPPTO curve. At point D, P_{ref} is changed back to P_{MPPT}, as shown in Eq. 5, and then, ω_r is restored to ω_0. The power reference for lines C to A can be expressed as shown in Eqs 18 and 19. It should be noted that to reduce the depth of the SFD, a small ΔP_r is inevitable; nevertheless, the rotor speed recovery is extended, and vice versa.

$$P_{set} = P_{set}(\omega_C) - \Delta P_r, \tag{18}$$

$$P_{set}(\omega_r) = P_{MPPT}(\omega_r). \tag{19}$$

To recover the rotor speed at point C, as shown in Figure 3, the swing equations on the DFIG and power system can be expressed as follows:

$$2H_{DFIG}\omega_r \frac{d\omega_r}{dt} = \Delta P_r, \tag{20}$$

$$2Hf_{sys}\frac{df_{sys}}{dt} = (\Delta P_G - \Delta P_L - \Delta P_r), \tag{21}$$

where H_{DFIG} is the inertial time constant of the DFIG.

As shown in Eqs 20 and 21, ΔP_r with rapid variation characteristics causes a subsequent disturbance to the power grid, which leads to an SFD; furthermore, the size of the SFD is dependent on ΔP_r. Figure 4 illustrates the results of the conventional stepwise IC strategy with different settings for ΔP_r. As shown in (20), with a large ΔP_r, the rotor speed recovery is rapid and a severe SFD is produced (as seen in Eq. 21).

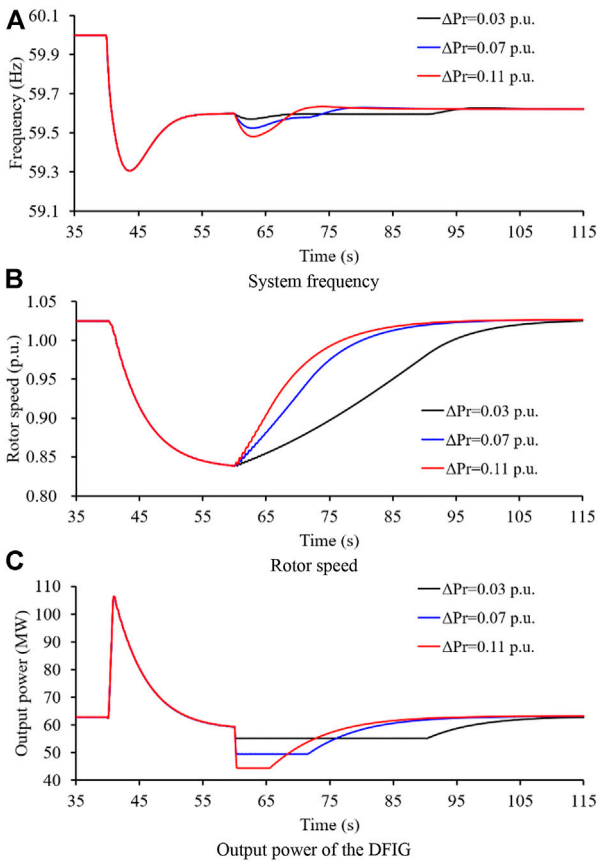

FIGURE 4
Results of the conventional scheme with various forms of ΔP_r.

Implementation of the conventional scheme may face several challenges, which are as follows: 1) The tradeoff between the depth of the SFD and rotor speed recovery is difficult to achieve. 2) The control strategy of the conventional RSR scheme may cause instability issues if a sudden disturbance occurs.

Proposed stepwise inertial control scheme

To address the abovementioned issues of the conventional stepwise IC scheme, this study suggests a dynamic power-based stepwise IC of a DFIG, which combines the FSP and RSRP, as shown in Figure 5.

When the system frequency exceeds the deadband, the DFIG starts up the stepwise IC controller. The power reference for stepwise IC is illustrated as follows:

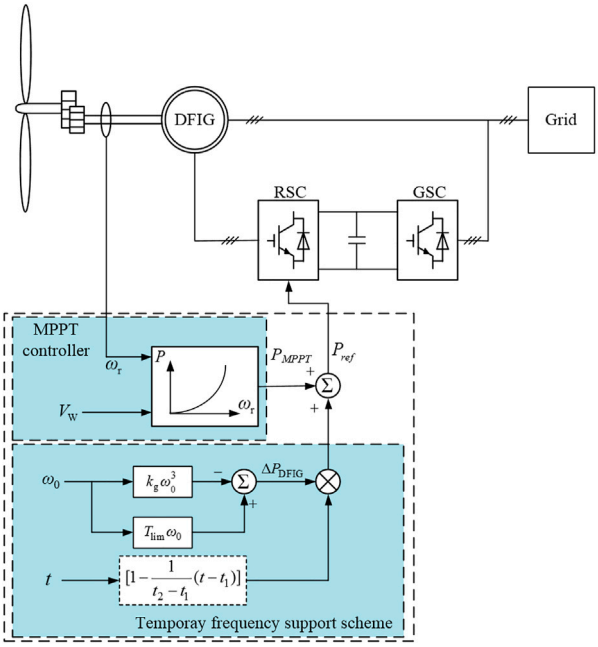

FIGURE 5
Control concept of dynamic power-stepwise IC scheme.

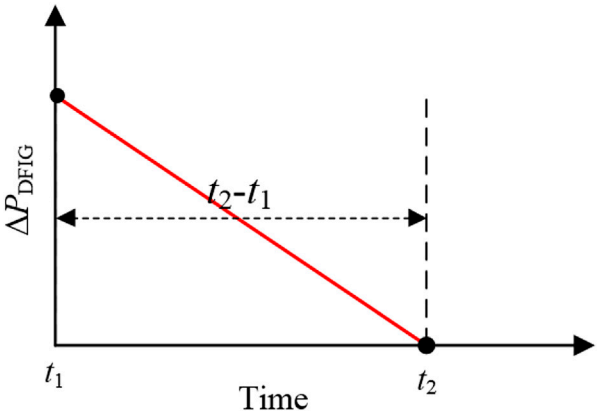

FIGURE 6
Regulation characteristics of ΔP_{DFIG}.

$$P_{ref}(\omega_r, t) = P_{MPPT} + \Delta P_{DFIG}, \tag{22}$$

$$\Delta P_{DFIG} = [P_{\mathrm{Tlim}}(\omega_0) - P_{\mathrm{MPPT}}(\omega_0)] \times \left[1 - \frac{1}{t_2 - t_1}(t - t_1)\right], \tag{23}$$

where ΔP_{DFIG} is the incremental power. t_1 is the instant of the initiation of the stepwise IC scheme. t_2 indicates the instant for

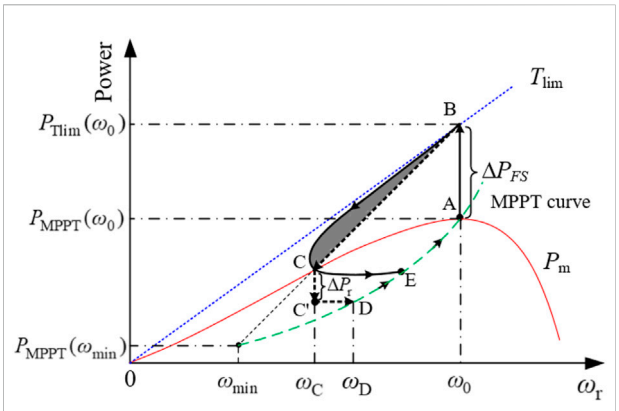

FIGURE 7
Operational concepts of the proposed and conventional stepwise IC schemes.

meeting the MPPTO curve, and thus, t_2–t_1 represents the scheduled time for decreasing the ΔP_{DFIG} to 0.

As illustrated in (Eq. 23) and Figure 6, it is evidenced that smaller t_2–t_1 is able to accelerate the rotor speed restoration, but a severe SFD tends to follow the sudden output drop. Hence, t_2–t_1 should be not set as too small a value. The large enough t_2–t_1 can avoid the risk of the SFD but considerably delays the rotor speed restoration. Normally, the rotor speed should be regained before the initiation of the secondary frequency drop. Thus, t_2–t_1 is set as 10.0–30.0s for different power systems considering the response time of secondary frequency response of the power system.

As shown in Figure 7, similar to the conventional stepwise IC scheme, at t_0, the power reference increases to $P_{\mathrm{Tlim}}(\omega_0)$ corresponding to the operating point A to point B. Afterward, different from the conventional stepwise IC, the incremental power smoothly decreases based on the linear function. Thus, the power reference smoothly decays and automatically switches to the MPPTO curve corresponding to the operating point B to operating point A through operating points C and E.

As illustrated in Figure 7 ($\omega_0 \rightarrow \omega_C$ phase), since the solid segment BC is higher than the dotted segment BC, more power is released to the electric grid in the initial stage of a disturbance with the same energy release; as a result, the MFD of the proposed stepwise IC strategy is reduced while ω_r is regained earlier than the conventional stepwise IC scheme. The reasons for the solid segment BC being higher than the dotted segment BC are explained as follows.

The derivative functions of Eqs 16 and 20 are represented as follows:

$$\frac{dP_{\mathrm{set}}}{d\omega_r} = \frac{P_{\mathrm{Tlim}}(\omega_0) - P_{\mathrm{MPPT}}(\omega_{\mathrm{min}})}{\omega_0 - \omega_{\mathrm{min}}}, \tag{24}$$

$$\frac{dP_{\mathrm{ref}}}{d\omega_r} = \frac{dP_{\mathrm{MPPT}}(\omega_r)}{d\omega_r} = 3k_g\omega_r^2. \tag{25}$$

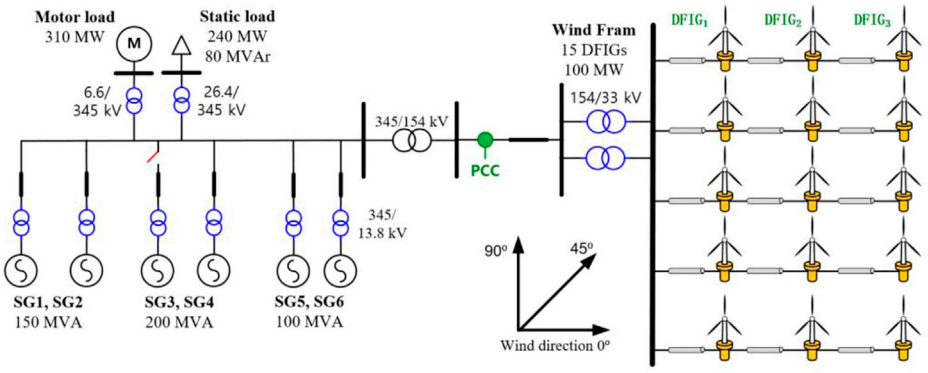

FIGURE 8
Test system.

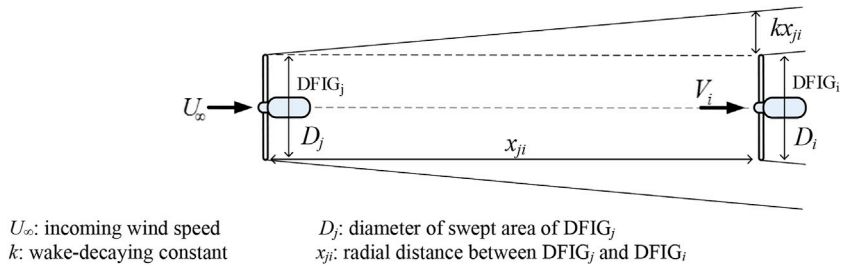

FIGURE 9
Shadow cone.

As shown in Eq. 24, $dP\text{set}/dt$ decreases with the increasing ω_r and is fixed at a constant wind speed condition. Comparing (24) and (25), with $\omega_0 \leq 1.12$ p. u. and $dP_{set}/d\omega_0 \geq dP_{ref}/d\omega_r$, as a result, the solid segment BC is higher than the dotted segment BC.

In addition, compared with the conventional fixed power-based rotor speed recovery scheme, the output power of the proposed stepwise IC scheme smoothly decreases and automatically switches to the MPPTO curve through the dynamic power reference suggested, as shown in Eq. 22. This process corresponds to the solid segment CE, as shown in Figure 7. Therefore, the smooth decreasing power is a benefit to reducing/removing the second drop on the system frequency and further reducing mechanical stresses on the shaft of the DFIG.

Model system and simulations

Simulations on various penetration levels of wind power are conducted to explore the performance of the proposed stepwise IC strategy. The model system shown in Figure 8, which comprises a wind farm and six steam turbine SGs, is employed. The droop coefficient for all conventional SGs is set to 5.0%. The deadband of the governor response for all synchronous generators is set to 33 mHz. IEEEX1 is used for voltage control of conventional SGs.

For calculating the wind speeds of the DFIGs in a wind power plant, the Park wake model, which is based on the Jenson model, is implemented, as illustrated in Figure 9. The wake wind speeds of the DFIGs are derived since the wind direction and cumulative impact of multiple shadowing are considered (Koch et al., 2005). The wind speed of a DFIG$_i$ and V_i can be calculated as follows:

$$V_i = U_\infty \left[1 - 2\sqrt{\sum_{\substack{j=1 \\ j \neq i}}^{n} \left\{ a_j \left(\frac{D_j}{D_i + 2kx_{ji}} \right)^2 \beta_{ji} \right\}^2} \right], \quad (26)$$

where β_{ji} indicates the ratio between the swept and overlapping areas of the DFIG$_i$, a_j is the factor of the axial induction of the DFIG$_j$, and n is the number of DFIGs in a wind farm.

TABLE 1 Parameters of the DFIG.

Item	Value	Unit
Apparent power	5.5	MVA
Active power	5.0	MW
Stator voltage	2.3	kV
Stator resistance	0.023	p.u
Stator leakage reactance	0.18	p.u
Magnetizing reactance	2.9	p.u
Rotor resistance	0.016	p.u
Rotor leakage reactance	0.16	p.u
Stable operating range of ω_r	0.70–1.25	p.u
Rated, cut-in, and cut-out speeds	11, 4, and 25	m/s

The wind speeds for the $DFIG_1$, $DFIG_2$, and $DFIG_3$ are 9.0 m/s, 8.4 m/s, and 7.8 m/s, respectively. The available rotor kinetic energies are 3.92, 1.89, and 1.66s, respectively. The parameters of the DFIG are shown in Table 1. To provide clear explanations of the proposed scheme, there are two settings for the proposed and conventional stepwise IC schemes. This first setting is that Δt of the proposed stepwise IC scheme for the first column DFIGs ($DFIG_1$), second column DFIGs ($DFIG_2$), and third column DFIGs ($DFIG_3$) are set as 28.5, 17.0, and 11.0s to achieve the same energy release with the conventional scheme; the second setting is that ΔP_r for all DFIGs are set as 0.05 p. u., which is referred in the Technical standards GB, (2018) and 0.10 p. u., respectively.

As a disturbance, the SG_3, which generates 120 MW, is tripped out. Furthermore, the wind penetration level of case 1 and case 2 are 13.6 and 27.3%, respectively. The performance of the proposed stepwise IC strategy is compared to those of the MPPTO and conventional stepwise IC strategy with respect to reducing the MFD, nadir-based frequency response (NBFR), second frequency nadir, and mechanical stresses.

Case 1: wind penetration level of 13.6%

As shown in Figure 10A, the MFD of the MPPTO is 1.222 Hz, which is higher than that of the conventional stepwise IC method by 0.240 Hz, since more kinetic energy is released for the conventional method while no kinetic energy is released for the MPPTO, as shown in Figure 10B. The MFD for the proposed stepwise IC method is 0.964 Hz, which is less than that of the conventional stepwise IC method by 0.018 Hz, even though the same rotor energy is released from DFGs as in the conventional stepwise IC schemes. The reason for this performance is that the injected power is more than that in the conventional stepwise IC method in the initial period of the disturbance (as seen in Figure 10B). The NBFR with the suggested stepwise IC method is 124.48 MW/Hz; however, NBFRs with the conventional stepwise IC method and MPPTO are 122.20 MW/Hz and 98.20 MW/Hz, respectively, as shown in Table 1, due to the higher frequency nadir in the proposed stepwise IC method.

As shown in Figures 10C, F, and I, the output powers of the conventional stepwise IC scheme suddenly decrease at different instants so that the system frequency drops again. As shown in Figure 10A, the depth of the SFD of the conventional stepwise IC scheme with large ΔP_r is less severe than the conventional stepwise IC scheme with small ΔP_r. However, the output powers of the $DFIG_1$, $DFIG_2$, and $DFIG_3$ smoothly decay over time until the reference of the output power switches to the MPPTO curve. This is the reason that the suggested stepwise IC scheme can reduce the depth of the SFD. In addition, since the suggested stepwise IC scheme can regulate the time for meeting the MPPTO curve without the requirement of mechanical power, it can ensure the rapid recovery of the rotor speed and system frequency stabilization, as illustrated in Figure 10.

As shown in Figures 10E, H, and K, for the conventional stepwise IC schemes and proposed stepwise IC scheme, mechanical stresses on the wind turbines are caused due to the rapid power increase flow of the disturbance. Such phenomena are inevitable while improving the frequency nadir. However, mechanical stresses of the wind turbines for the conventional stepwise IC schemes are caused due to the rapid power reduction and mechanical stresses become severe with the increasing ΔP_r. However, the proposed stepwise IC scheme can avoid mechanical stresses on the wind turbine in the RSRP since the incremental power smoothly decreases to zero, as shown in Figure 10L.

Case 2: wind penetration level of 27.3%

To realize a high wind penetration of 27.3%, SG_5 is out of service and the capacity of the wind power plant increases to 150 MW. Thus, the inertial response and primary frequency response of the power system become worse.

As illustrated in Figure 11, the frequency nadir and NBFR with the MPPTO are 58.619 Hz and 86.98 MW/Hz, respectively, which are lower than those of case 1 due to the increased wind power penetration. However, frequency nadirs and NBFRs for the conventional and proposed stepwise IC schemes become better than those in case 1 since the power output of wind power in MW is more than that in case 1. In addition, the improvements of the frequency nadir and NBFR for the suggested stepwise IC scheme are more than that in the conventional stepwise IC schemes.

Output powers of the conventional stepwise IC scheme suddenly decrease at different instants so that the system frequency drops again. As shown in Figure 11A, the depth of the SFD of the conventional stepwise IC scheme with large ΔP_r is less severe than the conventional stepwise IC scheme with small ΔP_r. In addition, mechanical stresses of the wind turbines are created owing to the rapid power reduction. However, the output powers of the $DFIG_1$, $DFIG_2$, and $DFIG_3$ smoothly decay over time until the reference of the output power switches to the MPPTO curve. This is the reason that the suggested stepwise IC scheme can reduce the depth of the SFD and reduce the mechanical stresses of the DFIGs.

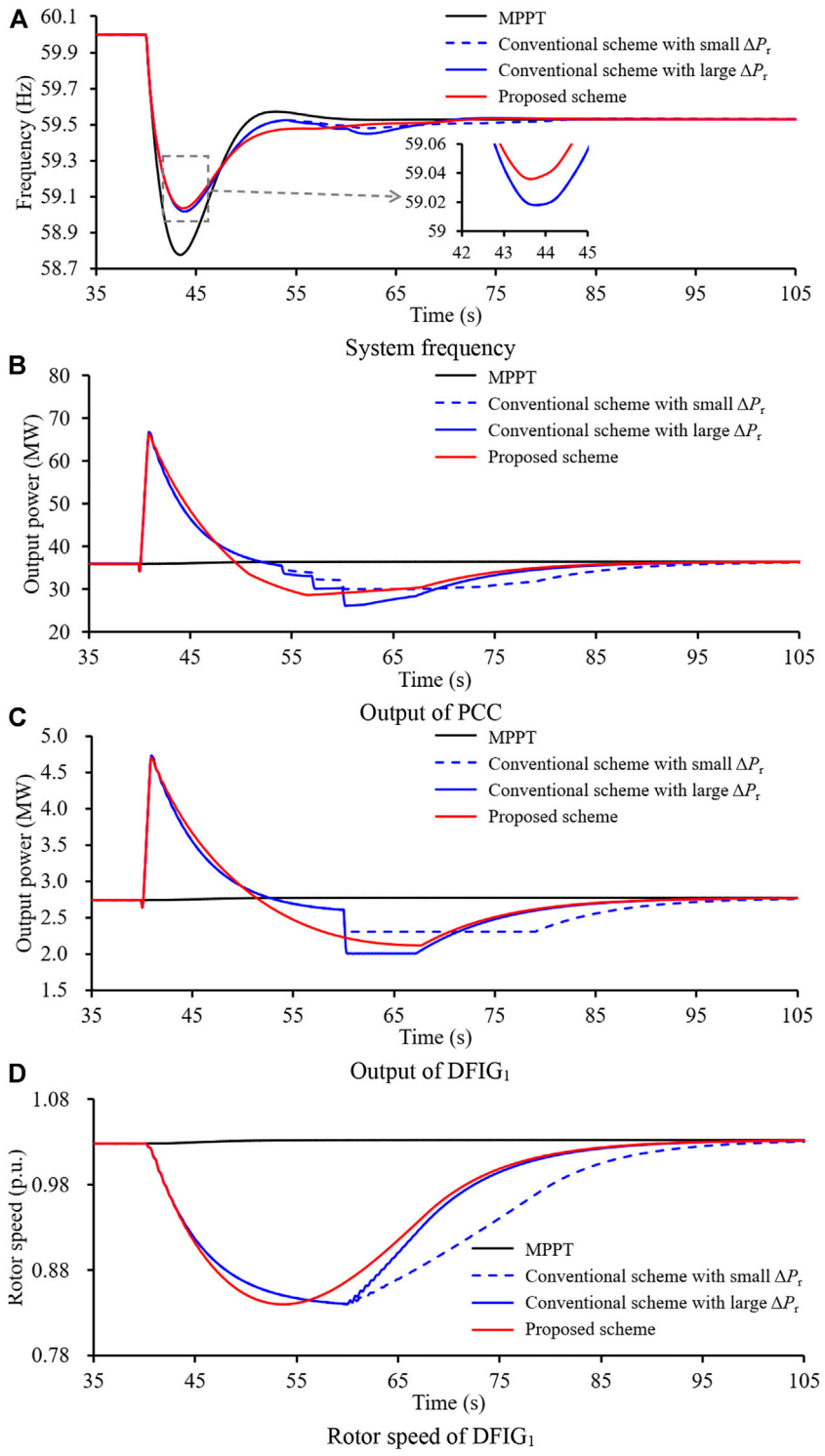

FIGURE 10
Results for case 1.

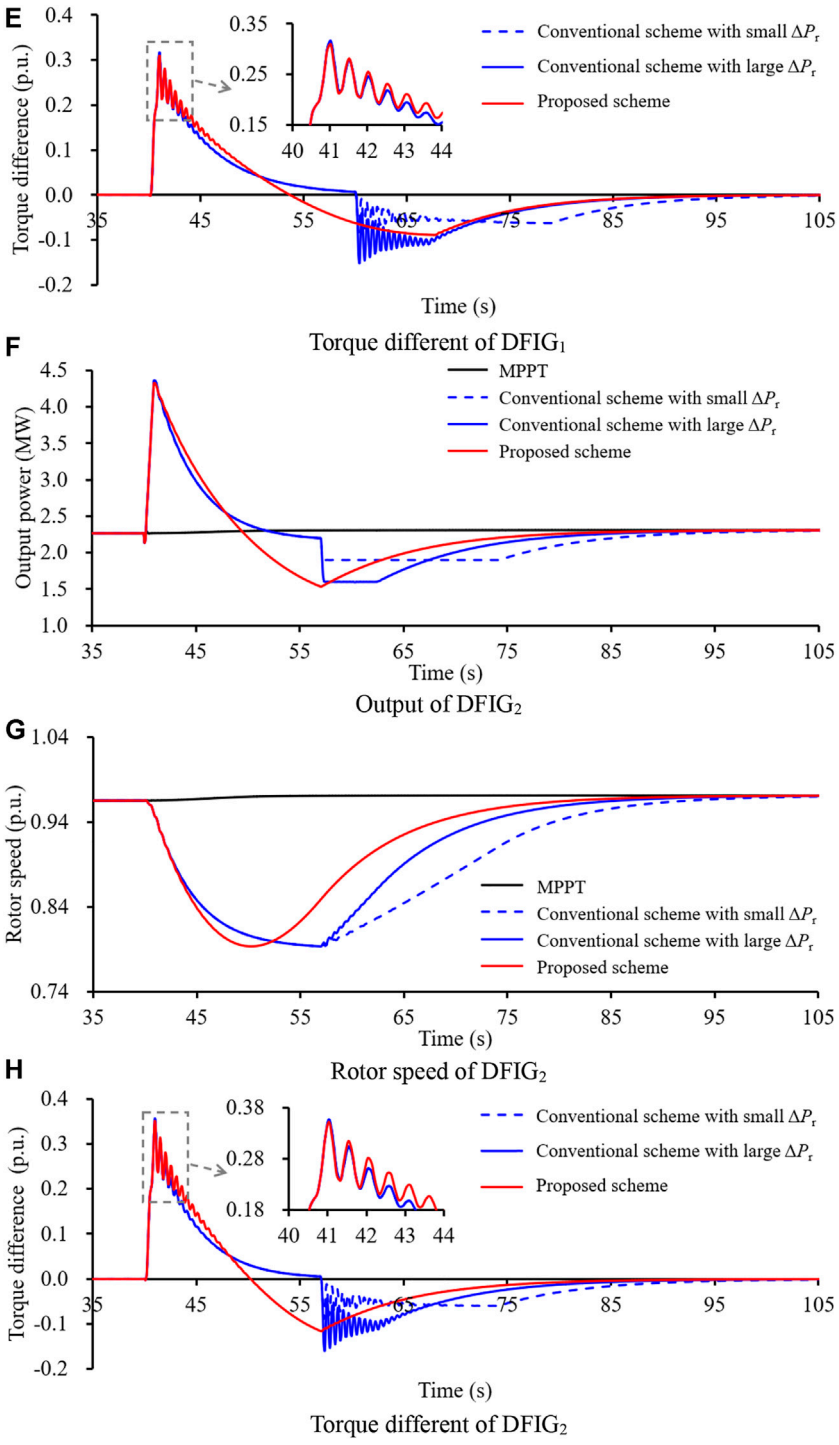

FIGURE 10
continued.

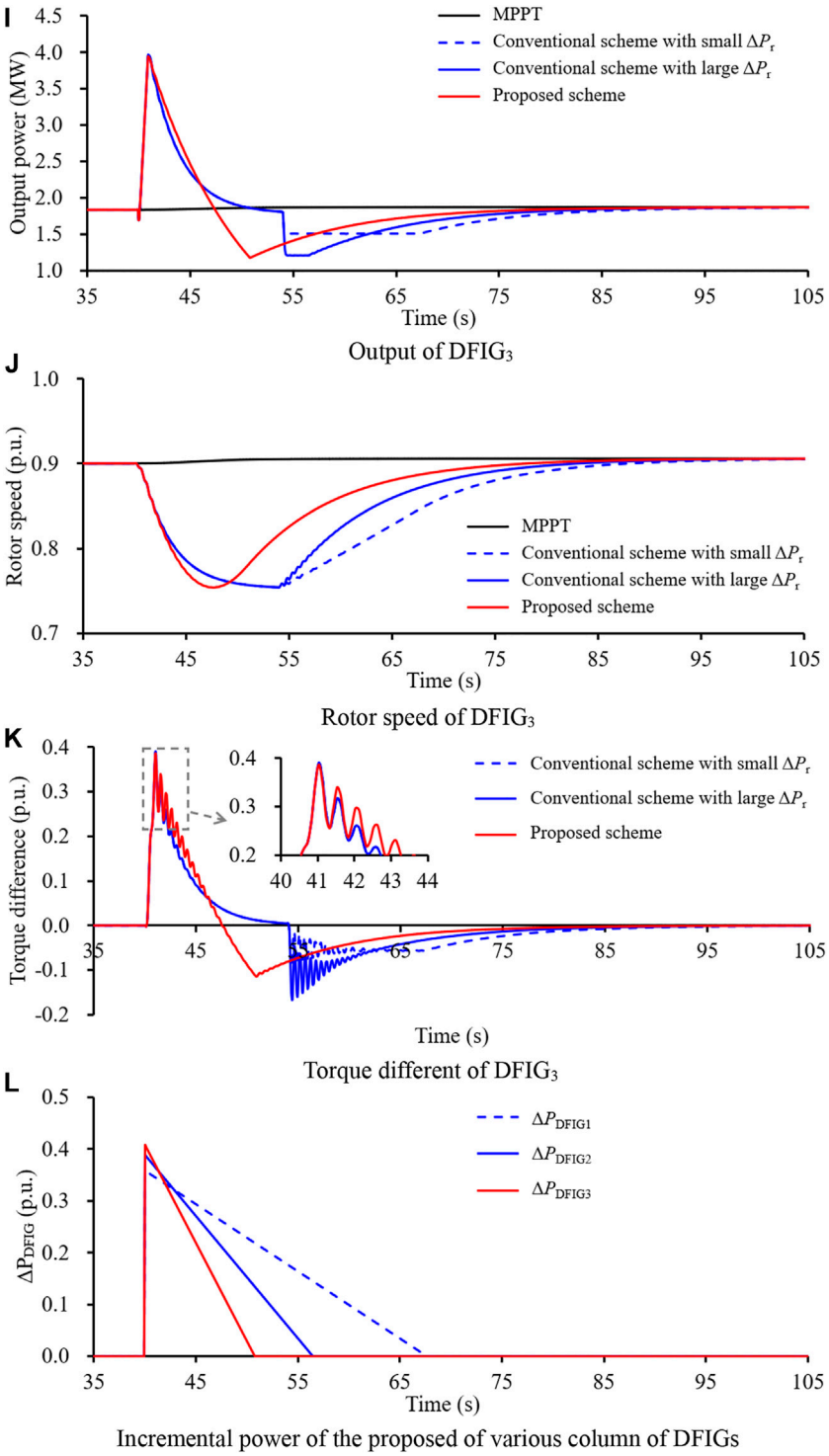

FIGURE 10
continued.

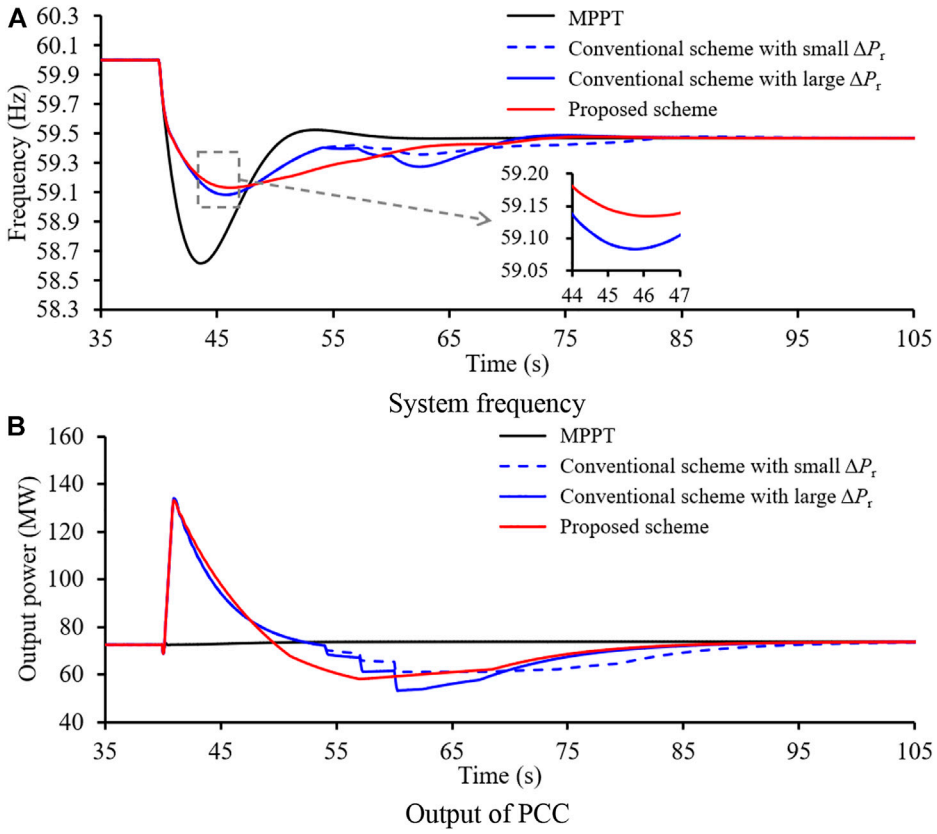

FIGURE 11
Results for case 2.

Conclusion

This study proposes a dynamic power-based temporary frequency support scheme for the wind power plant for minimizing the SFD while reducing the MFD. To this end, the reference of the output power increases to the torque limit. Afterward, the power reference smoothly decays with the dynamically decreasing incremental power and then automatically switches to the maximum power point tracking operation. Furthermore, to achieve realistic results, the wake effect is considered in this study.

The results indicate that the proposed stepwise IC strategy can improve the frequency nadir even though the same energy is released from the DFIGs as compared to the conventional stepwise IC schemes in the FSP. The depth of the SFD for the conventional stepwise IC scheme becomes notable and tends to be a lower value for a large wind generation-dominated power system; however, the proposed scheme can minimize the depth of the SFD and reduce mechanical stresses. Moreover, the performances with respect to reducing the MFD, reducing/removing the depth of the SFD, reducing mechanical stresses, and rapidly recovering the rotor speed are more notable in highly wind-penetrated power systems.

Data availability statement

The original contributions presented in the study are included in the article/Supplementary Materials; further inquiries can be directed to the corresponding author.

Author contributions

JY, DX, and JC designed the proposed strategy. All authors wrote and edited the manuscript.

Conflict of interest

The authors declare that the research was conducted in the absence of any commercial or financial relationships that could be construed as a potential conflict of interest.

Publisher's note

References

Boukhezzar, B., and Siguerdidjane, H. (2011). Nonlinear control of a variable speed wind turbine using a two mass model. *IEEE Trans. Energy Convers.* 26 (1), 149–162. doi:10.1109/tec.2010.2090155

Gevorgian, V., Zhang, Y., and Ela, E. (2015). Investigating the impacts of wind generation participation in interconnection frequency response. *IEEE Trans. Sustain. Energy* 6 (3), 1004–1012. doi:10.1109/tste.2014.2343836

Guo, X., Zhu, D., Zou, X., Yang, Y., Kang, Y., Tang, W., et al. (2022). Analysis and enhancement of active power transfer capability for DFIG-based WTs in very weak grid. *IEEE J. Emerg. Sel. Top. Power Electron.* 10, 3895–3906. doi:10.1109/JESTPE.2021.3089235

Hafiz, F., and Abdennour, A. (2015).Optimal use of kinetic energy for the inertial support from variable speed wind turbines, *Renew. Energy*, 80. 629. doi:10.1016/j.renene.2015.02.051

Hu, Y.-L., and Wu, Y.-K. (2019). Approximation to frequency control capability of a DFIG-based wind farm using a simple linear gain droop control. *IEEE Trans. Ind. Appl.* 55 (3), 2300–2309. doi:10.1109/tia.2018.2886993

Kang, M., Kim, K., Muljadi, E., Park, J. W., and Kang, Y. C. (2016). Frequency control support of a doubly-fed induction generator based on the torque limit. *IEEE Trans. Power Syst.* 31 (6), 4575–4583. doi:10.1109/tpwrs.2015.2514240

Kheshti, M., Ding, L., Nayeripour, M., Wang, X., and Terzijia, V. (2019). Active power support of wind turbines for grid frequency events using a reliable power reference scheme. *Renew. Energy* 139, 1241–1254. doi:10.1016/j.renene.2019.03.016

Koch, F., Gresch, M., Shewarega, F., Erlich, I., and Bachmann, U. (2005). "Consideration of wind farm wake effect in power system dynamic simulation," in Proc. Power Tech, 27-30 June 2005 (Russia: IEEE). doi:10.1109/PTC.2005.4524572

Lao, H., et al. .2020 Innovated inertia control of DFIG with dynamic rotor speed recovery. *CSEE J. Power & Energy Syst.*2096–0042 .doi:10.17775/CSEEJPES.2020.03180

Li, Y., Xu, Z., and Wong, K. P. (2017). Advanced control strategies of PMSG-based wind turbines for system inertia support. *IEEE Trans. Power Syst.* 32 (4), 3027–3037. doi:10.1109/tpwrs.2016.2616171

Morren, J., Pierik, J., and de Haan, S. W. H. (2006). Inertial response of variable speed wind turbines. *Electr. Power Syst. Res.* 76 (11), 980–987. doi:10.1016/j.epsr.2005.12.002

Peng, X., Yao, W., Yan, C., et al. (2020). Two-stage variable proportion coefficient based frequency support of grid connected DFIG-WTs. *IEEE Trans. Power Syst.*, 35, 962–974. doi:10.1109/TPWRS.2019.2943520

shi, Q., Li, F., and Cui, H. (2018). Analytical method to aggregate multi-machine SFR model with applications in power system dynamic studies. *IEEE Trans. Power Syst.* 33 (6), 6355–6367. doi:10.1109/tpwrs.2018.2824823

Technical standards GB (2018). *Wind turbines–Test procedure of gird adaptability*. Chinese: GB/T 36994.

Ullah, N. R., Thiringer, T., and Karlsson, D. (2008). Temporary primary frequency control support by variable speed wind turbines—potential and applications. *IEEE Trans. Power Syst.* 23 (2), 601–612. doi:10.1109/tpwrs.2008.920076

Vyver, J. V. d., Meersman, B., Vandevelde, L., and Vandoorn, T. L. (2016). Droop control as an alternative inertial response strategy for the synthetic inertia on wind turbines. *IEEE Trans. Power Syst.* 31 (2), 1129–1138. doi:10.1109/tpwrs.2015.2417758

Wang, J., Zhong, H., Yang, Z., Wang, M., Kammen, D. M., Zhu, L., et al. (2020). Exploring the trade-offs between electric heating policy and carbon mitigation in China. *Nat. Commun.* 11, 6054. doi:10.1038/s41467-020-19854-y

Wang, S., and Tomsovic, K. (2018). A novel active power control framework for wind turbine generators to improve frequency response. *IEEE Trans. Power Syst.* 33 (6), 6579–6589. doi:10.1109/tpwrs.2018.2829748

Wu, Y.-K., Yang, W. H., Hu, Y. L., et al. (2019). "Frequency regulation at a wind farm using a timing–varying inertia and droop controls," in ProceedingIEEE Trans. Ind. Appl., 07-10 May 2018.551 (Niagara Falls ON Canada: IEEE), 213–2224. doi:10.1109/ICPS.2018.8369978

Xiong, L., Liu, X., Liu, Y., and Zhuo, F.2020 Modeling and stability issues of voltage-source converter dominated power systems: A review. *CSEE J. Power Energy Syst.* (Early Access). doi:10.17775/CSEEJPES.2020.03590

Xiong, Y., Yao, W., Fen, J., Lin, S., Ai, X., Fang, J., et al. (2021). Two-level combined control scheme of VSC-mtdc integrated offshore wind farms for onshore system frequency support. *IEEE Trans. Power Syst.* 36 (1), 781–792. doi:10.1109/tpwrs.2020.2998579

Xu, G., and Xu, L. (2017). Improved use of WT kinetic energy for system frequency support. *IET Renew. Power Gener.* 11 (8), 1094–1100. doi:10.1049/iet-rpg.2016.0183

Yang, D., Jin, Z., Zheng, T., and Jin, E.2021 An adaptive droop control strategy with smooth rotor speed recovery capability for type III wind turbine generators. *Int. J. Electr. Power & Energy Syst.* 135, 107532. doi:10.1016/j.ijepes.2021.107532

Yang, D., Kim, J., Kang, Y. C., Muljadi, E., Zhang, N., Hong, J., et al. (2018). Temporary frequency support of a DFIG for high wind power penetration. *IEEE Trans. Power Syst.* 33 (3), 3428–3437. doi:10.1109/tpwrs.2018.2810841

Yang, D., Yan, G. -G., Zheng, T., Zhang, X., and Hua, L. (2022). Fast frequency response of a DFIG based on variable power point tracking control. *IEEE Trans. Ind. Appl.* 58 (4), 5127–5135. doi:10.1109/TIA.2022.3177590

frontiers | Frontiers in Energy Research

TYPE Original Research
PUBLISHED 19 October 2022
DOI 10.3389/fenrg.2022.1037825

OPEN ACCESS

EDITED BY
Liansong Xiong,
Xi'an Jiaotong University, China

REVIEWED BY
Huimin Wang,
University of Electronic Science and Technology of China, China
Hengyou Zhang,
Jilin University, China
Xiaokang Liu,
Politecnico di Milano, Italy

*CORRESPONDENCE
Qiaoming Shi,
shiqiaoming@nrec.com

SPECIALTY SECTION
This article was submitted to Process and Energy Systems Engineering, a section of the journal Frontiers in Energy Research

RECEIVED 06 September 2022
ACCEPTED 22 September 2022
PUBLISHED 19 October 2022

CITATION
Wei P, Chai B, Shi L, Shi Q, Liu R, Wang Y and Liu K (2022), RPC-based frequency control strategy of LCC-HVDC sending end power system with renewable energy. *Front. Energy Res.* 10:1037825.
doi: 10.3389/fenrg.2022.1037825

RPC-based frequency control strategy of LCC-HVDC sending end power system with renewable energy

Peng Wei[1], Bin Chai[2], Lei Shi[1], Qiaoming Shi[3]*, Ruopeng Liu[2], Yongping Wang[3] and Kai Liu[3]

[1]State Grid Ningxia Electric Power Co., Ltd., Yinchuan, China, [2]State Grid Ningxia Ultrahigh Voltage Company, Yinchuan, China, [3]NR Engineering Co., Ltd., Nanjing, China

Long-distance transmission of renewable energy *via* DC is currently a more economical transmission scheme. As the proportion of renewable energy at the generation end continues to rise, the inertia and damping level of the system is reduced, causing serious frequency-related issues. This paper first analyzes the working principle and control method of the LCC-HVDC system, summarizes the frequency control methods of the sending end power grid and their existing problems, and proposes a frequency control scheme for the LCC-HVDC sending end system based on the concept of rapid power compensation (RPC). Finally, the LCC-HVDC system model integrated with the large-capacity wind farm and thermal power plant is built in MATLAB/Simulink. Under conditions of load power fluctuation and sudden wind speed change, the proposed strategy fully utilizes the spare capacity of the system, effectively improves the frequency indexes of the system, and improves the frequency characteristics of the renewable energy sending end grid.

KEYWORDS

RPC, LCC-HVDC, sending end grid, renewable energy, frequency control

1 Introduction

In recent years, in order to reduce carbon emissions, the proportion of renewable energy in the power system, represented by wind power and photovoltaic power generation, has been increasing (Tamrakar et al., 2017; Ratnam et al., 2020; Song et al., 2022). Northwest China has sufficient renewable energy reserves, but the southeast coastal region is a large consumer of electric energy, which requires the vigorous development of renewable energy generation technology *via* the LCC-HVDC transmission system. LCC-HVDC system has the advantages of simple structure, low construction cost and more mature engineering construction, which is very suitable for long-distance large-capacity transmission of electric energy.However, the sending end system has a large proportion of renewable energy integration, resulting in a low level of system inertia and damping, insufficient system frequency regulation capability, and prominent frequency stability problems (Holttinen et al., 2022).

In order to analyze and solve the frequency stability problems brought by high proportion of renewable energy, Xiong et al. (2022) compared and analyzed typical frequency control strategies for renewable energy systems; Xiong et al. (2020) modeled and analyzed the stability of high-proportion renewable energy systems connected by voltage source converters (VSCs) and summarized the key techniques; Pawar et al. (2021) proposed a grid-connected control scheme for two-stage photovoltaic systems, which can effectively improve frequency stability; Morren et al. (2006) used the power reserve of the wind turbine to provide virtual inertia to support the primary frequency regulation of the grid. However, most of the above methods require the renewable energy generation side to reserve power, which leads to its inability to operate at the maximum power point, affecting the economical operation of the system and increasing the generation cost of the renewable energy system. In addition, operation of this mode causes damage to electrical/mechanical components and seriously shortens their service life in long-term operation.

The high voltage direct current (HVDC) transmission has the advantages of large transmission capacity, long transmission distance, and high regulation capability, which are well suited for long-distance transmission of renewable energy generation systems (Alassi et al., 2019; Shi et al., 2021).

Typical power system frequency regulation methods can be broadly classified into two categories: current-source type virtual inertia providing and voltage-source type virtual inertia providing (Dreidy et al., 2017; Kroposki et al., 2017; Tayyebi et al., 2020; He et al., 2022). The former introduces the rate of change of frequency (RoCoF) into the active power link of the converter control, changes the reference value of active power, and provides active power to the grid proportional to the RoCoF. The latter uses the virtual synchronous generator (VSG) technology, and introduces the swing equation and electromagnetic transient equation of the generator into the control of the converter. It has virtual voltage source characteristics and provides temporary inertia support for the system (Guan et al., 2015). For better economic performance, most of the long-distance HVDC power transmission uses the LCC-HVDC scheme, in which thyristor-based rectifiers/inverters (i.e., current-source inverters) are used, and the equipment has only one control degree of freedom, i.e., the conduction angle/inversion angle. Hence, it is impossible to use the VSC frequency regulation based on two degrees of freedom, and only the frequency regulation methods of the current-source converter are available, e.g., the proportional derivative (PD) control, the virtual inertia control (Holttinen et al., 2022), etc.

Focused on the frequency regulation in LCC-HVDC systems, Yogarathinam et al. (2017) analyzed the effect of inertia and effective short-circuit ratio on the frequency of doubly fed induction generator (DFIG) wind farms integrated with the LCC-HVDC system and under weak grid condition; Li et al. (2019) proposed the LCC-HVDC reserve power coordination control strategy for the multi-terminal feed-in DC transmission system to improve transient stability; Lee et al. (2020) proposed a coordinated control strategy for the LCC-HVDC system to support the frequency and AC voltage; Kwon et al. (2020) achieved real-time regulation of the grid frequency on the rectifier and inverter side by controlling the DC voltage and DC current of the LCC-HVDC system. The above control methods are relatively complex to implement and can cause the deviation of new energy generation from the maximum power point. The HVDC system usually has the feature of non-full power operation, which can be used to regulate the grid frequency on the sending side without the participation of the renewable energy, thus enabling the renewable energy system to operate in maximum power point tracking (MPPT) mode and improving the economic efficiency of the system. To this end, this paper analyzes the working principle of rapid power compensation (RPC) (Xiong et al., 2021; Liu et al., 2022), applies it to the renewable energy sending end, and proposes a frequency control scheme of the renewable energy integrated LCC-HVDC sending end system based on the RPC control strategy.

The remainder of this paper is organized as follows. Part 2 analyzes the operation principle of the renewable energy transmission system *via* LCC-HVDC. Part 3 summarizes the frequency stability of the sending end system and the common problems of existing solutions. Part 4 discusses the advantages of the RPC and proposes an RPC-based frequency control strategy for the LCC-HVDC sending end system. Part 5 verifies the proposed strategy through simulation.

2 LCC-HVDC sending end power system with renewable energy

2.1 Structure of LCC-HVDC sending end power system with renewable energy

The basic structure of the LCC-HVDC system is shown in **Figure 1**. The system consists of two major parts, i.e., the sending end and the receiving end. The sending end consists of the renewable energy (in the form of photovoltaic and wind turbines) and the conventional energy (in the form of traditional thermal power units), and the proportion of renewable energy is increasing. The receiving end is generally the next level of the power grid bus.

Take the wind power generation as an example. The DFIG is a widely used type of wind turbine, and its basic scheme is shown in **Figure 2**, which mainly consists of the wind turbine, the speed increasing gearbox, the generator, and bidirectional converter. The DFIG rotor is excited by the rotor side converter (RSC), and electric power is supplied to the grid by the grid side converter

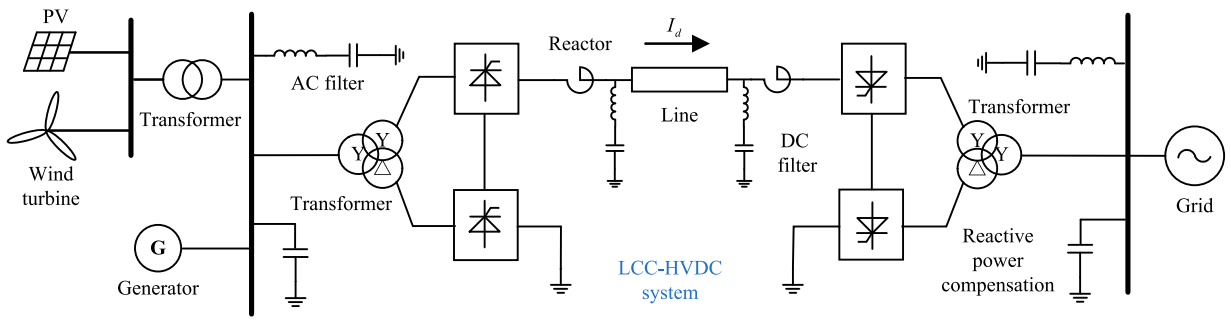

FIGURE 1
Structure of LCC-HVDC sending end power system with renewable energy.

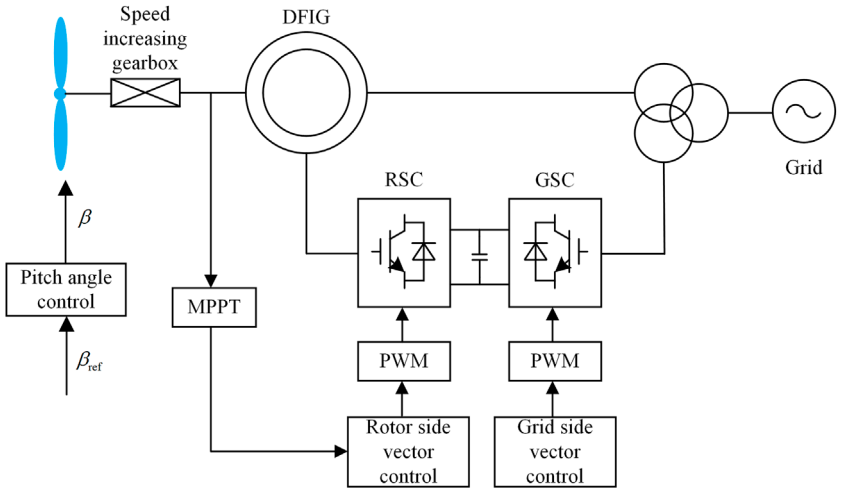

FIGURE 2
DFIG schematic diagram.

(GSC). The frequency of the rotor excitation current is controlled to keep the stator side current constant, i.e., to keep the output frequency of the grid constant.

When the number of pole pairs in the stator winding is p, the rotating magnetic field speed n_1 is proportional to the grid frequency f_1, i.e.,

$$n_1 = \frac{60 f_1}{p} \tag{1}$$

When the rotor side excitation current frequency is f_2, the rotating magnetic field speed is

$$n_2 = \frac{60 f_2}{p} \tag{2}$$

Due to the variable speed and constant frequency operation characteristics of the DFIG, when the rotor speed is n, we have

$$n_1 = n_2 + n \tag{3}$$

Substituting (Eq. 1) and (Eq. 2) into (Eq. 3), we get

$$f_1 = \frac{pn}{60} + f_2 \tag{4}$$

Namely, by adjusting the rotor excitation current frequency f_2, it is possible to generate power at a constant frequency and keep the grid frequency f_1 constant.

For the wind turbine, its blades convert the received wind energy into mechanical energy. The mechanical power converted from the captured wind power is

$$P_m = \frac{1}{2}\rho A C_p(\beta,\lambda) V^3 \tag{5}$$

where ρ is the air density, A is the rotating area of the wind turbine during rotation, C_p is the wind utilization factor, and V is the actual wind speed during operation. Except for C_p and V, the other parameters cannot be changed after the wind turbine ismanufactured. From (5), in a fixed wind speed, the mechanical

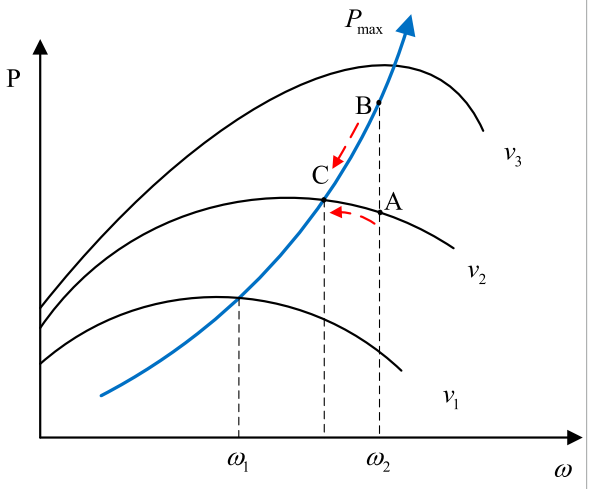

FIGURE 3
Schematic diagram of wind turbine MPPT.

power of the fan is decided by C_p, which is affected by the size of the fan, the blade tip speed ratio λ, and the pitch angle β. The relationship between the three can be written as

$$\begin{aligned} C_p(\beta,\lambda) &= 0.22\left(\frac{116}{\lambda_i} - 0.4\beta - 5\right)e^{-\frac{12.5}{\lambda_i}} \\ \frac{1}{\lambda_i} &= \frac{1}{\lambda + 0.08\beta} - \frac{0.035}{\beta^3 + 1} \\ \lambda &= \frac{\omega_r R}{V} \end{aligned} \tag{6}$$

where ω_r is the rotational speed of the fan impeller (in rad/s) and R is the length of the fan's paddle (in m).

To cope with different wind speed conditions, the DFIG can control the amount of wind energy captured by the turbine through the pitch angle control, and then control the active power output. The PI control is generally used and can be represented as

$$\begin{aligned} \beta_{ref} &= \frac{K_P T_1 s + 1}{T_1 s}\left(\omega_r - \omega_{ref}\right) \\ \beta &= \frac{1}{Ts + 1}\beta_{ref} \end{aligned} \tag{7}$$

where β_{ref} is the pitch angle reference value, β is the actual pitch angle, ω_{ref} is the rotor speed reference value, T_1 and T are the time constants, and K_P is the gain coefficient.

The power control part of the renewable energy generation system, which generally uses the MPPT control, can be illustrated by the maximum power point operation diagram of the wind power system shown in **Figure 3**. Each curve in the graph represents the relationship between the active power output and the wind turbine speed at different wind speeds, and the MPPT curve is a curve made by connecting the maximum power points of the wind turbine at different wind speeds. In order to obtain the maximum active power output, it is necessary to control the rotor speed of the turbine equal to the rotor speed of the generator, i.e. the mechanical power of the turbine is equal to the electromagnetic power of the generator. For the wind speed curve v_2, assume that point B is the operating point of the generator at speed ω_2, and point A is the operating point of the turbine at speed ω_2, but neither point A nor B is the maximum power point. At this time, the rotor operation equation is

$$J\frac{d\omega}{dt} = P_m - P_e \tag{8}$$

where J is the rotational inertia of the fan, P_m is the mechanical power of the fan, and P_e is the electromagnetic power. When the mechanical power of the wind turbine is less than the electromagnetic power, the rotor speed will decrease along the curve v_2, and at the same time, the working point corresponding to the MPPT curve moves downward until it reaches point C, where the mechanical power and the electromagnetic power reach equilibrium and the wind turbine achieves maximum power tracking. The MPPT is generally achieved by the perturbation-observation method and the conductivity increment method (Abo-Khalil and Lee, 2008), etc.

2.2 Principle of LCC-HVDC sending end power system with renewable energy

The converter small-signal model of the LCC-HVDC system (Karawita and Annakkage, 2010) can be written as the following state-space expression

$$\begin{bmatrix} \Delta I_R \\ \Delta I_I \\ \Delta V_{dc} \end{bmatrix} = \begin{bmatrix} K_a & K_b & K_c & K_d \\ K_e & K_f & K_g & K_h \\ K_i & K_j & K_k & K_l \end{bmatrix} \begin{bmatrix} \Delta V_R \\ \Delta V_I \\ \Delta I_{dc} \\ \Delta\alpha \end{bmatrix} \tag{9}$$

where ΔV_R, ΔV_I, ΔI_R, and ΔI_I represent the voltages and currents at the rectifier and inverter sides, respectively, ΔV_{dc} and ΔI_{dc} are the voltage and current of the DC line, $\Delta\alpha$ is the trigger angle, and the expressions of the coefficients K_a–K_l are detailed in Karawita and Annakkage (2010). It can be found that the renewable energy is transmitted through the converter station, and the control of the converter station allows the adjustment of the power delivered by the renewable energy.

Next, the DC transmission line is analyzed and modeled as a T-shaped equivalent circuit as shown in **Figure 4**, and the

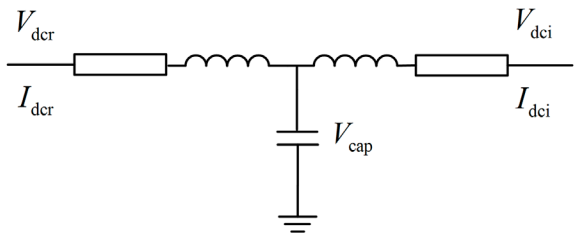

FIGURE 4
Schematic diagram of T-shaped transmission line.

linearized model of the DC line is represented as

$$\begin{bmatrix} \Delta\dot{I}_{dcr} \\ \Delta\dot{I}_{dci} \\ \Delta\dot{V}_{cap} \end{bmatrix} = \begin{bmatrix} -K_{dc1} & 0 & -K_{dc2} \\ 0 & -K_{dc3} & K_{dc4} \\ K_{dc5} & -K_{dc6} & 0 \end{bmatrix} \begin{bmatrix} \Delta I_{dcr} \\ \Delta I_{dci} \\ \Delta V_{cap} \end{bmatrix} + \begin{bmatrix} K_{dc7} & 0 \\ 0 & -K_{dc8} \\ 0 & 0 \end{bmatrix} \begin{bmatrix} \Delta V_{dcr} \\ \Delta V_{dcI} \end{bmatrix} \tag{10}$$

where $\dot{V}_{cap}$ is the midpoint capacitance voltage, ΔI_{dcr} and ΔI_{dci} are the DC voltages at the rectifier and inverter sides, respectively, and the detailed derivation and expressions of K_{dc1} to K_{dc8} are given in Karawita and Annakkage (2010).

To simplify the analysis, the internal resistance and reactance of the transformer can be ignored. Assuming that the total resistance on the line is R, and the DC voltages at the rectifier and inverter sides are U_{dr} and U_{di}, respectively, the line current can be written as

$$I_d = \frac{U_{dr} - U_{di}}{R} \tag{11}$$

where the DC voltages U_{dr} and U_{di} are controlled by the trigger angle α, the arc extinguishing angle γ, and the transformer ratios k_{T1} and k_{T2}, which can be written as

$$\begin{aligned} U_{dr} &= k_{T1} V_d = k_{T1} U_r \cos\alpha \\ U_{di} &= k_{T2} V_i = k_{T2} U_i \cos\gamma \end{aligned} \tag{12}$$

where U_r and U_i are the AC bus voltages at both ends of the line, and thus the power transmitted from the sending end and the power received by the receiving end are

$$\begin{aligned} P_{dr} &= U_{dr} I_d \\ P_{di} &= U_{di} I_d = U_{dr} I_d - R I_d^2 \end{aligned} \tag{13}$$

Through the above equations, it can be seen that the DC transmission power can be adjusted by adjusting the control angles of the converter and the tap ratio of the converter transformer. As the adjustment of the AC side transformer tap is done by the mechanical structure, the required adjustment time is long and difficult to adapt to rapid power adjustment. Hence, the system transmission power is generally adjusted quickly by adjusting the trigger angle and arc extinguishing angle.

For the control part of the LCC-HVDC system, the rectifier side often uses the constant current control, and the inverter side can use a fixed voltage control, fixed current control, fixed arc extinguishing angle control, or a combination of their control methods. The control strategy recommended by the CIGRE-HVDC model is usually used, i.e., a constant-current control strategy for the rectifier side and a constant-current or constant-arc-extinguishing-angle-control strategy for the inverter side (Atighechi et al., 2014).The LCC on the rectifier side controls the active power transmission of the system, and the LCC on the inverter side maintains the stability of the DC system.The detailed control structure is shown in **Figure 5**, where α_R and α_I are the final output quantities, representing the trigger angles at the rectifier and inverter sides, respectively.

The constant current control at rectifier side adopts the PI control, and the output is the trigger lead angle β, which is related to the trigger angle α as

$$\beta = \pi - \alpha \tag{14}$$

For the inverter side, the PI control is still used for the fixed current. To ensure the normal operation of the system and prevent the phase change failure, a safety margin of 0.1 pu is reserved for the current setting value. The constant arc-extinguishing angle control adopts the negative feedback PI control, and its output is the sum of the deviation of the arc-extinguishing angle setting value and the minimum arc-extinguishing angle measured at the inverter side in the previous cycle and the arc-extinguishing angle obtained by the current deviation control. This value is used to change the trigger angle of the inverter. The saturation link is set for both fixed current and fixed arc-extinguishing angle control. In addition, a voltage dependent current order limiter (VDCOL) is also set. When the DC voltage falls below a certain value due to a fault, the setting value of DC current regulator will be automatically lowered, and when the DC voltage is restored, the DC current will be automatically adjusted back to its setting value, and the current reference value is fixed during normal operation. In this model, the mid-point voltage of the DC transmission line is used as the starting voltage of the VDCOL link. During normal operation, the VDCOL does not work. When the DC voltage is lower than the upper limit set by VDCOL, this link reduces the current command of the converters on both sides to deal with the commutation failure.The dashed line in **Figure 5** shows the change of the current reference value after adopting the RPC strategy. The current deviation control is a correction of the current reference value to some extent. In addition, to ensure the effectiveness of the control, low-pass filtering is used for the measured values. In order to prevent the occurrence of faults such as phase change failure, a certain threshold value is reserved for the trigger angle, saturation units are added in the control

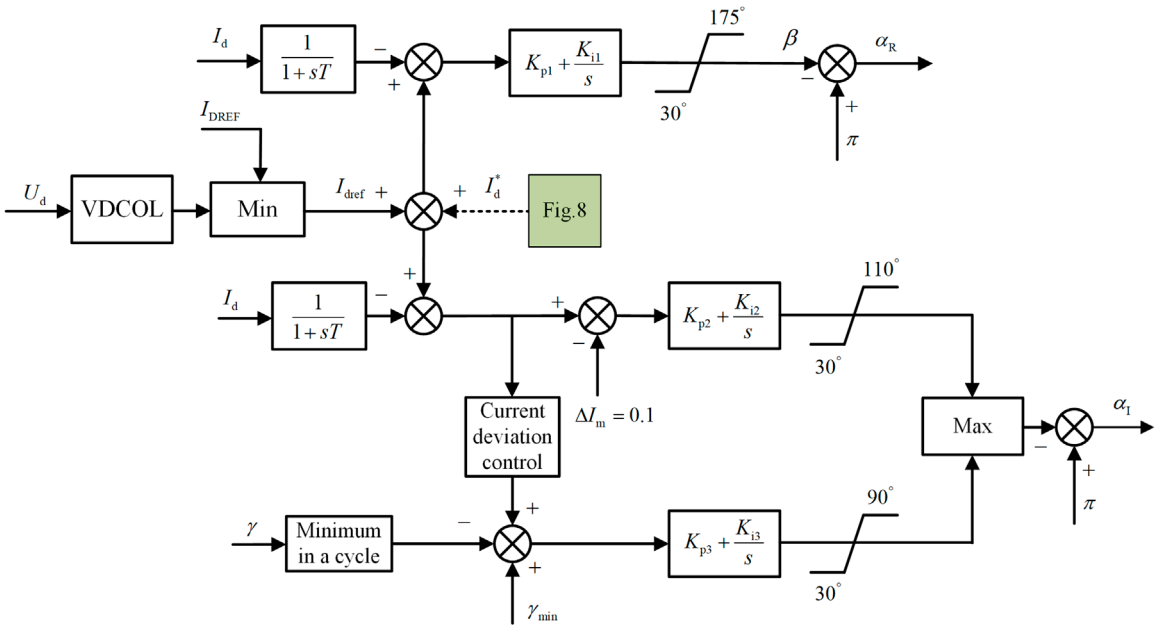

FIGURE 5
LCC-HVDC system control block diagram.

section, and the arc extinguishing angle is also set to its minimum value (18°). Detailed parameters are shown in Figure 5.

3 Frequency issues of sending end system and existing strategies

3.1 Frequency issues

The renewable energy sending end system *via* LCC-HVDC has major differences compared with the traditional HVDC transmission system, mainly including:

(1) The traditional HVDC transmission system transmits most of the power generated by thermal power units, only partly containing or not containing renewable energy power.
(2) Renewable energy generation systems use decoupled power electronic interface, so that renewable energy cannot respond to changes in system frequency as the rotor of the traditional generator. For instance, the photovoltaic power generation system connects to the bus *via* the converter interface, so that it cannot respond to the system frequency change caused by power disturbances.
(3) Due to the increase in the renewable energy proportion, the inertia and damping of the sending end system are significantly reduced. Compared with the traditional generator system, the same power disturbance will bring about greater frequency deviation; the probability of relay action increases, and the frequency safety of the sending end system faces greater challenges.
(4) The new energy transmission end system will also contain a certain amount of power plant end load, and may also contain part of the near end load. Most of these loads are connected to the power grid in the form of power electronic interfaces, which also reduces the inertia damping level of the system at the sending end, and the system frequency security is threatened.

At present, the main way to improve the frequency stability of the power grid at the sending end of the renewable energy system is through additional control in the renewable energy system, mainly including the VSG control and the PD control, both of which are used to improve the frequency stability of the system by equivalently enhancing the inertia and damping of the system.

3.2 Analysis of existing control strategies

3.2.1 VSG control

The VSG control adds the rotor equation of motion of the synchronous machine, i.e., the swing equation, into the control of converter, so that the converter has the swing characteristics similar to a synchronous machine, which can provide virtual inertia and damping to the system when the power disturbance occurs and enhance the system's ability to resist disturbances. The

swing equation can be written as

$$T_J \frac{df}{dt} = P_G - P_L - \Delta P_L + D(f_N - f) \tag{15}$$

where T_J is the system inertia coefficient, P_G is the total power of the generator, P_L is the load power, ΔP_L is the load power disturbance, and D is the damping factor.

Although VSG control enhances the ability of the system to resist disturbances, it has some drawbacks that limit its application. For example, the magnitudes of virtual inertia and damping need to be set artificially, making the design of parameters extremely difficult because the magnitude, timing, and location of the disturbance cannot be determined, and the virtual inertia and damping may exceed the energy that the system can provide. For the physical structure, the energy of the VSG generally comes from the capacitor bank, and the charging and discharging of the capacitor during frequency regulation accelerates its aging and reduces its service life. In addition, the VSG has problems such as power oscillation. All these limit the VSG technique applications in the renewable energy grid.

3.2.2 PD control

The droop control can correct the frequency deviation, which is essentially the proportional control; the inertia control can reduce the RoCoF of the system, which is basically the differential control. The use of these two control methods equivalently increases the inertia and damping coefficient of the system, whose output power can be expressed as

$$\begin{aligned} P_D &= K_D(f_N - f) \\ P_J &= sK_J(f_N - f) \end{aligned} \tag{16}$$

where K_D and K_J are the equivalently increased control coefficients using the droop control and the inertia control, respectively, s is the differential operator, f_N is the rated frequency of the system, and f is the actual output frequency of the system. The equivalently increased system inertia enhances the transient support capability of the system and reduces the RoCoF; the equivalently increased system damping enhances the steady-state support capability of the system and reduces the frequency deviation.

To obtain better frequency control effect, the droop control is combined with the inertia control, which is the PD control. The PD control is used to further improve the system frequency performance, and its output power can be expressed as

$$P_{PD} = (k_p + sk_d)(f_N - f) \tag{17}$$

where k_p and k_d are the proportional and differential coefficients, respectively. If k_p is set to a small value, the damping power is insufficient, resulting in a large frequency deviation; if k_d is set to a small value, the inertia power is insufficient, resulting in a large RoCoF. If the k_p and k_d parameters are set too large, the effective transmission power of the system is reduced because more power is involved in frequency regulation. The optimal PD control parameters depend heavily on the inertia and damping parameters of the system, whose values are difficult to obtain in practice, and inappropriate PD parameters may even deteriorate the system frequency indexes and bring adverse effects.

The above control method is achieved by using the reserve capacity of the renewable energy source to compensate for the system unbalanced power when the disturbance occurs. However, this will make the renewable energy system deviate from its maximum power point during normal operation and reduce the economic efficiency of the power generation system. In addition, the renewable energy system is influenced by the environment (such as wind speed, light, and temperature, etc.), and when the working conditions are extremely severe, even changing the control strategy of the renewable energy will not improve the frequency of the power grid at the sending end. Moreover, for wind turbines, frequent changes in their rotational speed will accelerate the aging and damage of mechanical structures such as drive shafts, reducing their service life.

Considering the voltage level and capacity of the power system will gradually increase, the maximum capacity of the HVDC system is generally larger than the actual transmission capacity because the system keeps a certain amount of rotating reserves. This spare capacity provides the possibility for frequency regulation using the LCC-HVDC system. By using the spare capacity, power compensation can be performed in the event of power disturbances, providing inertia and damping to the system, enhancing its ability to resist power disturbances. Since the frequency regulation power comes from the other end of the normally operating grid, the maximum power point of the renewable energy system is not affected, and the economic operation of the power generation system is maintained.In addition, due to the power grid at the other end of the frequency modulation energy source, it will not affect the frequency of the power grid at the sending end. There will be no problem of secondary drop in frequency.

4 Proposed frequency control strategy

From the analysis in the previous section, it can be seen that the magnitudes of P_D and P_J are proportional to their respective coefficients K_D, K_J and Δf, RoCoF. In order to compensate the unbalanced power of the system to the maximum, the output power of the converter can be set to the maximum reserve capacity of the system, P_{idmax}, corresponding to the basic principle of the RPC strategy. This process can be represented by **Figure 6**.

As shown by the power curves in **Figure 6**, when the sum of the two curves is constantly equal to the maximum power

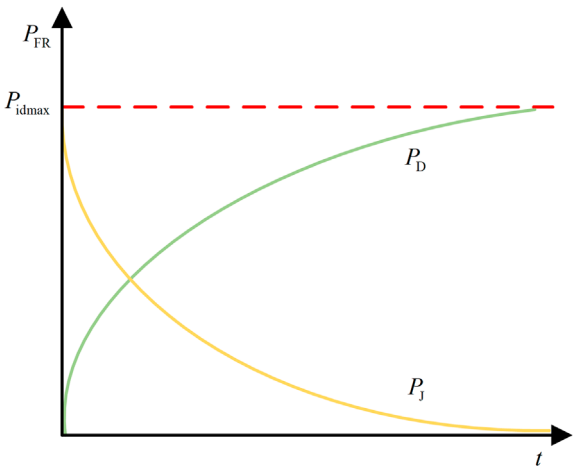

FIGURE 6
Illustration of power curves.

reserve, the unbalanced power of the system can be compensated to the maximum extent. Namely,

$$P_D + P_J \equiv P_{idmax} \tag{18}$$

The frequency characteristics of the system can be expressed in terms of the power delivered by the generation system and the power absorbed by the load as

$$T_J \frac{df}{dt} = P_\Sigma - P_L \tag{19}$$

where $T_J = 4\pi H$, H is the inertia coefficient of the system, and P_Σ and P_L represent the power generated and absorbed by the system, respectively. It should be noted that part of the power delivered by the power generation system is used to transmit to the load, and the other part is used for the frequency response, yielding

$$P_\Sigma = P_0 + K_L (f_N - f) \tag{20}$$

where P_0 is the load power, and K_L is the inherent frequency response coefficient of the system, which is related to the composition of the generation and load side systems.

When there is the additional frequency response power P_{FR} provided by the converter system, by combining with **Eq. 20**; **Eq. 19** can be rewritten as

$$T_J \frac{df}{dt} = P_{FR} - \Delta P_L + K_L (f_N - f) \tag{21}$$

Further, when the converter uses the RPC strategy (i.e., $P_{FR} = P_{idmax}$), (21) is rewritten as

$$T_J \frac{df_i}{dt} = P_{idmax} - \Delta P_L + K_L (f_N - f) \tag{22}$$

By solving this equation, the frequency deviation Δf_i and the RoCoF R_i are obtained as

$$\Delta f_i = f_N - f_i = \frac{\Delta P_L - P_{idmax}}{K_L}\left(1 - e^{-\frac{K_L}{T_J}t}\right) \tag{23}$$

$$R_i = \frac{df_i}{dt} = -\frac{\Delta P_L - P_{idmax}}{T_J} e^{-\frac{K_L}{T_J}t} \tag{24}$$

When the converter uses the PD control strategy, (**Eq. 21**) can be rewritten as

$$T_J \frac{df_{PD}}{dt} = P_{PD} - \Delta P_L + K_L (f_N - f) \tag{25}$$

Substituting (**Eq. 17**) into (**Eq. 25**), we can get

$$\Delta f_{PD} = f_N - f_{PD} = \frac{\Delta P_L}{K_L + k_p}\left(1 - e^{-\frac{K_L + k_p}{T_J + k_d}t}\right) \tag{26}$$

$$R_{PD} = \frac{df_{PD}}{dt} = -\frac{\Delta P_L}{T_J + k_d} e^{-\frac{K_L + k_p}{T_J + k_d}t} \tag{27}$$

Comparing and analyzing (**Eqs 18**, **23**, **24**, **26**, **27**), we have $\Delta f_i = \Delta f_{PD}$, $R_i = R_{PD}$ when and only when

$$k_p = \frac{K_L P_{idmax}}{\Delta P_L - P_{idmax}} \tag{28}$$

$$k_d = \frac{T_J P_{idmax}}{\Delta P_L - P_{idmax}} \tag{29}$$

Based on the above analysis, the RPC strategy can achieve the same frequency regulation effect as the optimal PD control when the backup capacity P_{idmax} of the converter output is the maximum frequency regulation power, and the RPC control strategy does not need the information of unknown parameters in the system, which reduces the difficulty of controller design and avoids further damage to the system frequency caused by unreasonable control parameters.

The change of system frequency is caused by the active power imbalance, and the frequency response process of the system can be reflected by the frequency offset and RoCoF indicators, based on which the degree of system power imbalance can be judged. For the LCC-HVDC system, when the power grid frequency at the sending end suddenly drops or rises, the power generated by the sending-end converter is required to increase or decrease to improve the frequency characteristics. When the power disturbance makes the system frequency indicators changes drastically, the RPC control mode is enabled; when the frequency indicators reach the droop control threshold interval, the control mode will be converted to the droop control; and finally when the frequency indicator satisfies the grid code specification, the system is in normal operation without the

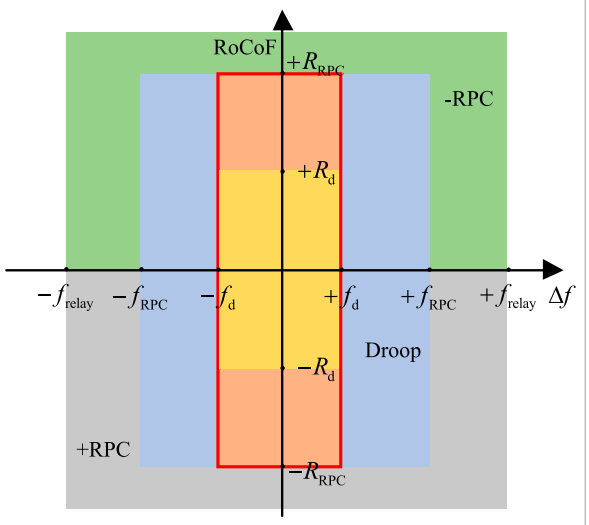

FIGURE 7
Logic conversion diagram of proposed control scheme.

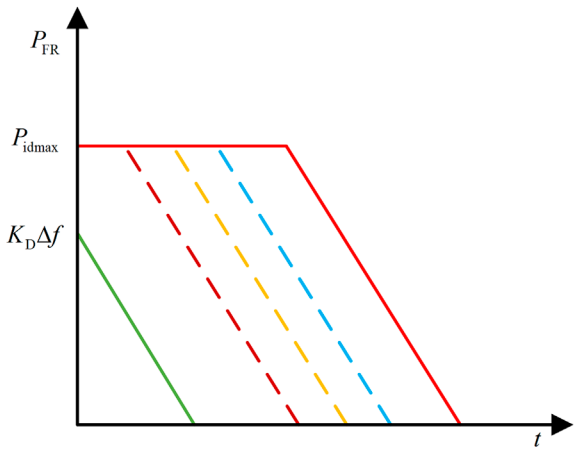

FIGURE 8
Frequency response power curves.

converter providing any frequency response power. The output power of the above method can be written as

$$P_{FR}=\begin{cases}0, & 0<|\Delta f|<f_d \text{ and } |\text{RoCoF}|<R_d\\ K_D\Delta f, & f_d<|\Delta f|<f_{RPC} \text{ and } |\text{RoCoF}|<R_{RPC}\\ -P_{idmax}, & \Delta f<-f_{RPC} \text{ or RoCoF}>R_{RPC}\\ +P_{idmax}, & \Delta f>f_{RPC} \text{ or RoCoF}<-R_{RPC}\end{cases} \tag{30}$$

The specific implementation of the RPC principle is shown in Figure 7, where f_d and f_{RPC} are the frequency deviation limits for the droop and RPC modes, f_{relay} is the limit value of the frequency offset relay, R_d is the RoCoF threshold for the steady-state operation mode and the droop control mode, and R_{RPC} is the RoCoF threshold for the RPC mode. The red line encircles the steady-state mode of operation, and the light yellow area is the operating interval where the RPC mode is converted to the steady-state mode (i.e., the power provided by the RPC allows the system to reach steady-state operation without droop control), and the RoCoF threshold (i.e., the interval from R_{RPC} to R_d) is reserved to prevent further power fluctuations. In addition, the RPC mode is divided into two cases, -RPC and +RPC, depending on whether the converter is absorbing power or emitting power.

According to Figure 7, the different modes are elaborated as follows.

(1) Mode I: Steady-state mode. When $0<|\Delta f|<f_d$ and $|\text{RoCoF}|<R_d$, the system is in steady-state operation mode. The converter does not need to provide additional frequency response power and the system operates normally.
(2) Mode II: Droop control mode. When $f_d<|\Delta f|<f_{RPC}$ and $|\text{RoCoF}|<R_{RPC}$, the system is in droop control mode, and the converter only needs to provide the power required for droop control. The purpose of setting this mode is to avoid the converter to run at maximum power for a long time, and it can smoothly exit the RPC mode to avoid the secondary frequency fluctuation caused by the sudden change of frequency regulation power due to mode switching.
(3) Mode III: RPC mode. When $\Delta f<-f_{RPC}$ or $\text{RoCoF}>R_{RPC}$, it indicates that the system generates too much power and needs to absorb the excess power; the system operates in -RPC mode, and the converter absorbs the excess power ($-P_{idmax}$) from the system.
(4) Mode IV: +RPC mode. When $\Delta f>f_{RPC}$ or $\text{RoCoF}<-R_{RPC}$, it indicates that the system generates less power and needs to provide additional compensation power; the system operates in +RPC mode, and the converter generates power with the value of $+P_{idmax}$.

The output frequency response power of the RPC strategy can be represented by Figure 8: in the event of a large disturbance, the system provides its maximum reserve power to resist the disturbance power instantaneously, and switches to droop control over time when the droop interval is reached by the frequency indicators, as shown by the dashed lines in Figure 8 representing different magnitudes of power disturbances. The larger the disturbance, the longer the RPC mode operation. When the steady-state indicators are satisfied, the converter no longer provides frequency response power.

Assuming that the power disturbance of the LCC-HVDC system is very large (i.e., $\Delta P_L>P_{idmax}$), the frequency response power provided by the converter is its maximum power reserve P_{idmax}. The maximum power reserve is used to support the grid frequency at the sending end until the system frequency indexes reach the droop mode interval, then the converter is

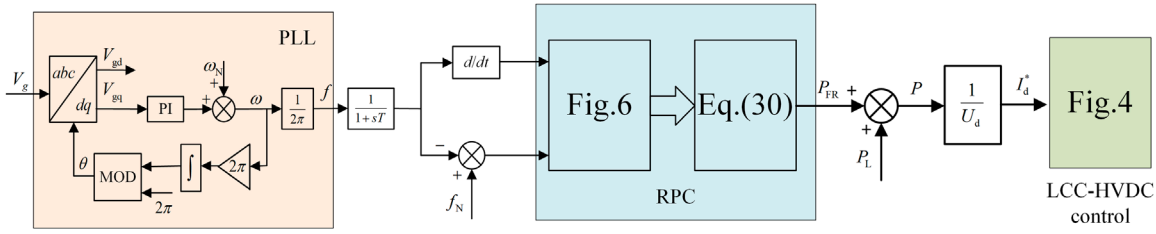

FIGURE 9
Proposed frequency control scheme for sending end of LCC-HVDC system.

TABLE 1 System parameters.

Parameter	Value	Parameter	Value
DC Voltage	500 kV	Sending end voltage	500 kV
DC current	2000 A	Receiving end voltage	345 kV
Line length	300 km	Line resistance	0.0015Ω/km
Line inductance	0.792×10^{-3}H/km	Line capacitance	14.4×10^{-9}F/km
Rectifier-side transformer ratio	0.9	k_p	700
Inverter-side transformer ratio	0.96	k_d	100
Droop factor	3×10^7	Reactance	0.5 H

TABLE 2 RPC control strategy parameters.

Frequency parameter	Value (Hz)	RoCoF parameter	Value (Hz/s)
f_d	0.05	R_d	0.5
f_{RPC}	0.2	R_{RPC}	1.5
f_{relay}	0.6	R_{relay}	2.5

switched to the droop control to smoothly exit the RPC mode and reduce the oscillation problem caused by the sudden change of power when switching modes. This implementation process is illustrated in detail in Figure 9. First, the frequency parameters required for the RPC control strategy are obtained through the phase-locked loop, and then the logic shown in Figure 7 is used to determine the operating interval to which this moment belongs. The control provides the required power, and finally changes the reference value of the DC current in the LCC-HVDC system.

5 Simulation verification

To verify the frequency control scheme proposed in this paper, the simulation model shown in Figure 1 was established in MATLAB/Simulink, where multiple wind turbines were used at the sending end to simulate a wind farm with a total installed capacity of 600 MW and one generator set to simulate a thermal power plant with an installed capacity of 900 MW, which was used to simulate a finite large system. The receiving end is approximated as an infinite grid. The reserve power capacity of the LCC-HVDC system is 30 MW, and the following simulation analysis was carried out for two operating conditions of load disturbance and wind speed fluctuation at the sending end of the grid. The system parameters are shown in Table 1, the parameters of the RPC control strategy are shown in Table 2, and the control parameters of the LCC-HVDC system are detailed in Atighechi et al. (2014).

5.1 Load disturbance condition

The load disturbance condition is simulated for two cases: single disturbance and continuous disturbances. The single disturbance corresponds to the 100 MW load shedding (which can be considered as a large disturbance), and the continuous disturbances include two consecutive events of load shedding (40 MW and 50 MW respectively).

For the single disturbance condition, the frequency characteristics of the natural response, droop control, PD control and RPC-based control are compared and analyzed. At 60 s, the

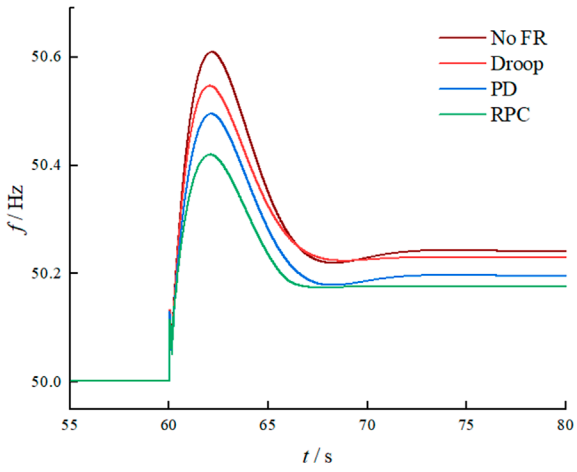

FIGURE 10
Sending end grid frequency in the event of 100 MW load shedding.

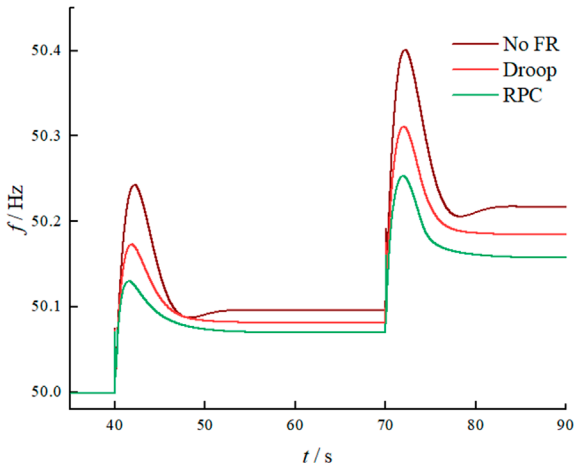

FIGURE 11
Sending end grid frequency in the event of continuous load shedding.

load shedding of 100 MW at the sending grid is simulated, and the frequency variation of the sending end grid is shown in Figure 10. From the figure, it can be seen that at the moment the load shedding starts at the sending grid, the system power changes abruptly, and the maximum frequency reached by the system is about 50.6 Hz when there is no additional control. The maximum frequencies of the system are 50.54 Hz, 50.49 Hz and 50.4 Hz when the droop control, PD control and RPC control are adopted respectively, and it can be seen that the RPC control strategy has the best effect, i.e., the maximum frequency it reaches is the smallest. After the disturbance, the steady-state frequency deviation is 0.24 Hz under the natural response, and both droop control and PD control properly reduce the steady-state frequency deviation of the system, and their values are 0.22 Hz and 0.19 Hz, respectively. The steady-state frequency deviation is the lowest (0.17 Hz) by using the RPC-based strategy, which has the best frequency deviation suppression effect.

Next, the case of continuous disturbances is simulated. The grid at the sending end reduces 40 MW load at 40 s and another 50 MW load at 70s, and the system simulation results are shown in Figure 11. It can be seen from the figure that the power disturbance occurred at 40s, the maximum frequency deviation under the natural response is 0.24Hz, when the droop control and RPC strategy are adopted, the maximum frequency deviation of the system is 0.17Hz and 0.12Hz respectively. It can be seen that the droop control and RPC strategy can restrain frequency fluctuation to a certain extent, but RPC strategy has the strongest ability to restrain frequency fluctuation. When the system frequency reaches a steady state, the system frequency under natural response is 50.1Hz. Under the droop control and RPC strategy, the system frequency is 50.08 Hz and 50.07 Hz respectively, which can reduce the steady-state frequency deviation, and the effect is relatively well.The frequency indicators are also within the allowable range of the grid. In summary, it can be seen that the RPC strategy has the best ability to suppress frequency fluctuations and restore steady-state frequency. Next, 50 MW load shedding occurred at 70s, the maximum frequency deviation of the natural response was 0.4Hz, and the maximum frequency deviations when the droop control and RPC strategy were adopted were 0.31 Hz and 0.25 Hz. When the steady state was reached, the natural response system frequencies, under droop control and RPC strategy are 50.21Hz, 50.18Hz, and 50.15Hz respectively. It can be seen that the RPC strategy can still achieve a better control effect for continuous disturbance, and significantly reduce the steady-state frequency deviation. For the droop control, although the frequency performance of the system is also improved, it is not as effective as the RPC strategy. Because the setting of the droop parameters is closely related to the disturbance size and system parameters, and the adaptability to the disturbance is poor.For the RPC control strategy, because its + RPC mode is the first to start, it completely utilizes the system reserved capacity; after the frequency indexes reach the droop mode interval, the RPC switches into the droop control mode, so that the system obtains the best frequency characteristics.

5.2 Wind speed fluctuation condition

The actual wind speed is not constant, and the power generation of the wind farm is always affected by the environment. In the simulation, the wind speed suddenly changes from the rated 11 m/s to 9 m/s at 50 s, and the frequency of the renewable energy generation system using

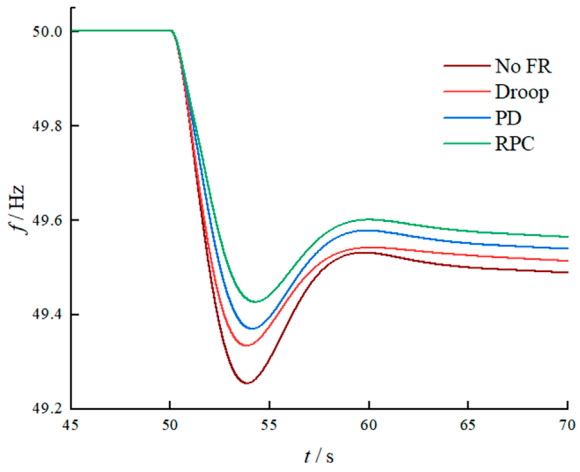

FIGURE 12
Sending end grid frequency in the event of sudden change in wind speed.

different controls is shown in Figure 12. At 50s, the wind speed suddenly changed from the rated 11 m/s to 9 m/s. The frequency characteristics of the new energy transmission system under different control are shown in Figure 12. It can be seen from the figure that the sudden wind speed fluctuation causes the frequency of the sending-end power grid to drop rapidly. The lowest point of the system frequency under the natural response is 49.25Hz. When the droop control, PD control and RPC control are used respectively, the lowest point frequency are 49.33 Hz, 49.37 Hz, and 49.43 Hz. When the system frequency is close to the steady state, the frequency is 49.5 Hz under the natural response, and the steady-state frequency ratio when using droop control, PD control and RPC strategy is 49.52 Hz, 49.55 Hz and 49.57 Hz. It can be seen that the RPC strategy has the best performance and ability to suppress frequency excursions and steady-state frequency recovery.Although the system fully utilizes the reserved capacity, for the grid with a very high percentage of renewable energy, the wind speed fluctuation brings larger power oscillation, and the power reserve of the LCC-HVDC system needs to be appropriately increased to further improve the frequency characteristics of the power grid at the sending end.

6 Conclusion

In this paper, a frequency control scheme based on the RPC principle is proposed for the renewable energy integrated LCC-HVDC sending end system. The frequency performances of the system with the droop control, PD control and RPC strategy are compared and analyzed. It is seen that the RPC strategy can effectively reduce the frequency deviation of the system, reduce the time required to reach steady state, and improve the steady-state frequency. The power reserve of the system can be appropriately increased to further improve the frequency characteristics of the grid.

Data availability statement

The original contributions presented in the study are included in the article/supplementary material, further inquiries can be directed to the corresponding author.

Author contributions

All the authors conceived and designed the study. PW, BC, and LS performed the simulation, and wrote the manuscript with the guidance from QS. RL, YW, and KL conceived and designed the simulations.

Funding

The work was supported by the State Grid Ningxia Electric Power Co., Ltd. Under grant B329CG210000.

Conflict of interest

Authors PW and LS were employed by the company State Grid Ningxia Electric Power Co., Ltd. Authors BC and RL were employed by the company State Grid Ningxia Ultrahigh Voltage Company. Authors QS, YW, KL were employed by the company NR Engineering Co., Ltd.

The authors declare that the research was conducted in the absence of any commercial or financial relationships that could be construed as a potential conflict of interest.

Publisher's note

References

Abo-Khalil, A. G., and Lee, D.-C. (2008). MPPT control of wind generation systems based on estimated wind speed using SVR. *IEEE Trans. Ind. Electron.* 55, 1489–1490. doi:10.1109/tie.2007.907672

Alassi, A., Bañales, S., Ellabban, O., Adam, G., and MacIver, C. (2019). HVDC transmission: Technology review, market trends and future outlook. *Renew. Sustain. Energy Rev.* 112, 530–554. doi:10.1016/j.rser.2019.04.062

Atighechi, H., Chiniforoosh, S., Jatskevich, J., Davoudi, A., Martinez, J. A., Faruque, M. O., et al. (2014). Dynamic average-value modeling of CIGRE HVDC benchmark system. *IEEE Trans. Power Deliv.* 29, 2046–2054. doi:10.1109/tpwrd.2014.2340870

Dreidy, M., Mokhlis, H., and Mekhilef, S. (2017). Inertia response and frequency control techniques for renewable energy sources: A review. *Renew. Sustain. Energy Rev.* 69, 144–155. doi:10.1016/j.rser.2016.11.170

Guan, M., Pan, W., Zhang, J., Hao, Q., Cheng, J., and Zheng, X. (2015). Synchronous generator emulation control strategy for voltage source converter (VSC) stations. *IEEE Trans. Power Syst.* 30, 3093–3101. doi:10.1109/tpwrs.2014.2384498

He, C., He, X., Geng, H., Sun, H., and Xu, S. (2022). Transient stability of low-inertia power systems with inverter-based generation. *IEEE Trans. Energy Convers.*, 1–10. doi:10.1109/tec.2022.3185623

Holttinen, H., Kiviluoma, J., Flynn, D., Smith, J. C., Orths, A., Eriksen, P. B., et al. (2022). System impact studies for near 100% renewable energy systems dominated by inverter based variable generation. *IEEE Trans. Power Syst.* 37, 3249–3258. doi:10.1109/tpwrs.2020.3034924

Karawita, C., and Annakkage, U. (2010). "Control block diagram representation of an HVDC system for sub-synchronous frequency interaction studies," in 9th IET International Conference on AC and DC Power Transmission, London, 19-21 October 2010 (ACDC), 1–5.

Kroposki, B., Johnson, B., Zhang, Y., Gevorgian, V., Denholm, P., Hodge, B.-M., et al. (2017). Achieving a 100% renewable grid: Operating electric power systems with extremely high levels of variable renewable energy. *IEEE Power Energy Mag.* 15, 61–73. doi:10.1109/mpe.2016.2637122

Kwon, D.-H., Kim, Y.-J., and Gomis-Bellmunt, O. (2020). Optimal DC voltage and current control of an LCC HVDC system to improve real-time frequency regulation in rectifier- and inverter-side grids. *IEEE Trans. Power Syst.* 35, 4539–4553. doi:10.1109/tpwrs.2020.2997793

Lee, G.-S., Kwon, D.-H., Moon, S.-I., and Hwang, P.-I. (2020). A coordinated control strategy for LCC HVDC systems for frequency support with suppression of AC voltage fluctuations. *IEEE Trans. Power Syst.* 35, 2804–2815. doi:10.1109/tpwrs.2020.2964336

Li, C., He, P., and Li, Y. (2019). LCC-HVDC auxiliary emergency power coordinated control strategy considering the effect of electrical connection of the sending-end power grid. *Electr. Eng.* 101, 1133–1143. doi:10.1007/s00202-019-00855-0

Liu, H., Liu, X., Xiong, L., Li, M., and Zhu, Y. (2022). Adaptive power compensation-based frequency regulation strategy of wind turbine system. *IEEE J. Emerg. Sel. Top. Circuits Syst.* 12, 260–267. doi:10.1109/jetcas.2022.3142452

Morren, J., de Haan, S., Kling, W., and Ferreira, J. (2006). Wind turbines emulating inertia and supporting primary frequency control. *IEEE Trans. Power Syst.* 21, 433–434. doi:10.1109/tpwrs.2005.861956

Pawar, B., Batzelis, E. I., Chakrabarti, S., and Pal, B. C. (2021). Grid-forming control for solar PV systems with power reserves. *IEEE Trans. Sustain. Energy* 12, 1947–1959. doi:10.1109/tste.2021.3074066

Ratnam, K. S., Palanisamy, K., and Yang, G. (2020). Future low-inertia power systems: Requirements, issues, and solutions - a review. *Renew. Sustain. Energy Rev.* 124, 109773. doi:10.1016/j.rser.2020.109773

Shi, Q., Liu, H., Liu, K., Wang, Y., Zhang, Q., Lu, Y., et al. (2021). Coordinated sending-end power system frequency regulation via UHVDC. *Electronics* 10, 1909. doi:10.3390/electronics10161909

Song, G., Cao, B., and Chang, L. (2022). Review of grid-forming inverters in support of power system operation. *Chin. J. Electr. Eng.* 8, 1–15. doi:10.23919/cjee.2022.000001

Tamrakar, U., Shrestha, D., Maharjan, M., Bhattarai, B. P., Hansen, T. M., and Tonkoski, R. (2017). Virtual inertia: Current trends and future directions. *Appl. Sci. (Basel).* 7, 654. doi:10.3390/app7070654

Tayyebi, A., Groß, D., Anta, A., Kupzog, F., and Dörfler, F. (2020). Frequency stability of synchronous machines and grid-forming power converters. *IEEE J. Emerg. Sel. Top. Power Electron.* 8, 1004–1018. doi:10.1109/jestpe.2020.2966524

Xiong, L., Liu, X., Liu, H., and Liu, Y. (2022). Performance comparison of typical frequency response strategies for power systems with high penetration of renewable energy sources. *IEEE J. Emerg. Sel. Top. Circuits Syst.* 12, 41–47. doi:10.1109/jetcas.2022.3141691

Xiong, L., Liu, X., Liu, Y., and Zhuo, F. (2020). Modeling and stability issues of voltage-source converter dominated power systems: A review. *CSEE J. Power Energy Syst.*, 1–18. doi:10.17775/CSEEJPES.2020.03590

Xiong, L., Liu, X., Zhang, D., and Liu, Y. (2021). Rapid power compensation-based frequency response strategy for low-inertia power systems. *IEEE J. Emerg. Sel. Top. Power Electron.* 9, 4500–4513. doi:10.1109/jestpe.2020.3032063

Yogarathinam, A., Kaur, J., and Chaudhuri, N. R. (2017). Impact of inertia and effective short circuit ratio on control of frequency in weak grids interfacing LCC-HVDC and DFIG-Based wind farms. *IEEE Trans. Power Deliv.* 32, 2040–2051. doi:10.1109/tpwrd.2016.2607205

frontiers | Frontiers in Energy Research

TYPE Original Research
PUBLISHED 15 November 2022
DOI 10.3389/fenrg.2022.1067202

OPEN ACCESS

EDITED BY
Liansong Xiong,
Xi'an Jiaotong University, China

REVIEWED BY
Xiaokang Liu,
Politecnico di Milano, Italy
Donghai Zhu,
Huazhong University of Science and Technology, China
Shunliang Wang,
Sichuan University, China

*CORRESPONDENCE
Yongheng Luo,
1873096384@qq.com

SPECIALTY SECTION
This article was submitted to Process and Energy Systems Engineering, a section of the journal Frontiers in Energy Research

RECEIVED 11 October 2022
ACCEPTED 31 October 2022
PUBLISHED 15 November 2022

CITATION
Zhang F, Wang Y, Huang D, Lu N, Jiang M, Wang Q, Luo Y and Jiang F (2022), Integrated energy system region model with renewable energy and optimal control method.
Front. Energy Res. 10:1067202.
doi: 10.3389/fenrg.2022.1067202

Integrated energy system region model with renewable energy and optimal control method

Feifei Zhang[1], Yueqiang Wang[1], Dong Huang[1], Nihui Lu[1], Mintao Jiang[1], Qi Wang[1], Yongheng Luo[2]* and Fei Jiang[2]

[1]State Grid Shanghai Electric Power Company Changxing Power Supply Company, Shanghai, China, [2]College of Electrical and Information Engineering, Changsha University of Science and Technology, Changsha, China

In the context of global energy transition, integrated regional energy systems containing renewable energy sources play an important role. While improving the economic and carbon efficiency of energy utilization, renewable energy sources also bring research challenges to the safe and reliable operation of energy systems. Based on the region concept, a region model and optimal control method for integrated energy systems containing renewable energy are proposed. Firstly, the key pipeline is taken as the observation object, and the feasible region model of the integrated energy system is determined according to the capacity of key equipment and its pipeline capacity with the multi-energy balance equation as the feasible constraint. Then, considering the mutual backup relationship of different equipment and pipelines, the regional integrated energy system security region model is constructed based on the N-1 security criterion, and the optimal control method based on the region concept is proposed. Finally, the validity of the model is analyzed with arithmetic examples, and the influence of the access capacity and access location of renewable energy on the feasible and safe regions of the regional integrated energy system is discussed. And according to the actual situation of the working state point, the optimal adjustment strategy based on the efficiency function and security constraint is given.

KEYWORDS

renewable energy, regional integrated energy system, feasible region, security region, optimal control methods

1 Introduction

Recently, due to extreme weather, Sichuan and Chongqing have faced a serious power rationing crisis. New energy sources, including wind energy and solar energy, are increasingly important for future energy development.(Li et al., 2018; Jiang et al., 2019; Jiang et al., 2022) On 21 May 2021, the National Development and Reform Commission and the National Energy Administration issued the Notice on the Establishment and Improvement of the Renewable Energy Electricity Consumption Guarantee Mechanism to assign responsibility for renewable energy consumption according to the actual situation of each province, so as to promote the construction

of a new power system and the achievement of the "dual carbon" goal. The user side oriented regional integrated energy system (RISE) is getting extensive attention and rapid development. It has the important characteristics of green energy supply, high efficiency and low carbon, multi energy coupling and complementation. At the same time, the user oriented location advantage can facilitate the local consumption and utilization of renewable energy, thus reducing transmission loss and improving the economic and carbon benefits of energy utilization. However, due to the multi energy and heterogeneous characteristics of the integrated energy system, the interconnected and coupled multi energy networks can improve energy utilization, but at the same time, the fault accidents will also affect each other. The fluctuation of renewable energy output will aggravate the risk of mutual transmission of failures and accidents, and also bring severe challenges to the safety state analysis and safety boundary construction of the entire energy system.

The concept of region is an important method in static security analysis, which can obtain the reliable and safe operation range of energy system through the method of constructing security boundary. In the field of single energy grid research, literature (Xiao et al., 2018) proposed a direct calculation method for the security region of distribution network, and described the causes and physical significance of various area characteristics in the security region. Literature (Su et al., 2021a) proposed a new method to calculate the security region of integrated energy system, which can reduce the error of existing schemes and improve the estimation accuracy. Literature (Li X. et al., 2022) explores the voltage security region under large-scale renewable energy access and establishes a general optimization model, which can significantly improve the calculation efficiency. Literature (Maihemuti et al., 2021) proposed a dynamic security stability region calculation method based on hybrid algorithm for the security problems brought about by the rapid development of renewable energy. Literature (Ding et al., 2016) proposed a robust two-layer voltage security region model for possible cascading tripping events in wind farms, and conducted a complete modeling for the network results. Literature (Su et al., 2021b) explored the dual time scale characteristics of IES based on the static security region theory, and established an accurate steady-state security region model. Compared with traditional methods, its calculation method has been greatly improved. Literature (Nguyen et al., 2019) is based on Brouwer fixed point theorem and applied to the calculation of fixed points of power flow equation. Finally, effective internal approximation of feasible solution can be found through local search. Literature (Liu et al., 2020) proposed a method to construct the security domain based on the grid structure, which can solve practical problems well and visualize the security domain in 2D and 3D. Literature (Li W. et al., 2022) analyzes the comprehensive impact of renewable energy output fluctuation on power system probabilistic power flow from an overall perspective. Literature (Lei et al., 2021) describes the security region fluctuation space model of AC/DC distribution network in a mixed scenario, considering the high proportion of photovoltaic access.

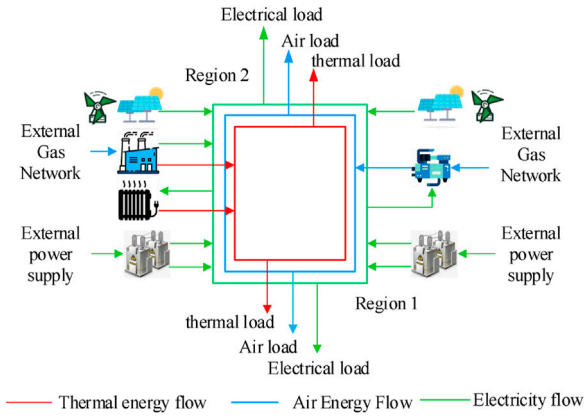

FIGURE 1
A typical RISE structure.

It can be seen from the appeal that the research on security region and security boundary has been widely applied in the power system, but the research on the integrated energy system with close multi energy coupling started late, especially the regional integrated energy system with renewable energy access. Based on this, this paper proposes a comprehensive energy system domain model with renewable energy and an optimal control method. Firstly, the feasibility region model of integrated energy system with renewable energy is analyzed, and the stability feasibility margin of the system is described intuitively from the perspective of the region. Then, a security domain model of integrated energy system with renewable energy is built to analyze the impact of renewable energy access capacity and location on the security domain. Finally, a security optimization control method based on domain concept is proposed, which considers the comprehensive energy system efficiency function and security operation constraints, so as to achieve safe, reliable and efficient operation.

2 Regional integrated energy system with renewable energy

RISE faces the customer side and has a natural location advantage, which plays an important role in the local consumption of renewable energy. It considers each discrete traditional energy network, diversified energy supply sources and diversified energy demand, and aims to realize the mutual coupling and synergy of each energy flow and the full

consumption of renewable energy. A typical structure of RISE is shown in Figure 1.

2.1 Analysis of energy supply structure

The RISE uses the original electric network and natural gas network as the basis, and expands the regional heat network according to the actual demand on the customer side. The main external energy sources of the RISE are the superior gas network, the superior power grid and the regional renewable energy sources. Two distributed energy stations are used to build a regional interconnected and interoperable integrated energy system. The distribution network generally adopts a radial or ring structure. The heat network is not suitable for long-distance and large-capacity transmission because of its unique transmission characteristics, so it is generally applied only at the campus level and adopts a radial grid structure. Natural gas network has less loss during transportation and is suitable for long-distance transmission, but requires compressor for pressurization. Meanwhile, in order to improve the safety and reliability of energy supply, the two regional distribution networks transmit interactive power through liaison lines, while the regional gas and heat networks adopt multi-source interconnection to ensure inter-regional mutual assistance and interoperability.

Taking the typical RISE in Figure 1 as an example, the key equipment and key structures of the distributed energy station are analyzed and introduced. Region 1 is built as a distributed energy station with mainly thermoelectric coupling, providing electrical and thermal energy for both regions, while taking into account the access to renewable energy in Region 1. The key equipment of the grid is two main transformers which are used as standby for each other, and the key lines include power feeders and renewable energy access feeders, etc; the equipment of the heat network includes CHP (Combined Heat and Power) units, gas boiler GB (Gas Boiler), circulating pump CP (Circulating Pump), and the key lines include hot water piping. Pump), and key lines with hot water pipelines. Area 2 is built as an electricity-gas coupled distributed energy station to provide electricity and natural gas for both areas, while taking into account the renewable energy access in Area 2. The key equipment of the grid is two main transformers with mutual backup, and the key lines include power feeders and renewable energy access feeders, etc. The equipment of the gas network includes several compressors C (Compressor) with mutual backup, and the key lines are natural gas transmission pipelines.

2.2 Probabilistic modeling of renewable energy

The two-parameter weibull-based stochastic probability model is widely used in engineering and also has good results in performing modeling of wind turbines (Ghofrani et al., 2013). The wind turbine probability distribution P_{wout} can be expressed as

$$f(V_h) = \left(\frac{k_w}{c_w}\right)\left(\frac{V_h}{c_w}\right)^{(k_w-1)} \exp\left[-\left(\frac{V_h}{c_w}\right)^{k_w}\right], \tag{1}$$

$$P_{wout} = \begin{cases} 0, & 0 \le V_h \le V_{in},\ V_{out} \le V_h, \\ P_{w\max}\dfrac{V_h - V_{in}}{V_r - V_{in}}, & V_{in} \le V_h \le V_r, \\ P_{w\max}, & V_r \le V_h \le V_{out}, \end{cases} \tag{2}$$

Where: k_w denotes shape factor, c_w denotes scale factor; Vr, V_h, V_{out}, V_{in} denote rated wind speed value, actual wind speed, cut-out wind speed and cut-in wind speed respectively; $P_{w\max}$ denotes maximum output power of wind turbine. And for PV generator sets, based on Beta probability distribution model has better results (Zhang et al., 2013), then the PV generator set output model can be expressed as

$$f(S_h) = \frac{\Gamma(\alpha_p + \beta_p)}{\Gamma(\alpha_p)\Gamma(\beta_p)}\left(\frac{S_h}{S_r}\right)^{\alpha_p - 1}\left(1 - \frac{S_h}{S_r}\right)^{\beta_p - 1}, \tag{3}$$

$$P_{\mathrm{pv},out} = \begin{cases} P_{\mathrm{pv,max}}\dfrac{S_h}{S_r}, & S_h \le S_r, \\ P_{\mathrm{pv,max}}, & S_h > S_r, \end{cases} \tag{4}$$

Where: a_p denotes shape factor, β_p denotes scale factor; S_h denotes light intensity and rated light intensity; $P_{\mathrm{PV,\ max}}$ denotes maximum output power of PV generator set.

3 Feasible region for integrated regional energy systems with renewable energy

The study of the feasible region of the RISE can provide an intuitive understanding of the feasible margin of stability of the whole energy system from a global perspective, and can provide a theoretical basis for short-time dispatch operation, which is of great practical significance. (Relationship with the security region). At the same time, the high proportion of renewable energy access will have a non-negligible impact on the feasible region of the RISE, based on the probabilistic model of renewable energy, the feasible region of the RISE is analyzed.

3.1 The feasible region definition and boundary model

The feasible region is the maximum supply range of the energy system that can guarantee normal energy use without failure. The feasible region portrays the boundary of stable system operation under different load demands and equipment operation states. When the load demand or equipment operation capacity crosses the feasible region, the tidal distribution will not have practical significance. In the RISE, each energy subsystem is coupled with each other, which inevitably makes its feasible region also have interlocking relationships. In this paper, each key pipeline is selected as the energy supply state observation point of the RISE, and its operation state already contains the key equipment operation, and at the same time, it can be tide optimization and control. Define the operation state vector $\boldsymbol{L} = [L_1, L_2, L_m]$ of the whole integrated energy system, which represents the energy supply state of a total of m key pipelines.

Under the key equipment and grid structure constraints, the feasible region of the integrated regional energy system can be expressed as

$$S = \{\boldsymbol{L} | f(\boldsymbol{L}) = 0, g(\boldsymbol{L}) \le 0\}, \tag{5}$$

Where: $f(L) = 0$ indicates the equation constraint of the critical pipe network under normal operation; $g(L) \le 0$ indicates the inequation constraint of the critical pipe network under normal operation. The equation constraint of RISE is the multi-energy flow balance constraint, including the energy balance equation of distribution network system, thermal system and natural gas system. There are many related researches, so I will not repeat them here.

3.2 Feasible boundary analysis

The feasible region contains not only the equation constraints of the reaction energy balance relationship, but also the inequality constraints of critical pipelines and critical equipment. Under normal conditions, the operational constraints of the integrated regional energy system are mainly determined by the capacity of equipment and the allowable through-capacity of pipelines. To determine the feasible region of the RISE, the following principles are followed: 1) the through capacity of the key pipeline cannot exceed the upper and lower operating boundaries of the pipeline. 2) The through capacity of key pipelines connected with key equipment cannot exceed the capacity of key equipment 3) The minimum capacity of pipelines should ensure the energy supply of their coupled equipment. Figure 2 is taken as an example to illustrate the inequality boundary of the regional integrated energy system with renewable energy.

For the power system pipeline $\boldsymbol{L} = \{L|L_1,L_2,L_3,L_4,L_7,L_{10}\}$, the pipeline constraint analysis is performed. Pipeline L_1 and pipeline L_4 operate in similar states, both have renewable energy intervention, and renewable energy generation has probability, which makes the key pipeline operation boundary has certain probability, and the probability function $\varphi(x)$ can be applied to probabilize renewable energy, and the probability function of photovoltaic power generation is $P_{pv}\varphi_1(x)$, and the probability function of wind power generation is $P_w\varphi_2(x)$. The probability model of $\varphi(x)$ can be detailed in Section 2.2. After considering the effects of transformer capacity and renewable energy generation, the feasible boundaries of L_1 and L_4 are

$$L_{10} < L_1 < \min\left(C_{L1}, C_{T1} + P_{pv}\phi_1(x)\right), \tag{6}$$

$$(P_{C1} + P_{C2} + P_{C3} + P_{C4}) < L_4 < \min\left(C_{L4}, C_{T4} + P_w\phi_2(x)\right), \tag{7}$$

Where: C_{L1} denotes the capacity of pipeline 1; C_{T1} denotes the capacity of transformer T1;P_{C1},P_{C2},$P_{C3,}$ and P_{C4} denote the electrical power required by compressors C1,C2, C3and C4, respectively; for the analysis of the impact of renewable energy generation on the feasible region, Figure 3 denotes the probability boundary diagram of critical pipeline 1 with PV generation. The probability boundary diagram of critical pipeline L_4 with wind power generation is shown in Figure 3. For the operation upper boundary of pipeline L_1, there are two cases: when the capacity of pipeline L_1 is large enough, its operation upper boundary is determined by the capacity of the transformer connected to it and PV generation, and its probability boundary is shown in Figure 3; when the capacity of pipeline L_1 is not large enough, its operation upper boundary is determined by the capacity of L_1, and at the same time, the transformer will not be in full-load operation to ensure the full consumption and safe operation of renewable energy.

In normal operation, the distribution network is open-loop operation, L_2 and L_3 operating state is similar, and its operating boundary is determined by its own capacity and the connected transformer, and its operating boundary can be expressed as

$$0 < L_2 < \min(C_{T2}, C_{L2}), \tag{8}$$

$$0 < L_3 < \min(C_{T3}, C_{L3}), \tag{9}$$

Where: C_{Ti} shows the transformer Ti capacity; C_{Li} shows the pipeline i capacity. The feasible boundary of pipeline L_{10} is

$$0 < L_{10} < \min(C_{L10}, L_1), \tag{10}$$

The feasible lower boundary of pipeline L_7 needs to consider the reliable operation of the circulation pump, and its feasible boundary can be expressed as

$$(P_{CP1} + P_{CP2}) < L_7 < C_{L7} \tag{11}$$

Where: P_{CPi} indicates the electrical power required by the circulation pump CP_i. For the natural gas pipeline $L = \{L|L_8,L_9\}$, the main

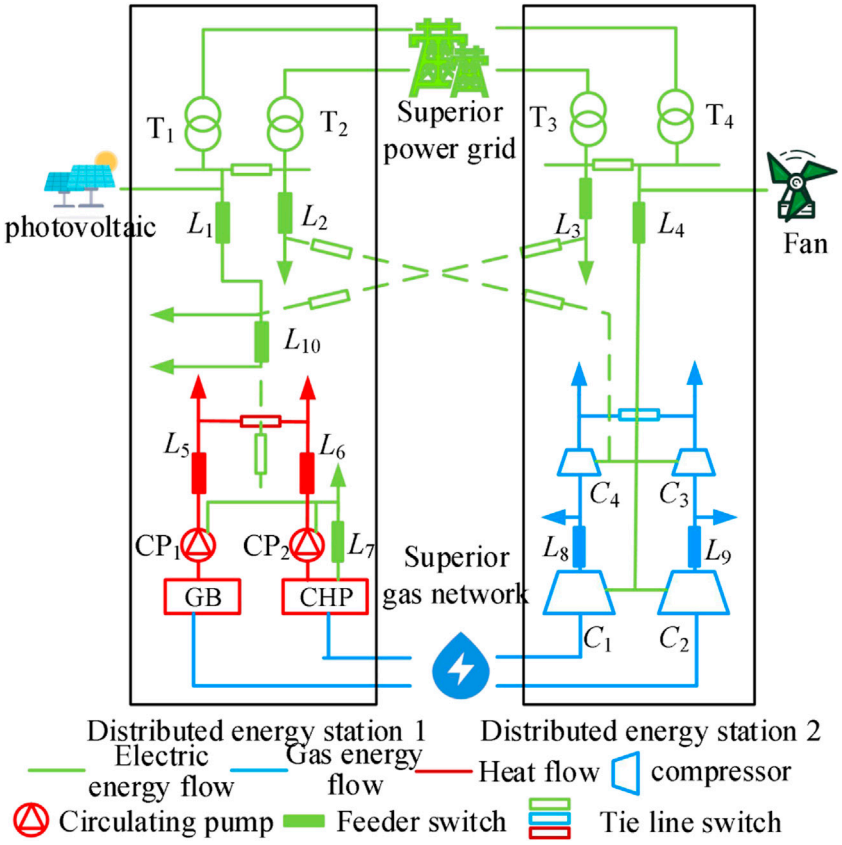

FIGURE 2
Regional integrated energy system diagram including renewable energy.

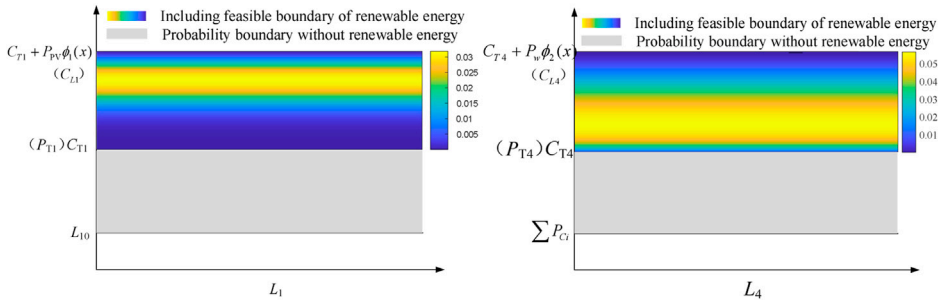

FIGURE 3
Probability boundary diagram of L_1 and L_4.

consideration is the capacity of the upper-level coupling equipment and the pipeline, and its operation boundary is

$$0 < L_8 < \min(C_{C1}, C_{L8}), \tag{12}$$

$$0 < L_9 < \min(C_{C2}, C_{L9}), \tag{13}$$

Where: C_{Ci} denotes the capacity of compressor C_i. For the heat line $L = \{L|L_5,L_6\}$, the line L_6 needs to consider the influence of specific heat capacity of CHP unit, and the line L_5 needs to consider the influence of the connected circulation pump, then its operation boundary is

$$0 < L_5 < \min\left(C_{\mathrm{CP1}}, \eta C_{GB}, C_{L5}\right), \tag{14}$$

$$C_{\mathrm{CHP,min}} L_7 < L_6 < \min\left(C_{L6}, C_{\mathrm{CP2}}, C_{CHP,\max} L_7, C^{e}_{\mathrm{CHP}}\right), \tag{15}$$

Where: C_{CPi} denotes the capacity of circulating pump CP_i; $C_{CHP,min}$, $C_{CHP,max}$ denote the minimum thermoelectric ratio and maximum thermoelectric ratio respectively; C_{GB} denotes the capacity of gas boiler; C^{e}_{CHP} denotes the electrical capacity of CHP unit.

4 Regional comprehensive energy system security region including renewable energy

The security region is the area where the RISE can guarantee the maximum energy supply in case of N-1 failure. The safety region is an intuitive depiction of the safe operation of the whole energy system from the perspective of N-1 safety criterion, which provides a theoretical basis for the long-term safe operation of the integrated energy system. N-1 safety criterion is widely used in the scheduling operation and planning design of the integrated energy system, but the access of renewable energy affects the N-1 safety boundary, and this paper analyzes the safety region of the RISE based on the probabilistic model of renewable energy.

4.1 Security region definition and boundary model

The main differences between the security region and the feasible region are as follows: First, the security region mainly depicts the maximum operating boundary that the energy system can guarantee reliable energy supply in case of N-1 failure of key equipment or key pipelines; The feasible region mainly describes the maximum operation boundary of the energy system to ensure reliable operation under normal operation conditions. Second, security region provides theory for long-term operation planning of energy system; The feasible region mainly aims at the short-term scheduling operation of the energy system. Thirdly, in case of failure, the overload capacity of key equipment and pipelines shall be considered. Under normal circumstances, it is not required. The security Region is included in the feasible region, which is the operation region established according to different constraints and purposes. During the construction of security boundary and security region, the equality constraint is consistent with the feasible region. See Section 3.1 for details, which will not be repeated here.

4.2 Security boundary analysis

N-1 safety boundary analysis is mainly aimed at key equipment and pipelines. Because of their high probability of failure in the integrated energy system, the failure is often the most serious. The safety region of the energy system is determined by redistributing the load after the failure with the idea of globalization. The key equipment and key pipelines are standby for each other, so it is necessary to consider the interconnected energy subsystems as a whole.

The key equipment of the power system includes CHP units, transformers T1, T2, T3, T4, and key pipelines $\boldsymbol{L} = \{L|L_1,L_2,L_3,L_4,L_7,L_{10}\}$. First, analyze the failure of key equipment. T1 and T2 are standby for each other, and their joint analysis is carried out. When T1 or T2 fails, the load carried by the fault transformer can be transferred to another transformer through the interconnection switch between them. The output of photovoltaic power generation can play a complementary role to electric energy, but it will also make the safety upper bound of L_1 and L_2 appear probabilistic. Its safety boundary can be expressed as

$$L_{10} < L_1 + L_2 < \min\left(C_{\mathrm{T1}}, C_{\mathrm{T2}}\right) + P_{pv}\phi_1(x). \tag{16}$$

Similarly, wind power makes the upper boundary of L_3 and L_4 safety boundary probabilistic, and the formula is

$$\sum P_{Ci} < L_3 + L_4 < \min\left(C_{\mathrm{T3}}, C_{\mathrm{T4}}\right) + P_w\phi_2(x). \tag{17}$$

When CHP unit fails, the load connected to L_7 will be supplied by L_{10} feeder through tie line, so L_{10} safety boundary formula is

$$\left(P_{\mathrm{CP1}} + P_{\mathrm{CP2}}\right) < L_{10} < \left(C_{L10} - L_7\right). \tag{18}$$

N-1 safety boundary is jointly constrained by safety boundary of key equipment and safety boundary of key pipe network. In case of failure of key pipelines, other pipelines will supply energy through tie lines, so it is necessary to analyze the key pipelines connected through tie lines in pairs. For the associated pipeline pair $\{L_2, L_4\}$, L_2 failure, distributed energy station 2 supplies energy to another station. Taking L_2 pipeline failure as an example, the system operates under failure as shown in the Figure 4. Then L_2 security constraint boundary is

$$0 < L_2 < \min\left[\left(C_{\mathrm{T3}} + C_{\mathrm{T4}} + P_w\phi_2(x) - L_3 - L_4\right), \left(C_{L4} - L_4\right)\right]. \tag{19}$$

In case of L_4 failure, the distributed energy station 1 supplies energy to L_4, so the safety constraint boundary of L_4 is

$$\sum P_{Ci} < L_4 < \min\left[\left(C_{\mathrm{T1}} + C_{\mathrm{T2}} + P_{pv}\phi_1(x) - L_1 - L_2\right), \left(C_{L2} - L_2\right)\right]. \tag{20}$$

For the associated pipeline $\{L_7, L_{10}\}$, when L_{10} fails, CHP unit will provide energy for the failed line L_{10}. The security constraint is

$$0 < L_{10} < \min\left(C^{e}_{\mathrm{CHP}} - L_7, C_{L7} - L_7, L_6/C_{\mathrm{CHP,min}}\right), \tag{21}$$

Where: C^{e}_{CHP} represents the maximum capacitance of CHP unit. In case of L_7 fault, L_{10} will provide energy to the fault line L_7 through the tie line, and its safety constraints are

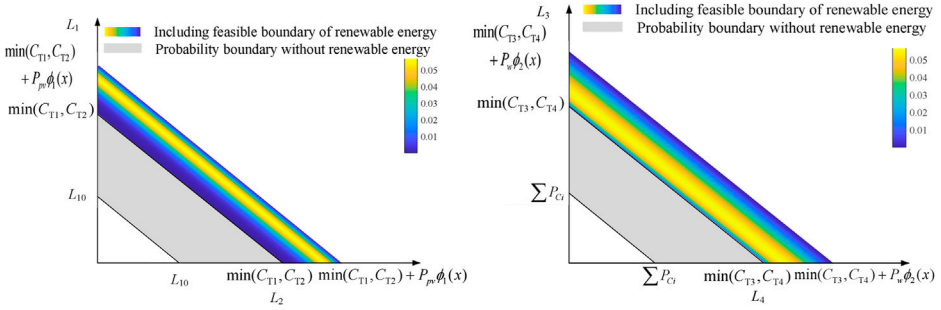

FIGURE 4
Probability boundary diagram of (L_1,L_2) and (L_3,L_4).

$$\sum P_{CPi} < L_7 < \min\left\{\max\left[\left(C_{T1} + C_{T2} + P_{pv}\phi_1(x) - L_1 - L_2\right), \left(C_{T3} + C_{T4} + P_w\phi_2(x) - L_3 - L_4\right)\right], \left(C_{L10} - L_{10}\right)\right\}. \quad (22)$$

In case of associated $\{L_3, L_{10}, L_1\}$ and L_3 faults, the distributed energy station 1 transformer unit and CHP unit will supply energy to L_3 through tie lines, and the safety boundary formula is

$$0 < L_3 < \min\left[\left(C_{T1} + C_{T2} + P_{pv}\phi_1(x) - L_1 - L_2\right), \left(C_{L1} - L_1\right)\right] + \min\left[\left(C^e_{\mathrm{CHP}} - L_7\right), L_6/C_{\mathrm{CHP,min}}, \left(C_{L7} - L_7\right), \left(C_{L10} - L_{10}\right)\right]. \quad (23)$$

In case of L_1 fault, distributed energy station 2 and CHP unit supply energy for L_1 through tie line, then its safety boundary is

$$0 < L_1 < \min\left[\left(C_{T3} + C_{T4} + P_w\phi_2(x) - L_3 - L_4\right), \left(C_{L3} - L_3\right)\right] + \min\left[\left(C^e_{\mathrm{CHP}} - L_7\right), \left(C_{L7} - L_7\right), \frac{L_6}{C_{\mathrm{CHP,min}}}, \left(C_{L10} - L_{10}\right)\right]. \quad (24)$$

The key equipment of the thermal system includes circulating pumps CP1 and CP2, gas boilers GB and CHP units. The key pipelines are $\{L_5, L_6\}$. Key equipment are standby for each other. When gas boiler GB or circulating pump CP1 or pipeline L_5 fails, the load will be provided by CHP unit, and the safety boundary is

$$0 < L_5 < \min\left[\left(C^h_{\mathrm{CHP}} - L_6\right), \left(C_{\mathrm{CP2}} - L_6\right), \left(C_{L6} - L_6\right), \left(C_{\mathrm{CHP,max}}L_7 - L_6\right)\right], \quad (25)$$

Where: C^h_{CHP} represents the heat capacity of CHP unit. When CHP unit or circulating pump CP2 or pipeline L_6 fails, its load will be provided by gas boiler GB and circulating pump CP2, and its safety boundary is

$$0 < L_6 < \min\left[\left(C_{\mathrm{GB}} - L_5\right), \left(C_{\mathrm{CP1}} - L_5\right), \left(C_{L5} - L_5\right)\right], \quad (26)$$

Where: C_{GB} represents the capacity of gas fired boiler GB.

The key equipment of natural gas system includes compressor C1, C2, C3, C4, and key pipelines L_8 and L_9. In case of failure of compressor C1 or pipeline L_8, the load carried by L_8 will be provided by C2 through L_9 and tie line, and the safety boundary is

$$0 < L_8 < \min\left[\left(C_{\mathrm{C2}} - L_9\right), \left(C_{L9} - L_9\right)\right]. \quad (27)$$

In case of failure of compressor C2 or pipeline L_9, the load carried by L_9 will be provided by C1 through L_8 and tie line, and the safety boundary is

$$0 < L_9 < \min\left[\left(C_{\mathrm{C1}} - L_8\right), \left(C_{L8} - L_8\right)\right]. \quad (28)$$

5 Optimal control method based on region concept

Based on the boundary analysis method of feasible region and security region, the probability boundary of the two regions is determined according to the solution method of the region. The operation objectives of the feasible area and the security area are different. The feasible area explores the operation area of the integrated energy system under the constraint of equipment capacity, and the security area explores the safe and reliable operation area of the integrated energy system under the N-1 security criteria. In the actual control operation, the RISE can be safely dispatched according to the actual situation of the two regions.

5.1 Solution method of region

Both the feasible region and the security region need to determine the maximum energy supply range of the regional integrated energy system containing renewable energy under the characteristic operation scenario, namely the upper bound of safe operation. The models of the maximum energy supply range of the feasible region and the security region are

$$\begin{aligned} &\max \sum L_i, \\ &s.t.\begin{cases} h(\boldsymbol{L}) = 0, \\ \bar{\boldsymbol{g}} \le g(\boldsymbol{L}) \le \underline{\boldsymbol{g}}, \end{cases} \end{aligned} \tag{29}$$

Where: $\bar{\boldsymbol{g}}$ and $\underline{\boldsymbol{g}}$ are the lower bound and upper bound vectors of unequal constraints respectively. The models of appeal feasible region and security region belong to large-scale nonlinear programming problems. The primal couple interior point method is a typical method for solving large-scale nonlinear programming problems. In combination with the actual problem of region solution, its standard formula can be expressed as

$$\begin{aligned} &\text{obj.}\min\ -f(\boldsymbol{L}) - \mu\sum_{j=1}^{r}\log(l_r) - \mu\sum_{j=1}^{r}\log(u_r), \\ &s.t.\boldsymbol{h}(\boldsymbol{L}) = 0, \\ &\quad \boldsymbol{g}(\boldsymbol{L}) + \boldsymbol{\mu} = \bar{\boldsymbol{g}}, \\ &\quad \boldsymbol{g}(\boldsymbol{L}) - \boldsymbol{l} = \underline{\boldsymbol{g}}, \end{aligned} \tag{30}$$

Where: L is the power of each key pipeline; μ, L is the relaxation variable vector; According to the general form of the primal couple interior point method, the equation can be solved by using the Lagrangian function, which will not be repeated here.

5.2 Optimization control method

In the actual operation of the regional integrated energy system, it may not fully meet the operation criteria of the security region, so it is necessary to optimize the control and adjustment of its operation status. Combined with the theory of feasible region and security region, the optimal control operation method of regional integrated energy system is proposed. In order to ensure the safe and reliable operation of the regional integrated energy system under fault, its operation status shall be included in the security region. The efficiency of a regional integrated energy system is closely related to its equipment utilization. The efficiency function (EF) based on the feasible region is defined, which represents the equipment operation utilization rate based on the Region concept. The formula is

$$EF = \min\left\{\frac{L_i}{L_i^{\max}} \times 100\%, i = 1, 2, \cdots, M\right\}, \tag{31}$$

Where: $L_i^{\max}$ represents the maximum energy supply capacity in the feasible area of the i-th pipeline; M represents a total of M pipelines. When the regional integrated energy system is optimized and controlled, the security region is taken as its security constraint, and the efficiency function is taken as the overall operation objective, the optimization model can be expressed as

$$\max\ EF(\boldsymbol{L})\ s.t.\boldsymbol{L} \in O, \tag{32}$$

Where: O represents the security area of the energy system in the region. However, when the current operating state is outside the security area of the regional integrated energy system, it is necessary to adjust the operating state first, and then optimize the state control. The adjustment principle is to determine the adjustment strategy based on the shortest parallel path (i.e. Manhattan distance), and the adjustment strategy can be expressed as

$$d = \sum_{i=1}^{M}\left|L_i - L_i^U\right|, \tag{33}$$

Where: L_i^U represents the safety upper limit of the i-th pipeline, and L_i represents the output power of the i-th pipeline before adjustment. The flow of optimization control method based on region concept is shown in Figure 5

6 Example analysis

6.1 Example parameters.

The calculation example parameters are set according to a comprehensive energy demonstration project to supply electricity, heat and gas. The main parameters are shown in the attached table. The power system adopts 10 kV low-voltage distribution network (Liu et al., 2020), and the overall power factor in the system is 0.9. The loop network hydraulic system is adopted for the thermal system, and the flow rate of the hydraulic pipeline is less than 3 m/s (Liu et al., 2020). The natural gas system adopts the sub high pressure natural gas network, and the flow rate of the pipeline is less than 10 m/s (Liu et al., 2020). Two distributed energy stations supply energy to the area at the same time. Simplify the pipeline and analyze the key pipeline. The topology diagram is shown in the attached table.

In the regional integrated energy system, each equipment has a certain overload capacity. In case of system failure, the equipment needs to be overloaded for a short time to reduce the occurrence of load loss. In this example, the overload capacity coefficient is set as 1, which can be set according to the actual situation. The simulation experiment is based on a PC, the CPU is AMD Ryzen 7 5700G with Radeon Graphics @ 3.8GHz, and the memory is 16 GB.

6.2 Feasible region of regional integrated energy system

Based on the analysis in Sections 3.1, 3.2, the feasible region of the regional comprehensive energy system is obtained according to the feasible region solution method in Section 5.1. The maximum energy supply capacity of each pipeline without renewable energy is shown in Table 1.

It can be seen from the analysis in Section 3.2 and Table 1 that in normal operation, it is unnecessary to consider the mutual

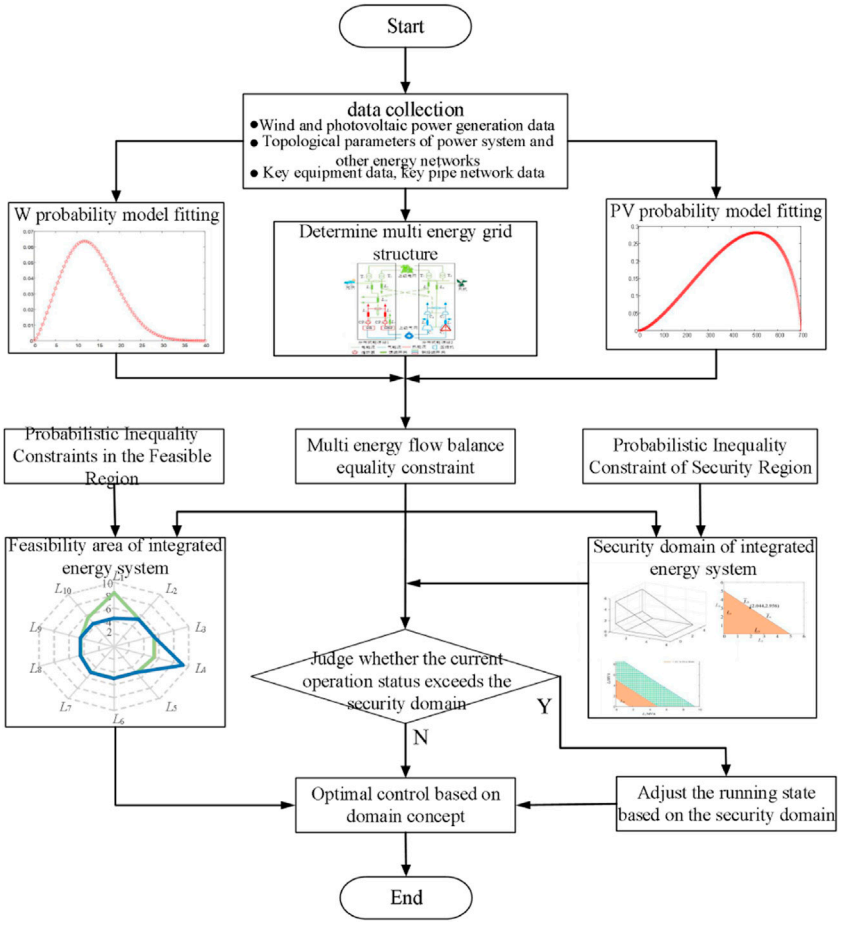

FIGURE 5
Flow chart of optimization control method based on region concept.

TABLE 1 Table of maximum energy supply capacity of systems without renewable energy.

Pipeline	Maximum load of pipeline/MW	Pipeline	Maximum load of pipeline/MW
1	4.5	6	5
2	5.4	7	5
3	5.4	8	4.5
4	5.4	9	4.5
5	5	10	4.5

standby relationship of each equipment, and its maximum energy supply capacity is mainly related to its own capacity and superior equipment. CHP units have a deep degree of energy coupling. Although their thermal output and electrical output are mutually constrained, their electrical output and thermal output are relatively fixed under the maximum energy supply. Therefore, under the condition of maximum energy supply, the output of each pipeline is relatively fixed.

In the case of renewable energy access, it is bound to affect the feasible area of the regional integrated energy system. As shown in the Figure 6, the change diagram of feasible region of regional integrated energy system under different renewable energy access

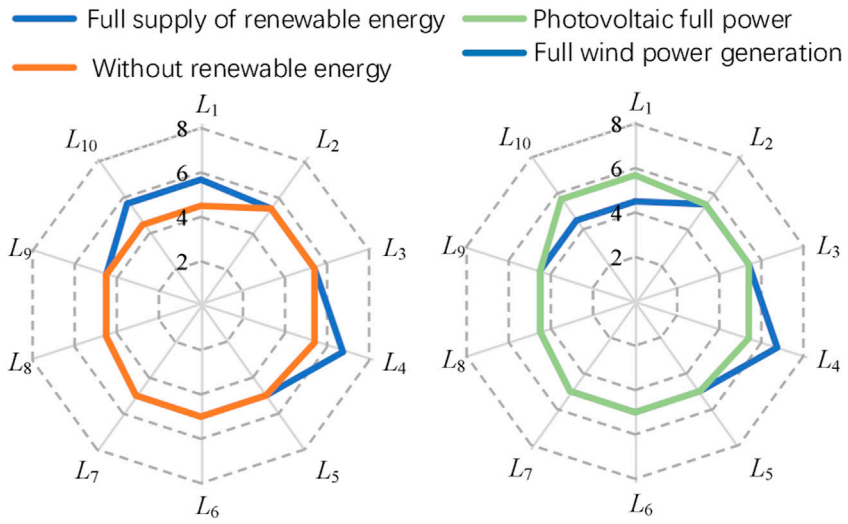

FIGURE 6
Change chart of feasible region of regional comprehensive energy system.

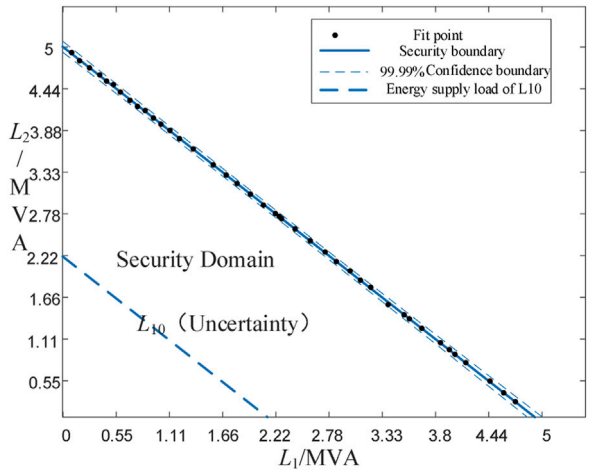

FIGURE 7
(L_1, L_2) safety boundary fitting diagram.

conditions. When wind power is fully generated, the maximum energy supply of L_4 will increase by 1.35MW; When photovoltaic full generation is connected, the maximum energy supply of L_1 and L_{10} will increase by 1.179 MW. When renewable energy is fully developed, the maximum energy supply range is increased from 49.2 MW to 52.908MW, and the maximum energy supply capacity is increased by 7.54%. To sum up, renewable energy access will increase the maximum energy supply range of corresponding pipelines and regional integrated energy systems to a certain extent. However, it is constrained by the carrying allowance of corresponding pipelines. Even if renewable energy is fully produced, the maximum energy supply has not been greatly improved.

6.3 Security region of regional integrated energy system

Based on the analysis in Sections 4.1, 4.2, the security region of the regional comprehensive energy system can be obtained according to the security region solution method in Section 5.1. The maximum energy supply capacity is 25.079 MW without renewable energy. Under the constraint condition of the safety area, the pipelines are mutually constrained and standby, and it is difficult to intuitively describe the coupling relationship in the full dimension observation, thus the accurate boundary of safe operation cannot be determined. In this paper, the security region of the al integrated energy system is determined by analyzing the relationship between the coupling standby pipeline combination.

In the case that renewable energy is not connected, select coupling pipelines (L_1, L_2) for two-dimensional safety zone observation. By solving multiple state points of the safety zone model and fitting them, the upper bound of safe operation of pipelines (L_1, L_2) can be obtained, as shown in Figure 7. L_{10} is a lower feeder of L_1, and the lower bound of safe operation of pipelines (L_1, L_2) is the L_{10} energy supply load. However, since there is no standby coupling relationship between L_{10} and L_2, it is uncertain in the (L_1, L_2) two-dimensional security region.

Similarly, the two-dimensional safety region of the thermal pipeline coupling combination (L_5,L_6) and the natural gas

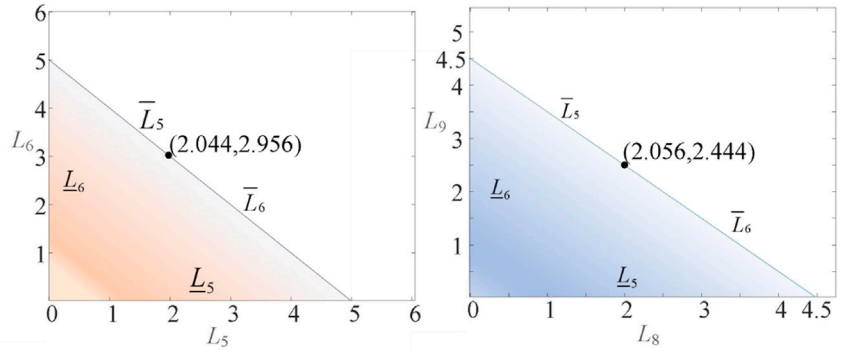

FIGURE 8
Two dimensional security region diagram.

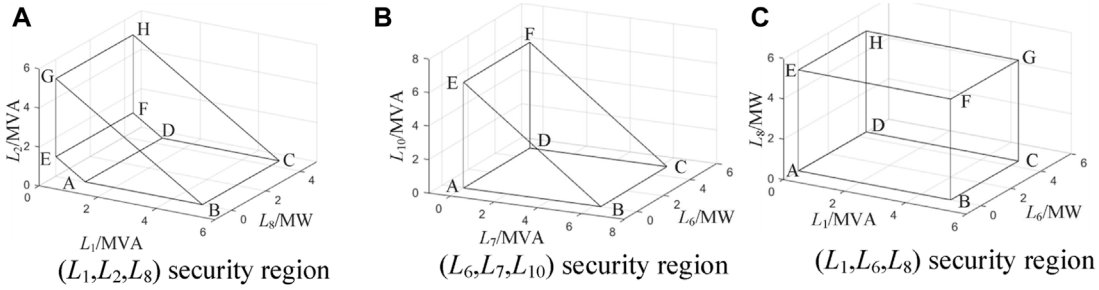

FIGURE 9
RISE three-dimensional security zone map.

coupling pipeline combination (L_8,L_9) can be obtained, as shown in the Figure 8. See the appendix for the combined safety areas of other coupling pipelines. The points on the boundary of the security region are the maximum energy supply points of the coupling pipeline combination, and the points below the boundary are the safe operation points.

The two-dimensional security region can only analyze the security constraint relationship of the mutual standby coupling pipeline, and cannot effectively observe the mutual constraint relationship under multi energy sources. Therefore, three-dimensional security region is required to describe the mutual constraint relationship under multi energy sources. The security region of electric power and natural gas multi energy pipelines (L_1,L_2,L_8) is shown in Figure 9A, the security region of electric power and thermal power multi energy pipelines (L_6,L_7,L_{10}) is shown in Figure 9B, and the security region of electric power, thermal power and natural gas multi energy pipelines (L_1,L_6,L_8) is shown in Figure 9C.

In the three-dimensional security region, when the operation state of the regional integrated energy system is within the region, it means that the system is in a safe and reliable operation state under this state. Take (L_1,L_2,L_8) security region as an example to illustrate the relationship between upper and lower boundaries. For pipelines (L_1,L_2), they have a mutual standby relationship. Face BCHG is the upper bound of common security, face ADEF is the lower bound of common security, which is determined by the energy supply load of L_{10}, EFHG is the lower bound of L_1 security, and ABCD is the lower bound of L_2 security. For pipeline L8, its upper safety boundary is surface CDFH and its lower safety boundary is surface ABGE.

Whether renewable energy is accessed, access location and access capacity will have an impact on the security region. This paper analyzes and discusses the impact of renewable energy on the security region from three situations: full generation of renewable energy, full generation of photovoltaic power and full generation of wind power. When photovoltaic full generation is connected, the upper limit of L_1 and L_2 energy supply is increased by 5MVA. With photovoltaic access, the two-dimensional security region has been greatly improved, and the energy supply area of two-dimensional security region (L_1,L_2) has been increased by 32MVA^2. The security region changes are shown in Figure 10.

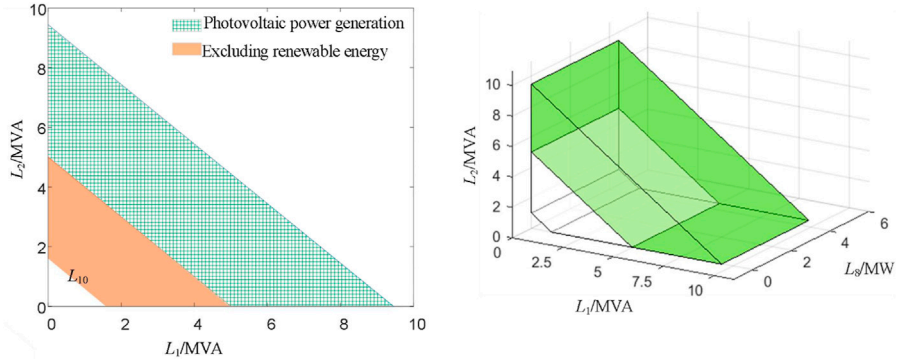

FIGURE 10
Change diagram of security region under photovoltaic access.

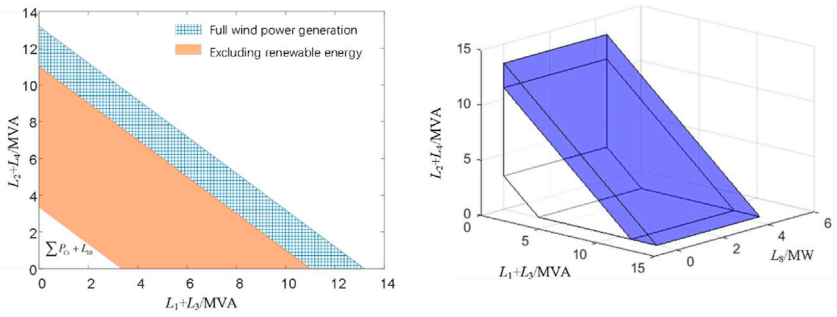

FIGURE 11
Change diagram of security region under wind power access.

The change of three-dimensional security region (L_1,L_2,L_8) is shown in Figure 10. After PV is connected, the two-dimensional and three-dimensional security areas have been greatly improved. The main reason is that there is still a margin for the pipeline configuration capacity compared with the transformer capacity. If the load in this area continues to increase, the energy supply capacity in this area can be increased by increasing the transformer capacity.

When full generation of wind power is connected, the mutual standby relationship between L_1 and L_2 remains unchanged, but the mutual standby relationship between L3 and L4 changes. Through in-depth analysis of the energy supply data of L_1、L_2、L_3 and L4, it is found that (L_1,L_3) and (L_2,L_4) have a mutual standby relationship, which can also be reflected in the physical grid structure. The security region changes of [(L_1, L_3), (L_2, L_4)] are shown in Figure 11. After the wind power is connected, the two-dimensional and three-dimensional security regions are both improved, 26.8832MVA^2, respectively, but the scope of improvement is less. The main reason is that the pipeline configuration capacity has less margin than the power capacity of transformers and other power sources. If the load in this area continues to increase, priority can be given to increasing the pipeline configuration capacity to improve the energy supply capacity in this area.

Analyze the energy supply data of L_1, L_2, L_3 and L_4 when renewable energy is fully connected. The original mutual standby constraint relationship is changed. The operation constraint of L_1 and L_3 is determined by their standby relationship, and the operation constraint of L_1 and L_3 is determined by their standby relationship. Under the condition of full access to renewable energy, the energy supply scope of (L_1,L_3,L_2,L_4) security zone is expanded, and the energy supply area is expanded from 49.5MVAMW to 70.83MVA MW, an increase of 43.1% as shown in Figure 12.

To sum up, the access location and access capacity of renewable energy will have an impact on the feasible domain and the security domain. On the one hand, the access of renewable energy improves the upper bound of corresponding pipelines, and on the other hand, changes the backup constraints between pipelines. The randomness of renewable energy and the change of reserve constraints

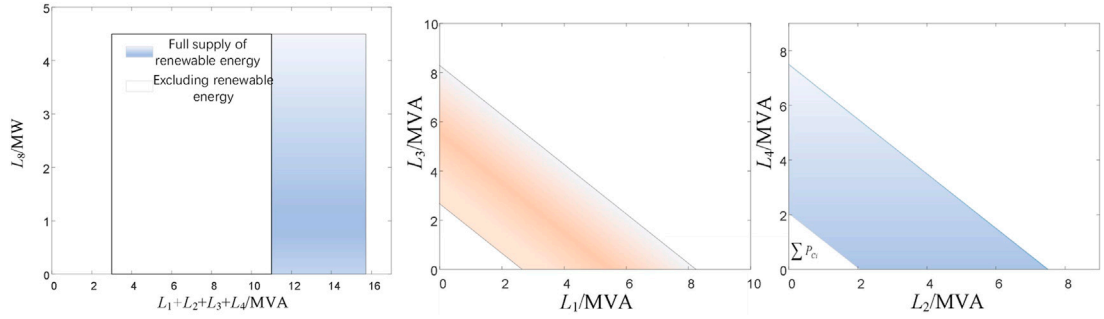

FIGURE 12
Change Diagram of Security region under Full Access of Renewable Energy.

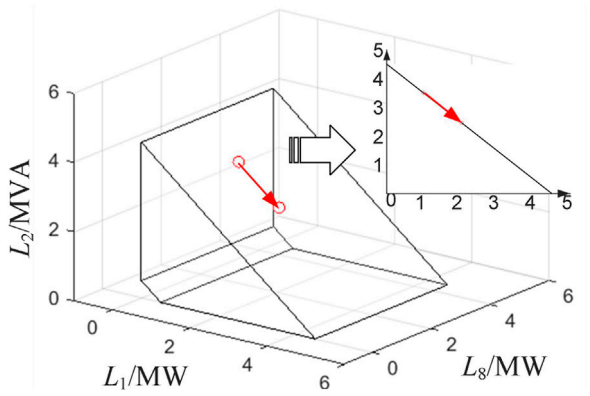

FIGURE 13
Q1 operation adjustment diagram.

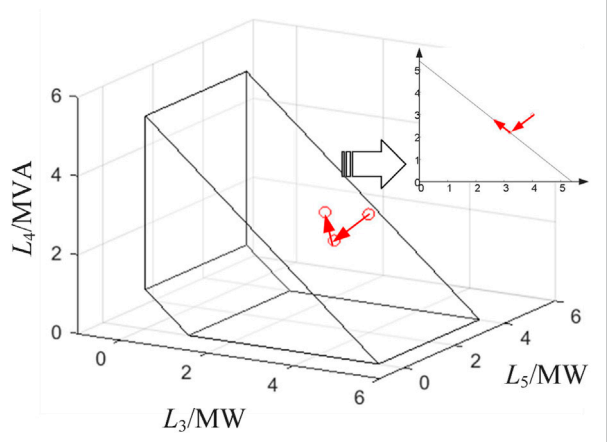

FIGURE 14
Q2 operation adjustment diagram.

make the scope of the system security region uncertain, but the scope of the change of the security upper bound is a certain range. Different access locations of renewable energy will affect the increase of feasible area and security area. In the above calculation example, the PV and wind power access locations are different, and their grid structures are different. The increase of feasible domain and security domain after access is different. Renewable energy access will increase the capacity of feasible area and security area, but it is constrained by the grid structure and corresponding pipeline capacity of the connected location.

The optimization control based on region concept has two cases: one is to optimize the performance of the operation point in the security region. Second, the operation point is outside the security region, so it needs to be load reduced and adjusted before efficiency optimization. Select operation status points Q1 (1, 3.5, 2, 2, 2, 3, 4, 2, 2, and 0.5) and Q2 (3, 4.5, 4, 3, 2, 3, 2, 2, 2, 2, and 2) for example.

For operation point Q1, renewable energy in the region is not connected. First, determine whether it is within the security region. It can be seen from the results in Section 5.2.1 that it does not exceed the boundary of the security region, but it requires optimal control of efficiency. According to the definition of efficiency function, the optimization function is obtained, the operation state of Q_1 point and the feasible threshold value are substituted into the function, and the optimized operation state of efficiency function: Q'_1 (2.045, 2.455, 2, 2, 2.5, 2.5, 2.5, 4, 2, 2, and 0.5) can be obtained through optimization solution. Adjustment diagram of its operation adjustment process is shown in the Figure 13.

For the operating point Q_2, the photovoltaic power in the area is in the full power state. First, judge whether it is in the security region. Since (L_3, L_4) has exceeded the boundary of the security region, it is necessary to make security adjustment

first, calculate the Mandaton distance between the operating point and the security boundary, and then optimize the efficiency function. After the adjustment, Q'_2 (3.41, 4.09, 2.7, 2.7, 2.5, 2.5, 4, 2, 2, and 2), its operation adjustment process is shown in the Figure 14.

7 Conclusion

Aiming at the problem of high proportion of renewable energy access, this paper proposes a comprehensive energy system region model with renewable energy and an optimal control method. Firstly, the feasible region model of integrated energy system is determined according to the capacity of key equipment and its pipeline. Then, considering the mutual standby relationship of different equipment and pipelines, based on N-1 safety criteria, a regional integrated energy system security region model is constructed, and an optimization control method based on the region concept is proposed. Finally, the effectiveness of the model is analyzed with a numerical example, and the impact of renewable energy access capacity and location on the feasibility and security regions of the regional integrated energy system is discussed. The following conclusions are drawn:

1) Renewable energy access will certainly increase the security area, but also make security randomization.
2) Under different access conditions of renewable energy, the mutual standby relationship of key pipelines will change, which will change the security boundary.
3) The improvement of the security area by renewable energy access is mainly affected by key pipelines.

Data availability statement

The original contributions presented in the study are included in the article/Supplementary Material, further inquiries can be directed to the corresponding author.

Author contributions

FZ and YL contributed to the conception and design of the proposed method. All authors wrote and edited the manuscript.

Funding

This work is supported by State Grid Shanghai Electric Power Company Science and Technology Project (5209KZ21N005).

Conflict of interest

The authors declare that the research was conducted in the absence of any commercial or financial relationships that could be construed as a potential conflict of interest.

Publisher's note

All claims expressed in this article are solely those of the authors and do not necessarily represent those of their affiliated organizations, or those of the publisher, the editors and the reviewers. Any product that may be evaluated in this article, or claim that may be made by its manufacturer, is not guaranteed or endorsed by the publisher.

Supplementary material

The Supplementary Material for this article can be found online at: https://www.frontiersin.org/articles/10.3389/fenrg.2022.1067202/full#supplementary-material

References

Ding, T., Bo, R., Sun, H., Li, F., and Guo, Q. (2016). A robust two-level coordinated static voltage security region for centrally integrated wind farms. *IEEE Trans. Smart Grid* 7 (1), 460–470. doi:10.1109/TSG.2015.2396688

Ghofrani, M., Arabali, A., Etezadi-Amoli, M., and Fadali, M. S. (2013). A framework for optimal placement of energy storage units within a power system with high wind penetration. *IEEE Trans. Sustain. Energy* 4 (2), 434–442. doi:10.1109/TSTE.2012.2227343

Jiang, F., Peng, X., Tu, C., Guo, Q., Deng, J., and Dai, F. (2022). An improved hybrid parallel compensator for enhancing PV power transfer capability. *IEEE Trans. Ind. Electron.* 69 (11), 11132–11143. doi:10.1109/TIE.2021.3121694

Jiang, F., Tu, C., Guo, Q., Shuai, Z., He, X., and He, J. (2019). Dual-functional dynamic voltage restorer to limit fault current. *IEEE Trans. Ind. Electron.* 66 (7), 5300–5309. doi:10.1109/TIE.2018.2868254

Lei, P. E. I., Wei, Z., Chen, S., Zhao, J., and Yin, H. (2021). Security region of variable photovoltaic generation in AC-DC hybrid distribution power networks. *Power Syst. Technol.* 45 (10), 4084–4093. doi:10.13335/j.1000-3673.pst.2020.2012

Li, W., Wang, W., Wang, H., Wu, J., and Zhang, Y. (2022). Probabilistic power flow analysis method for power system with renewable energy based on security region theory [J]. *Acta Energiae Solaris Sin.* 43 (8), 1–7. doi:10.19912/j.0254-0096.tynxb.2020-0453

Li, X., Jiang, T., Bai, L., Kou, X., Li, F., Chen, H., et al. (2022). Orbiting optimization model for tracking voltage security region boundary in bulk power grids. *CSEE J. Power Energy Syst.* 8 (2), 476–487. doi:10.17775/CSEEJPES.2020.00720

Li, Y., Zou, Y., Tan, Y., Cao, Y., Liu, X., Shahidehpour, M., et al. (2018). Optimal stochastic operation of integrated low-carbon electric power, natural gas, and heat delivery system. *IEEE Trans. Sustain. Energy* 9 (1), 273–283. doi:10.1109/TSTE.2017.2728098

Liu, L., Wang, D., Hou, K., Jia, H. J., and Li, S. y. (2020). Region model and application of regional integrated energy system security analysis. *Appl. Energy* 260, 114268. doi:10.1016/j.apenergy.2019.114268

Maihemuti, S., Wang, W., Wang, H., Wu, J., and Zhang, X. (2021). Dynamic security and stability region under different renewable energy permeability in IENGS system. *IEEE Access* 9, 19800–19817. doi:10.1109/ACCESS.2021.3049236

Nguyen, H. D., Dvijotham, K., and Turitsyn, K. (2019). Constructing convex inner approximations of steady-state security regions. *IEEE Trans. Power Syst.* 34 (1), 257–267. doi:10.1109/TPWRS.2018.2868752

Su, J., Chiang, H. -D., and Alberto, L. F. C. (2021a). Two-time-scale Approach to characterize the steady-state security region for the electricity-gas integrated energy system. *IEEE Trans. Power Syst.* 36 (6), 5863–5873. doi:10.1109/TPWRS.2021.3081700

Su, J., Chiang, H. -D., Zeng, Y., and Zhou, N. (2021b). Toward complete characterization of the steady-state security region for the electricity-gas integrated energy system. *IEEE Trans. Smart Grid* 12 (4), 3004–3015. doi:10.1109/TSG.2021.3065501

Xiao, J., cao, Y., Tan, Y., Cao, Y., Liu, X., and Shahidehpour, M., (2018). Full-dimensional direct observation of distribution system security region. *Trans. china Electrotech. Soc.* 9 (1), 273–283. doi:10.19595/j.cnki.1000-6753.tces.191038

Zhang, S., Cheng, H., Zhang, L., Bazargan, M., and Yao, L. (2013). Probabilistic evaluation of available load supply capability for distribution system. *IEEE Trans. Power Syst.* 28 (3), 3215–3225. doi:10.1109/TPWRS.2013.2245924

frontiers | Frontiers in Energy Research

TYPE Original Research
PUBLISHED 14 December 2022
DOI 10.3389/fenrg.2022.1089465

OPEN ACCESS

EDITED BY
Liansong Xiong,
Xi'an Jiaotong University, China

REVIEWED BY
Yongbin Wu,
Southeast University, China
Yue Wang,
Xi'an Jiaotong University, China
Yonghui Liu,
Hong Kong Polytechnic University, Hong Kong SAR, China, in collaboration with reviewer YW
Zhenxiong Wang,
Xi'an Jiaotong University, China
Lei Liu,
School of Electrical Engineering, Xi'an Jiaotong University in collaboration with reviewer ZW

*CORRESPONDENCE
Jianquan Shi,
shijianquan@njit.edu.cn

SPECIALTY SECTION
This article was submitted to Process and Energy Systems Engineering, a section of the journal Frontiers in Energy Research

RECEIVED 04 November 2022
ACCEPTED 28 November 2022
PUBLISHED 14 December 2022

CITATION
Bi C, Wu J, Qian Y, Luo X, Xie J, Shi J and Luo F (2022), Power optimization control of VSC-HVDC system for electromechanical oscillation suppression and grid frequency control.
Front. Energy Res. 10:1089465.
doi: 10.3389/fenrg.2022.1089465

Power optimization control of VSC-HVDC system for electromechanical oscillation suppression and grid frequency control

Chaohao Bi[1], Jiaqi Wu[1], Yang Qian[2], Xin Luo[1], Jianxiang Xie[1], Jianquan Shi[2]* and Fang Luo[1]

[1]Guangzhou Power Supply Bureau, Guangdong Power Grid Co., Ltd., Guangdong, China, [2]School of Automation, Nanjing Institute of Technology, Nanjing, China

The voltage source converter (VSC) based high-voltage DC (HVDC) transmission system usually adopts damping and inertia control to quickly and independently adjust the active- and reactive- power, to improve the frequency stability and suppress the electromechanical oscillations of the power grid. This paper first analyzes the effect of the proportional-derivative (PD) controller parameter on the HVDC output power. The study shows that when the proportional-derivative controller parameter is increased to the limit value, HVDC will operate in the rapid power compensation (RPC) mode. Namely, according to the positive or negative polarities of the rotor speed deviation and the grid frequency deviation, the active- and reactive- power limits are used as the reference to rapidly control the output power, thereby minimizing the system's unbalanced power, the rotor oscillation, and the frequency fluctuation. To this end, this paper proposes a coordinated active-/reactive- power control strategy for the VSC-HVDC system based on the RPC mode to suppress the grid electromechanical and frequency oscillations. The RPC mode enables HVDC to quickly release/absorb power, to compensate for system's required power shortage or suppress excess power. When the speed deviation, the frequency deviation, and their rates of change meet the requirements, the damping control is used to make HVDC exit the RPC mode and further enhance the ability of the VSC-HVDC system. Simulation results prove the effectiveness of the proposed power optimization control strategy.

KEYWORDS

VSC-HVDC, grid electromechanical oscillations, grid frequency control, rapid power compensation, damping control

1 Introduction

With the continuous advancement of the low-carbon energy strategy in China, there are continuously increasing applications of large-scale generation of new energies,

Liu et al. (2020); You et al. (2022), and the installed proportion of synchronous generators (SGs) has gradually decreased. The rotating reserve and inertia have been significantly reduced, the frequency fluctuations and electromechanical oscillations of the power grid frequently occur, posing a great threat and challenge to the safe and stable operation of the power grid. As a result, maintaining grid frequency stability and effectively suppressing electromechanical oscillations are critical issues, Kundur et al. (2004). Power electronics connected to the public grid must actively participate in frequency control and oscillation suppression, Xu and Wang (2021).

Existing solutions mainly include: 1) The power system stabilizer to compensate for the negative damping, Kumar (2016); 2) The installation of synchronous condensers to improve the inertia level and damping ability of the power system to suppress electromechanical oscillations and frequency fluctuations, Nguyen et al. (2019); 3) The use of reactive power compensation devices such as the static synchronous compensator to regulate the reactive power output and change the voltage level and power flow distribution of the system, thereby suppressing the grid electromechanical oscillations, Li et al. (2020); 4) The use of energy storage devices to quickly emit or absorb active and reactive power to maintain the active power balance in the system and suppress power oscillations, yet energy storage devices are more expensive and difficult to apply on a large scale, Zhu et al. (2019); 5) The use of the power of the new energies such as photovoltaic and wind generations to compensate for the power deficits or surpluses in the power system Yang et al. (2021), but new energy generations typically operate in the maximum power point tracking mode; if used for grid frequency control and electromechanical oscillation suppression, a certain amount of capacity must be reserved for active participation in the regulation of the system dynamic process at any time, which will sacrifice their inherent power generation capacity, Li et al. (2020).

Currently, the voltage source converter (VSC) based high-voltage DC (HVDC) transmission system is one of the best solutions for large-scale renewable energy exploiting, and has been widely applied in practical projects such as grid-connected wind farms, weak grid power transmission, and islanding power supply, Zhang et al. (2011); Lee et al. (2018). As the VSC-HVDC system has the advantage of fast and independent control of active and reactive power, and it does not require reactive power compensation from the AC grid, it has attracted a lot of attention for suppressing electromechanical oscillations and maintaining power system frequency stability, Wang et al. (2019); Xiong et al. (2021b). Sun et al. (2021) states that when the VSC-HVDC system uses a constant power control strategy, the damping level of the power system cannot be increased. For this reason, the VSC-HVDC system should operate in the variable power control mode to inject real-time adjustable active or reactive power into the SG network based on the change of the grid state, in order to enhance the suppression of electromechanical and frequency oscillations by the VSC-HVDC system. In addition, Varma and Maleki (2019) points out that when the VSC absorbs or emits reactive power to change its voltage at the integration point and improve the grid power distribution, it functions as a STATCOM that can quickly and smoothly modulate the reactive power without the need for a large amount of reactive power provided by the grid Xiong et al. (2015).

To realize that HVDC actively participates in the frequency control and suppresses electromechanical oscillations, the VSC control needs to be improved, such as by adding droop control, inertia control, and proportional-derivative (PD) control, Peng et al. (2020); Shi et al. (2021). Droop control and inertia control cannot adjust the magnitude and speed of frequency change at the same time, Xiong et al. (2022); Wang et al. (2015); the PD control necessitates high precision on system parameters, and the expected control performance is difficult to achieve, Li et al. (2020); Ling et al. (2021). Accordingly, Fang et al. (2018) improved the original virtual inertia control, and proposed a virtual SG (VSG) control with characteristics similar to SGs. To suppress the inherent power oscillation problem of the VSG control and improve the frequency response speed, Kerdphol et al. (2019) proposed an improved VSG strategy based on the fuzzy logic algorithm. However, various improved VSG strategies require information on grid inertia and damping parameters to obtain the optimal inertia and damping control parameters, Ali et al. (2019). To this end, Xiong et al. (2021a) developed a frequency trajectory planning control that decouples from the grid's disturbances and inertia/damping information that cannot be obtained.

All the previously discussed schemes make the VSC provide appropriate power support as soon as possible to recover the power balance. Obviously, when the frequency and the rotor oscillation exceed their limits, the adjustment power will also exceed the operating range that VSC can withstand. At this time, the VSC over-voltage and -current protection will be triggered, and the additional control mentioned above will lose its intended functionality. Therefore, the VSC control to suppress the frequency fluctuation and electromechanical oscillation must consider the limited VSC control capability under large disturbances. To this end, a coordination control for the VSC-HVDC active/reactive power, based on the Rapid Power Compensation (RPC) mode, is proposed to suppress the electromechanical oscillation and frequency fluctuation, and enhance the safe and stable operation of the power grid under large disturbances. Finally, the effectiveness and superiority of the proposed work are verified by various simulation results.

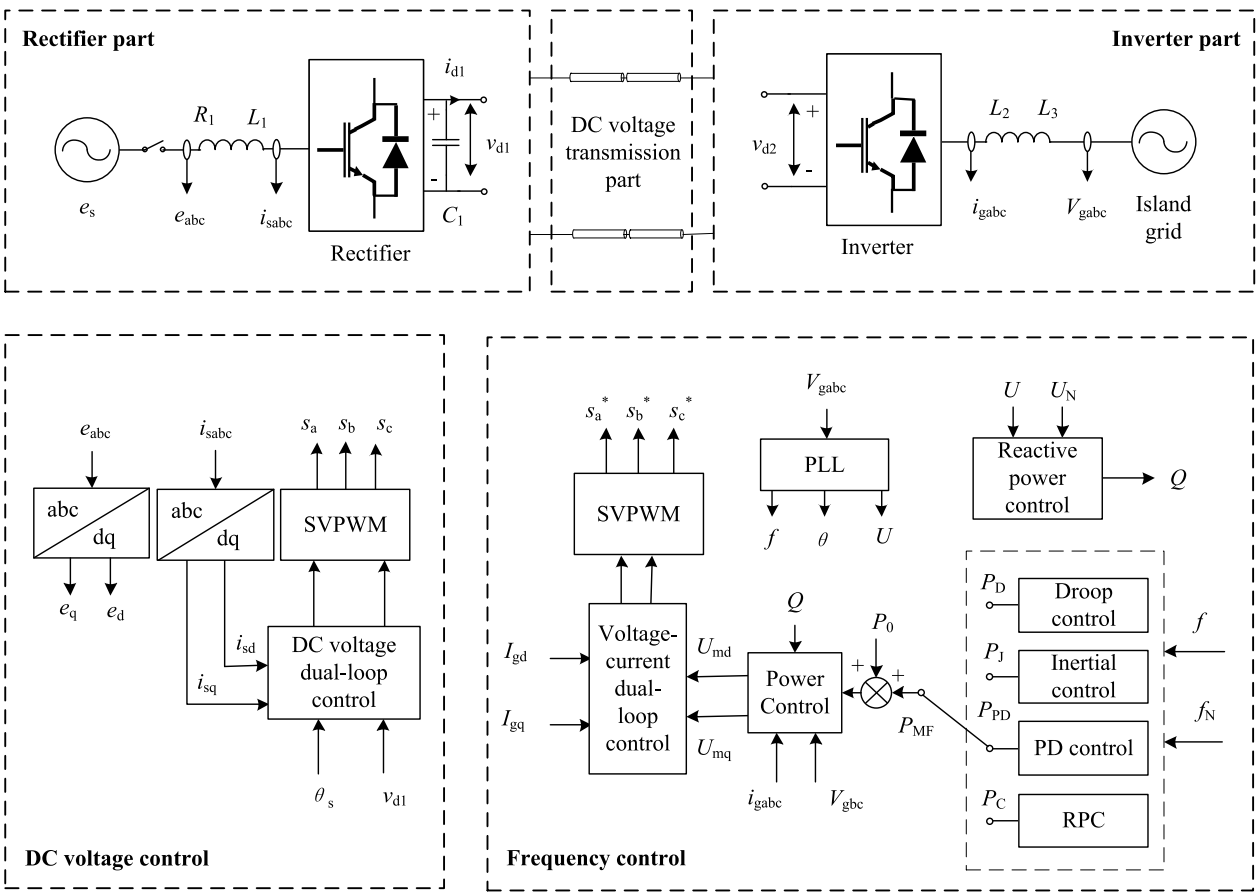

FIGURE 1
The VSC-HVDC system structure and its converter control structure.

2 VSC-HVDC system structure and its control strategy

The basic structure of the VSC-HVDC is shown in Figure 1 e_{abc} and i_{sabc} are the voltage and line current at the sending-end grid, respectively; θs is the grid voltage phase angle; v_{d1} and v_{d2} are the DC voltages at the rectifier end and the inverter end, respectively; i_d is the DC line current; V_{gabc} and i_{gabc} are the voltage and current at the receiving-end grid, respectively, and U_N and f_N are the rated voltage and frequency, respectively; P_D, P_J, P_{PD}, and P_C are the regulated power provided by the droop control, the inertia control, the PD control, and the RPC control, respectively; P_0 and Q are the steady-state active- and reactive-power provided by VSC-HVDC to the receiving-end grid, respectively. Through the phase-locked loop, Liu et al. (2022a); Liu et al. (2022b), V_{gabc} provides the frequency f, phase θ, and voltage amplitude U at the receiving-end grid, and

$$\begin{cases} \omega = 2\pi f \\ \theta = \int \omega \mathrm{d}t \end{cases} \tag{1}$$

At the sending end, the reactance L_1 of the rectifier limits the rise of the short-circuit current; the capacitor C_1 suppresses the DC voltage fluctuation. The VSC-HVDC system usually adopts a constant DC voltage control to effectively maintain the DC voltage stability; the inner loop tracks the VSC current change in real time, and the outer loop controls power and voltage. When the grid voltage is stable, by neglecting the power loss of the VSC itself, we have

$$P = i_{d1} v_{d1} = 3 e_d i_{sd} / 2 \tag{2}$$

Both v_{d1} and P are proportional to the d-axis component i_{sd} of the rectifier output current, according to which the control rule of the sending-end VSC can be obtained, as shown in Figure 2, where the active and the reactive power are decoupled and controlled separately. If the reactive power reference of the sending end VSC is set to 0, the inner loop can realize steady-state-error-free control to i_{sd} and i_{sq} Xie et al. (2014). In addition, since the rectifier realizes the DC voltage regulation, the VSC of the receiving-end grid only needs to track the dispatch

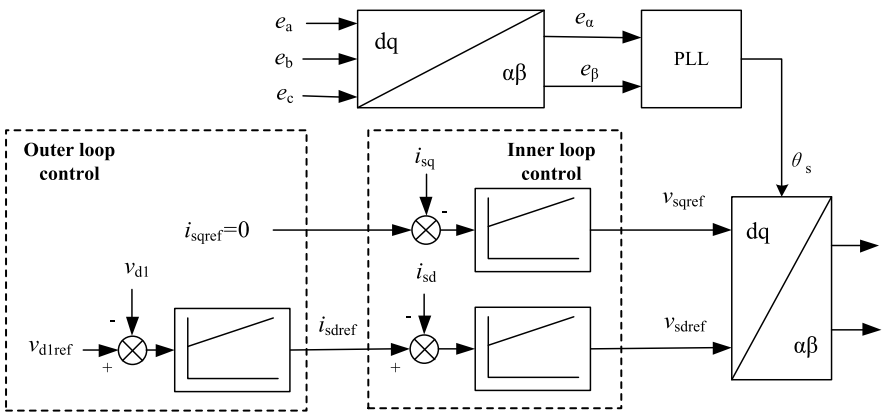

FIGURE 2
Control strategy of the sending-end converter of the VSC-HVDC system.

instructions of the local grid; at the same time, it can be designed to additionally suppress the electromechanical oscillations and frequency fluctuations of the receiving-end grid.

3 VSC-HVDC suppressing electromechanical oscillations and frequency fluctuations of receiving-end grid

To analyze the principle and strategy of the VSC-HVDC to suppress the electromechanical oscillations and frequency fluctuations of the receiving-end grid, this paper uses an equivalent SG to represent the receiving-end grid, as shown in Figure 3. In addition, to simulate the electromechanical oscillations of the rotor speed of the SG around the rated speed, the equivalent SG is operated in parallel with an infinite bus, so that the SG rotor speed is always clamped around the rated value. When it is necessary to simulate the frequency fluctuation where the frequency deviates from the rated frequency, the infinite bus system can be disconnected. With reference to Figure 3, P_m is the mechanical input power of the prime mover, P_e is the SG electromagnetic power, and P_v and Q_v are the active- and reactive- power injected into the SG network by the VSC-HVDC. I_{abc} and V_{abc} are the current and voltage at the point of common coupling (PCC). U is the voltage between system two and the PCC, and E is the voltage between the SG and the PCC. Z_1, Z_2, Z_3, and Z_4 are equivalent impedances of corresponding lines.

When suppressing the electromechanical oscillations and frequency fluctuations, the inverter VSC2 of HVDC usually adds the damping and the inertia control on top of the direct current control in Figure 4, where I_d is the measured current and I_q is the measured reactive current; I_{dref} and I_{qref} are the reference values of active and reactive currents, respectively. ω_0 and ω denote the rated and detected values of rotor speed of the SG (oscillation suppression mode) or grid angular frequency (frequency control mode), respectively; k_{p1}, k_{p2}, k_{d1}, and k_{d2} are gains of the P and D controllers corresponding to the active and reactive control loops, respectively.

As can be seen from Figure 4, after coupling I_{dref} and I_{qref} with the rotor speed (grid frequency), the power output of the VSC-HVDC system can be modulated quickly and independently, by controlling the reference values of active and reactive DC current components separately (on the d and q axes in the dq coordinate system), injecting controllable active and reactive power into the receiving-end network and improving the damping capacity and inertia effect of the system. The relevant principles and analysis can be found in Li et al. (2020).

Chi et al. (2019) points out that the damping control is based on the P controller to achieve power modulation, which helps to improve the damping capability of the system, and the inertia control is implemented with the help of the D controller to improve the system inertia. Also, the above strategies are conventional controls for grid-connected inverters to suppress electromechanical oscillations. Through the PI controller, I_d and I_q can track their references, I_{dref} and I_{qref} (Chi et al., 2019), and thus quickly and effectively regulate the active- and reactive-power from the VSC, finally realizing the suppression of electromechanical oscillations and frequency fluctuations of the receiving-end grid, and reducing the fluctuation range of the rotor speed and the grid frequency.

Based on the linearized model in Li et al. (2020), when the active- and reactive- power of the VSC-HVDC system are injected into the infinite system, the inertia coefficient T_J and the damping coefficient T_D of the power system can be obtained respectively as

$$T_J = 2H + \beta k_{d1} + \mu k_{d2} \tag{3}$$

$$T_D = D + \beta k_{p1} + \mu k_{p2} \tag{4}$$

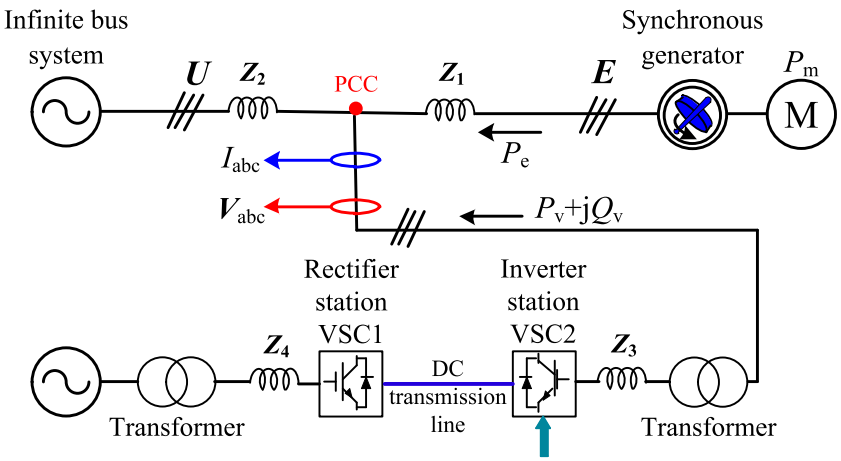

FIGURE 3
Integration of the HVDC into the system with oscillations and frequency fluctuations.

where D and H are the damping and inertia inherent to the power system; β and μ are the VSC2 control coefficients for active and reactive controls, respectively.

Obviously, the larger k_{d1} and k_{d2} are, the larger T_J is, the stronger the inertia provided to the grid, which can effectively suppress the rate of change of speed/frequency $d\omega/dt$; the larger k_{p1} and k_{p2} are, the larger T_D is, which can effectively suppress the speed/frequency deviation $\Delta\omega$. However, when the grid suffers from a large disturbance resulting in a large $d\omega/dt$ and $\Delta\omega$, to effectively suppress the power unbalance, a large range of power variations is required to be output by VSC (i.e., the PD controller gain should be increased), which may exceed the VSC2 design capacity S and power transmission limits shown in Figure 5.

If the current control dynamic in Figure 4 is ignored, the regulation power of the VSC in the receiving-end grid under the damping control, the inertia control, and the PD control can be roughly expressed as:

$$P_D = K_D(f_N - f) \tag{5}$$

$$P_J = -K_J\frac{df}{dt} \tag{6}$$

$$P_{PD} = K_p(f_N - f) - K_d\frac{df}{dt} \tag{7}$$

where K_D is the damping control coefficient, K_J is the inertia control coefficient, and K_p and K_d are the proportional and differential coefficients of the PD controller, respectively.

Obviously, if the gains of the damping control, the inertia control, and the PD controller are reduced, the VSC regulation power can be reduced to prevent VSC overload protection, but at the same time, the inertia and damping of the power system at the receiving end will also be weakened. For this reason, the influence law of the PD controller gains on VSC power output is analyzed in this paper.

4 RPC mode of VSC-HVDC system

Assume that I_m characterizes the maximum current of the VSC; $I_{d\,max}$ and P_{max} are the I_d limit and power transmission limit, respectively. Since VSC2 cannot absorb active power, the power and current values P_v, Q_v, I_d, and I_q shown in Figure 3 and Figure 4 satisfy the following constraints

$$\begin{cases} S = \sqrt{P_v^2 + Q_v^2} \\ I_m = \sqrt{I_d^2 + I_q^2} \\ 0 \le I_d \le I_{dmax} \\ -I_m \le I_q \le \sqrt{I_m^2 - I_{dmax}^2} \\ 0 \le P_v \le P_{max} \\ -S \le Q_v \le \sqrt{S^2 - P_{max}^2} \end{cases} \tag{8}$$

With reference to Figure 6, where the HVDC operates with the damping control as an example, if k_p is increased, the VSC active power will also gradually increase (with P_0 being the steady-state output value of the VSC active power), and the VSC will operate in linear damping control and non-linear damping control modes, respectively. Among them, the non-linear control is caused when k_p is amplified to a certain degree. When the rotor speed/grid frequency is greater than the rated value, the VSC active output value will be 0, as shown in Figure 6 for t_1–t_2; conversely, the VSC will output active power at the limit value P_{max}.

Similarly, when the gain of D controller k_d increases to a certain degree, the VSC will output active power at a constant value of 0 or P_{max} for a specific period of time (i.e., the non-linear inertia control is used), and the controller will not be able to adjust the output power of the VSC.

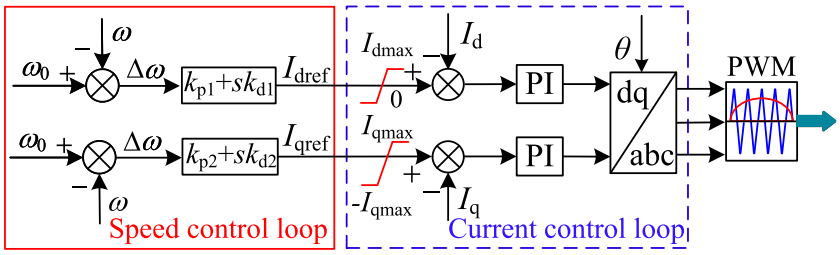

FIGURE 4
Control strategy of the VSC-HVDC to suppress oscillations and frequency fluctuations.

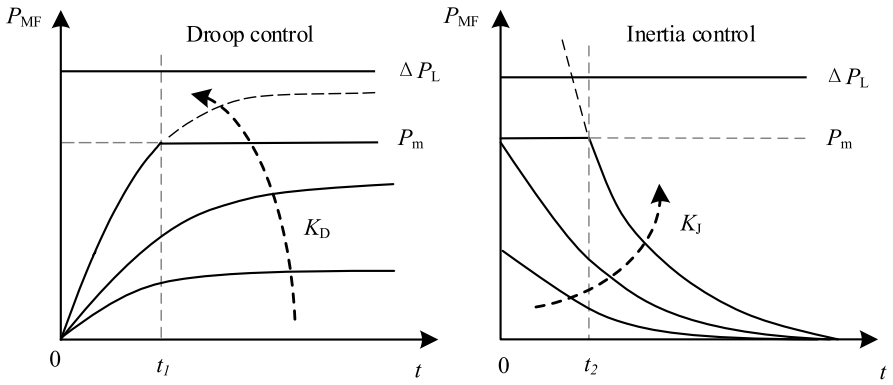

FIGURE 5
VSC power variation law under two typical control strategies.

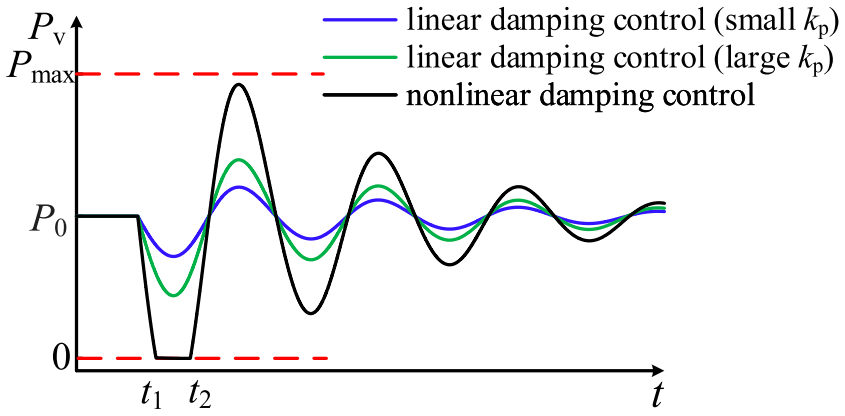

FIGURE 6
VSC active power output under different P controller gains.

The non-linear control is caused when the damping and inertia support of the HVDC are enhanced to a certain degree, and the ability of the non-linear control to suppress electromechanical oscillations and grid frequency fluctuations is also better than the damping and inertia control (Chi et al., 2019). Therefore, when k_{p1}, k_{p2}, k_{d1}, and k_{d2} in the speed/frequency control are amplified to the limit, depending on the positive and negative polarity of the deviation, the power output of VSC2 in the full time range is:

1. Delivering constant active power alternately, using the active limit power P_{max} of the inverter station VSC2 or 0 as the output reference;
2. Continuously absorbing or emitting constant reactive power with the remaining capacity of the inverter station as the limit value.

In this paper, the operation mode with the above two conditions of alternating constant power is referred to as the RPC mode of the VSC-HVDC system, which can maximize the suppression of grid electromechanical oscillations and frequency deviations. The theoretical analysis is shown as follows.

If the grid is under steady-state condition, then P_m and P_e are equal and the system power balance is met; if the grid load increases suddenly and the power change is ΔP_m, a power shortage will occur, resulting in a continuous reduction in rotor speed/grid frequency ($\Delta\omega = \omega_0 - \omega > 0$). Therefore, the VSC-HVDC system should increase the active output or absorb reactive power to suppress the deceleration energy of the SG rotor and grid frequency.

If the VSC-HVDC system increases the active power by ΔP_e, which yields $0 < \Delta P_e < \Delta P_m$, the SG swing equation and the grid frequency response can be described as

$$T_J \frac{d\omega}{dt} = P_m - (P_e + \Delta P_m - \Delta P_e) = \Delta P_e - \Delta P_m \tag{9}$$

As an example, if the VSC-HVDC system operates in the RPC control mode to regulate only the active power, then $\Delta P_e = P_{max} - P_0$. According to Eq. 9, we have

$$\left|\frac{d\omega}{dt}\right| = \frac{\Delta P_m - P_{max} + P_0}{T_J} \tag{10}$$

For VSC-HVDC to operate with the inertia control, the corresponding VSC active power should satisfy

$$\Delta P_e = k_d \left|\frac{d\omega}{dt}\right| \le P_{max} - P_0 \tag{11}$$

Considering that at the starting moment when the power system suffers from electromechanical oscillations/grid frequency fluctuations ($t = 0$), $|d\omega/dt|$ is its corresponding maximum value, while the VSC-HVDC has not yet generated additional active power to suppress the unbalanced active power of the system under the action of the control strategy, i.e., $\Delta P_e = 0$; at this time, $|d\omega/dt|_{max}$ is

$$\left|\frac{d\omega}{dt}\right|_{max} = \left|\frac{d\omega}{dt}\right|_{t=0} = \frac{\Delta P_m}{T_J} \tag{12}$$

If the VSC-HVDC is made to operate with the linear inertia control, the maximum D controller gain is

$$k_{dmax} = \frac{P_{max} - P_0}{|d\omega/dt|_{max}} = \frac{P_{max} - P_0}{\Delta P_m} T_J \tag{13}$$

Eq. 9 and Eq. 13 show that: after the HVDC provides inertia to the grid using the inertia control (with the gain taking its maximum value), the rotor swing equation/grid frequency response equation can be described as

$$T_J \frac{d\omega}{dt} = \Delta P_e - \Delta P_m = \frac{P_{max} - P_0}{\Delta P_m} T_J \frac{d\omega}{dt} - \Delta P_m \tag{14}$$

From Eq. 14, the value of $|d\omega/dt|$ at this point is

$$\left|\frac{d\omega}{dt}\right| = \frac{\Delta P_m{}^2}{T_J(\Delta P_m - P_{max} + P_0)} \tag{15}$$

Obviously, from the comparison of $|d\omega/dt|$ shown in Eq. 10 and Eq. 15, it follows that

$$\begin{aligned} &\frac{\Delta P_m{}^2}{T_J(\Delta P_m - P_{max} + P_0)} - \frac{\Delta P_m - P_{max} + P_0}{T_J} \\ &= \frac{\Delta P_m{}^2 - (\Delta P_m - P_{max} + P_0)^2}{T_J} \\ &= \frac{(P_{max} + P_0 + 2)(P_{max} - P_0) + 2P_0 P_{max}}{T_J} > 0 \end{aligned} \tag{16}$$

The comparison results of the rate of change of SG rotor speed and grid frequency under different control strategies [see Eq. 16] show that: in the case of the same maximum available VSC capacity, the suppression ability of the VSC-HVDC system based on the RPC control mode for $d\omega/dt$ is significantly stronger than that of the linear inertia control strategy; similarly, the suppression ability of the VSC-HVDC system based on the RPC control mode for the speed/frequency deviation $\Delta\omega$ is stronger than that of the conventional damping control strategy. The essential reason for the best regulation performance of the RPC strategy is that its supporting power to the receiving end grid can reach the maximum power output by the VSC. It should be noted that under the optimal control parameters, the oscillation suppression effect and grid frequency control effect of the PD control are equivalent to those of the RPC control, but the optimal PD control parameters are difficult to obtain. In contrast, the RPC control not only quickly compensates for the power shortage of the receiving end grid, but also avoids the problems of grid parameter measurement and controller parameter optimization. Table 1 summarizes the comparison of advantages and disadvantages between the RPC control strategy and the conventional control strategy.

5 RPC based strategy for electromechanical oscillation suppression and frequency control

Based on the above analysis and conclusions, this paper integrates the respective advantages of the RPC mode and the damping control strategy, and proposes a coordinated active/reactive power control for the VSC-HVDC system to suppress grid oscillations and frequency fluctuations. With reference to Figure 7, the basic control and switching principles are:

TABLE 1 Comparison of advantages and disadvantages between typical control strategies.

Control	Advantages	Disadvantages
Droop	Remarkable $\Delta\omega$ suppression effect	Weak $d\omega/dt$ suppression ability Too slow initial adjustment speed
Inertia	Remarkable $d\omega/dt$ suppression effect	Weak $\Delta\omega$ suppression ability Too weak end-stage control
PD	Good $\Delta\omega$ and $d\omega/dt$ suppression effect	Complicated parameter design Expected effect can be hardly achieved
RPC	Good $\Delta\omega$ and $d\omega/dt$ suppression effect Simple solution and easy to implement	Not applicable to small disturbances

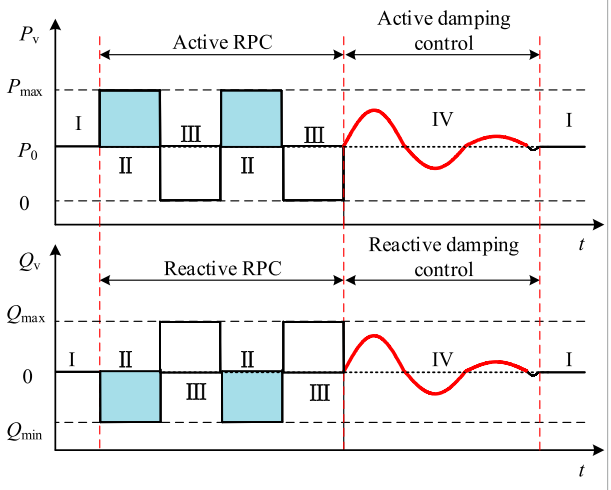

FIGURE 7
VSC-HVDC system power output under RPC mode.

1. If $d\omega/dt$ and $\Delta\omega$ are large, the VSC-HVDC system should switch to the RPC mode, to quickly compensate for system power shortage or suppress system excess power, and efficiently suppress $\Delta\omega$, $d\omega/dt$, and other speed indicators to avoid triggering the related relay protection devices of the power system. Under this mode, the VSC output active- and reactive- power should be switched to

$$\begin{cases} P = P_{max} \\ Q = -\sqrt{S^2 - {P_{max}}^2} \end{cases} \tag{17}$$

2. When $d\omega/dt$ and $\Delta\omega$ meet the requirements, an additional damping control makes the VSC-HVDC system exit the RPC mode and gradually return to the power delivery mode, and continue to provide damping torque to reduce the oscillation area of the SG rotor and grid frequency.

The switching conditions and power commands corresponding to different conditions are discussed below. In the following discussion, ω_d, ω_{th}, and R_{th} are the thresholds of $|\Delta\omega|$ and $|d\omega/dt|$, respectively, and $0 < \omega_d < \omega_{th}$ and $R_{th} > 0$. ω_d is the $|\Delta\omega|$ threshold for VSC switching to the damping control, ω_{th} is the $|\Delta\omega|$ threshold for VSC entering the RPC mode, and R_{th} is the $|d\omega/dt|$ threshold for VSC switching to the RPC mode.

1. Condition I: When $d\omega/dt$ and $\Delta\omega$ are within the safety interval, i.e.,

$$\begin{cases} \omega_0 - \omega_d < \omega < \omega_0 + \omega_d \\ \left|\frac{d\omega}{dt}\right| \le R_{th} \end{cases} \tag{18}$$

the system is in steady state or the oscillations/fluctuations have been suppressed and the VSC should operate in steady-state transmission mode without adjusting its power output, i.e., $P = P_0$, and $Q = 0$.

2. Condition II: If $d\omega/dt$ and $\Delta\omega$ simultaneously satisfy

$$\begin{cases} \omega_0 - \omega = \Delta\omega > \omega_{th} \\ \left|\frac{d\omega}{dt}\right| > R_{th} \end{cases} \tag{19}$$

then there is a serious power deficit in the grid, VSC-HVDC should increase the active power in time to compensate for this power deficit. I_d should be immediately increased to I_{dmax}, to provide continuous positive and fast active power compensation to the grid. At this time, $P = P_{max}$ to significantly suppress $\Delta\omega$ and $d\omega/dt$. The remaining capacity of the inverter is used to absorb the grid reactive power to the maximum extent, regulate the PCC voltage, reduce the SG output power, and suppress the power angle increase. The reactive current I_q and Q commands are

$$\begin{cases} I_q = \sqrt{I_m^2 - I_{mppt}^2} \\ Q = -\sqrt{S^2 - P_{mppt}^2} \end{cases} \tag{20}$$

3. Condition III: If $d\omega/dt$ and $\Delta\omega$ simultaneously satisfy

$$\begin{cases} \omega_0 - \omega = \Delta\omega < -\omega_{th} \\ \left|\frac{d\omega}{dt}\right| > R_{th} \end{cases} \tag{21}$$

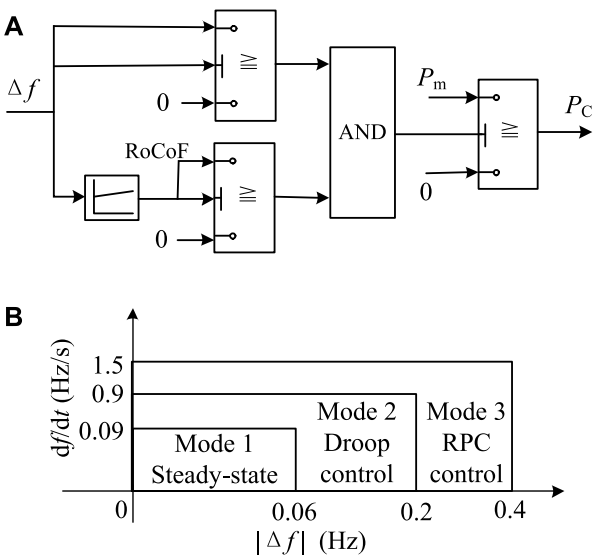

FIGURE 8
VSC frequency control based on RPC mode. **(A)** Control diagram. **(B)** Working mode switching.

then there is a power surplus in the system. The VSC-HVDC system should immediately minimize the active output, i.e., I_d should be immediately reduced to 0 in reverse, so that the active output P of the VSC-HVDC system is 0, while all the remaining capacity of the inverter station VSC2 will be used to transmit reactive power to the system, increasing the electromagnetic power of the SG, and providing reverse fast power compensation to the grid to suppress the active power surplus of the power system. At this time, the reactive current command of the current loop is set to $I_q = -I_m$, and the reactive power of the inverter station is $Q = S$.

4. Condition IV: If the rotor speed indexes $d\omega/dt$ and $\Delta\omega$ satisfy

$$\begin{cases} \omega_d < |\omega_0 - \omega| \le \omega_{th} \\ \left|\frac{d\omega}{dt}\right| \le R_{th} \end{cases} \tag{22}$$

then the SG has a slight rotor oscillation phenomenon or a small range of grid frequency fluctuation. In order to ensure that the VSC-HVDC system delivers active power as much as possible, it should gradually return to the steady-state generation mode and switch to the damping control strategy of active/reactive power coordination to provide the necessary damping torque to the grid, suppressing the electromechanical oscillations and grid frequency fluctuations as much as possible and improving the frequency quality of the SG network. At this time, the active- and reactive- power at the inverter side of the

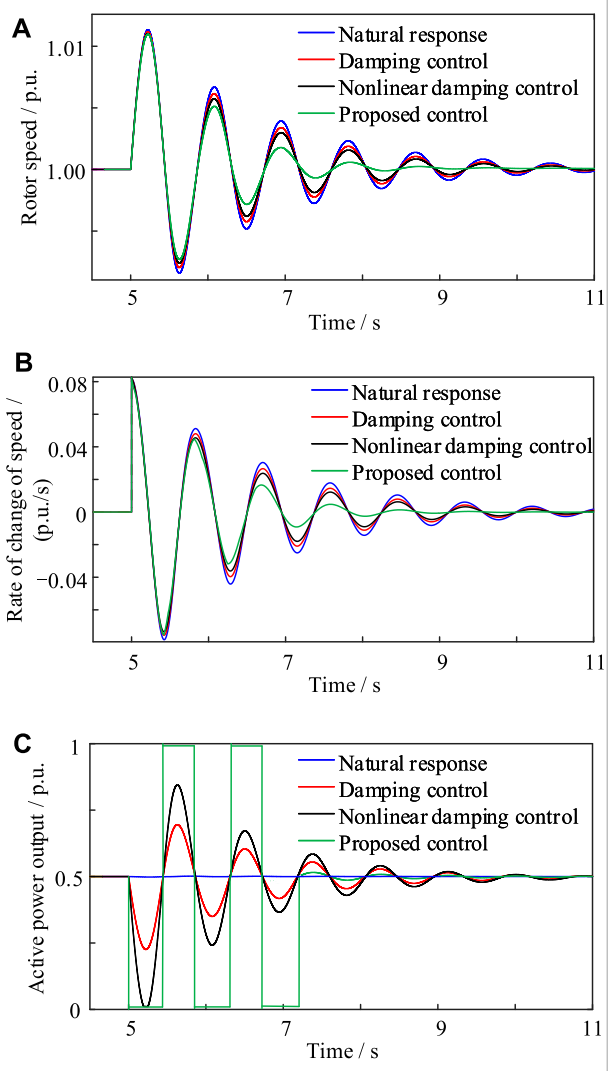

FIGURE 9
Oscillation suppression. **(A)** Rotor speed. **(B)** Rate of change of speed. **(C)** HVDC power.

VSC-HVDC system are set to be

$$\begin{cases} P = 1.5 V_d k_{p1} \Delta\omega + P_0 \\ Q = -1.5 V_d k_{p2} \Delta\omega \end{cases} \tag{23}$$

When HVDC uses the RPC control to suppress large frequency fluctuations of the receiving-end grid caused by large disturbances, the relevant thresholds must strictly comply with the grid frequency indexes defined by the grid code, i.e., the frequency deviation Δf or the rate of change of frequency (RoCoF) df/dt. For example, GB/T 33593–2017, the grid integration standard for distributed energy sources in China, stipulates that the frequency deviation $|\Delta f|$ shall not exceed 0.2 Hz during continuous operation, and shall not exceed 0.5 Hz when the relay action terminates power transmission. To

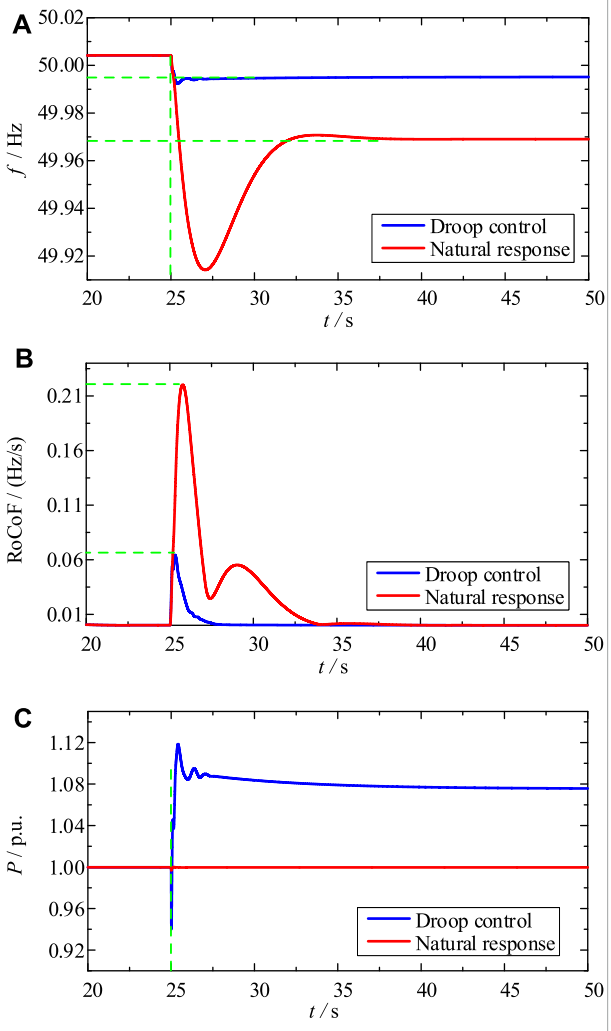

FIGURE 10
Frequency control under small disturbance. **(A)** Grid frequency. **(B)** RoCoF. **(C)** Inverter power.

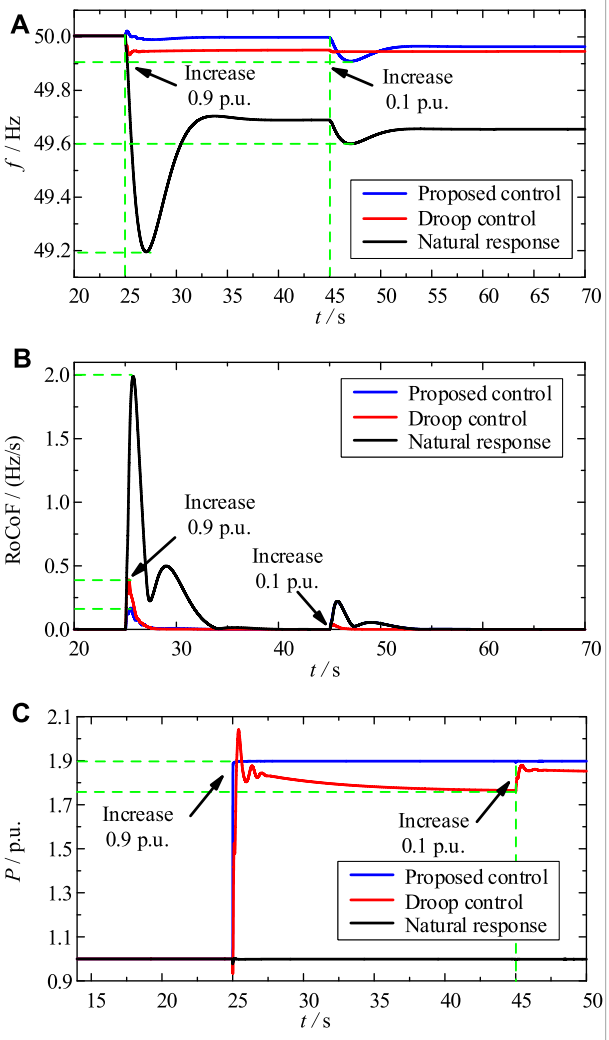

FIGURE 11
Frequency control under hybrid disturbance. **(A)** Grid frequency. **(B)** RoCoF. **(C)** Inverter power.

ensure that the power grid can meet the above frequency index requirements under various disturbances, a necessary margin must be reserved for the HVDC system when it suppresses frequency fluctuations. Accordingly, the RPC based frequency control will be implemented according to Figure 8, where $P_C = P_m < \Delta P_L$; if Δf or df/dt reaches the action threshold of the RPC control, the VSC power command is directly set to the maximum power capacity P_m. Similarly, when the grid frequency indexes decrease to the designed threshold, the VSC control mode switches to the damping control mode (i.e., droop control); when the grid frequency returns to the rated value, the VSC resumes the conventional constant power control mode. With reference to Figure 8, the three modes are autonomously switched according to the detected frequency of the receiving-end grid, to enhance the frequency fluctuation suppression effect and ensure the frequency stability of the receiving-end grid.

Obviously, when electromechanical oscillations or frequency fluctuations occur in the sending-end grid, the rectifier can also adopt a similar method to make the VSC-HVDC system actively suppress the electromechanical oscillation process or frequency fluctuation problem in the sending-end grid.

6 Simulation verification

In this paper, the MATLAB/Simulink platform is used to compare and verify the suppression capability of the VSC-HVDC system against grid electromechanical oscillations and frequency fluctuations, when the RPC mode is combined with the

damping control strategy. The simulation topology is shown in Figure 4.

6.1 Electromechanical oscillation suppression

The mechanical power of the prime mover of the receiving end grid changes abruptly at 5 s, causing an electromechanical oscillation. The VSC is made to operate in the absence of power control ($k_p = 0$), and in the presence of conventional damping control ($k_p = 300$) and non-linear damping control ($k_p = 700$) by adjusting the P controller gain. The SG rotor speed under the above control strategies is compared with the coordination strategy proposed in this paper, and the simulation results are shown in Figure 9.

As shown in Figures 9A,B, compared with the working condition of the VSC-HVDC system without power control (i.e., $k_p = 0$), the electromechanical oscillation amplitude and the oscillation amplitude of SG rotor speed gradually decrease as the parameter k_p increases. However, the rotor oscillation period does not change, indicating an almost unchanged inertia level despite the fact that the grid damping capability is enhanced. The corresponding active power output waveforms of the inverter station VSC2 under different control strategies are given in Figure 9C. Note that in this case $\Delta\omega$ is small when switching to the damping control strategy to modulate the power output, and therefore k_p can be appropriately amplified (here the value is taken as 1,000).

It can be concluded that the linear damping control strategy is not conducive to enhancing the ability of the VSC-HVDC to suppress the grid electromechanical oscillation. When the coordinated suppression strategy proposed in this paper is adopted, the SG rotor recovers to its rated speed significantly faster, and the amplitude of rotor oscillation is significantly reduced. At the same time, the rotor speed variation rate $d\omega/dt$ is substantially suppressed. This indicates that the oscillation suppression effect of the proposed strategy is stronger than that of the damping control and the local RPC strategy.

6.2 Frequency fluctuation suppression

In this simulation scenario, the infinite bus in Figure 3 is removed to simulate the capacity-limited receiving end grid. To simulate the operating condition where the power grid is subject to small disturbances, a disturbance of 0.1 p.u. Is suddenly added to the receiving end power grid at $t = 30$ s, when the droop control starts frequency control (see Figure 10). Under the condition of small disturbance, the frequency deviation using the droop control is reduced by 0.09 Hz compared with the natural response, the maximum value of the rate of change of frequency (RoCoF) is 0.14 Hz/s smaller than that of the natural response, and the compensation power to the receiving-end grid is significantly increased. It can be seen that the suppression effect of the droop control on frequency deviation is more prominent than that of RoCoF. At this time, the frequency is within the allowable range of the system during steady-state operation, and the HVDC system can smoothly exit the droop control mode.

To simulate the large disturbance, a disturbance of 0.9 p.u. Is suddenly added to the receiving end grid at $t = 25$ s (see Figure 11). The simulation results show that: with the proposed strategy, the HVDC system can adjust the operation mode autonomously, and quickly compensate for the power shortage of the receiving-end grid; the frequency of the receiving-end system is stabilized to 49.96 Hz within 3 s, and the maximum RoCoF is only 0.15 Hz/s. Conversely, under the same interference condition, the frequency control capability of the droop control is extremely limited. Obviously, the RPC control has a strong suppression effect on both frequency deviation and RoCoF.

The adaptive performance of the proposed HVDC control is further tested by adding a disturbance of 0.1 p.u. at $t = 45$ s. The test results (see Figure 11) show that the proposed control strategy can ensure that the HVDC system can autonomously sense the frequency change trend of the receiving end grid under different disturbance conditions, adjust the inverter operation mode, and continuously and dynamically match the real-time operating condition of the receiving-end power grid to always effectively suppress its frequency fluctuation problem.

7 Conclusion

Under the VSC capacity constraints, this paper compares the suppression level of rotor speed and frequency change rate for HVDC operating in the RPC mode and with the linear control. HVDC operating in the RPC mode has significantly suppression ability of electromechanical oscillations and frequency fluctuations. Then, this paper integrates the RPC mode and the damping control, and designs four operating conditions and power commands to regulate the HVDC power. The proposed active/reactive power coordination strategy, based on the RPC mode, can quickly suppress the system power imbalance and significantly improve the suppression effect of the HVDC on electromechanical oscillations and frequency fluctuations. Simulation results show that the supporting power introduced by the conventional control and its response speed are much smaller than the shortage power required when the grid is disturbed. Conversely, the RPC control can fully utilize the VSC power reserve, quickly and sufficiently compensating for the lack power, stabilizing the grid frequency

in time and effectively suppressing the electromechanical oscillation.

Data availability statement

The original contributions presented in the study are included in the article/supplementary material, further inquiries can be directed to the corresponding author.

Author contributions

All the authors conceived and designed the study. CB, JW, and YQ performed the simulation. CB, JW, and XL conceived and designed the simulations. YQ and JX wrote the manuscript with the guidance from JS and FL.

Conflict of interest

CB, JW, XL, JX, and FL were empolyed by Guangzhou Power Supply Bureau, Guangdong Power Grid Co., Ltd.

The remaining authors declare that the research was conducted in the absence of any commercial or financial relationships that could be construed as a potential conflict of interest.

Publisher's note

All claims expressed in this article are solely those of the authors and do not necessarily represent those of their affiliated organizations, or those of the publisher, the editors and the reviewers. Any product that may be evaluated in this article, or claim that may be made by its manufacturer, is not guaranteed or endorsed by the publisher.

References

Ali, H., Magdy, G., Li, B., Shabib, G., Elbaset, A. A., Xu, D., et al. (2019). A new frequency control strategy in an islanded microgrid using virtual inertia control-based coefficient diagram method. *IEEE Access* 7, 16979–16990. doi:10.1109/ACCESS.2019.2894840

Chi, Y., Tang, B., Hu, J., Tian, X., Tang, H., Li, Y., et al. (2019). Overview of mechanism and mitigation measures on multi-frequency oscillation caused by large-scale integration of wind power. *CSEE J. Power Energy Syst.* 5, 433–443. doi:10.17775/CSEEJPES.2019.01100

Fang, J., Tang, Y., Li, H., and Li, X. (2018). A Battery/Ultracapacitor hybrid energy storage system for implementing the power management of virtual synchronous generators. *IEEE Trans. Power Electron.* 33, 2820–2824. doi:10.1109/TPEL.2017.2759256

Kerdphol, T., Watanabe, M., Hongesombut, K., and Mitani, Y. (2019). Self-adaptive virtual inertia control-based fuzzy logic to improve frequency stability of microgrid with high renewable penetration. *IEEE Access* 7, 76071–76083. doi:10.1109/ACCESS.2019.2920886

Kumar, A. (2016). Power system stabilizers design for multimachine power systems using local measurements. *IEEE Trans. Power Syst.* 31, 2163–2171. doi:10.1109/TPWRS.2015.2460260

Kundur, P., Paserba, J., Ajjarapu, V., Andersson, G., Bose, A., Canizares, C., et al. (2004). Definition and classification of power system stability IEEE/CIGRE joint task force on stability terms and definitions. *IEEE Trans. Power Syst.* 19, 1387–1401. doi:10.1109/TPWRS.2004.825981

Lee, H.-Y., Asif, M., Park, K.-H., and Lee, B.-W. (2018). Feasible application study of several types of superconducting fault current limiters in HVDC grids. *IEEE Trans. Appl. Supercond.* 28, 1–5. doi:10.1109/TASC.2018.2799745

Li, C., Wu, Y., Sun, Y., Zhang, H., Liu, Y., Liu, Y., et al. (2020a). Continuous under-frequency load shedding scheme for power system adaptive frequency control. *IEEE Trans. Power Syst.* 35, 950–961. doi:10.1109/TPWRS.2019.2943150

Li, M., Xiong, L., Chai, H., Xiu, L., and Hao, J. (2020b). Mechanism of PV generation system damping electromechanical oscillations. *IEEE Access* 8, 135853–135865. doi:10.1109/ACCESS.2020.3011456

Ling, Y., Li, Y., and Xiang, J. (2021). Load support by droop-controlled distributed generations. *IEEE Trans. Ind. Electron.* 68, 8345–8355. doi:10.1109/TIE.2020.3013764

Liu, X., Spadacini, G., and Pignari, S. (2020). Physically based modeling of hand-assembled wire bundles for accurate emc prediction. *IEEE Trans. Electromagn. Compat.* 62, 914–922. doi:10.1109/temc.2019.2922455

Liu, X., Wu, B., and Xiu, L. (2022a). A fast positive-sequence component extraction method with multiple disturbances in unbalanced conditions. *IEEE Trans. Power Electron.* 37, 8820–8824. doi:10.1109/TPEL.2022.3161734

Liu, X., Xiong, L., Wu, B., Qian, Y., and Liu, Y. (2022b). Phase locked-loop with decaying DC transient removal for three-phase grids. *Int. J. Electr. Power & Energy Syst.* 143, 108508. doi:10.1016/j.ijepes.2022.108508

Nguyen, H. T., Yang, G., Nielsen, A. H., and Jensen, P. H. (2019). Combination of synchronous condenser and synthetic inertia for frequency stability enhancement in low-inertia systems. *IEEE Trans. Sustain. Energy* 10, 997–1005. doi:10.1109/TSTE.2018.2856938

Peng, Q., Yang, Y., Liu, T., and Blaabjerg, F. (2020). Coordination of virtual inertia control and frequency damping in PV systems for optimal frequency support. *CPSS Trans. Power Electron. Appl.* 5, 305–316. doi:10.24295/CPSSTPEA.2020.00025

Shi, Q., Liu, L., Wang, Y., Lu, Y., Zou, Q., Zhang, Q., et al. (2021). Cooperative synthetic inertia control for wind farms considering frequency regulation capability. *Front. Energy Res.* 9, 738857. doi:10.3389/fenrg.2021.738857

Sun, K., Xiao, H., Liu, S., and Liu, Y. (2021). Machine learning-based fast frequency response control for a VSC-HVDC system. *CSEE J. Power Energy Syst.* 7, 688–697. doi:10.17775/CSEEJPES.2020.01410

Varma, R. K., and Maleki, H. (2019). PV solar system control as STATCOM (PV-STATCOM) for power oscillation damping. *IEEE Trans. Sustain. Energy* 10, 1793–1803. doi:10.1109/TSTE.2018.2871074

Wang, J., Huang, M., Fu, C., Li, H., Xu, S., and Li, X. (2019). A new recovery strategy of HVDC system during AC faults. *IEEE Trans. Power Deliv.* 34, 486–495. doi:10.1109/TPWRD.2019.2892410

Wang, Y., Meng, J., Zhang, X., and Xu, L. (2015). Control of PMSG-Based wind turbines for system inertial response and power oscillation damping. *IEEE Trans. Sustain. Energy* 6, 565–574. doi:10.1109/TSTE.2015.2394363

Xie, Y., Huang, J., Liu, X., Zhuo, F., Liu, B., and Zhang, H. (2014). "Pv system modeling and a global-planning design for its controller parameters," in 2014 IEEE Applied Power Electronics Conference and Exposition, Fort Worth, TX, USA, 16-20 March 2014 (IEEE), 3132–3135.

Xiong, L., Liu, L., Liu, X., and Liu, Y. (2021a). Frequency trajectory planning based strategy for improving frequency stability of droop-controlled inverter based standalone power systems. *IEEE J. Emerg. Sel. Top. Circuits Syst.* 11, 176–187. doi:10.1109/JETCAS.2021.3052006

Xiong, L., Liu, X., Liu, H., and Liu, Y. (2022). Performance comparison of typical frequency response strategies for power systems with high penetration

of renewable energy sources. *IEEE J. Emerg. Sel. Top. Circuits Syst.* 12, 41–47. doi:10.1109/JETCAS.2022.3141691

Xiong, L., Liu, X., and Liu, Y. (2021b). Decaying dc and harmonic components detection for absorbing impact load currents in weak grids. *IEEE Trans. Power Deliv.* 36, 1907–1910. doi:10.1109/TPWRD.2020.3038077

Xiong, L., Zhuo, F., Liu, X., Zhu, M., Chen, Y., and Wang, F. (2015). "Research on fast open-loop phase locking scheme for three-phase unbalanced grid," in 2015 IEEE Applied Power Electronics Conference and Exposition (APEC), Charlotte, NC, USA, 15-19 March 2015 (IEEE), 1672–1676.

Xu, Y., and Wang, H. (2021). Torque limit-based inertial control of a dfig for rapid frequency stabilization. *Front. Energy Res.* 9, 788989. doi:10.3389/fenrg.2021.788989

Yang, D., Sang, S., and Zhang, X. (2021). Two-phase short-term frequency response scheme of a dfig-based wind farm. *Front. Energy Res.* 9, 781989. doi:10.3389/fenrg.2021.781989

You, J., Xu, D., and Cao, J. (2022). Dynamic power-based temporary frequency support scheme for a wind farm. *Front. Energy Res.* 10, 1005796. doi:10.3389/fenrg.2022.1005796

Zhang, L., Harnefors, L., and Nee, H. P. (2011). Interconnection of two very weak AC systems by VSC-HVDC links using power-synchronization control. *IEEE Trans. Power Syst.* 26, 344–355. doi:10.1109/TPWRS.2010.2047875

Zhu, Y., Liu, C., Sun, K., Shi, D., and Wang, Z. (2019). Optimization of battery energy storage to improve power system oscillation damping. *IEEE Trans. Sustain. Energy* 10, 1015–1024. doi:10.1109/TSTE.2018.2858262

frontiers | Frontiers in Energy Research

TYPE Original Research
PUBLISHED 06 January 2023
DOI 10.3389/fenrg.2022.1088563

OPEN ACCESS

EDITED BY
Liansong Xiong,
Xi'an Jiaotong University, China

REVIEWED BY
Ning Li,
Xi'an University of Technology, China
Zhenxiong Wang,
Xi'an Jiaotong University, China
Lei Liu,
School of Electrical Engineering, Xi'an Jiaotong University, China, in collaboration with reviewer ZW

*CORRESPONDENCE
Qunying Liu,
lqy1206@126.com

SPECIALTY SECTION
This article was submitted to Process and Energy Systems Engineering, a section of the journal Frontiers in Energy Research

RECEIVED 03 November 2022
ACCEPTED 19 December 2022
PUBLISHED 06 January 2023

CITATION
Liu Q, Song Y, Jiang Y, Xu Y and Chen S (2023), Coordinated voltage control for improved power system voltage stability by incorporating the reactive power reserve from wind farms.
Front. Energy Res. 10:1088563.
doi: 10.3389/fenrg.2022.1088563

Coordinated voltage control for improved power system voltage stability by incorporating the reactive power reserve from wind farms

Qunying Liu[1]*, Yingxing Song[1], Yazhou Jiang[2], Yin Xu[3] and Shuheng Chen[4]

[1]School of Automation Engineering, The University of Electronic Science and Technology, Chengdu, China, [2]Department of the Electrical and Computer Engineering of Clarkson University, Potsdam, NY, United States, [3]School of Electrical Engineering, Bejing Jiaotong University, Beijing, China, [4]School of Mechanical and Electrical Engineering, University of Electronic Science and Technology, Chengdu, China

The absorption and output characteristics of reactive power of the doubly-fed induction generator (DFIG) greatly influence the voltage stability of PCC (Point of Common Coupling) where the wind farms are integrated into the bulk power grid. This study proposes a reactive power compensation strategy for coordinated voltage control (CVC) of PCC with large-scale wind farms to achieve the expected voltage quality of the power grid through a minimum amount of control actions in emergencies. To this end, the mechanism of reactive power and voltage control inside DFIG is first analyzed. Then, the concept of reactive power reserve (RPR) sensitivity concerning control actions is introduced and an index of voltage stability margin is proposed to evaluate and analyze the distance between the current operating point and the voltage collapse point by analyzing the relationship between reactive power reserve and voltage stability margin. In the event of an emergency, critical reactive power reserves are obtained to reduce the dimension and complexity of the control problem. The sensitivity of reactive power reserve and the control are formulated into a convex quadratic programming problem to optimize the control strategies for voltage stability. The proposed technology has been validated on the IEEE 39-bus system.

KEYWORDS

reactive power reserve, voltage stability margin, convex quadratic programming problem, wind power, power system

1 Introduction

Because of the development of power electronics control techniques, high penetration of wind farm dominated by DFIG will become a prominent characteristics of power system motivated by the "double carbon" strategy recognized by the whole world. However, grid integration of multiple wind farms through long transmission lines brings about great challenges to system voltage stability due to the stochasticity and variability of wind generations, which tends to cause the tripping of wind farms, even a widespread event or potential system collapse. The RPR is a critical metric to maintain voltage stability, which is an essential information source for voltage stability boundary estimation (Dong et al., 2005). Therefore, it is important to assess the reactive power reserve of the key buses based on the local information (Sissine, 2007). Considering the voltage control cost and the control effects, to

control all the voltage buses is unrealistic. Hence, to find the important buses which are sensitive to reactive power compensation is recognized to be prominent to improve voltage stability.

According to the research published in recent years, CVC has commonly included three steps: 1)Discovering the relationship of voltage stability margin and RPR to determine the buses sensitive to the reactive power (El-Araby and Yorino, 2018; Han et al., 2018); 2) Calculating the RPR in power system (Li et al., 20132013; Jankowski et al., 20172017); 3)Controlling voltage by coordinating the active power production, reactive compensation devices and transformers (Qinyu et al., 20182018; Ouyang et al., 2019), especially in the power system inter-collected with wind farm (Leonardi and Ajjarapu, 2012; Huang et al., 2020). Ref. (Ghosh et al., 2020).has proposed a dynamic CVC architecture for reactive power capability enhancement of the DFIG-based wind power generation. To improve the control effect, ref. (Zhang et al., 2020). has proposed an optimal sensitivity to online track the accurate RPR of wind farms. ref. (Ren et al., 2022).based on the tabu search algorithm, the reactive power compensation amount of each field area is calculated with the minimum nodal voltage index and the maximum margin index as the objective function.Based on the local voltage profile to identify the emergency, (Ma et al., 2022). has performed a adaptive voltage control. Based on the clustered effective reactive reserve, (Park et al., 2021). Has proposed an indicator to identify the risk of dynamic voltage stability.Based on the second-order trajectory sensitivity analysis, (Hu et al., 2021). Has proposed a robust DVR assessment method to determine both the inductive and capacitive DVR. (Oliveira and Bollen, 2022). Has proposed a dynamic CVC strategy to enhance the reactive power capability of the DFIG during grid faults.

The CVC strategy tends to formulate a MLP (Multi-objectives Linear Programming) problems (Grudinin, 1998; Gabash and Li, 2012), the control effect depends on whether the optimal solution of MLP is found. Due to the complexity, insecure convergence, and high computational cost, how to calculate the optimal solutions, and also improve the convergence at the same time is still a hot topic (Sun et al., 2017).

The optimal solutions tend to include the reactive power compensation location, the reactive power compensation amount and the voltage improvement, and so on. In (De and Goswami, 2014), Artificial Bee Colony algorithm has been used to solve optimum power flow (OPF) problems, which is formed by three new RPP methods. In (Ding et al., 2016), the conic relaxation based branch flow formulation has been employed to set up a mixed integer convex programming model, and the second order cone programming based column-and-constraint generation algorithm is utilized to solve the proposed two-stage robust reactive power optimization model. In (Mugemanyi et al., 2020), the chaotic bat algorithm is applied to solve the optimal reactive power dispatch problem taking into account small-scale, medium-scale and large-scale power systems. In (Ibrahim et al., 2022), a voltage secure multi-period optimal reactive power dispatch problem has been formulated and OPTALG and GridOpt have been used to solve the optimization problem.

According to the aforementioned research, few studies have explored the relationship between control action and RPR. Hence the precise control is difficult to perform. However, the search for the optimal solution in reactive power optimization is still time-consuming, which makes it difficult to apply the above methods online. For these reasons, our research work is focused on two aspects:

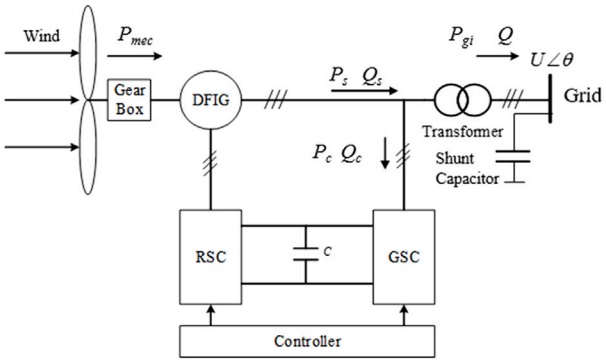

FIGURE 1
Configuration of doubly-fed induction generator.

1) To determine the key buses and weak areas of the system for voltage stability, the calculation method of R sensitivity with respect to control actions is proposed. Based on RPR sensitivity, the point-to-point voltage support capability is analyzed to determine the priority and weighting factor of different control variables (e.g., active power of DFIG, equivalent susceptance of shunt capacitor, and load shedding);
2) The convex quadratic programming problem with voltage stability as the objective is established. A convex quadratic programming problem is formulated with inequality constraint in this research to obtain an optimal control amount. Furthermore, the modified genetic algorithm (MGA) approach is proposed to solve it with less computation complexity while achieving better convergence.

This paper is organized as follows: Section 2 introduces the concept of voltage reactive power sensitivities with respect to control actions and Section 3 describes how the index of voltage stability margin is established. The control strategy of reactive power compensation is explained in Section 4. How to determine the optimal control amount is discussed in Section 5. Section 6 shows the results of the proposed approach applied to the IEEE 39-bus system. Finally, the conclusion and future work are addressed in Section 1.

2 The mechanism of reactive power reserves of DFIG for control actions

To define the concept of reactive power reserve of the doubly-fed induction generator, the reactive regulation characteristic of DFIG is analyzed. The definition of traditional reactive power control inside DFIG is introduced in (Mugemanyi et al., 2020). The typical configuration of the DFIG system is shown in Figure 1.

In Figure 1, the rotor-side converter (RSC) is used to control the maximum of the active power production, and the grid-side converter (GSC) is used to control the reactive power before participating in the voltage support. P_{mec} is the mechanical power of the wind turbine; P_s and Q_s are the active power and reactive power of the stator, respectively; P_c and Q_c are the active power and reactive power output of the grid-side converter; P_{g_i} and Q are the active power and reactive power output of a doubly-fed induction generator. The output of active power of the DFIG is:

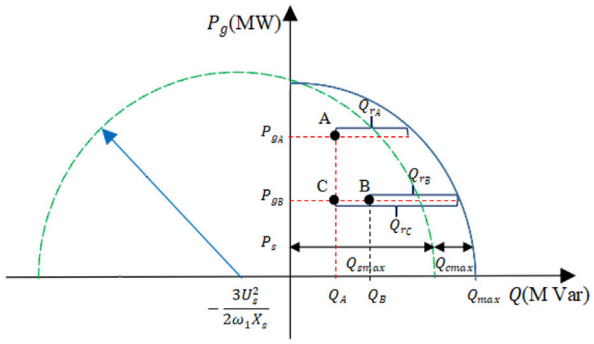

FIGURE 2
PQ Curve of doubly-fed Wind Turbine.

$$P_{gi} = (1-s)P_s \tag{1}$$

The output of reactive power of the DFIG is Q, which is composed of the reactive power Q_s on the stator side and the reactive power Q_c from the converter on the grid side (Ibrahim et al., 2022). The operating range of the stator side reactive power of a doubly-fed induction generator is mainly limited by the current of the rotor side converter. For a given active power P_s of the stator, the maximum limit of reactive power on the stator side is:

$$Q_{\text{smax}} = -\frac{3U_s^2}{2\omega_1 X_s} + \sqrt{\left(\frac{9X_m^2}{4X_s^2}U_s^2 I_{r\max}^2\right) - P_s^2} \tag{2}$$

In Eq. 2, U_s is the value of the stator voltage; X_m and X_s are the excitation reactance of the generator and equivalent reactance of the stator, respectively, I_{rmax} is the maximum current allowed by the rotor; s is the slip ratio. ω_1 denotes the synchronous rotational angular velocity. The maximum reactive power limit of the converter on the grid side is

$$Q_{\text{cmax}} = \sqrt{S_g^2 - S^2 P_s^2} \tag{3}$$

In Eq. 3, S_g is the capacity of the converter. The reactive power capacity of the converter on the grid side is mainly limited by the capacity of the converter. Combining the reactive power regulation capability of the stator and the converter on the grid side, the maximum limit of reactive power regulation of a single DFIG is

$$Q_{\max} = -\frac{3U_s^2}{2\omega_1 X_s} + \frac{P_{gi}}{(1-s)^2\sqrt{\left(\frac{9X_m^2}{4X_s^2}U_s^2 I_{r\max}^2\right) - \frac{P_{gi}^2}{(1-s)^2}}} + \sqrt{s_g^2 - \frac{s^2 P_{gi}^2}{(1-s)^2}} \tag{4}$$

The reactive power reserve refers to the reserved adjustable margin for the DFIG, which can adjust the terminal voltage fast. In some emergencies, such as asymmetrical short-circuit faults, the reactive power reserve can be used to support the deteriorating voltage stability. The capacity of reactive power reserve RPR of the doubly-fed induction generator can be expressed as

$$Q_r = Q_{\max} - Q \tag{5}$$

During the operation process, the reactive power reserve of DFIG is determined both by itself and the demand from the grid side. On the DFIG side, it can be obtained from the PV and PQ curves. Because the total capacity is a given value, the change in the active power of the DFIG tends to cause the decreased reactive power reserve, which as a result will influence the voltage stability. The PQ curve of the stator side of the DFIG is shown by the dotted line in Figure 2, which is a semi-circle with $(-\frac{3U_s^2}{2\omega_1 X_s}, 0)$ as the center.

By considering the output of the grid-side converter, the PQ curve of the DFIG is shown by the solid line. On the grid side, two potential control actions have been considered: the shunt capacitor switching and the load shedding. Reactive power reserve sensitivity with respect to the changes in the three control actions is formulated as follows.

2.1 The reactive power reserve sensitivity with respect to the active power output of DFIG

According to Eq. 5 and Figure 2, when the system operates at point A, the minimum RPR requirement on the DFIG side is violated. To bring the RPR back to a safe operational point, the active power generation is reduced from P_{g_A} to P_{g_B}, thereby changing the amount of RPR from Q_A to Q_B. As a result, active power output indirectly affects the voltage level on the DFIG side. Eq 6 describes the sensitivity of RPRs for active power:

$$\begin{aligned}\frac{\partial Q_{rk}}{\partial P_{gi}} &= \frac{\partial Q_{\max k}}{\partial P_{gi}} - \frac{\partial Q_k}{\partial P_{gi}} \\ &= -\frac{P_{gi}}{(1-s)^2\sqrt{\left(\frac{9X_m^2}{4X_s^2}U_s^2 I_{r\max}^2\right) - \frac{P_{gi}^2}{(1-s)^2}}} \\ &\quad -\frac{s^2 P_{gi}}{(1-s)^2\sqrt{s_g^2 - \frac{s^2 P_{gi}^2}{(1-s)^2}}} - \left(\frac{\partial Q_{li}}{\partial P_{gi}} + \frac{\partial Q_{Ti}}{\partial P_{gi}}\right)\end{aligned} \tag{6}$$

In Eq. 6, Q_{l_i} represents the reactive power load at bus Q_{T_i} is the injected reactive power at bus;

2.2 The reactive power reserve sensitivity with respect to shunt capacitor

Shunt capacitors always cause positive increments of RPRs. Once the switching of shunt capacitors is employed, the reactive power production of the DFIG changes from point A to point C as described in Figure 2. Eq 7 describes the sensitivity of RPRs for shunt capacitors. In Eq 7, B_m corresponds to the shunt capacitor bank at bus m.

$$\begin{aligned}\frac{\partial Q_{rk}}{\partial B_m} &= \frac{\partial Q_{\max k}}{\partial B_m} - \frac{\partial Q_k}{\partial B_m} = -\left(\frac{\partial Q_{li}}{\partial B_m} + \frac{\partial Q_{Tn}}{\partial B_m}\right) \\ &= -\sum_{j=1}^{n}\left(\frac{\partial Q_{Ti}}{\partial \theta_j}\frac{\partial \theta_j}{\partial B_m} + \frac{\partial Q_{Ti}}{\partial V_j}\frac{\partial V_j}{\partial B_m}\right)\end{aligned} \tag{7}$$

where, θ_j and V_j are the bus phase angles and the magnitude at bus i, respectively.

2.3 The reactive power reserve sensitivity with respect to load shedding

When an emergency occurs, the voltage drops sharply, load shedding is the most direct measure employed to change the reactive power production of the DFIG from point A to point C as described in Figure 2. Equations 8 and 9 represent RPR sensitivities to active and reactive load shedding, respectively:

$$\begin{aligned}\frac{\partial Q_{rk}}{\partial P_{l_m}} &= \frac{\partial Q_{\max k}}{\partial P_{l_m}} - \frac{\partial Q_k}{\partial P_{l_m}} = -\left(\frac{\partial Q_{li}}{\partial P_{l_m}} + \frac{\partial Q_{Tn}}{\partial P_{l_m}}\right) \\ &= -\sum_{j=1}^{n}\left(\frac{\partial Q_{Ti}}{\partial \theta_j}\frac{\partial \theta_j}{\partial P_{l_m}} + \frac{\partial Q_{Ti}}{\partial V_j}\frac{\partial V_j}{\partial P_{l_m}}\right)\end{aligned} \tag{8}$$

$$\begin{aligned}\frac{\partial Q_{rk}}{\partial Q_{l_m}} &= \frac{\partial Q_{\max k}}{\partial Q_{l_m}} - \frac{\partial Q_k}{\partial Q_{l_m}} = -\left(\frac{\partial Q_{li}}{\partial Q_{l_m}} + \frac{\partial Q_{Tn}}{\partial Q_{l_m}}\right) \\ &= -\sum_{j=1}^{n}\left(\frac{\partial Q_{Ti}}{\partial \theta_j}\frac{\partial \theta_j}{\partial Q_{l_m}} + \frac{\partial Q_{Ti}}{\partial V_j}\frac{\partial V_j}{\partial Q_{l_m}}\right)\end{aligned} \tag{9}$$

In Eqs 8, 9, P_{l_m} and Q_{l_m} are the active and reactive power loads at bus m. In Eqs 6, 9, the terms $\frac{\partial Q_{T_i}}{\partial \theta_j}$ and $\frac{\partial Q_{T_i}}{\partial V_j}$ are obtained by the partial derivative calculation of reactive power injection at bus i:

$$Q_{Ti} = V_i\sum_{j=1}^{n}V_j\left(G_{ij}\sin\theta_{ij} - B_{ij}\cos\theta_{ij}\right) \tag{10}$$

where, G_{ij} and B_{ij} represent the corresponding elements of the admittance matrices; θ_{ij} is the difference in phase angle between buses i and j; V_i and V_j are the voltage amplitude at buses i and j. As the value of B_{ij} is generally small and negligible, the derivative of the reactive power load with respect to θ_j and V_j are given in (11) and 12:

$$\frac{\partial Q_{Ti}}{\partial \theta_j} = 2V_i\sum_{j=1}^{n}V_jG_{ij}\cos\theta_{ij} \tag{11}$$

$$\frac{\partial Q_{Ti}}{\partial V_j} = 2\sum_{j=1}^{n}V_jG_{ij}\sin\theta_{ij} \tag{12}$$

The terms $\frac{\partial \theta_j}{\partial P_{g_i}}, \frac{\partial V_j}{\partial P_{g_i}}, \frac{\partial \theta_j}{\partial B_m}, \frac{\partial V_j}{\partial B_m}, \frac{\partial \theta_j}{\partial P_{l_m}}, \frac{\partial V_j}{\partial P_{l_m}}, \frac{\partial \theta_j}{\partial Q_{l_m}}, \frac{\partial V_j}{\partial Q_{l_m}}$ are obtained by the power flow equation:

$$f(x, \alpha, u) = 0 \tag{13}$$

In Eq. 13, x represents the vector of system state variables (θ, V); α represents the control variable $(P_{g_i}, B_m, P_{l_m}, Q_{l_m})$ mentioned in this paper; u represents the disturbance variables in power systems, such as short-circuit fault, non-fault lines tripping, generator tripping, and so on. Considering that the system is operated at an initial steady state $(x^{(0)}, \alpha^{(0)}, u^{(0)})$, when various types of disturbances occur, the operating state of the system is deviated from the normal state, with an offset of Δx. The system will perform a series of adjustments according to the amount of $\Delta\alpha$ to maintain the stable state of the system.

$$f\left(x^{(0)} + \Delta x, \alpha^{(0)} + \Delta\alpha, u^{(0)} + \Delta u\right) = 0 \tag{14}$$

Assuming that the variation of steady state is small, the Taylor series expansion is performed in Eq. 14 and the other terms above the second order are ignored. The resulting simplification of the Taylor series is shown as

$$f\left(x^{(0)}, \alpha^{(0)}, u^{(0)}\right) + J_x\Delta x + J_\alpha\Delta\alpha + J_u\Delta u = 0 \tag{15}$$

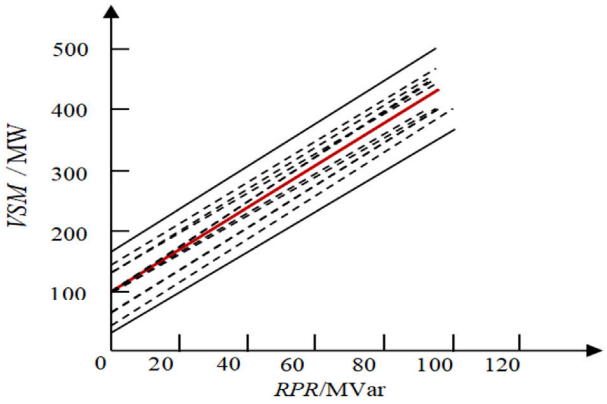

FIGURE 3
The relationship between RPR and VSM.

In Eq. 15, J_x represents the derivative of the power flow equations for the system state variables; J_α is the derivative of the power flow equations for the control variables; J_u is the derivative of the power flow equations with respect to the disturbance variables. By deducing Eq. 15, the relationship between state variables and control variables is given in Equation 18:

$$J_x\Delta x + J_\alpha\Delta\alpha + J_u\Delta u = 0 \tag{16}$$

$$\Delta x = J_x^{-1}\left(J_\alpha\Delta\alpha + J_u\Delta u\right) \tag{17}$$

$$\Delta x = -\frac{\partial x}{\partial \alpha}\Delta\alpha - \frac{\partial x}{\partial u}\Delta u \tag{18}$$

With Eq. 18, the RPR sensitivity with respect to control actions has been introduced. In order to construct the relationship between the reactive power reserves and the voltage stability margin, the next step is to analyze the index of the voltage stability criterion.

3 The index of voltage stability criterion

According to the traditional PV curve, the load of the power system increases gradually. For each incremental load, the power flow is recalculated to determine the bus voltage corresponding to the load. The increment of the load is stopped when the voltage collapse point or the nose of the PV curve is reached. The knee is a bifurcation point, exceeding which means that the system becomes unstable. This bifurcation point is marked as the maximum operating point. The voltage stability margin is usually measured by the distance between the current operating point and the maximum operating point [25, 26]. This measure provides an absolute and direct estimate of how much margin the system still has before approaching a collapse point, which also means that the voltage collapse is imminent when the system has a margin of 0 MW. Previous research has shown that the voltage stability margin (VSM) of the grid side can usually be improved through appropriate reactive power reserve (RPR) management [27-29]. For individual reactive power sources, it is found that the RPR of individual sources does not exhibit a consistent correlation with the VSM. The relationship between RPR and VSM can be approximately linear [30], which is shown in Figure 3.

For the entire voltage control area, not all doubly-fed induction generators have adequate reactive power capability, only a reduced number of critical doubly-fed induction generators will be targeted to enhance the voltage stability margin. Experimental results have shown that the VSM of all systems is linearly related to the sum of critical RPRs as follows:

$$VSM = k\sum_{i=1}^{n} RPR_i + b \tag{19}$$

where k is the slope of the margin-reserve correlation line; b is a constant; $\sum_{i=1}^{n} RPR_i$ is the sum of critical RPR.

4 Formulation of the convex quadratic programming problem

4.1 Objective function

The goal of adjusting and managing the control quantity is to maintain the voltage level after disturbances through the least control actions and the reactive compensation. The solution of the convex quadratic control problem shown in Eq. 20 will determine the minimal amount of control actions needed to improve critical RPRs.

$$F = \min\left(\sum_{i=1}^{n_{P_g}} \omega_i^{P_g}\left(\Delta P_{gi}^2\right) + \sum_{j=1}^{n_{B_m}} \omega_i^{B_m}\left(\Delta B_m^2\right) + \sum_{l=1}^{n_{P_{lm}}} \omega_l^{P_{lm}}\left(\Delta P_{lm}^2\right) + \sum_{l=1}^{n_{Q_{lm}}} \omega_l^{Q_{lm}}\left(\Delta Q_{lm}^2\right)\right) \tag{20}$$

In Eq. 20, ΔP_{g_i}, ΔB_m, ΔP_{l_m} and ΔQ_{l_m} represent the control actions, whose weights are given by $\omega_i^{P_g}$, $\omega_j^{B_m}$, $\omega_l^{P_{lm}}$ and $\omega_l^{Q_{lm}}$, respectively. The terms n_{P_g}, n_{B_m}, $n_{P_{lm}}$ and $n_{Q_{lm}}$ represent the total number of critical DFIG, the total number of shunt capacitor banks, and the total number of load shedding, respectively.

4.2 Constraint condition

Commonly, the reactive power reserve margin of the doubly-fed induction generators will not be reduced below the minimum value. Eq 21 gives the reactive power reserve limitation.

$$RPR_{i0} + \sum_{i=1}^{n_{pg}} \frac{dRPR_i}{dP_{gi}}\Delta P_{gi} + \sum_{j=1}^{n_{Bm}} \frac{dRPR_i}{dB_m}\Delta B_m + \sum_{l=1}^{n_{P_{lm}}} \frac{dRPR_i}{dP_{l_m}}\Delta P_{l_m} + \sum_{l=1}^{n_{Q_{lm}}} \frac{dRPR_i}{dQ_{l_m}}\Delta Q_{l_m} \geq RPR_{i\min} \tag{21}$$

where $R\,PR_{i0}$ is the initial reactive reserve margin; R PRimin is the minimum limit of RPR. According to Eq. 19, the full expression of RPRi and b are displayed, which is shown as Eq. 22, where the reactive power reserve sensitivities with respect to changes in the output of active power, the shunt capacitor switching, and the active and reactive load shedding are represented by $dRPR_i/dP_{gi}$, $dRPR_i/dB_m$, $dRPR_i/dP_{l_m}$ and $dRPR_i/dQ_{l_m}$, respectively.

$$VSM_0 + K\sum_{i=1}^{n}\left(\sum_{i=1}^{n_{pg}} \frac{dRPR_i}{dP_{gi}}\Delta P_{gi} + \sum_{j=1}^{n_{Bm}} \frac{dRPR_i}{dB_m}\Delta B_m + \sum_{l=1}^{n_{P_{lm}}} \frac{dRPR_i}{dP_{l_m}}\Delta P_{l_m} + \sum_{l=1}^{n_{Q_{lm}}} \frac{dRPR_i}{dQ_{l_m}}\Delta Q_{l_m}\right) \geq VSM_{\min} \tag{22}$$

Equation 22 ensures that the amount of VSM will be raised above the minimum value. VSM_0 is the initial voltage stability margin of the system, VSM_{min} is the minimum limit of VSM.

$$V_{i\min} \leq \left(\sum_{i=1}^{n_{pg}} \frac{dV_i}{dP_{gi}}\Delta P_{gi} + \sum_{j=1}^{n_{Bm}} \frac{dV_i}{dB_m}\Delta B_m + \sum_{l=1}^{n_{P_{lm}}} \frac{dV_i}{dP_{l_m}}\Delta P_{l_m} + \sum_{l=1}^{n_{Q_{lm}}} \frac{dV_i}{dQ_{l_m}}\Delta Q_{l_m} + V_{i0}\right) \leq V_{i\max} \tag{23}$$

In Eq. 23, bus voltage changes around the initial value can be easily impacted by the active power output, the capacitor compensation, and the active and reactive power of the load. Therefore, the voltage in Eq. 23 is considered to be expressed by the sum of the initial value V_{i0} and the changed values affected by the different control actions. The voltage of each PQ bus must be within its lower limits ($V_{i_{min}}$) and upper limits ($V_{i_{max}}$) when control actions are applied. The normal voltage range used throughout this work is given in Eq. 24. The last four inequalities on control variables are designed to ensure that the control actions always work within a proper range of operation.

$$0.9 \leq V_i \leq 1.05\,p.u \tag{24}$$

$$\Delta P_{gi}^{\min} \leq \Delta P_{gi} \leq \Delta P_{gi}^{\max} \tag{25}$$

$$\Delta B_m^{\min} \leq \Delta B_m \leq \Delta B_m^{\max} \tag{26}$$

$$\Delta P_{l_m}^{\min} \leq \Delta P_{l_m} \leq \Delta P_{l_m}^{\max} \tag{27}$$

$$\Delta Q_{l_m}^{\min} \leq \Delta Q_{l_m} \leq \Delta Q_{l_m}^{\max} \tag{28}$$

constraints of load reactive power removal respectivelywhere $\Delta P_{g_i}{}^{max}$ and $\Delta P_{g_i}{}^{min}$ are the upper and lower limit constraints of active output reduction of wind turbine respectively; $\Delta B_m{}^{max}$ and $\Delta B_m{}^{min}$ are the upper and lower limit constraints of the compensation amount of the shunt capacitor respectively; $\Delta P_{l_m}{}^{max}$ and $\Delta P_{l_m}{}^{min}$ are the upper and lower limit constraints of load active power removal respectively; $\Delta Q_{l_m}{}^{max}$ and $\Delta Q_{l_m}{}^{min}$ are the upper and lower limit.

By combining Eqs 20-28, an optimization problem is formed. The description of the method is shown in Figure 4.

It is assumed that the method converges under the condition that all limits are satisfied. If the VSM constraint is not satisfied, the process continues until it is converged. It needs to note that once the contingency cases increase, the number of constraints and variables increases. Hence, the computation of the optimization problem will increase significantly. Therefore, a fast and reliable solving method is important.

5 determination of the optimal control amount based on the improved genetic algorithm

In this paper, an improved genetic algorithm (IGA) is used to solve the planning problem and search for the optimal control amount. The

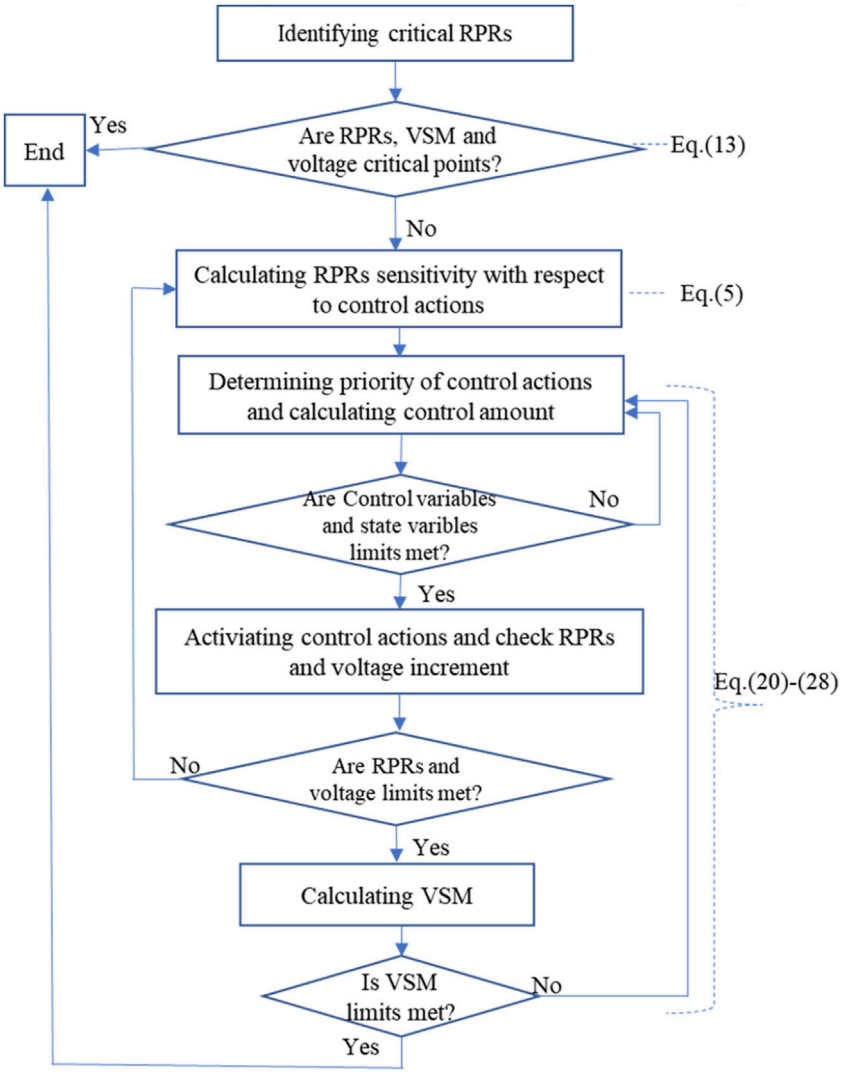

FIGURE 4
Flow chart for solving minimum control quantity.

improved genetic algorithm includes the hybrid coding method for the improvement of coding, binary coding method is used for discrete control variables such as the transformer tap and the reactive power compensation switching of shunt capacitor group, and real coding method is used for continuous variables such as generator terminal voltage and load active and reactive power. To improve the initial population, an initial population with a quantity twice that of the traditional genetic algorithm (TGA) at random is generated in IGA, and then the fitness function value of all individuals in the population is calculated. Through comparison, the fitness function values are arranged in descending order, and half of the individuals with lower fitness function values are discarded. The other half of the individuals with higher fitness function values are taken as the initial population for subsequent iterative calculation. The initial population number obtained after improvement is the same as that of the TGA. However, the average value of the fitness function value of the newly generated population is higher, so that the convergence speed can be improved during power flow calculation. In order to avoid the local optimal solution and loss of population diversity caused by the premature maturity of excellent individuals, the quadratic fitness function value calculation method is adopted, by reducing the difference of fitness function values among individuals. After the first fitness function value is calculated, the average value of the fitness function value is calculated, and then the quadratic fitness function value is calculated. The implementation process of the improved genetic algorithm for the above multi-objective optimization problem is as follows:

Step 1: Obtaining the basic state value of power system by Newton Raphson power flow calculation;
Step 2: Determining the weak bus of the system and the compensation position of the parallel capacitor; then the preselected control variables are screened according to the RPR sensitivity.
Step 3: Starting the IGA, and coding the control variable and system state variable by using the binary code and real code, randomly generating double initial population;
Step 4: Calculating the fitness value of individuals in the initial population, retaining half of the individuals with larger fitness value, calculating the secondary fitness value, and

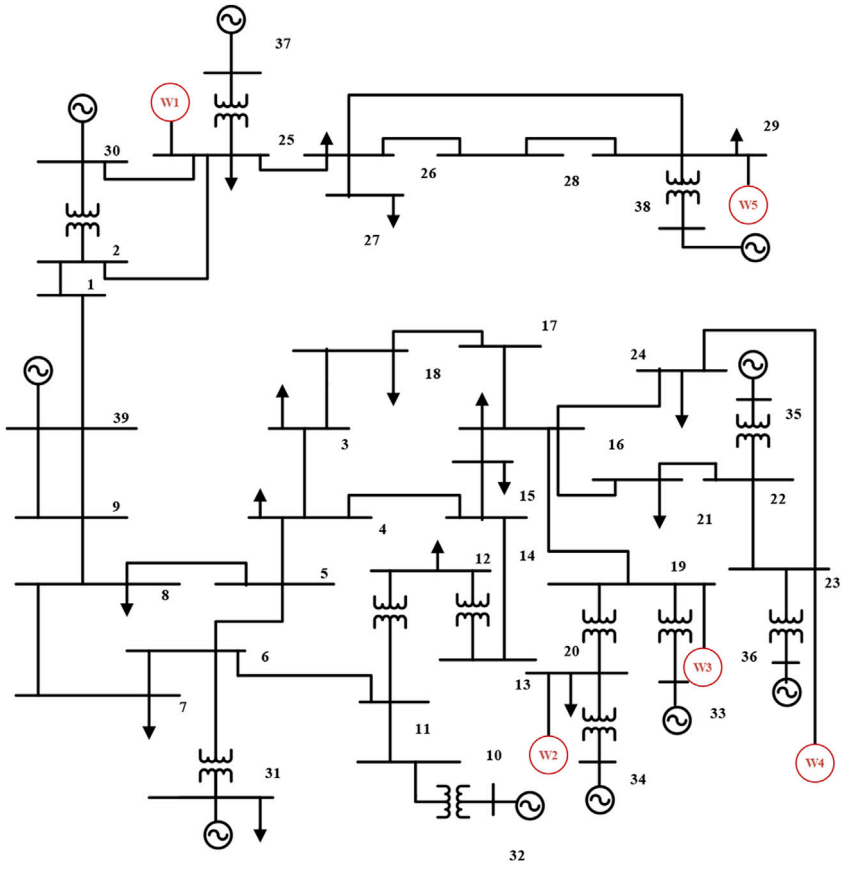

FIGURE 5
Structure Diagram of IEEE-39 bus system with DFIGs.

selecting the excellent species group according to the results.

Step 5: Calculating the crossing probability and carry out the crossing operation; calculating the mutation probability and perform mutation operation;

Step 6: Recording the applied amount of various control variables, the increase amount of reactive power reserve margin, voltage and power and the increase of voltage stability margin calculated by the new species group;

Step 7: Making a judgment based on the three termination criteria in IGA. If any of the three criteria is met, continuing to step 8, or going back to step 2

Step 8: Outputting the minimum value imposed by the system control variables, reactive power reserve margin, voltage stability margin, and other state variable values.

6 The control strategy and simulation results

The IEEE 39-bus system depicted in Figure 5 is adopted to test the proposed analytical approach. The algorithm is simulated by using PSASP software and consists of ten synchronous generators, 39 buses interconnected by 46 lines, and 12 transformers. Five DFIGs with a rated capacity of 150 MW each are integrated at five different buses without replacing the existing conventional units connected to them. The five bus numbers are 19, 20, 23, 25, and 29, respectively.

TABLE 1 Comparison with the TGA and IGA at bus 12 after reactive power control.

	Results by TGA	Results by IGA
VSM (p.u)	0.189	0.201
Improved VSM	8%	19%
Convergence generation	66	41

In the simulation process, only the RPRs at DFIG buses are calculated. Line 6-11 is assumed to suffer a three-phase-short-circuited fault at 0.5 s and is tripped at 0.7s. The reactive power distribution and voltage level in the system are changed. Voltage at bus 12 falls to about 0.9 p.u. Because the active power reduction of wind farm and load shedding tend to cause frequency oscillation and economic losses, the weight of these related control variables is set to 50%, and the weight factor values of all shunt capacitors are set to 100%. The TGA and IGA are applied to the IEEE-39 bus system for multi-objective optimization comparison:

1) Parameter settings of TGA: population size is 50, evolutionary generation is 120, crossover probability Pc = 0.5, mutation probability Pm = 0.01, and the maximum allowable number of iterations is 120.

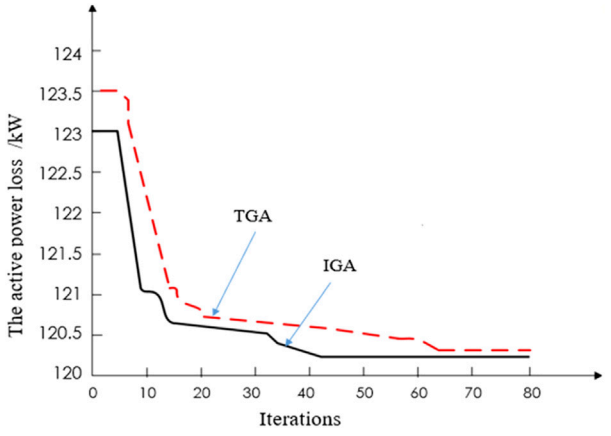

FIGURE 6
The relationship between the total active power loss and iterations when bus 12 is compensated.

2) Parameter setting of IGA: IGA is set according to the improved parameters used in (1). The initial population number is 50, the evolutionary generation is 120, the upper and lower limits of crossover probability are 0.9 and 0.6, and the upper and lower limits of mutation probability are 0.01 and 0.005.

The optimal solution obtained by the IGA and TGA is shunt capacitor compensation at bus 12 with 1.32 MVar. When the control is performed, Table 1 shows the comparison of VSM improvement and convergence generation between the TGA and IGA.

In Table 1, when the optimal solution is reached, the number of iterations of TGA is 66, while the number of iterations of IGA is 41, which is 25 times less than that of TGA, which indicates that IGA has a faster convergence speed. However, the VSM obtained by IGA is more than that by TGA. At the same time, the active power loss of the system (shown in Figure 6) is reduced from the initial value of 123 kw to 120.2 kw at the iteration ending.

Then the loads in the load buses are increased until some bus is first approaching the collapse point, it is shown in Figure 7 that the RPRs of all the DFIGs are significantly reduced with Generator 3, 4 consuming almost all the RPRs and losing their voltage regulating capability, thus forming the critical RPRs and their minimum limits. To improve the critical RPRs, three kinds of control measures are investigated.

6.1 Reduce the active power output of the DFIG

According to the sensitivity data in Table 2, the reduction of the active power output can improve the RPR itself. The improvement is due to a significant increase in the amount of reactive power production. Moreover, reducing active power production tends to slightly improve the RPRs of the nearby units. In this case, the active power outputs P_{g_3} and P_{g_4} at DFIG 3 and DFIG 4 are regulated: the lower limits for those control variables are assumed to be 0 MW. To observe the control effect, the active power outputs of both DFIG are set to 0.1 MW and the variations of the RPRs are shown in Figure 8. It can be seen that when the active power outputs at DFIG3 and DFIG4 are reduced to 0.1 MW, the reactive power reserve margin increases from 32.3 MVar to 51 MVar and from 30.1 Mvar to 44.1MVar, respectively. At the same time, the reactive power reserves of other DFIGs are also slightly increased. However, output reduction of active power leads to economic losses and may not be the best way to enhance the critical RPRs of DFIG.

6.2 Installation of the shunt capacitors

Shunt capacitors with low investment cost are the most common equipment to compensate reactive power and play an important role to achieve desirable voltage stability margin. The values of sensitivity in Table 2 show the improvement of reactive power reserves. The shunt capacitors are installed on the buses 4, 7,

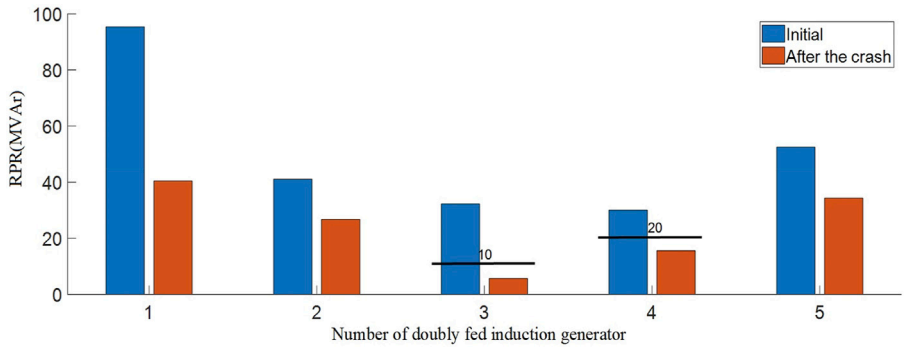

FIGURE 7
The change of RPR after the collapse.

TABLE 2 sensitivity of rpr for three control measures.

	Active power of the DFIG					Shunt capacitor						Load shedding						
	ΔP_{g_1}	ΔP_{g_2}	ΔP_{g_3}	ΔP_{g_4}	ΔP_{g_5}	ΔB_4	ΔB_7	ΔB_8	ΔB_{12}	ΔB_{15}	ΔB_{18}	ΔP_{l_4}	ΔQ_{l_4}	ΔP_{l_8}	ΔQ_{l_8}	$\Delta P_{l_{15}}$	$\Delta Q_{l_{15}}$	$\Delta P_{l_{16}}$	$\Delta Q_{l_{16}}$
Q_{r_1}	−1.32	−0.08	−0.13	−0.11	−0.02	0.89	0.38	0.97	0.29	1.22	1.17	−0.43	−1.80	−0.54	−1.20	−0.18	−1.20	−0.09	−1.50
Q_{r_2}	0.00	−1.08	−0.14	−0.12	−0.02	1.18	0.12	1.14	0.08	1.58	1.49	−0.42	−1.30	−0.65	−1.50	−0.03	−2.80	−0.18	−1.61
Q_{r_3}	0.00	−0.08	−1.60	−0.11	−0.03	1.53	0.29	1.82	0.16	2.53	2.39	−0.75	−1.60	−0.92	−1.17	−0.09	−1.40	−0.39	−1.25
Q_{r_4}	0.00	−0.06	−0.13	−1.22	−0.01	0.43	0.17	0.53	0.08	0.75	0.71	−0.19	−1.50	−0.31	−1.23	−0.06	−1.30	−0.16	−1.82
Q_{r_5}	0.00	−0.05	−0.15	−0.13	−1.31	1.66	0.52	1.88	0.05	2.44	2.32	−0.79	−1.58	−1.09	−1.60	−0.26	−0.80	−0.08	−0.30

8, 12, 15, and 18 and the maximum allowable shunt capacitance is limited to 20MVar. Improvements in RPRs are presented in Figure 9.

6.3 Load shedding

Although load shedding is not often recommended, it can be used as the last resort to maintain the power balance and prevent voltage collapse. In the IEEE-39 bus system, the loads at buses 4, 7, 8, 15, and 16 are shed with a constant power factor. The control effect of load shedding is presented in Figure 10. It is shown that when the reactive load at bus 15 is removed, the reactive power reserve margin of DFIG 3 is increased from 32.3 MVar to 47.4 MVar.

After each control variable is analyzed, all control variables will be tested together in a linear optimization problem and a few iterations are needed to achieve all imposed requirements. As mentioned before, the overall system VSM is linearly related to the sum of critical RPRs, and the value of the parameter k is 0.3112 by using the change of VSM to divide the sum of all the changes of critical RPRs.

Because generation shedding and load shedding can lead to frequency oscillations and economic losses, the weights associated with those variables are set to 50%, whereas the values of the weight factor of all shunt capacitors are still set to 1.0. To meet the requirements of RPRs and the limitation of VSM at the same time, two rounds of control measures have been implemented and the control actions for each round are shown in Table 3. According to the sensitivity priority, although 19 control variables are considered, only 14 control variables work to improve the VSM. Remarkably, there is a significant augment of reactive compensation on bus 18 and load shedding on buses 4 and 15. After iterations, when all the critical RPRs and control variables limits are met, the total amount of VSM is increased from 50.048 MW to 59.9896MW, with an increase of 19.9% as shown in Figure 11. In this process, the active power at the load is gradually increased and the active power of the DFIG is reduced, although this will slightly reduce voltage value at bus 12, it will be maintained at an appropriate stable value. The load center is often where the demand for reactive power is large. The implementation of reactive power compensation among the load center can effectively reduce the transmission of long distances of reactive power flow on the line, which has a direct and obvious effect on reducing the line loss. According to the principle of local balance of reactive power, buses 4, 7, 8, 12, 15, and 16 are determined as the compensation points. As seen from Figure 12, by applying control measures on the local key buses, not only the voltage stability of these key vulnerable buses is significantly improved, but also the voltage stability of the whole system is improved to a certain extent.

Table 4 shows the comparison of improved voltage stability between the TGA and the IGA. Because the intersection rate and variation rate of the traditional genetic algorithm remains constant, the convergence speed of the algorithm is slow, and the problem of premature convergence often occurs. To solve this problem, the modified adaptive genetic algorithm is adopted. When the optimization process falls into the trend of the local optimal solution, the intersection rate and variable rate are increased and when the group tends to diverge in the solution space, the

10.3389/fenrg.2022.1088563

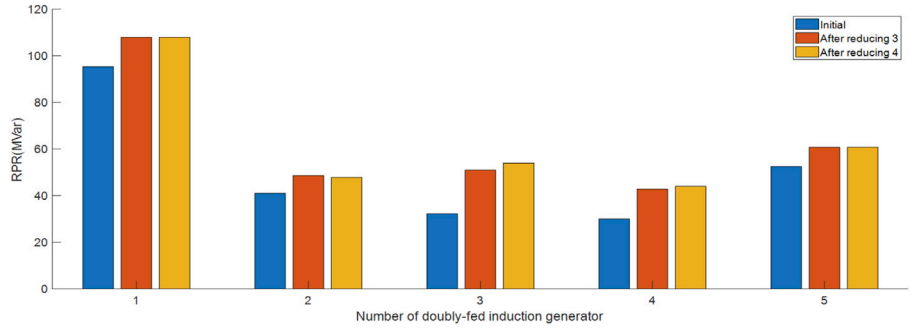

FIGURE 8
The effect of power generation reduction on RPR.

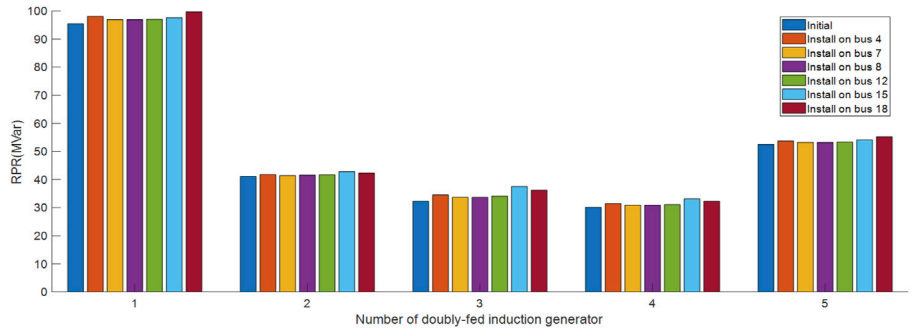

FIGURE 9
The effect of shunt capacitors on RPR.

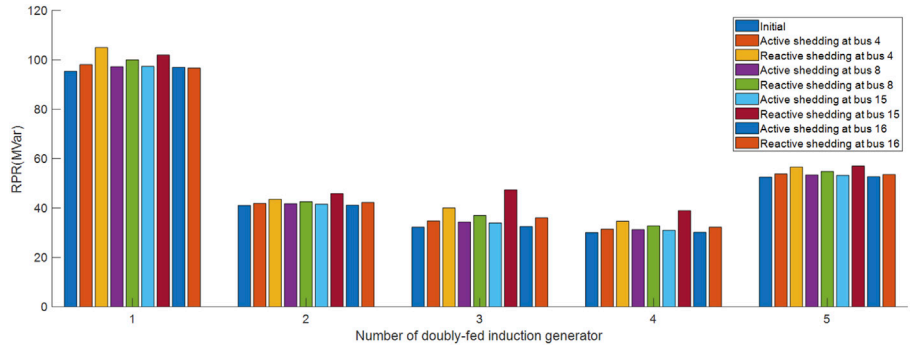

FIGURE 10
The effect of load shedding on RPR.

TABLE 3 The minimum quantity of control variable.

	ΔP_{g_3}	ΔP_{g_4}	ΔB_4	ΔB_7	ΔB_8	ΔB_{12}	ΔB_{15}	ΔB_{18}	ΔP_{l_4}	ΔQ_{l_4}	ΔQ_{l_8}	$\Delta Q_{l_{15}}$	$\Delta P_{l_{16}}$	$\Delta Q_{l_{16}}$
Round 1 (p.u.)	−0.187	−0.167	0.362	0.372	0.369	0.258	0.443	0.462	−0.057	−0.203	−0.065	−0.102	−0.026	−0.075
Round 2 (p.u.)	−0.022	−0.096	0.035	0.008	0.059	0.103	0.002	0.006	−0.003	−0.008	−0.009	−0.023	−0.005	−0.019
Total (p.u.)	−0.209	−0.263	0.397	0.380	0.428	0.361	0.445	0.468	−0.060	−0.211	−0.074	−0.125	−0.031	−0.094

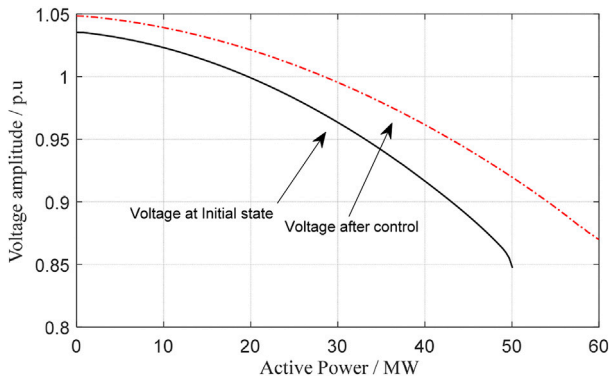

FIGURE 11
VSM enhancement after the minimum control is applied.

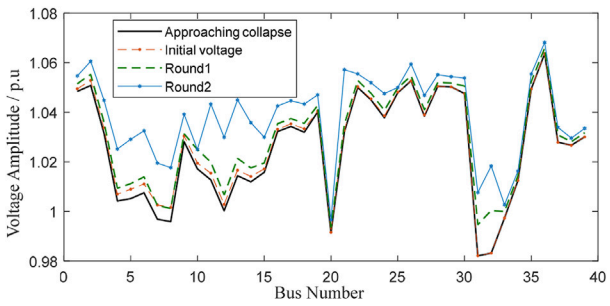

FIGURE 12
Bus Voltage enhancement after two rounds of control.

TABLE 4 Effect of Control measures on Voltage Stability margin of fragile bus.

Bus number	VSM/p.u (Initial)	VSM/p.u (TGA)	VSM/p.u (IGA after round 1)	VSM/p.u (IGA after round 2)
BUS 4	0.147	0.162	0.161	0.170
BUS 7	0.218	0.229	0.234	0.250
BUS 8	0.210	0.218	0.225	0.244
BUS 12	0.173	0.189	0.187	0.201
BUS 15	0.202	0.223	0.232	0.250
BUS 16	0.160	0.183	0.189	0.224

intersection rate and variation rate are reduced. The simulation results show that the total CPU time for IGA to calculate the two rounds of control measures for the IEEE-39 Bus system is approximately 15 s while the running time of the TGA is 32 s. The total time estimates include the PV curve, sensitivity, and optimization calculations.

7 Conclusions

In this paper, a method based on convex quadratic programming is proposed to coordinate different reactive power reserves for improved voltage stability margin of the power system with DFIG wind farms.Built upon the control mechanism of reactive power reserve in a doubly-fed induction generator, three main control measures, i.e., DGIG control, shunt capacitor banks, and load shedding, are proposed and compared to improve the RPRs to maintain system voltage stability and the results show that the reduced power generation of DGIG can both improve its reactive power reserve and the RPR of the other units, which makes it more suitable to provide the reactive power reserves for voltage stability.To fully unlock the value of the DGIG wind farms, the sensitivity method is used to detect and remove the unnecessary control variables, which further reduces the dimension and complexity of the convex quadratic programming problem for voltage control. The improved genetic algorithm is used to solve the proposed convex quadratic programming problems. Compared with the traditional genetic algorithm, the IGA has a shorter operation time without sacrificing the accuracy of the results. Further research should be focused on implementing additional control variables and applying them to larger networks.

Data availability statement

The original contributions presented in the study are included in the article/supplementary material, further inquiries can be directed to the corresponding author.

Author contributions

QL is responsible for the whole idea and the deduction of the method; YS is responsible for the simulation; YJ is responsible for the algorithm verification,English writing and improvements; YX is responsible for the modify the thoery analysis of CVC; SC is responsible for the verification and analysis of the simulation.

Conflict of interest

The authors declare that the research was conducted in the absence of any commercial or financial relationships that could be construed as a potential conflict of interest.

Publisher's note

References

De, M., and Goswami, S. (2014). Optimal reactive power procurement with voltage stability consideration in deregulated power system. *IEEE Trans. Power Syst.* 29 (5), 2078–2086. doi:10.1109/tpwrs.2014.2308304

Ding, T., Liu, S., Yuan, W., Bie, Z., and Zeng, B. (2016). A two-stage robust reactive power optimization considering uncertain wind power integration in active distribution networks. *IEEE Trans. Sustain. Energy* 7 (01), 301–311. doi:10.1109/tste.2015.2494587

Dong, F., Chowdhury, B. H., Crow, M. L., and Acar, L. (2005). Improving voltage stability by reactive power reserve management. *IEEE Trans. Power Syst.* 20 (01), 338–345. doi:10.1109/tpwrs.2004.841241

El-Araby, E. S. E., and Yorino, N. (2018). Reactive power reserve management tool for voltage stability enhancement. *IET Generation, Transm. Distribution* 12 (8), 1879–1888. doi:10.1049/iet-gtd.2017.1356

Gabash, A., and Li, P. (2012). Active-reactive optimal power flow in distribution networks with embedded generation and battery storage. *IEEE Trans. Power Syst.* 27 (4), 2026–2035. doi:10.1109/tpwrs.2012.2187315

Ghosh, S., Isbeih, Y., Bhattarai, R., Mohamed, S., Ehab, F. E., and Sukumar, K. (2020). A dynamic coordination control architecture for reactive power capability enhancement of the DFIG-based wind power generation. *IEEE Trans. Power Syst.* 35 (04), 3051–3064. doi:10.1109/tpwrs.2020.2968483

Grudinin, N. (1998). Reactive power optimization using successive quadratic programming method. *IEEE Trans. Power Syst.* 13 (4), 1219–1225. doi:10.1109/59.736232

Han, T., Chen, Y., Ma, J., Zhao, Y., and Chi, Y. (2018). Surrogate modeling-based multi-objective dynamic VAR planning considering short-term voltage stability and transient stability. *IEEE Trans. Power Syst.* 33 (1), 622–633. doi:10.1109/tpwrs.2017.2696021

Hu, B., Niu, T., Li, F., Xie, K., Li, W., and Jin, H. (2021). Dynamic var reserve assessment in multi-infeed LCC-HVDC networks. *IEEE Trans. Power Syst.* 36 (01), 68–80. doi:10.1109/tpwrs.2020.3008491

Huang, S., Wu, Q., Zhao, J., and Liao, W. (2020). Distributed optimal voltage control for VSC-hvdc connected large-scale wind farm cluster based on analytical target cascading method. *IEEE Trans. Sustain. Energy.* 11 (04), 2152–2161. doi:10.1109/tste.2019.2952122

Ibrahim, T., Tomas Rubira, T., Rosso, A., Patel, M., Guggilam, S., and Mohamed, A. (2022). Alternating optimization approach for voltage-secure multi-period optimal reactive power dispatch. *IEEE Trans. Power Syst.* 37 (5), 3805–3816. doi:10.1109/tpwrs.2021.3133358

Jankowski, R., Kosmecki, M., and Kubanek, A. (2017). Novel voltage stability assessment method based on reactive power reserve measurements[C]//Proceedings of the 2017 11th IEEE International Conference on Compatibility, Power Electronics and Power Engineering (CPE-POWERENG). IEEE, Cadiz, Spain 65–70.

Leonardi, B., and Ajjarapu, V. (2012). An approach for real time voltage stability margin control via reactive power reserve sensitivities. *IEEE Trans. power Syst.* 28 (2), 615–625. doi:10.1109/tpwrs.2012.2212253

Li, Y., Zhao, J., Liu, Z., Li, P., Zhang, X., and Tang, X., (2013). Proceedings of the IEEE international conference of IEEE region 10 TENCON 2013). IEEE, 1–4. Xi'an, China. Assessment method of dynamic reactive power valuation for transient voltage stability.

Ma, H., Wang, G., Gao, X., Zou, Z., and Dong, Y. (2022). An adaptive voltage control using local voltage profile mode and similarity ranking. *Front. Energy Res.* 10, 1–12. doi:10.3389/fenrg.2022.865151

Mugemanyi, S., Qu, Z., Rugema, F., Dong, Y., Bananeza, C., and Wang, L. (2020). Optimal reactive power dispatch using chaotic bat algorithm. *IEEE ACCESS* 8, 65830–65867. doi:10.1109/access.2020.2982988

Oliveira, R. A., and Bollen, M. H. J. (2022). Susceptibility of large wind power plants to voltage disturbances–recommendations to stakeholders. *J. Mod. Power Syst. Clean Energy* 10 (2), 416–429. doi:10.35833/mpce.2020.000543

Ouyang, J., Tang, T., Yao, J., and Li, M. (2019). Active voltage control for DFIG-based wind farm integrated power system by coordinating active and reactive powers under wind speed variations. *IEEE Trans. Energy Convers.* 34 (3), 1504–1511. doi:10.1109/tec.2019.2905673

Park, B., Im, S., Kim, D., and Lee, B. (2021). Clustered effective reactive reserve to secure dynamic voltage stability in power system operation. *IEEE Trans. Power Syst.* 36 (2), 1183–1192. doi:10.1109/tpwrs.2020.3020119

Qinyu, B., Lin, Y., Jiayi, M., Lu, T., and Youyin, W. (2018). Proceedings of the China international conference on electricity distribution (CICED). IEEE,Tianjin, China 2029–2033.Analysis of influence with connected wind farm power changing and improvement strategies on grid voltage stability

Ren, X., Wang, H., Wang, Z., Wang, Q., Li, B., Wu, H., et al. (2022). Reactive voltage control of wind farm based on tabu algorithm. *Front. Energy Res.* 10, 1–8. doi:10.3389/fenrg.2022.902623

Sissine, F. (2007). *Energy independence and security act of 2007: A summary of major provisions*. Washington, DC, USA: Congressional Research Service, the Library of Congress.

Sun, Q., Cheng, H., and Song, Y. (2017). Bi-objective reactive power reserve optimization to coordinate long-and short-term voltage stability. *IEEE Access* 6, 13057–13065. doi:10.1109/access.2017.2701826

Zhang, K., Geng, G., and Jiang, Q. (2020). Online tracking of reactive power reserve for wind farms. *IEEE Trans. Sustain. Energy* 11 (2), 1100–1102. doi:10.1109/tste.2019.2929673

frontiers | Frontiers in Energy Research

TYPE Original Research
PUBLISHED 10 January 2023
DOI 10.3389/fenrg.2022.1115146

OPEN ACCESS

EDITED BY
Di Cao,
University of Electronic Science and Technology of China, China

REVIEWED BY
Tianhua Zhu,
Aalborg University, Denmark
Bo Chen,
Tianjin University, China
Changkun Du,
Beijing Institute of Technology, China

*CORRESPONDENCE
Shuhuai Shi,
shishuhuai@126.com

SPECIALTY SECTION
This article was submitted to Process and Energy Systems Engineering, a section of the journal Frontiers in Energy Research

RECEIVED 03 December 2022
ACCEPTED 23 December 2022
PUBLISHED 10 January 2023

CITATION
Shi S, Du J, Xia B, Xia D, Guan H and Wang F (2023), Research on optimum extended phase-shift control with minimum peak-to-peak current of DAB converter applied to small DC power grid.
Front. Energy Res. 10:1115146.
doi: 10.3389/fenrg.2022.1115146

Research on optimum extended phase-shift control with minimum peak-to-peak current of DAB converter applied to small DC power grid

Shuhuai Shi[1]*, Junli Du[1], Binbing Xia[2], Dawei Xia[1], Honglu Guan[1] and Feng Wang[2]

[1]State Grid Henan Electric Power Research Institute, Zhengzhou, China, [2]School of Electrical Engineering, Xi'an Jiaotong University, Xi'an, China

The Dual Active Bridge (DAB) DC-DC converter has the ability of bidirectional power transmission and the modulation scheme that is easy to implement, which can ensure the efficient transmission of energy in the system. Therefore, it is often used in various scenarios of small DC grid, such as energy storage, photovoltaic system, electric vehicle charging and so on. The main methods to improve the efficiency of dual active bridge include reducing the effective value of current and widening the soft switching area. Based on the above idea, an optimized extended phase-shift (EPS) modulation strategy is proposed in this paper. The modulation strategy achieves the goal of reducing the effective value of the current through the constraint optimization of the corresponding variables, and then improves the efficiency of the converter. In this paper, the working principles of several typical modulation strategies are introduced in detail, and then the power characteristics and soft-switching characteristics of the new method and other commonly used modulation schemes are analyzed and compared. Finally, the effectiveness of the optimization method for extended phase-shift modulation strategy is verified by the dual active bridge experimental prototype.

KEYWORDS

dual-active-bridge converter, efficiency, soft switching, modulation strategy, constrained optimization

1 Introduction

Simple equipment structure and strong ability to connect different distributed generations (Marquardt, 2010; Lin et al., 2016; Liu et al., 2020). In DC distributed energy generation system, DC/DC converters connect different DC voltage buses and renewable resources (Xiong et al., 2015; Zhao et al., 2015; Liu et al., 2022a). Therefore, its performance determines the economy, reliability and stability of the whole DC distribution system (Cornea et al., 2017; Pannala et al., 2020; Xiong et al., 2022).

However, the duty cycle of the trigger pulse under phase-shift modulation is fixed, which increases the difficulty of adjusting the soft switching region. Therefore, reference (Xu et al., 2004; Inoue and Akagi, 2007; Park and Choi, 2014; Chen et al., 2017; Li and Shi, 2019) proposed an asymmetric duty cycle modulation (ADM) scheme with duty cycle as the control variable. Compared with phase-shift modulation, ADM control significantly reduces the current stress and expands the soft-switching range, and its advantages are more obvious when the input voltage does not match the output voltage (Xie et al., 2014; Khan et al., 2015; Hou and Li, 2021; Quan et al., 2022). In addition, ADM control can

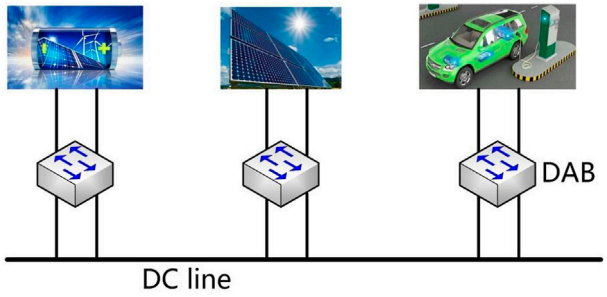

FIGURE 1
The DAB converter applied to small DC power grid topology.

also be applied to other DC converters, such as double-active half-bridge and three-phase double-active bridge (Kim et al., 2009; Ngo et al., 2012; Chakraborty and Chattopadhyay, 2018; Huang et al., 2019). However, the ADM control contains only two degrees of freedom, which limits the flexibility of the control (Xiong et al., 2021; Zhou et al., 2021; Liu et al., 2022b).

In order to further reduce the current stress characteristics and expand the soft switching region, and then improve the efficiency of DAB, anoptimized EPS modulation scheme is proposed to further reduce the current stress and widen soft-switching range. Firstly, the multi-duty modulation is introduced in detail, including the working principle, typical working waveform and steady-state characteristics. Then, based on MATLAB simulation, the optimization of the current RMS is realized. After that, the comprehensive performance of multi-duty modulation and other traditional modulation methods of DAB is compared, including current RMS, peak current and soft switching characteristics. Finally, a DAB experimental prototype is built, and the effectiveness of the proposed method is verified by experiments.

2 Dual active bridge DC/DC converter

2.1 Operation principle of dual active bridge DC-DC converter

The typical structure of DAB converter in small DC power grid is shown in Figure 1. A typical configuration of the basic structure of topology of the DAB converter is shown in Figure 2, mainly comprising two symmetrical full bridges, an inductor L and a high frequency transformer. The ratio of the transformer is n. The two symmetrical full-bridges are composed of IGBT switches and its corresponding anti-parallel diodes, so they have the advantage of bidirectional energy transmission ability. V_1 and V_2 are the input and output voltages of the converter, respectively. V_{H1} and V_{H2} are the AC equivalent voltages on the primary and secondary sides of the high-frequency transformer, respectively. The voltage matching ratio k is defined herein as follows.

$$k = \frac{V_1}{nV_2} \tag{1}$$

According to the voltage matching ratio k and the transmission power P of the converter, the operation modes of the DAB converter can be divided into the following four types.

1) $k > 1$, $p > 0$: Forward Boost Transfer Mode. 2) $k < 1$, $p > 0$: Forward Buck Transfer Mode. 3) $k > 1$, $p < 0$: Reverse boost transfer model. 4) $k < 1$, $p < 0$: Reverse Buck Transfer Mode.

2.2 Fundamentals of extended phase-shift modulation

The modulation optimization strategy of DAB converter mainly focuses on the modulation scheme and the optimization objective function. The modulation scheme determines the operation mode and steady state of the DAB converter. The selection of the optimization target is closely related to the optimization effect and the implementation method. Therefore, the basic principle and typical operation waveforms of EPS modulation are introduced in this section.

Under the control of EPS, the primary H-bridge is modulated with an inner phase-shift ratioD_1 which is between Q_1 and Q_4, and the secondary H-bridge is modulated by SPS. D_2 is the external phase shift ratio between IGBT Q_1 and Q_5.

Figure 3 shows the four typical operating waveforms under EPS modulation schemes and device conduction interval without direct power transfer. Figure 3 also shows the AC equivalent waveforms V_{H1} and V_{H2}, the inductor current i_L waveform, and the trigger pulse waveform of the switch tube in two typical working modes under the control of EPS. When the voltage conversion ratio $k > 1$ ($k < 1$), DAB works in buck (boost) mode. The equations of transmission power are expressed as follows.

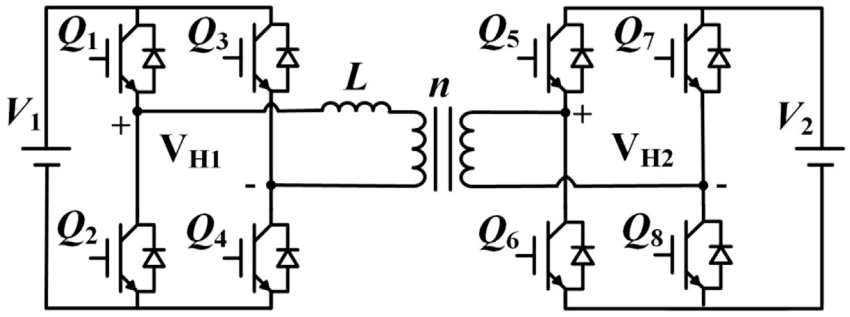

FIGURE 2
The typical topology of DAB converter.

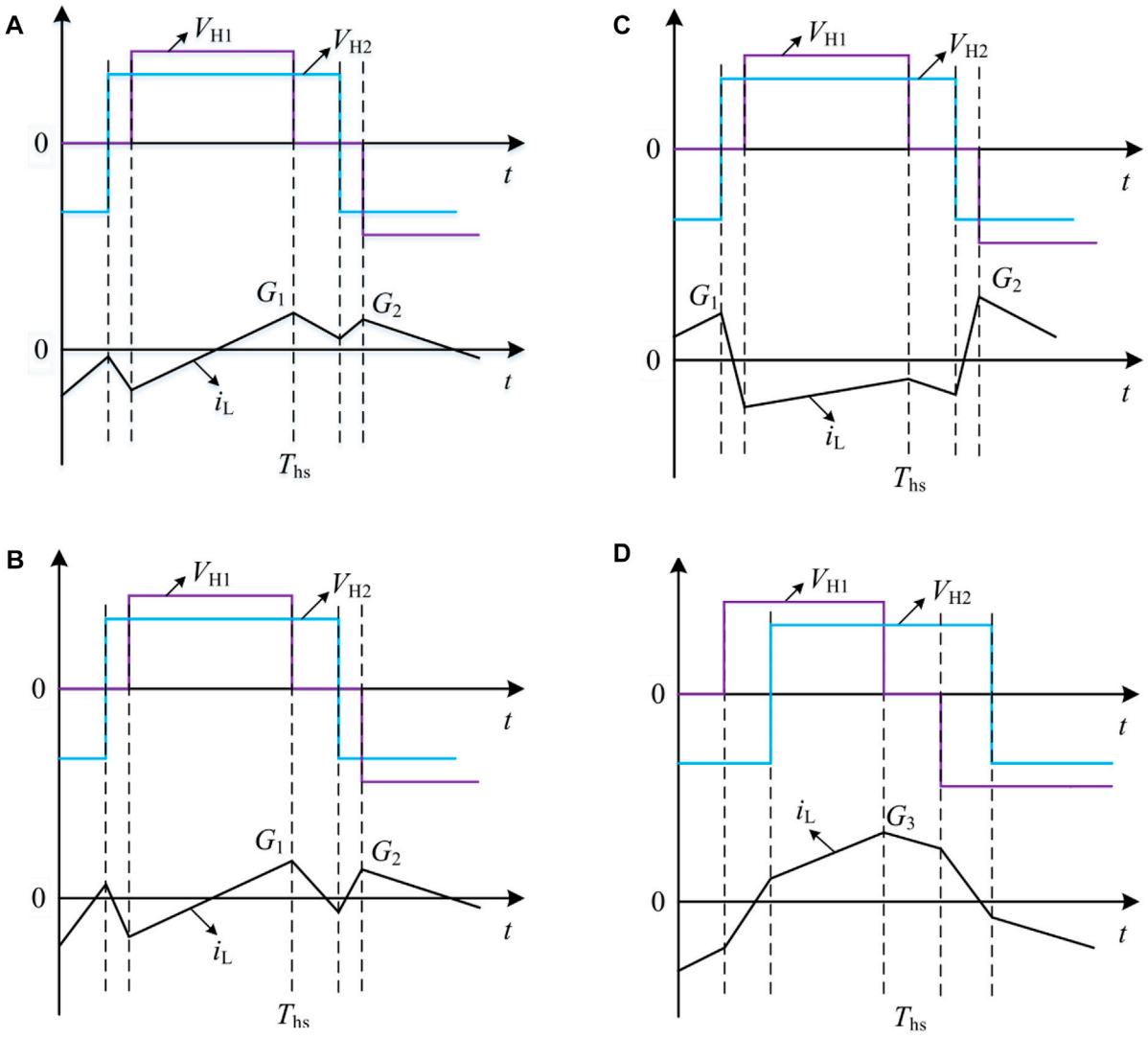

FIGURE 3
The operation waveform for EPS modulation of DAB converter: **(A)** EPS mode A; **(B)** EPS mode B; **(C)** EPS mode C; **(D)** EPS mode D.

$$P = \frac{1}{T_{hs}} \int_0^{T_{hs}} V_{h1} i_L dt = \frac{nV_1V_2}{4f_sL}(1 - D_1)(2D_2 - D_1) \quad (2)$$

$$P = \frac{1}{T_{hs}} \int_0^{T_{hs}} V_{h1} i_L dt = \frac{nV_1V_2}{4f_sL}\left(-D_1^2 + 2D_1D_2 - D_1 - 2D_2^2 + 2D_2\right) \quad (3)$$

The reference transmission power can be defined as follows.

$$P = \frac{nV_1V_2}{8f_sL} \quad (4)$$

3 Optimized EPS modulation strategy

Determining the optimization objectives and constraints of EPS control, this paper takes EPSoperating mode 2 as an example to analyze soft-switching characteristics and corresponding optimizations.

The ZVS condition is important to reduce switching losses. The ZVS of each IGBT depends on the current direction at each switching instant. In EPS Mode 2, all devices can achieve ZVS. Figure 4 shows a detailed analysis of ZVS in EPS operating mode 2.

In this paper, the RMS current is taken as the optimization target to further reduce the device loss and copper loss. EPS control contains two control degrees of freedom (D_1–D_2) and its optimization is also restricted by power level P and voltage matching ratio k, which increases the difficulty of current RMS optimization, and also makes the traditional optimization methods such as derivation method and Lagrange multiplier method no longer applicable. Therefore, the optimization of the effective value of the current under EPS control needs to be realized by means of a reasonable optimization algorithm.

For EPS control, the optimization objective is to minimize the current effective value, where the current effective value is expressed as follows, where the voltage matching ratio k is a given value, and the duty cycles D_1–D_2 are the quantities to be solved.

$$i_{RMS}^2 = i(D_1, D_2, k, P) \quad (5)$$

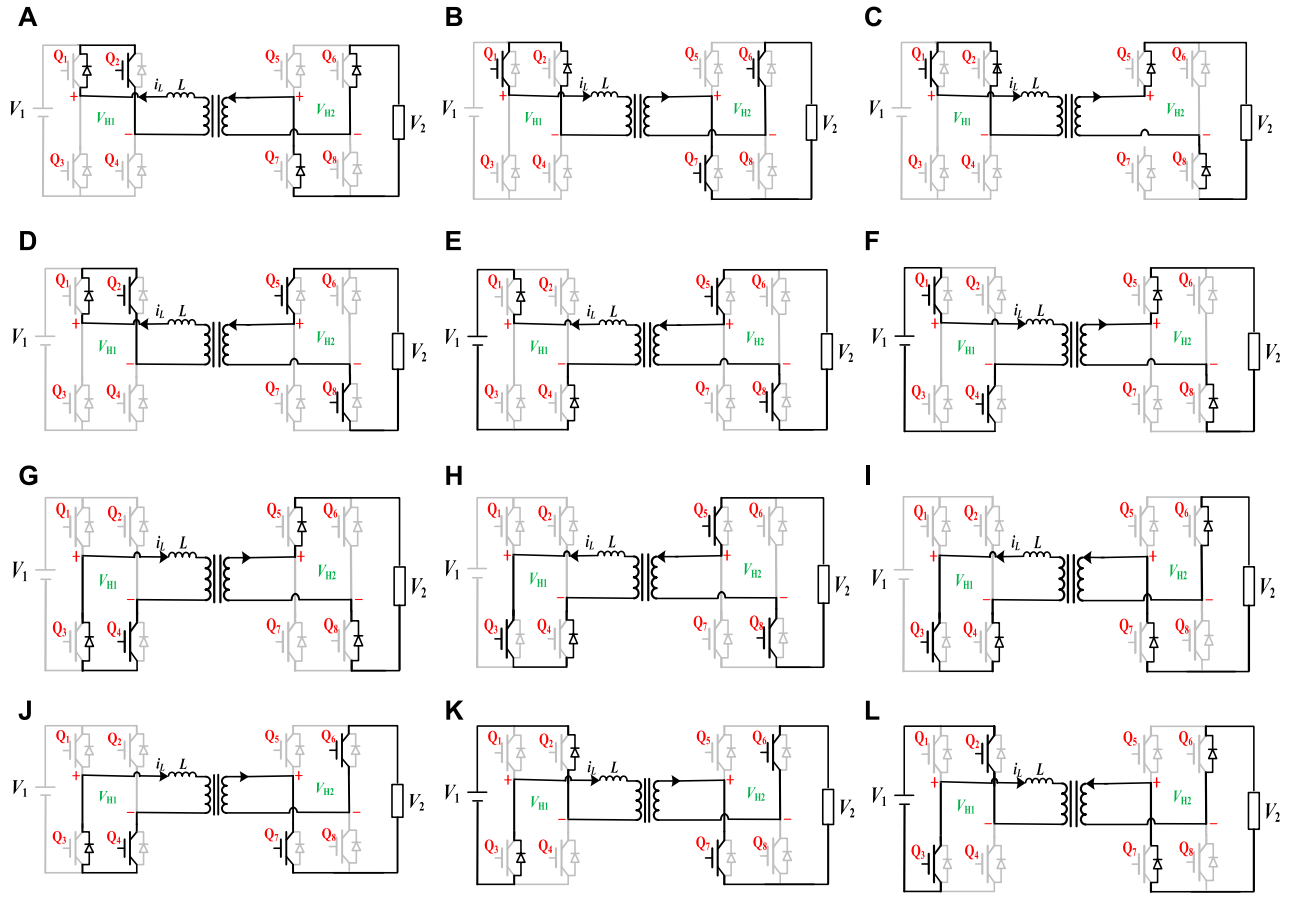

FIGURE 4
The circuit configuration of detailed ZVS analysis under optimized EPS mode: **(A)** period 1 from t0 to t1; **(B)** period 2 from t1 to t2; **(C)** period 3 from t2 to t3; **(D)** period 4 from t3 to t4; **(E)** period 5 from t4 to t5; **(F)** period 6 from t5 to t6; **(G)** period 7 from t6 to t7; **(H)** period 8 from t7 to t8; **(I)** period 9 from t8 to t9; **(J)** period 9 from t9 to t10; **(J)** period 10 from t10 to t11; **(K)** period 11 from t11 to t12; **(L)** period 12 from t12 to t13.

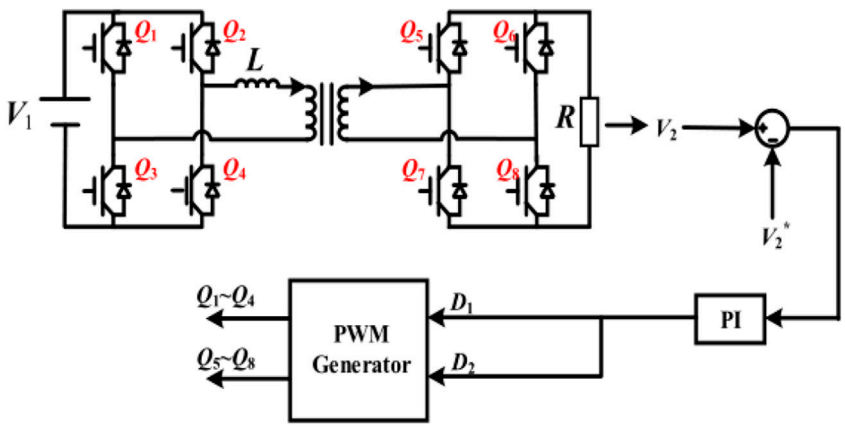

FIGURE 5
The control block diagram of DAB converter under optimized EPS control.

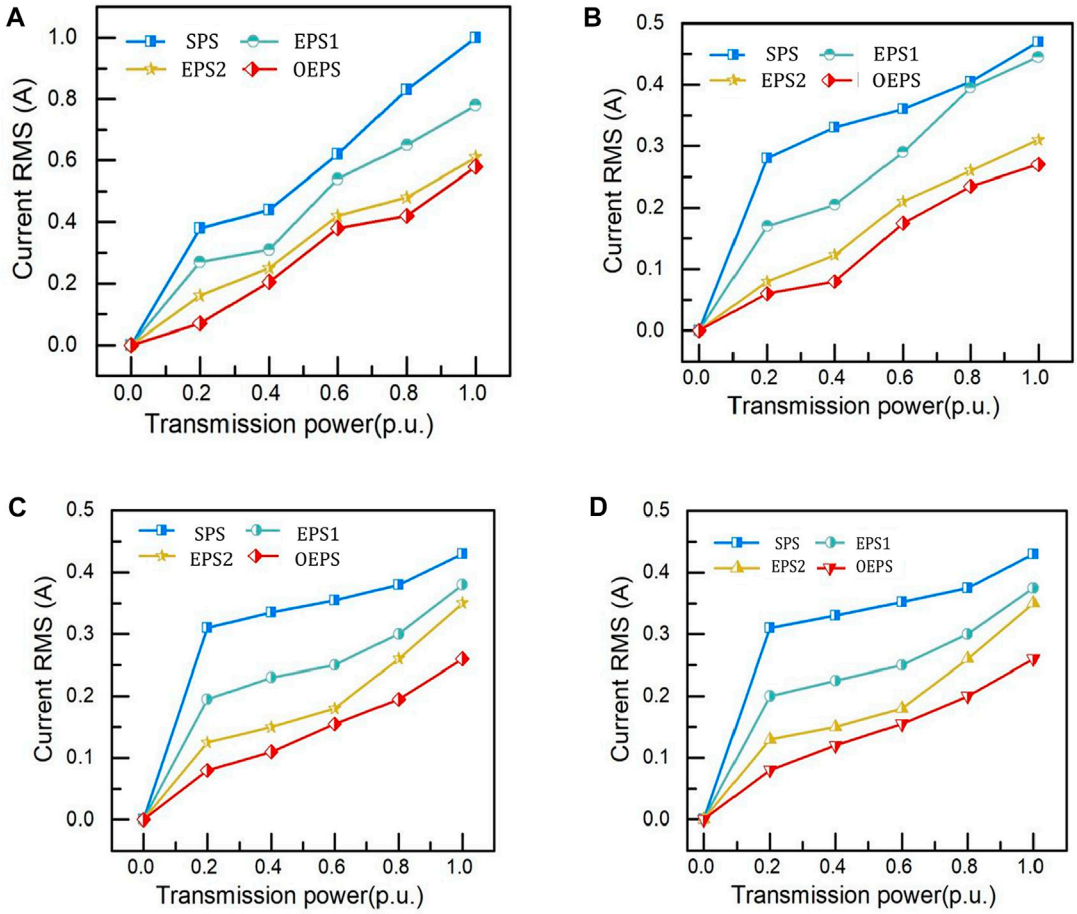

FIGURE 6
The Comparison of current RMS values under different modulation strategies and *k*: **(A)** *k* = .25; **(B)** *k* = .5; **(C)** *k* = 1; **(D)** *k* = 2.

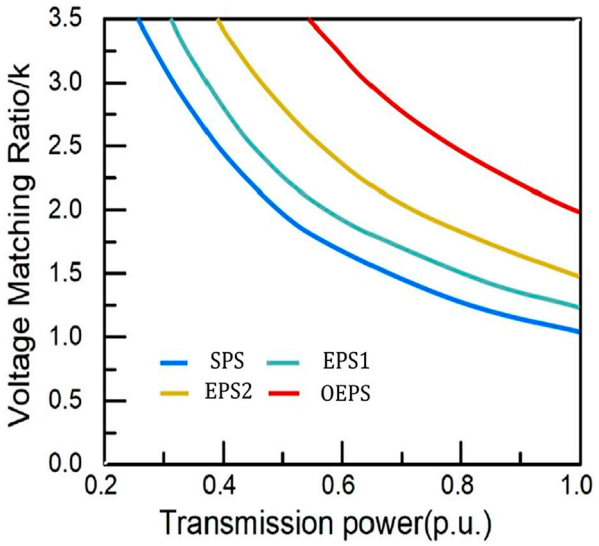

FIGURE 7
The soft-switching performance under different modulation schemes.

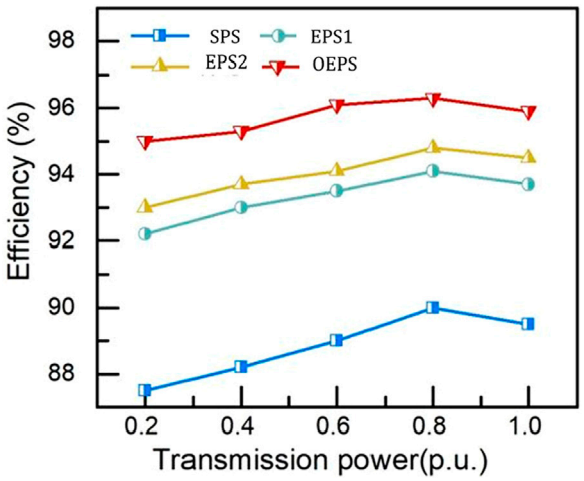

FIGURE 8
The efficiency comparison between different modulation schemes.

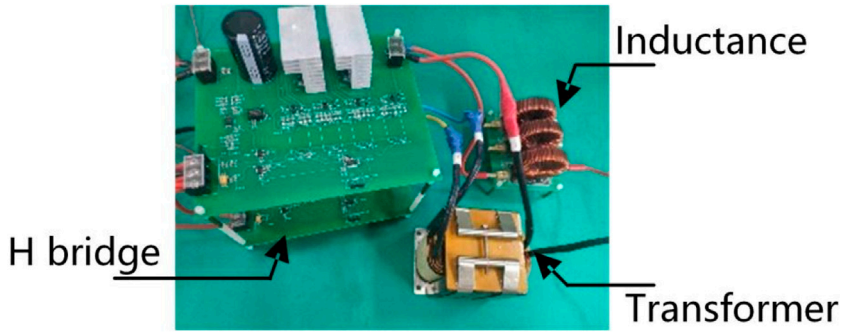

FIGURE 9
The DAB-based experimental prototype.

TABLE 1 Parameters of the DAB-based prototype.

Parameter	Inductor L	Switching frequency (kHz)	Input voltage (V)	Output voltage (V)
value	550uH	10	50	50

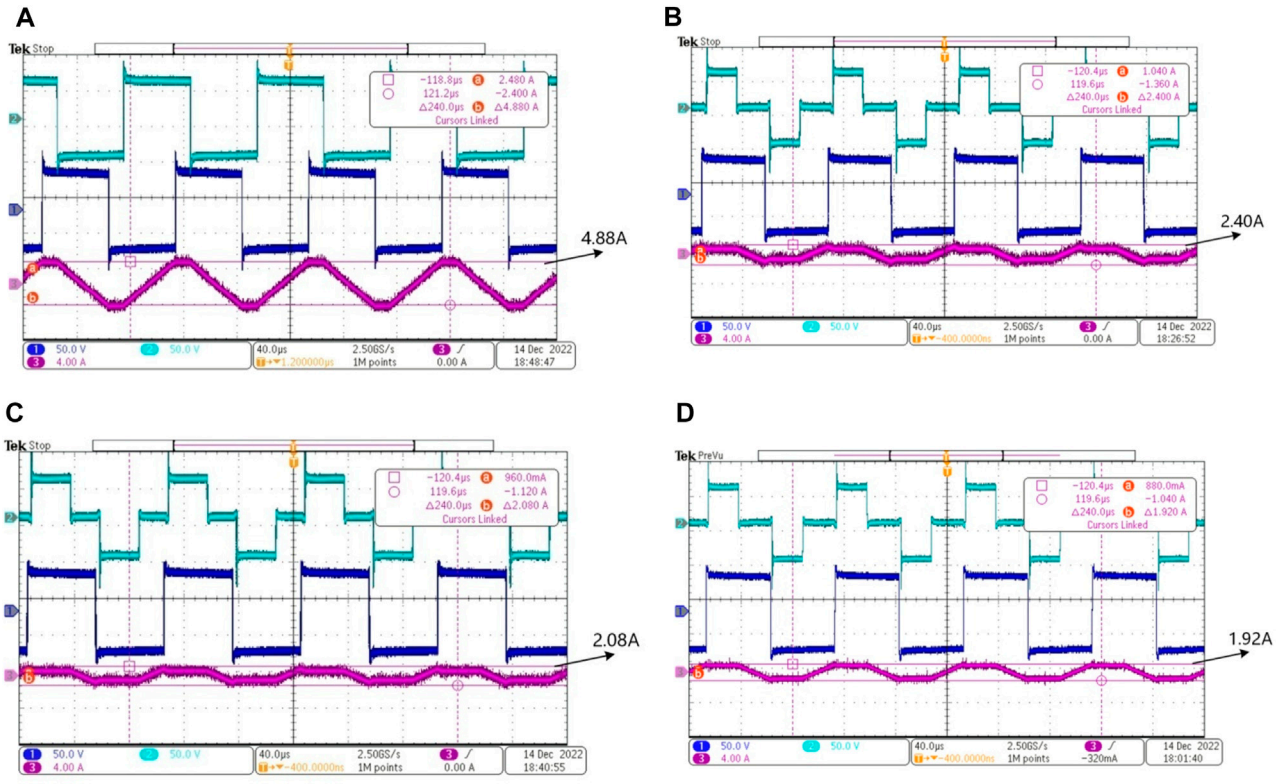

FIGURE 10
The waveform under different modulation schemes: **(A)** Optimized EPS; **(B)** EPS 1; **(C)** EPS 2; **(D)** SPS.

The switching loss of the switch tube includes turn-on loss and turn-off loss, and the reduction of the turn-on loss can be realized by optimizing the modulation method to make each device realize ZVS. The premise of ZVS is that the turn-on voltage of the device drops to 0 before the device is turned on. Therefore, if the diode is turned on before the switch tube is turned on, the ZVS of the IGBT can be realized. In EPS operating mode 1, all devices achieve ZVS.

Therefore, the current RMS optimization under EPS control has two non-equality constraints: boundary condition and ZVS.

TABLE 2 The lowest current stress with all semiconductors ZVS.

Modulation strategy	Minimum peak current (A)
SPS	4.88
EPS 1	2.40
EPS 2	2.08
Optimized EPS	1.92

(1) ZVS: Current direction at each switching instant.

$$eg:\ \mathrm{i}(t_1) < 0 \tag{6}$$

(2) Operation boundary in each operation mode. The current RMS optimization under EPS control also has the equality constraint that the transmission power should be equal to the given value of the transmission power, as shown in formula.

$$P = P_{\mathrm{ref}} \tag{7}$$

Figure 5 is a control block diagram of the DAB converter under the control of the EPS. And calculating the voltage matching ratio according to $V1$ and $V2$, performing constraint optimization calculation on the calculated duty ratio, and obtaining the duty ratios $D1$ and $D2$ according to k. Then according to the EPS modulation method proposed in this paper, the trigger signals of all IGBTs are obtained to make DAB operate normally.

4 Comparison of operating characteristics of different modulation strategies

In order to verify the effectiveness of the above theoretical analysis and the optimized EPS control, this paper compares the traditional SPS control, EPS control 1 andEPS control 2 and the optimizedEPS control under the same transmission power.

4.1 Current RMS comparison

Figures 6A–D, respectively show the distribution of the current effective value corresponding to different modulation strategies in the full power range under different voltage matching ratios. It can be seen that the current effective value under SPS control is the largest, and the current effective value is obviously larger under the matching ratio of light load and low voltage. Optimized EPS control proposed in this paper, EPS control 1 and EPS control 2 can effectively reduce the RMS current of the converter by increasing the modulation control variable. Among these modulation strategies, the optimized EPS modulation has the lowest effective control current in the whole power range.

4.2 Soft switching range comparison

The increase in switching losses may have a negative impact on the efficiency improvement and heat dissipation of the DAB converter. Widening the soft switching region of the converter is beneficial to eliminating the turn-on loss of the DAB switch tube, especially widening the ZVS region of all IGBTs. Figure 7 shows the soft switching regions of the above modulation strategy under different transmission power P and voltage matching ratios k. It can be seen from the figure that, compared with other modulation strategies, the ZVS region of all IGBT devices under optimized EPS control is the widest. Therefore, the optimized EPS control can extend the soft-switching range and effectively reduce the switching losses of the switches.

4.3 Efficiency comparison

The efficiency comparison of different modulation strategies is shown in Figure 8, from which it can be seen that the efficiency of the optimized EPS control method proposed in this paper is the highest in the full power range.

5 Experimental verification

The DAB converter test platform is shown in Figure 9. It consists of two symmetrical H-bridges, a high-frequency transformer, an inductor and a DSP controller. Table 1 shows the specific parameter values of the experimental platform, in which the transformation ratio of the high-frequency transformer is $n = 1$.

Figures 10A–D are experimental waveforms of optimized EPS control, SPS, EPS control 1, and EPS control 2, respectively, at a transmission power $p = .45$ (p.u.) with a voltage matching ratio $k = 1$. Table 2 lists the minimum values of the peak-to-peak current and the effective current of all device under different modulations. Based on the experimental results in Figure 10 and Table 2, it can be seen that, compared with the existing modulation methods, optimized EPS control proposed in this paper has better performance in terms of the expansion of the soft switching region and the reduction of the current effective value.

6 Conclusion

An optimized EPS modulation strategy is proposed in this paper, which can reduce the RMS current and broaden the soft-switching region, and then improve the efficiency of DAB converter. The optimized EPS modulation strategy uses the algorithm of constrained optimization for achieving the optimization goal of reducing the effective value of current. Compared with the traditional optimization methods, the proposed method has the advantages of low operation complexity and high optimization speed. The above results are verified by MATLAB simulation. Finally, based on the built DAB experimental platform, the RMS current, soft-switching range and efficiency of the proposed optimized EPS modulation strategy are compared with those of other commonly used modulation strategies. The comparison of multiple dimensions shows that the proposed optimized EPS modulation strategy can reduce the RMS current and improve the efficiency, and broaden the soft-switching range of the device. This method provides the

possibility for DAB converter to be applied in the scenario of high efficiency and high power density.

Data availability statement

The original contributions presented in the study are included in the article/supplementary material, further inquiries can be directed to the corresponding author.

Author contributions

SS and JD contributed to the conception of the study and performed the data analyses and wrote the manuscript. BX and HG performed the simulation validation. DX and FW contributed significantly to analysis and manuscript preparation.

Conflict of interest

Authors SS, JD, DX, and HG were employed by the company State Grid Henan Electric Power Research Institute.

The remaining authors declare that the research was conducted in the absence of any commercial or financial relationships that could be construed as a potential conflict of interest.

Publisher's note

References

Chakraborty, S., and Chattopadhyay, S. (2018). Fully ZVS, minimum RMS current operation of the dual-active half-bridge converter using closed-loop three-degree-of-freedom control. *IEEE Trans. Power Electron.* 33 (12), 10188–10199. doi:10.1109/TPEL.2018.2811640

Chen, Y., Zhang, N., Wang, K., Yang, J., and Kang, Y. (2017). A series resonant filament power supply with variable structure and oscillation-free switching strategy for high-voltage accelerator application. *IEEE Trans. Power Electron.* 32 (11), 8229–8236. doi:10.1109/TPEL.2017.2690800

Cornea, O., Andreescu, G-D., Muntean, N., and Hulea, D. (2017). Bidirectional power flow control in a DC microgrid through a switched-capacitor cell hybrid DC–DC converter. *IEEE Trans. Industrial Electron.* 64 (4), 3012–3022. doi:10.1109/TIE.2016.2631527

Hou, N., and Li, Y. (2021). Communication-free power management strategy for the multiple DAB-based energy storage system in islanded DC microgrid. *IEEE Trans. Power Electron.* 36 (4), 4828–4838. doi:10.1109/TPEL.2020.3019761

Huang, J., Li, Z., Shi, L., Wang, Y., and Zhu, J. (2019). Optimized modulation and dynamic control of a three-phase dual active bridge converter with variable duty cycles. *IEEE Trans. Power Electron.* 34 (3), 2856–2873. doi:10.1109/TPEL.2018.2842021

Inoue, S., and Akagi, H. (2007). A bidirectional DC–DC converter for an energy storage system with galvanic isolation. *IEEE Trans. Power Electron.* 22 (6), 2299–2306. doi:10.1109/TPEL.2007.909248

Khan, M. A., Ahmed, A., Husain, I., Sozer, Y., and Badawy, M. (2015). Performance analysis of bidirectional DC–DC converters for electric vehicles. *IEEE Trans. Industry Appl.* 51 (4), 3442–3452. doi:10.1109/TIA.2015.2388862

Kim, J., Jeong, I., and Nam, K. (2009). "Asymmetric duty control of the dual-active-bridge DC/DC converter for single-phase distributed generators," in 2009 IEEE Energy Conversion Congress and Exposition, San Jose, CA, USA, 20-24 Sept. 2009, 75–82.

Li, R., and Shi, F. (2019). Control and optimization of residential photovoltaic power generation system with high efficiency isolated bidirectional DC–DC converter. *IEEE Access* 7, 116107–116122. doi:10.1109/ACCESS.2019.2935344

Lin, W., Wen, J., Yao, L., and Yang, B. (2016). "Step-up unidirectional DC-DC autotransformer for HVDC applications," in Power Electronics and Motion Control Conference, Hefei, 22-26 May 2016, 703–707.

Liu, X., Grassi, F., Spadacini, G., and Pignari, S. A. (2020). Physically based modeling of hand-assembled wire bundles for accurate EMC Prediction. *IEEE Trans. Electromagn. Compat.* 62 (3), 914–922. doi:10.1109/TEMC.2019.2922455

Liu, X., Wu, B., and Xiu, L. (2022a). A fast positive-sequence component extraction method with multiple disturbances in unbalanced conditions. *IEEE Trans. Power Electron.* 37 (8), 8820–8824. doi:10.1109/tpel.2022.3161734

Liu, X., Xiong, L., Wu, B., Qian, Y., and Liu, Y. (2022b). Phase locked-loop with decaying DC transient removal for three-phase grids. *Int. J. Electr. Power & Energy Syst.* 143, 108508. doi:10.1016/j.ijepes.2022.108508

Marquardt, R. (2010). "Modular Multilevel Converter: An universal concept for HVDC-Networks and extended DC-Bus-applications," in Power Electronics Conference, Sapporo Japan, 21-24 June, 502–507. doi:10.1109/IPEC.2010.5544594

Ngo, T., Won, J., and Nam, K. (2012). "A single-phase bidirectional dual active half-bridge converter," in 2012 Twenty-Seventh Annual IEEE Applied Power Electronics Conference and Exposition Orlando, FL, USA, 05-09 February 2012, 1127–1133.

Pannala, S., Patari, N., Srivastava, A. K., and Padhy, N. P. (2020). Effective control and management scheme for isolated and grid connected DC microgrid. *IEEE Trans. Industry Appl.* 56 (6), 6767–6780. doi:10.1109/TIA.2020.3015819

Park, J., and Choi, S. (2014). Design and control of a bidirectional resonant DC–DC converter for automotive engine/battery hybrid power generators. *IEEE Trans. Power Electron.* 29 (7), 3748–3757. doi:10.1109/TPEL.2013.2281826

Quan, S., Su, S., and Zhao, N. (2022). Design method of dual active bridge based on the optimum efficiency. *J. Electr. Eng.* 17 (02), 56–64. doi:10.11985/2022.02.007

Xie, Y., Huang, J., Liu, X., Zhuo, F., Liu, B., Zhang, H., et al. (2014). "PV system modeling and a global-planning design for its controller parameters," in Proceedings of the IEEE Applied Power Electronics Conference and Exposition - APEC 2014, Fort Worth, TX, USA, 16-20 March 2014, 3132–3135.

Xiong, L., Zhuo, F., Liu, X., Wang, F., Chen, Y., Zhu, M., et al. (2015). "Research on fast open-loop phase locking scheme for three-phase unbalanced grid," in Proceedings of the 2015 IEEE Applied Power Electronics Conference and Exposition (APEC), 15-19 March 2015, 1672–1676.

Xiong, L., Liu, L., Liu, X., and Liu, Y. (2021). Frequency trajectory planning based strategy for improving frequency stability of droop-controlled inverter based standalone power systems. *IEEE J. Emerg. Sel. Top. Circuits Syst.* 11 (1), 176–187. doi:10.1109/JETCAS.2021.3052006

Xiong, L., Liu, X., Liu, Y., and Zhuo, F. (2022). Modeling and stability issues of voltage-source converter-dominated power systems: A review. *CSEE J. Power Energy Syst.* 8 (6), 1530–1549. doi:10.17775/CSEEJPES.2020.03590

Xu, D., Zhao, C., and Fan, H. (2004). A PWM plus phase-shift control bidirectional DC–DC converter. *IEEE Trans. Power Electron.* 19 (3), 666–675. doi:10.1109/TPEL.2004.826485

Zhao, B., Song, Q., Liu, W., and Zhao, Y. (2015). Universal high-frequency-link characterization and practical fundamental-optimal strategy for dual-active-bridge DC-DC converter under PWM plus phase-shift control. *IEEE Trans. Power Electron.* 30 (12), 6488–6494. doi:10.1109/TPEL.2015.2430934

Zhou, L., Gao, Y., Ma, H., and Krein, P. T. (2021). Wide-load range multiobjective efficiency optimization produces closed-form control solutions for dual active bridge converter. *IEEE Trans. Power Electron.* 36 (8), 8612–8616. doi:10.1109/TPEL.2021.3054970

frontiers | Frontiers in Energy Research

TYPE Original Research
PUBLISHED 10 January 2023
DOI 10.3389/fenrg.2022.1087775

OPEN ACCESS

EDITED BY
Weihao Hu,
University of Electronic Science and Technology of China, China

REVIEWED BY
Zhao Zhihong,
Nanjing University of Science and Technology, China
Shuzheng Wang,
Nanjing Institute of Technology (NJIT), China

*CORRESPONDENCE
Ning Li,
lining83@xaut.edu.cn

SPECIALTY SECTION
This article was submitted to Process and Energy Systems Engineering, a section of the journal Frontiers in Energy Research

RECEIVED 02 November 2022
ACCEPTED 18 November 2022
PUBLISHED 10 January 2023

CITATION
Li N, Li Z, Cao Y, Wei D, Xiao Z and Zhang Y (2023), Current stress optimization control strategy of the buck topology with the variable frequency/amplitude mode. *Front. Energy Res.* 10:1087775. doi: 10.3389/fenrg.2022.1087775

Current stress optimization control strategy of the buck topology with the variable frequency/amplitude mode

Ning Li[1]*, Zhuang Li[1], Yujie Cao[1], Deng Wei[1], Zihan Xiao[1] and Yan Zhang[2]

[1]School of Electrical Engineering, Xi'an University of Technology, Xi'an, China, [2]School of Electrical Engineering, Xi'an Jiaotong University, Xi'an, China

The Buck circuit is a common topology in DC-DC converter. The existing control strategies have the advantages of short modulation time and high dynamic performance, but they also have the disadvantages of poor active modulation of the working mode of the converter and large current stress. In response to the above problems, an improved frequency/amplitude modulation control strategy is proposed in this paper. The relationship between the output power and the peak inductor current in three modes, namely, Discontinuous Conduction Mode Critical Conduction Mode (CRM) and Continuous Conduction Mode is derived. The precise control strategy of the inductor peak current is introduced based on the traditional voltage loop control strategy to realize the free control of the system working mode and reduce the current stress during the working process. Finally, the experimental platforms of 100V/12V and 220/80V are established respectively. The experimental results show that the flexible switching circuit operating mode in the full load range can be realized under the new control method. In the 100/12V experimental platform, the current stress of the switch tube is optimized by at least 10.7%, and the average system efficiency is improved by 2.21%, with the same main circuit parameters.

KEYWORDS

variable frequency control, variable amplitude control, current stress, Buck converter, efficiency

1 Introduction

DC/DC power conversion is an important research field of power electronics technology, and the Buck circuit is widely used as a step-down converter (Wang et al., 2019a; Chen et al., 2021; Kim et al., 2022a; Liu et al., 2022a; Asad et al., 2022; Talebian et al., 2022; Zhao et al., 2022). With the rapid development of modern information science, how to optimize the performance of the Buck circuit has become a research hot spot in the field of DC/DC power converters.

The circuit control strategy is one of the focuses of current researches, which can be divided into the variable amplitude control and the variable frequency control (Lin et al., 2022; Ripamonti et al., 2019; Liu et al., 2022b; ul Ain et al., 2021). The variable amplitude control is to complete the control target by changing the amplitude of the controlled variable. The variable frequency control modulates the output of the circuit by changing the operating frequency of the switch tube. Both types of control strategies can achieve the goal of regulated output, but they have their own advantages and disadvantages (Nguyen et al., 2019; Hwang et al., 2021; Kim et al., 2022b).

The variable amplitude control strategy controls the output voltage by changing the amplitude of the reference voltage in the single voltage loop, and realizes the control of the system by adding the adjustment of the inductor current amplitude in the voltage and current double closed loop (Nan et al., 2018; Al-Baidhani et al., 2021; Kim and Shin, 2021). The peak current control collects the inductor current as an input signal of the comparator, which feeds back not only the output voltage but also the inductor current to improve the transient response characteristics of the converter (Alexandru and Mircea, 2019; Chen and Lai, 2019). Corresponding to the peak current control, the valley current collects the lowest value of the inductor current as the input signal of the comparator, which is symmetrical with each other in some specific cases (Abdelhamid et al., 2019). The peak current control is more suitable for the case of long conduction time, while the valley current control solves the deficiency that the peak current modulation is not suitable for the short conduction time of the switch tube. Compared with the traditional voltage loop control, the dynamic response speed of the valley current control has been improved, and the control accuracy has also been improved (Wang et al., 2019b), but when the duty cycle is less than 0.5, the valley current control will generate sub-harmonics oscillation. To solve the problem of sub-harmonic oscillation, the average current control (Yang et al., 2018) was proposed. The average current control method has strong anti-noise ability, so it has been widely used. In addition, the current loop is stable over a wide range of input voltages. Several methods were proposed to calculate the average inductor current, using an approach based on average small signal modeling to capture the dynamics of the inner current loop. However, the design of closed-loop parameters in application was more complicated, which increased the complexity of its application. The charge control (Sun et al., 2019) was a special current control, which used the integral value of the inductor current in one cycle as the input of the control loop to control the amount of charge entering the loop in one cycle. Under this control method, the current flowing into the system could be controlled more effectively, with better transient performance and good modulation accuracy, which could meet the high requirements of the power supply. However, its sensitivity to dynamic parameter changes was weak, and harmonic oscillation would occur under light load conditions.

There are also some researches for the variable frequency control at home and abroad. The variable frequency control under the constant on-time is to change the frequency of the control quantity to control the energy transfer under the condition of ensuring a certain conduction time of the switch tube, and finally realize the follow-up of the system expectations. (Calam et al., 2019). realized the modulation of the output voltage under this control method. Compared with the traditional variable amplitude control, the transient performance of the system was improved, but the steady-state accuracy of its control was still insufficient. Compared with the variable frequency control with constant on-time, (Fang and Redl, 2015), proposed a variable frequency control based on a constant off-time. Under the normal working range, for the disturbance of the inductor current, the transient control effect was faster and more stable than the traditional ones, but the steady-state accuracy of the system was still insufficient. Hysteresis control was also a kind of variable frequency control, which changed the frequency of the collected objects by changing the loop width, so as to ensure the stability of the system. (Redl and Sun, 2009). adopted the current hysteresis tracking control method, which had fast current tracking speed and high precision, but the switching frequency was not constant, which increased the switching loss in practical applications and was prone to make noise.

Although the traditional control strategies can improve the dynamic response speed of the converter, the operability and accuracy of the mode switching involved in both the variable frequency control and the variable amplitude control needs to be improved. In practical applications, the Buck converter needs to work in different modes according to the actual working conditions. When the circuit is under light load conditions, the energy demand is low. To reduce the loss in the energy transfer process, the circuit needs to work in the DCM or CRM; in the case of high power, in order to reduce the stress and loss of the switch tube and reduce the ripple of the output voltage and current, the circuit needs to work in the CRM or CCM.

To further improve the working performance of the Buck converter, this paper proposes a Buck circuit variable frequency and amplitude control strategy based on the inductor current. This strategy combines the advantages of the variable amplitude control with those of the variable frequency control. By establishing the relationship of the peak current of the inductor, the output power and the switching frequency, the proposed strategy realizes the function of the system to follow the load change and adjust the working mode. At the same time, the control strategy proposed in this paper ensures that the switch tube works in the mode of the minimum current stress in the full load range, which reduces the stress requirement of the switch tube and improves the average efficiency of the system.

In this paper, the design process of control parameters is discussed based on the variable frequency and amplitude strategy of the Buck circuit with inductor current, and the optimal condition of the switch tube stress is analyzed. The accuracy

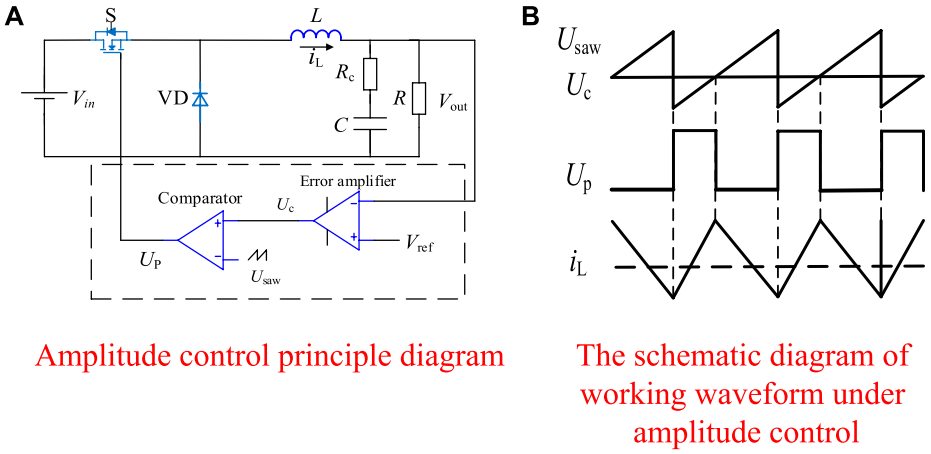

FIGURE 1
Buck converter variable amplitude control.

and effectiveness of this control strategy are verified by the simulation and experiments.

This paper is organized as follows: Section 2 discusses the shortcomings of traditional control strategies. Section 3 proposes the variable frequency and the amplitude control strategy. Section 4 conducts tests on the experimental platforms of 100/12V and 220/80V, respectively, to demonstrate the effectiveness of the proposed control strategy. Section 5 is the conclusion.

2 Analysis on the control method of the buck circuit

2.1 The buck circuit variable amplitude control principle

The single-voltage control is the most basic switch converter control method in the variable amplitude control, and it is also one of the most widely used control methods.

Figure 1 is the schematic diagram and control waveforms of the variable amplitude control under single voltage feedback.

It can be seen from Figure 1A that the voltage-type control used the output voltage sampling as the input signal of the control loop. The direct proportional relationship between its input and output can be represented by (1):

$$V_{\text{out}} = \frac{1}{T}\int_0^T u_{out}(t)dt = DV_{in} \tag{1}$$

where D is the duty cycle.

As shown in Figure 1B, the duty cycle of the switch tube drive signal U_{p} was adjusted by changing the amplitude, and finally the purpose that the output follows the given was achieved.

The design and analysis of the traditional variable amplitude control is relatively simple. It can only be detected when the output voltage changes and feedback for correction, so the dynamic response speed is slow; due to the voltage amplitude control alone, only the voltage can be fed back. If there is a sudden current change in the circuit, the over-current situation has no protective effect; and it is impossible to set the working mode of the converter under the traditional control.

2.2 The buck circuit variable frequency control principle

The single-voltage control is the most basic switch converter control method in the variable amplitude control, and it is also one of the most widely used control methods.

The variable frequency control principle of the Buck converter is shown in Figure 2. It was adjusted by changing the operating frequency of the switch tube. Its control principle can be represented by (2):

$$V_{\text{out}} = \frac{1}{T}\int_0^T u_{out}(t)dt = t_{\text{on}}V_{in}f \tag{2}$$

where t_{on} is the on-time of the switch tube, and f is the operating frequency of the switch tube. t_{on} remains unchanged.

Compared with the traditional variable amplitude control, the Buck variable frequency control has better dynamic performance; however, the control stability of this control method is not good, and it is affected by the equivalent series resistance of the output capacitor; at the same time, the control accuracy of the output voltage is poor, it is also impossible to accurately set the working mode of the converter.

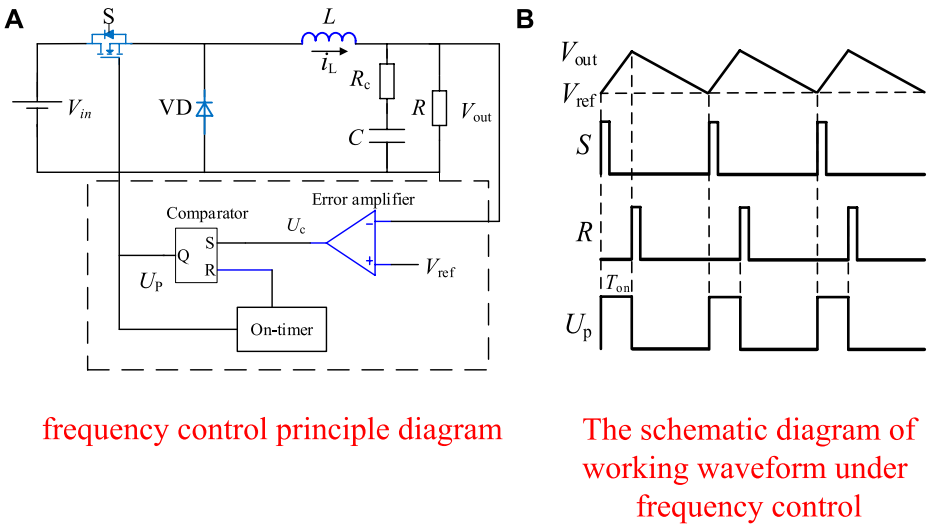

FIGURE 2
Buck converter variable frequency control.

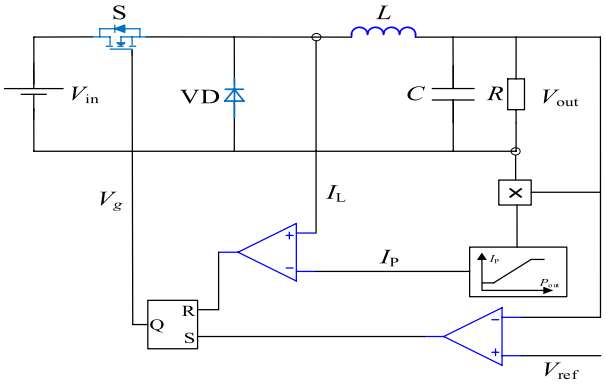

FIGURE 3
Schematic diagram of the variable amplitude/frequency control.

3 Control strategy with controllable working mode

3.1 Mode-controllable buck circuit control strategy

In view of the shortcomings of the above methods, in order to further improve the system performance, this paper proposes a variable amplitude/frequency control method with the controllable mode, the control principle diagram is shown in Figure 3, and the control block diagram is shown in Figure 4.

Under this control method, while realizing the fast dynamic response of the system, the operating mode of the converter could be precisely controlled according to the size of the load, and the current stress of the switch tube could be reduced.

In the schematic diagram shown in Figure 3, V_{in} and V_{out} are the input voltage and output voltage of the Buck converter respectively, I_L is the inductor current, I_o is the output current, V_g is the driving signal, S is the switch tube, V_D is the diode, and L is the Inductor, C is the output capacitance, and R is the load resistance. In the outer loop control, the output voltage V_{out} and the reference voltage V_{ref} passed through the voltage comparator to generate a driving signal to control the conduction of the switch tube; In the inner loop control, the output voltage V_{out} and the output current I_o passed through the multiplier to obtain the output power P_{out} of the load, and P_{out} was converted by the function editor to obtain the corresponding inductor peak current I_p. Finally, the inductor peak current I_p and the inductor current I_L passed through the current comparator to generate a driving signal to control the turn-off of the switch tube.

Based on the control strategy shown in Figure 4, the function of adjusting the system output could be achieved, and the system working mode could be precisely controlled. When the output voltage V_{out} dropped to the reference voltage V_{ref}, the voltage comparator output a high level, the RS flip-flop was set, the Q terminal output a high level, a driving signal was generated, the switch S was controlled to turn on, and the output voltage V_{out} began to rise; At the same time, the output power P_{out} passed through the function editor, and the reference value I_p of the current comparator was generated according to the relationship between the output

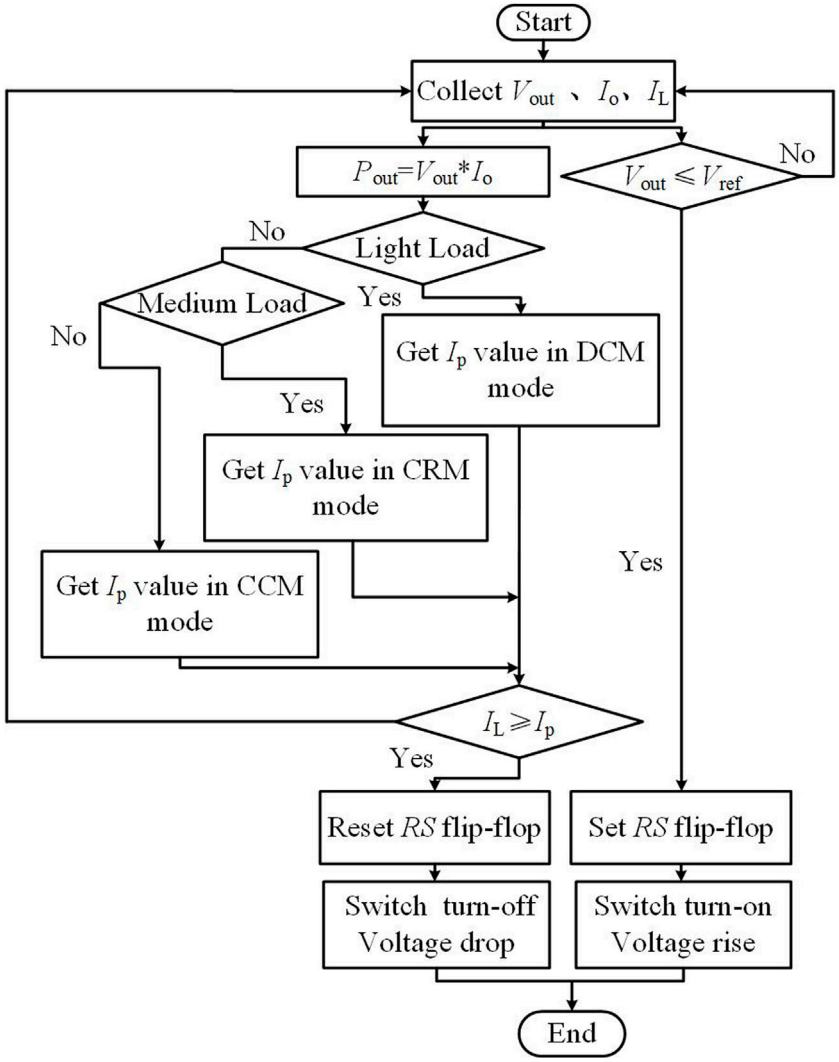

FIGURE 4
Block diagram of the variable amplitude/frequency control.

power and the peak current of the inductor. When the inductor current I_L rose to the peak current I_p, the current comparator output a high level, the flip-flop was reset, the *Q* terminal output a low level, and the switch *S* was controlled to turn off.

Under the control method in this paper, when the inductor was determined, the circuit could work in the best operating mode under different loads, thereby reducing the current stress of the switch tube. Under a certain working condition, the on-off time of the switch tube was adjusted corresponding to different loads, and the frequency of the control signal was changed. At the same time, the peak reference value of the inductor current was also adjusted according to the load changes to ensure that the entire circuit worked under the set conditions.

The Buck converter with the variable amplitude and frequency control could realize the switching design of the circuit working mode and met the strict requirements of the system average efficiency and no-load standby. In this paper, according to the relationship between the peak inductor current I_p and the output power P_{out}, the function editor was used to design and change the parameters to adjust the operating frequency of the switch tube, and finally realize the selection and switching of the working mode of the Buck converter with the load change.

3.1.1 I_P control in the CRM

When the circuit inductor was fixed, if the circuit was to work in this mode, it needed to meet the conditions of (2):

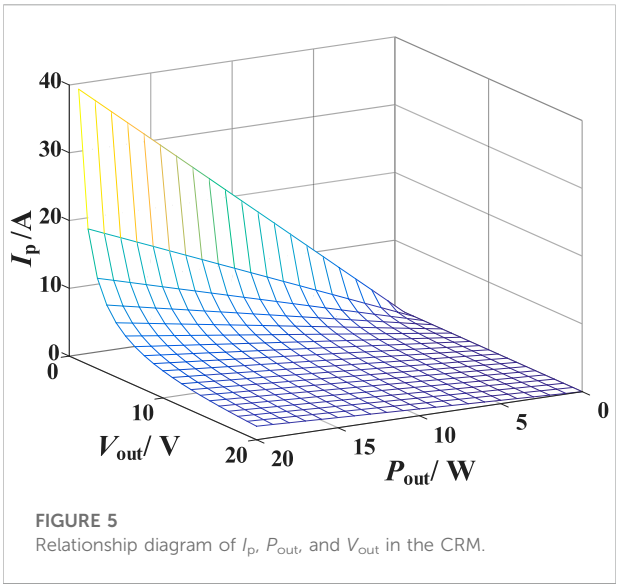

FIGURE 5
Relationship diagram of I_p, P_{out}, and V_{out} in the CRM.

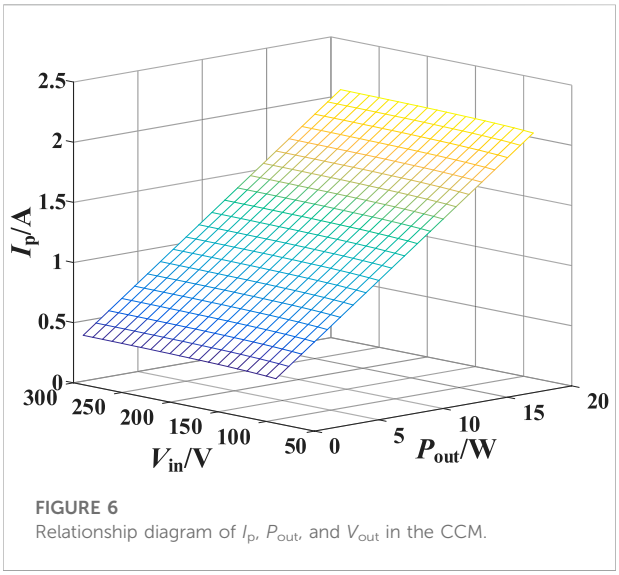

FIGURE 6
Relationship diagram of I_p, P_{out}, and V_{out} in the CCM.

$$\frac{L}{RT} = \frac{1-D}{2} \tag{3}$$

where T represents the period of the switch tube, D is the duty cycle, L is the inductor, and R is the load.

The size of R indirectly reflected the size of the output power. When the output power satisfied Equation 2, the circuit would work in the CRM.

The output current can be expressed duty cycle D as (3):

$$\frac{1}{2}(1-D)\frac{V_{out}}{L}t_{off} = I_o \tag{4}$$

t_{off} is the turn-off time of the switch tube.

By combining the above equations, the relationship of the output power and the peak value of the inductor current can be derived as shown in (4):

$$I_p = \frac{2P_{out}}{V_{out}} \tag{5}$$

From Equation 4, the relationship of the peak current I_p of the inductor current, the output power P_{out}, and the output voltage V_{out} could be obtained, thus, the curve of the relationship of I_p, P_{out} and V_{out} could be obtained, as shown in Figure 5. When the output voltage remained constant, the peak current I_p and the output power P_{out} had a linear relationship. Based on this, the design of the working conditions could be realized. When the relationship between the peak current I_p and the output power P_{out} satisfied Equation 4, the circuit worked in the critical mode; when the peak current I_p was constant, the output power P_{out} was lower than the corresponding peak current, the circuit would work in the discontinuous mode; when the peak current I_p was constant and the output power P_{out} was higher than the corresponding peak current I_p, the circuit would work in the continuous mode.

3.1.2 I_p control in the CCM

The conditions for the circuit to operate in this mode are

$$\frac{V_{out}^2 T}{2L} - \frac{V_{out}^3 T}{2L}\frac{1}{V_{in}} < P_{out} \tag{6}$$

When the output power satisfied the above, the circuit would work in the CCM. The control loop would adjust the inductor current peak value according to the load change to ensure that the circuit worked in the CCM.

The relationship between I_p and P_{out} in the CCM can be obtained as follows:

$$I_p = \frac{V_{out}}{2L}T - \frac{V_{out}^2}{2LV_{in}}T + \frac{P_{out}}{V_{out}} \tag{7}$$

Figure 6 shows the relationship of I_p, P_{out} and V_{in} in the CCM. When the input voltage remained unchanged, when the output power increased, the peak value of the inductor current would increase accordingly. When the output power remained unchanged, the increase in the input voltage would cause the peak value of the inductor current to increase.

3.1.3 I_p control in the DCM

The analysis showed that the conditions for the circuit to work in this mode are

$$D < \frac{12}{V_{in}} \tag{8}$$

In this mode, when the duty cycle D and the input voltage V_{in} met the constraints of the above, the circuit would work in the DCM.

When the circuit worked in the DCM, according to the Buck principle, the following can be obtained:

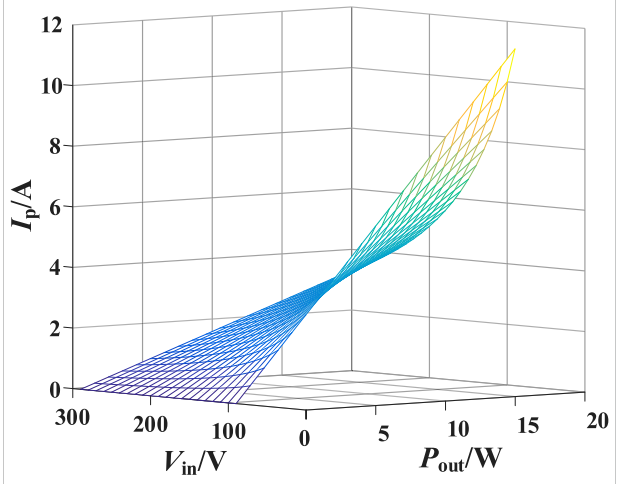

FIGURE 7
Relationship of I_p, P_{out}, and Vi_n in the DCM

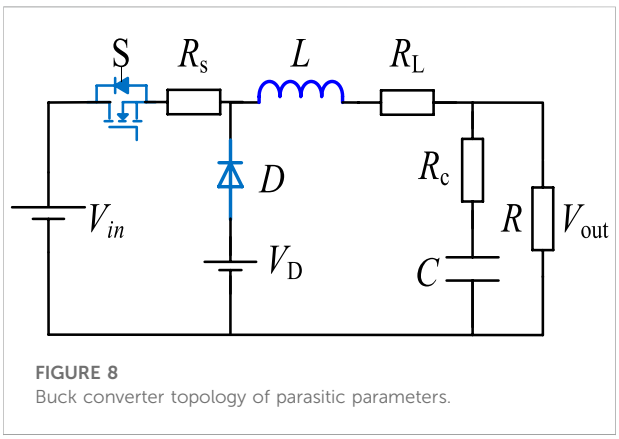

FIGURE 8
Buck converter topology of parasitic parameters.

$$(V_{in} - V_{out})DT = V_{out}\delta T \tag{9}$$

$$I_L = \frac{1}{2}\Delta I_L (D + \delta) \tag{10}$$

where δ is the duty cycle of the inductor current falling time, and δT is the continuation time for the switch tube to disconnect the inductor. Thus, the relationship between I_p and P_{out} in the DCM can be obtained as follows:

$$I_p = \frac{2P_{out}}{V_{in}} \times \frac{T}{t_{on}} \tag{11}$$

Figure 7 shows the relationship of I_p, P_{out} and V_{in} in the DCM. It can be seen from Figure 6 that when the input voltage remained unchanged, the peak value of the inductor current would make the same change with the output power; when the output power remained unchanged, the inductor current was inversely proportional to the input voltage.

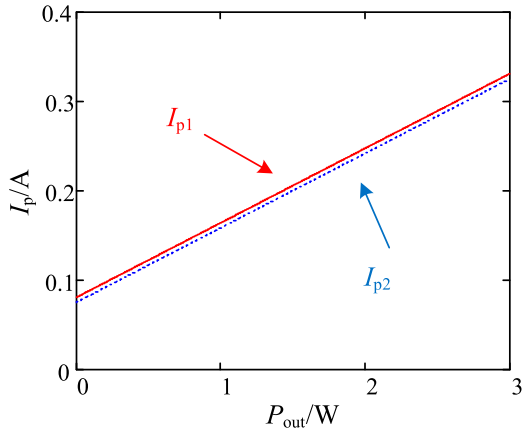

FIGURE 9
Relationship of I_p and P_{out}.

3.1.4 Analysis of the parasitic parameters

When considering the influence of the parasitic parameters, the above control method is also applicable. The main circuit with the parasitic parameters is shown in Figure 8. R_s is the on-resistance of the switch tube, R_c is the equivalent resistance of the output capacitor, R_L is the on-resistance of the inductor, and V_D is the on-voltage drop of the diode.

Considering the parasitic parameters, the relationship between the inductor peak current and output power can be expressed by the following equation:

$$I_p = \begin{cases} \dfrac{2 \cdot P_{out}}{(V_{in} - P_{out}/V_{out} \cdot R_L + V_D) \cdot D} & DCM \\ 2 \cdot \dfrac{P_{out}}{V_{out}} & CRM \\ \dfrac{A + B + C - D}{2 + P_{out}/V_{out}} T + \dfrac{P_{out}}{V_{out}} & CCM \end{cases} \tag{12}$$

Where

$$\begin{cases} A = V_{out} \cdot V_{in} - {V_{out}}^2 \\ B = (V_{in} - V_{out}) \cdot V_D \\ C = (V_{in} - 2V_{out} - V_D) \cdot \left(\dfrac{P_{out}}{V_{out}} \cdot R_L\right) \\ D = (V_{out} + V_D) \cdot \left(\dfrac{P_{out}}{V_{out}} \cdot R_s\right) - \left(\dfrac{P_{out}}{V_{out}}\right)^2 \cdot (R_L + R_s) \end{cases}$$

Taking the CCM as an example, when the input voltage was constant, the relationship between the inductor current and the output power with the parasitic parameters is as follows:

I_{p1} is the peak value of the inductor current with the parasitic parameters, and I_{p2} is the peak value of the inductor current in the rational circuit.

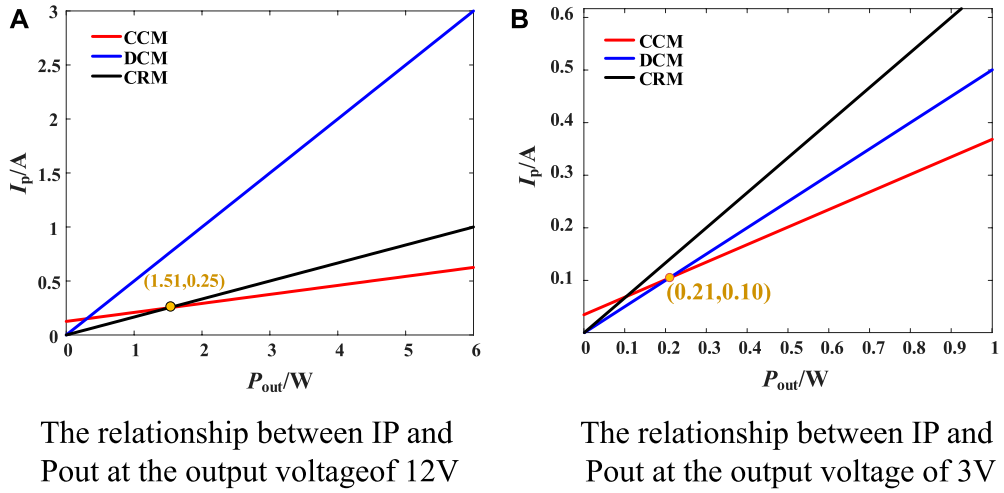

The relationship between IP and Pout at the output voltageof 12V

The relationship between IP and Pout at the output voltage of 3V

FIGURE 10
Working condition diagram.

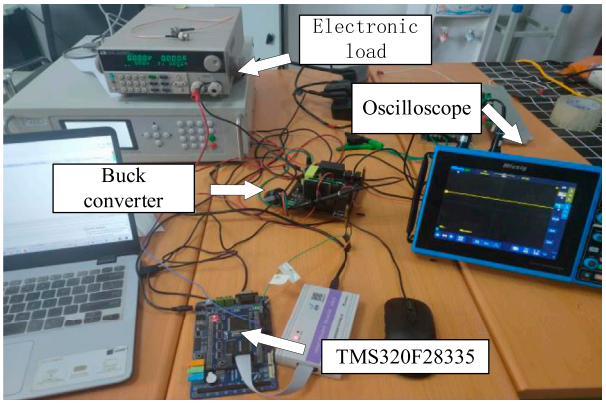

FIGURE 11
Photograph of experimental setup.

It can be seen from Figure 9 that the influence of the circuit with the parasitic parameters on the relationship between the peak value of the inductor current and the output power could be approximately ignored.

3.2 Current stress of the switch tube.

The control strategy proposed in this paper could change the peak value of the current and the working frequency by improving control degrees of freedom, which reduced the current stress of the switch tube controlled by the duty cycle alone.

TABLE 1 Main parameters of the Buck converter with rated power of 3W

Main parameters	Value
Rated power Po-max/W	3
Input voltage Vin/V	100
Output voltage Vout/V	12
Capacitance C/μF	50
inductor L/mH	0.7
Output resistance R/Ω	48

TABLE 2 Main parameters of the Buck converter with rated power of 100W

Main parameters	Value
Rated power Po-max/W	100
Input voltage Vin/V	220
Output voltage Vout/V	80
Capacitance C/μF	50
inductor L/mH	0.7
Output resistance R/Ω	48

Figure 9 shows that the optimal working mode under different conditions was selected to achieve the control effect of the lowest current stress of the switch tube.

In Figure 10A, with the output voltage being 12V, when the output power was less than 1.51W, the control circuit worked

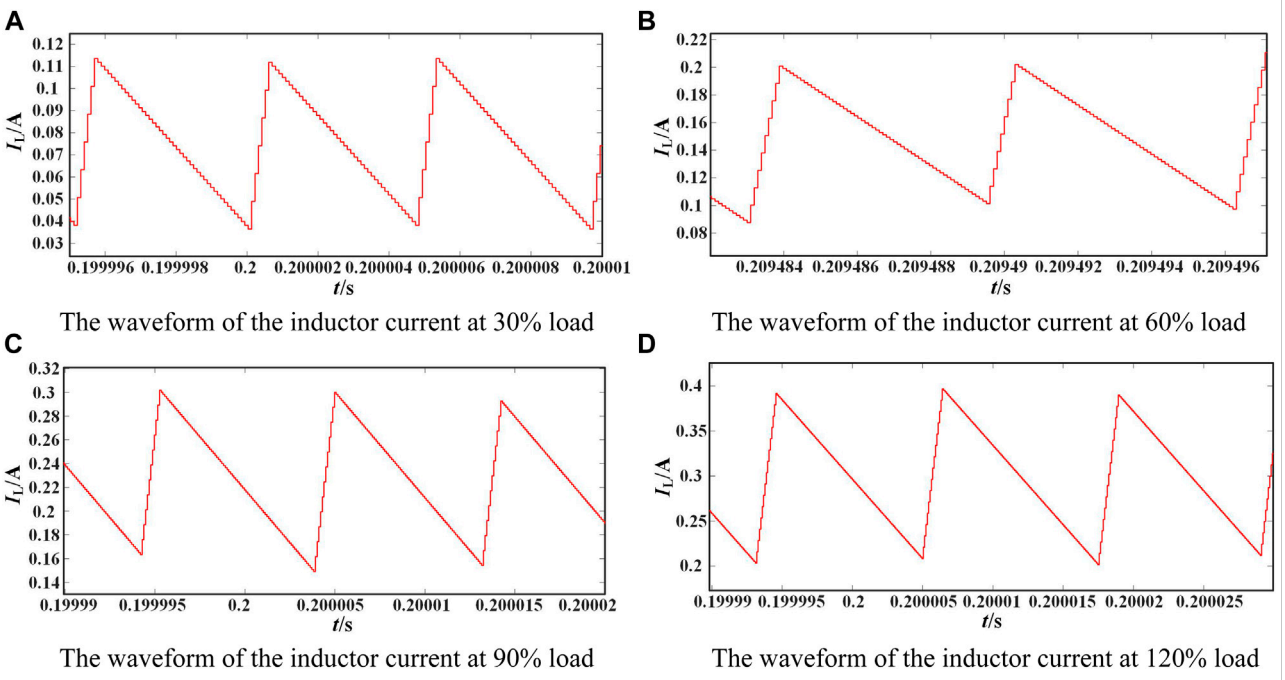

FIGURE 12
Inductor current waveforms with different loads in CCM at 3W rated power.

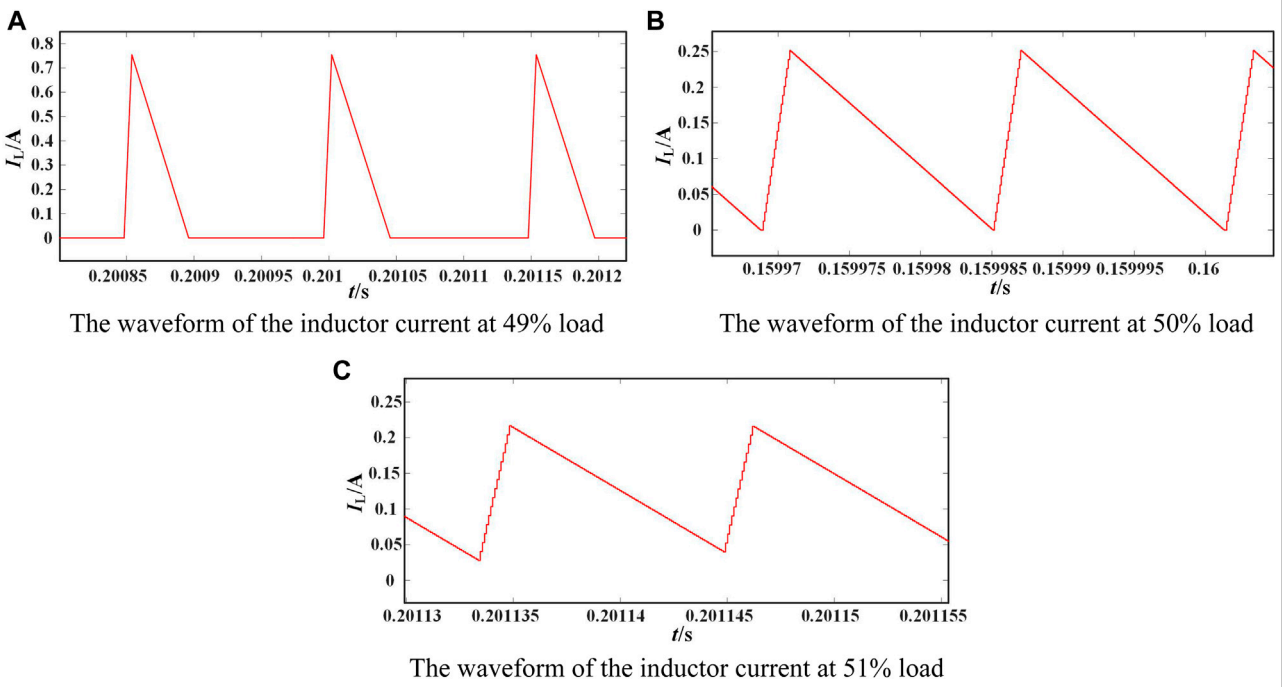

FIGURE 13
Inductor current waveforms with the mode switching at 3W rated power.

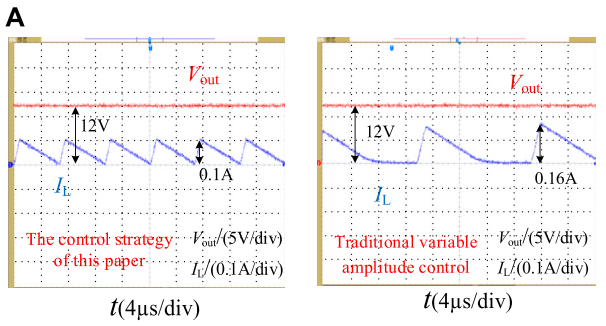

The waveform of inductance current and output voltage at 20% load

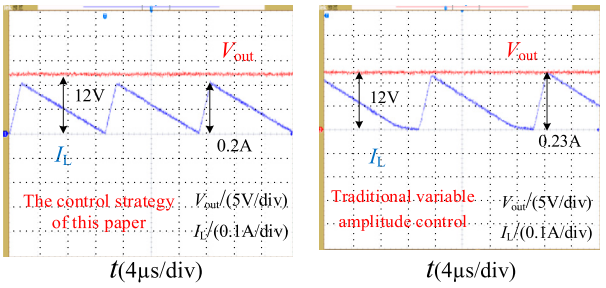

The waveform of inductance current and output voltage at 40% load

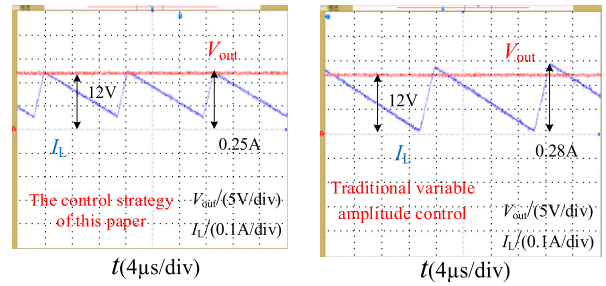

The waveform of inductance current and output voltage at 60% load

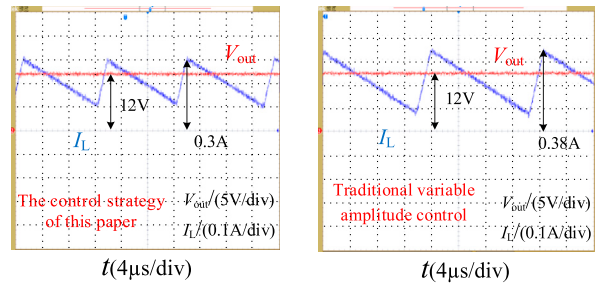

The waveform of inductance current and output voltage at 80% load

FIGURE 14
Waveforms under different loads at 3W rated power.

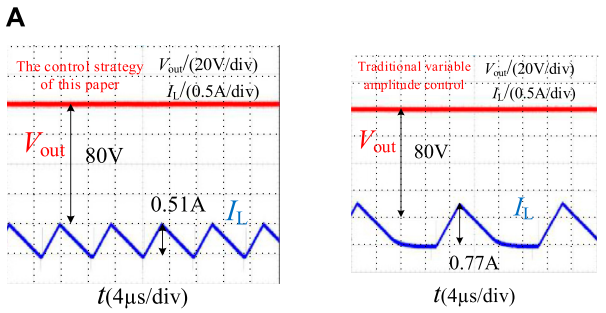

The waveform of inductance current and output voltage at 20% load

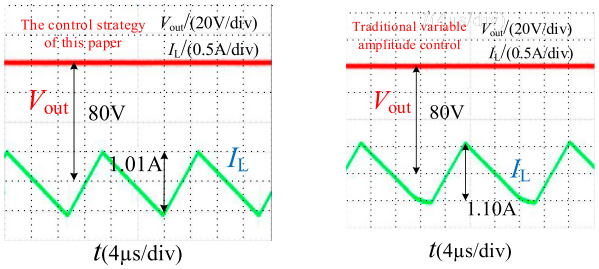

The waveform of inductance current and output voltage at 40% load

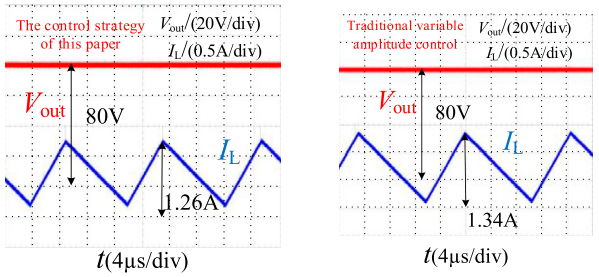

The waveform of inductance current and output voltage at 60% load

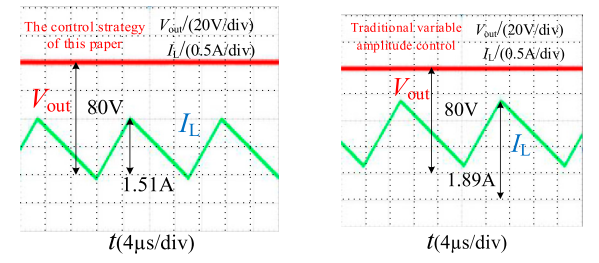

The waveform of inductance current and output voltage at 80% load

FIGURE 15
Waveforms under different loads at 100W rated power.

TABLE 3 Comparative analysis of current stress with rated power of 3W

Load (%)	Control method	I_{peak} (A)	Optimization
20	Traditional variable amplitude control	0.16	37.5%
	The control strategy of this paper	0.10	
40	Traditional variable amplitude control	0.23	13.0%
	The control strategy of this paper	0.20	
60	Traditional variable amplitude control	0.28	10.7%
	The control strategy of this paper	0.25	
80	Traditional variable amplitude control	0.38	21.1%
	The control strategy of this paper	0.30	

TABLE 4 Comparative analysis of current stress with rated power of 100W

Load (%)	Control method	I_{peak} (A)	Optimization
20	Traditional variable amplitude control	0.77	33.77%
	The control strategy of this paper	0.51	
40	Traditional variable amplitude control	1.10	8.18%
	The control strategy of this paper	1.01	
60	Traditional variable amplitude control	1.34	5.97%
	The control strategy of this paper	1.26	
80	Traditional variable amplitude control	1.89	20.11%
	The control strategy of this paper	1.51	

TABLE 5 Comparative between the theoretical value and the actual Value``

Power level (W)	Data type	20% load (A)	40% load (A)	60% load (A)	80% load (A)
3	Actual data	0.10	0.20	0.25	0.30
	Theoretical data	0.10	0.20	0.246	0.296
100	Actual data	0.51	1.01	1.26	1.51
	Theoretical data	0.50	1.00	1.269	1.52

in the CRM; when the output power was greater than 1.51W, the control circuit worked in the CCM. In this control mode, the current stress of the switch tube could be reduced to the minimum, and its current stress could be expressed by the following:

$$\begin{cases} I_P = \dfrac{2P_{out}}{V_{out}} & (P_{out} \le 1.51) \\ I_P = \dfrac{V_{out}}{2L}T - \dfrac{V_{out}^2}{2LV_{in}}T + \dfrac{P_{out}}{V_{out}} & (P_{out} > 1.51) \end{cases} \tag{13}$$

In Figure 10B, with the output voltage being 3V, when the output power is less than 0.21W, the control circuit worked in the DCM; when the output power was greater than 0.21W, the control circuit worked in the CCM. In this control mode, the current stress of the switch tube could be reduced to the minimum, and its current stress can be expressed by the following:

$$\begin{cases} I_P = \dfrac{2P_{out}}{DV_{in}} & (P_{out} \le 0.21) \\ I_P = \dfrac{V_{out}}{2L}T - \dfrac{V_{out}^2}{2LV_{in}}T + \dfrac{P_{out}}{V_{out}} & (P_{out} > 0.21) \end{cases} \tag{14}$$

Through the variable amplitude and frequency control, the optimal working mode could be selected according to different circuit conditions, thereby reducing the current stress of the switch tube and accurately controlling the switching of circuit modes.

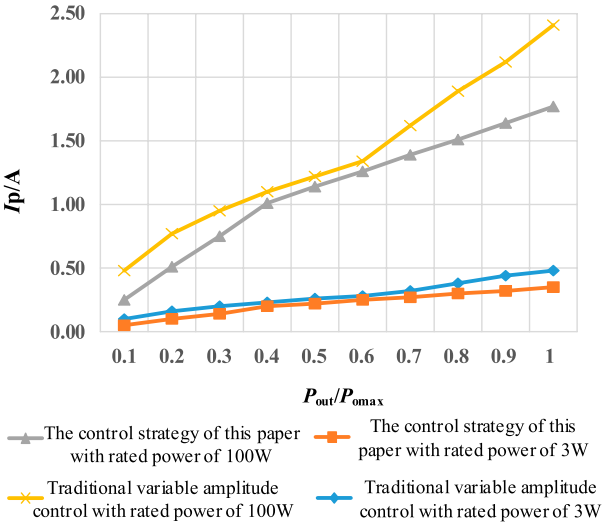

FIGURE 16
Comparative analysis of current stress.

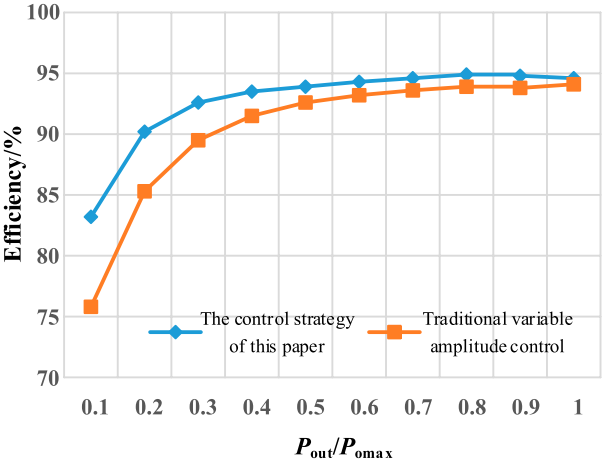

FIGURE 17
Efficiency comparisons under different loads.

4. Experiment analysis

In this paper, the parameters of the Buck converter under the variable amplitude and frequency control were designed and verified by the simulation and experiments. Firstly, the circuit was designed to work in the single mode with the full load range, so that the feasibility of the control method in this paper could be verified. Secondly, the system was controlled to work in the optimal current stress mode in the full load range to improve the working performance of the converter. Finally, this paper conducted simulation through Matlab/Simulink, and built the experimental platform as shown in Figure 11 to verify the validity of this theory. The experimental parameters are shown in Table 1. The operating frequency of the traditional variable amplitude control circuit was set to 60kHz, and the period of the switch tube and the output voltage were stable and unchanged. The new control strategy improved the accuracy of the output voltage by changing the frequency and amplitude of the inductor current, while ensuring that the circuit could work in the set mode.

4.1 Simulation verification of the full load range

The simulation in Figure 12 verified that the circuit worked in the CCM, and the inductor current was in continuous mode under different loads. Under different loads, the circuit could work in the continuous mode under the full load and the heavy load, which showed the feasibility of the proposed control strategy. The peak value of the inductor current was adjusted for different loads. The simulation results were in line with the theoretical derivation. Different output powers generated the corresponding reference value of the peak current, and then control the peak value changes of the inner loop of the current.

Figure 13 verified the precise switching control of the circuit operating modes. Figure 13A shows the circuit works in the DCM with 49% load. Figure 13 (b) shows that the circuit works in the CRM with 50% load. Figure 13 (c) shows that the circuit works in the CCM with 51% load. The working mode of the circuit could be accurately controlled by the variable frequency and the variable amplitude in this paper. The experimental results were in line with the theoretical derivation.

4.2 Current stress comparison verification

In order to verify the effectiveness of this method, the experimental verification with a power of 100W was added. The experimental parameters are shown in Table 2. In the case of the same hardware circuit, the current stress of the switch tube was compared with the traditional voltage single loop.

Figure 14 and Figure 15 are the waveforms diagram of the inductor current under the traditional control and the proposed control strategy of this paper with different loads, 3W and 100W respectively. Using the control strategy in this paper, it could be found that with 20% and 40% load, the circuit worked in the CRM, and with 60% and 80% load, the circuit worked in the CCM. The control circuit of the new method worked in the optimal working mode of the current stress, and the current stress was obviously optimized compared with the results under

the traditional voltage loop. The current stress comparison results of the control strategy in this paper and the traditional control strategy under the rated power of 3W and 100W are shown in Table 3 and Table 4, respectively.

Table 5 shows a comparison of experimental data and theoretical values to demonstrate the effectiveness of the new method. No matter the output power is 3W or 100W, the peak current of the inductor current can match the theoretical value, which can optimize the stress of the device and improve the efficiency of the system.

The control circuit of the new method worked in the optimal working mode of the current stress, and the current stress was obviously optimized compared with the results under the traditional voltage loop. The current stress transformation trend under the full load range is shown in Figure 16, from which it can be seen that under the control strategy of this paper, the current stress can be significantly optimized.

Figure 17 is a comparison diagram of the efficiency under the traditional control and the control strategy of this paper with different loads. The analysis showed that since the circuit worked in the mode with the smallest current stress, the conduction loss was effectively reduced, the average efficiency of the converter was higher than that of the traditional control strategy, and the efficiency could be increased by 0.5% with the full load. Under light load conditions, the efficiency would decrease due to the increased proportion of the system stray losses. Under the control strategy in this paper, the light-load efficiency was significantly improved compared with the light-load efficiency under the traditional control strategy, and the average efficiency of the converter in the full load range was also optimized, and the average efficiency was improved by 2.21%.

5 Conclusion

In this paper, the variable amplitude and frequency control strategy is proposed to precisely control the working mode of the converter, and the control accuracy of the converter could be improved by adding control degrees of freedom. It solved the problem of large current stress in the traditional variable amplitude control strategy, and meanwhile improved the average efficiency of the system. In this paper, this control strategy was applied to the Buck converter. When the load changes in the full range, when the input power also changes at the same time, how to further ensure that the circuit works in the optimal mode, this can be in the follow-up study in-depth analysis. Through the theoretical analysis and experimental verification, the conclusion is as follows:

1) The established control model of the inductor current peak value and output power could control the working mode of the converter and improved the accuracy of the converter control.
2) The mode with the optimal current stress was selected according to the load changes to ensure the minimum current stress of the switch tube, and the current stress in the full load range was increased up to 37.5%.
3) The light-load efficiency of the converter was significantly improved, and the average efficiency in the full-load range was also optimized, increasing by 2.21%.

Data availability statement

The original contributions presented in the study are included in the article/Supplementary material, further inquiries can be directed to the corresponding author.

Author contributions

Conceptualization, NL; methodology, NL, ZL, and YC; software, ZL; validation, ZL; resources, NL; data curation, NL, DW, ZX, and YZ; writing—original draft preparation, ZL; writing—review and editing, NL, ZL, and YC; supervision, DW, ZX, and YZ; funding acquisition, NL. All authors have read and agreed to the published version of the manuscript.

Funding

National Natural Science Foundation of China (52177193); Key Research and Development Program of Shaanxi Province(2022GY-182); China Scholarship Council (CSC) State Scholarship Fund International Clean Energy Talent Project (Grant No. [2018]5046,[2019]157). Xi 'an Science and Technology Plan Project (22GXFW0078).

Conflict of interest

The authors declare that the research was conducted in the absence of any commercial or financial relationships that could be construed as a potential conflict of interest.

Publisher's note

References

Abdelhamid, E., Bonanno, G., Corradini, L., Mattavelli, P., and Agostinelli, M. (2019). Stability properties of the 3-level flying capacitor buck converter under peak or valley current programmed control. *IEEE Trans. Power Electron.* 34 (8), 8031–8044. Aug. doi:10.1109/tpel.2018.2877943

Al-Baidhani, H., Salvatierra, T., Ordóñez, R., and Kazimierczuk, M. K. (2021). Simplified nonlinear voltage-mode control of PWM DC-DC buck converter. *IEEE Trans. Energy Convers.* 36 (1), 431–440. doi:10.1109/tec.2020.3007739

Alexandru, I. C., and Mircea, B. (2019). "Analysis and design of a current mode buck converter with digitally controlled output voltage," in 2019 International Semiconductor Conference. Sinaia, Romania: CAS, 309–312. doi:10.1109/SMICND.2019.8923781

Asad, M., Singha, A. K., and Rao, R. M. S. (2022). Dead time optimization in a GaN-based buck converter. *IEEE Trans. Power Electron.* 37 (3), 2830–2844. doi:10.1109/tpel.2021.3116126

Calam, R. C. M., Hora, J. A., Gerasta, O. J. L., Zhu, X., and Dutkiewicz, E. (2019). "A self-calibrating off-time controller for WSN/IoT synchronous non-inverting buck-boost DC-to-DC converter application," in 2019 IEEE International Circuits and Systems Symposium (ICSyS), 1–4.

Chen, J. -J., Hwang, Y. -S., Ku, Y., Li, Y. -H., and Chen, J. -A. (2021). A current-mode-hysteretic buck converter with constant-frequency-controlled and new active-current-sensing techniques. *IEEE Trans. Power Electron.* 36 (3), 3126–3134. doi:10.1109/tpel.2020.3017809

Chen, W., and Lai, J. (2019). A novel dynamic ramp valley control in a current-mode adaptive on-time controller for the on-chip buck converter. *IEEE Trans. Power Electron.* 34 (6), 5830–5841. doi:10.1109/tpel.2018.2866737

Fang, C., and Redl, R. (2015). Subharmonic instability limits for the peak-current-controlled buck converter with closed voltage feedback loop. *IEEE Trans. Power Electron.* 30 (2), 1085–1092. Feb. doi:10.1109/tpel.2014.2312354

Hwang, Y. -S., Chen, J. -J., Ku, Y. -T., and Yang, J. -Y. (2021). An improved optimum-damping current-mode buck converter with fast-transient response and small-transient voltage using new current sensing circuits. *IEEE Trans. Ind. Electron.* 68 (10), 9505–9514. Oct. doi:10.1109/tie.2020.3020030

Kim, D., and Shin, J. -W. (2021). Dynamic response of buck converter with auxiliary current control: Analysis and design of practical implementation. *IEEE Trans. Power Electron.* 36 (12), 13917–13929. Dec. doi:10.1109/tpel.2021.3087607

Kim, J. -S., Yoon, J. -O., and Choi, B. -D. (2022). A high-light-load-efficiency low-ripple-voltage PFM buck converter for IoT applications. *IEEE Trans. Power Electron.* 37 (5), 5763–5772. doi:10.1109/tpel.2021.3131594

Kim, S. -K., Kim, K. -C., and Ahn, C. K. (2022). Output-voltage-tracking control for buck converters using variable convergence rate mechanism without current feedback. *IEEE Trans. Ind. Electron.* 69 (3), 2938–2946. doi:10.1109/tie.2021.3065610

Lin, J., Su, M., Sun, Y., Li, X., Xie, S., Zhang, G., et al. (2022). Accurate loop gain modeling of digitally controlled buck converters. *IEEE Trans. Ind. Electron.* 69 (1), 725–739. doi:10.1109/tie.2021.3050389

Liu, X., Wu, B., and Xiu, L. (2022). A fast positive-sequence component extraction method with multiple disturbances in unbalanced conditions. *IEEE Trans. Power Electron.* 37 (8), 8820–8824. doi:10.1109/tpel.2022.3161734

Liu, X., Xiong, L., Wu, B., Qian, Y., and Liu, Y. (2022). Phase locked-loop with decaying DC transient removal for three-phase grids. *Int. J. Electr. Power & Energy Syst.* 143, 108508. doi:10.1016/j.ijepes.2022.108508

Nan, C., Ayyanar, R., and Xi, Y. (2018). A 2.2-MHz active-clamp buck converter for automotive applications. *IEEE Trans. Power Electron.* 33 (1), 460–472. doi:10.1109/tpel.2017.2672522

Nguyen, M., Tran, T., and Lim, Y. (2019). A family of PWM control strategies for single-phase quasi-switched-boost inverter. *IEEE Trans. Power Electron.* 34 (2), 1458–1469. Feb. doi:10.1109/tpel.2018.2831674

Redl, R., and Sun, J. (2009). Ripple-based control of switching regulators—an overview. *IEEE Trans. Power Electron.* 24 (12), 2669–2680. Dec. doi:10.1109/tpel.2009.2032657

Ripamonti, G., Saggini, S., Corradini, L., Rizzolatti, R., Faccio, F., Michelis, S., et al. (2019). A dual-edge pulsewidth modulator for fast dynamic response DC–DC converters. *IEEE Trans. Power Electron.* 34 (1), 28–32. doi:10.1109/tpel.2018.2836385

Sun, Q., Ma, Y., Ye, Z., Wang, X., and Zhang, H. (2019). A pseudo-constant frequency constant on-time buck converter with internal current ripple injection and output DC offset cancellation. *IEEE Access* 7, 175443–175453. doi:10.1109/ACCESS.2019.2957784

Talebian, I., Alavi, P., Marzang, V., Babaei, E., and Khoshkbar-Sadigh, A. (2022). Analysis, design, and investigation of a soft-switched buck converter with high efficiency. *IEEE Trans. Power Electron.* 37 (6), 6899–6912. doi:10.1109/tpel.2021.3132463

ul Ain, Q., Khan, D., Jang, B. G., Basim, M., Shehzad, K., Asif, M., et al. (2021). A high-efficiency fast transient COT control DC–DC buck converter with current reused current sensor. *IEEE Trans. Power Electron.* 36 (8), 9521–9535. Aug. doi:10.1109/tpel.2021.3052198

Wang, Y., Ruan, X., Leng, Y., and Li, Y. (2019). Hysteresis current control for multilevel converter in parallel-form switch-linear hybrid envelope tracking power supply. *IEEE Trans. Power Electron.* 34 (2), 1950–1959. doi:10.1109/tpel.2018.2835640

Wang, Y., Xu, J., and Yin, G. (2019). Cross-regulation suppression and stability analysis of capacitor current ripple controlled SIDO CCM buck converter. *IEEE Trans. Ind. Electron.* 66 (3), 1770–1780. doi:10.1109/tie.2018.2838103

Yang, W. -H., Yang, H. -A., Huang, C. -J., Chen, K. -H., and Lin, Y. -H. (2018). A high-efficiency single-inductor multiple-output buck-type LED driver with average current correction technique. *IEEE Trans. Power Electron.* 33 (4), 3375–3385. doi:10.1109/tpel.2017.2709039

Zhao, J., Ye, Q., and Lai, X. (2022). A frequency stable on-time control buck converter with reference and frequency compensation technique using low ESR output capacitor. *IEEE Trans. Ind. Electron.* 69 (4), 3536–3545. doi:10.1109/tie.2021.3071677

frontiers | Frontiers in Energy Research

TYPE Original Research
PUBLISHED 17 January 2023
DOI 10.3389/fenrg.2022.1079623

OPEN ACCESS

EDITED BY
Liansong Xiong,
Xi'an Jiaotong University, China

REVIEWED BY
Zhang Donghui,
Nanjing University of Aeronautics and Astronautics, China
Yongbin Wu,
Southeast University, China
Zaki Ud Din,
National University of Sciences and Technology (NUST), Pakistan

*CORRESPONDENCE
Shangzhou Zhang,
zhangshangzhou@slxy.edu.cn

SPECIALTY SECTION
This article was submitted to Process and Energy Systems Engineering, a section of the journal Frontiers in Energy Research

RECEIVED 25 October 2022
ACCEPTED 10 November 2022
PUBLISHED 17 January 2023

CITATION
Zhang S (2023), Influence of driving and parasitic parameters on the switching behaviors of the SiC MOSFET. *Front. Energy Res.* 10:1079623. doi: 10.3389/fenrg.2022.1079623

Influence of driving and parasitic parameters on the switching behaviors of the SiC MOSFET

Shangzhou Zhang[1,2]*

[1]College of Electronic Information and Electrical Engineering, Shangluo University, Shangluo, China, [2]Research Center of Shangluo Distributed New Energy Application Technology, Shangluo, China

The SiC MOSFET has lower conduction loss and switching loss than the Si IGBT, which helps to improve the efficiency and power density of the converter, especially for those having strict requirements for volume and weight, for example, electrical vehicles (EVs), on-board chargers (OBCs), and traction drive systems (TDS). However, the faster switching speed will cause overshoot and oscillation problems, which will affect the efficiency and security of the SiC devices and power electronic systems. For the SiC MOSFET to be better used, combining a theoretical analysis, the double-pulse test platform is built. The controllable principles of SiC MOSFETs are validated. The turn-on and turn-off delay, switching delay, switching di/dt, switching du/dt, switching overshoot, and switching loss of SiC MOSFETs under different driving and parasitic parameters are explored. Finally, some valuable suggestions for designing are proposed for a better application of the SiC MOSFET.

KEYWORDS

SiC MOSFET, parasitic parameter, driving parameter, overshoot, oscillation

1 Introduction

The SiC MOSFET is a typical wide-bandgap power semiconductor device (Zeng and Li, 2018). Compared with the Si IGBT, the SiC MOSFET has lower conduction loss and switching loss, which means the efficiency of the converter can be improved, especially in high-frequency applications. At the same time, the operation temperature of the SiC MOSFET is higher than that of the Si IGBT, which reduces the size of the heat sink, so the power density of the converter can be improved too. Therefore, the SiC MOSFET is considered to have potential in electric vehicles, photovoltaic power generation, and high-frequency power supplies (Camacho et al., 2017; Xie et al., 2021). However, due to the high switching speed of the SiC MOSFET, the current and voltage overshoot would reduce the electromagnetic compatibility of the converter. In addition, the overshoots and oscillations will accelerate the aging of the device and eventually cause its failure (Sun et al., 2021).

Various literature works studied the overshoots and oscillations of the SiC MOSFET during the switching transients. The influence of the source inductance and drain inductance on the overshoots is reported in Li et al. (2016) and Yang et al. (2022).

TABLE 1 Comparison of key parameters between the SiC MOSFET and Si IGBT.

	SiC MOSFET	Si IGBT
Name	C2M0080120D	IXGH20N120B
Breakdown voltage	1,200 V	1,200 V
Continuous current	36 A	40 A
On-state characteristics	80 mΩ	2.9 V
Gate charge	62 nC	72 nC
Input capacitance	950 pF	1,700 pF
Turn-on loss	265 μJ	2,100 μJ
Turn-off loss	135 μJ	3,500 μJ

TABLE 2 Influences of circuit parameters on the switching behaviors.

	$(di/dt)_{on}$	$(dv/dt)_{on}$	$(di/dt)_{off}$	$(dv/dt)_{off}$	E_{on}	E_{off}
$R_g\uparrow$		↓	↓	↓		↑
$C_{gs}\uparrow$	↓	-	↓	-	↑	↑
$C_{gd}\uparrow$	-	↓	-	↓	↑	↑
$C_{ds}\uparrow$	-	↓	-	↓	↑	↑
$L_{loop}\uparrow$	↑	-	↑	-		↑
$L_s\uparrow$	↓	-	↓	-	↑	↑

Considering different parasitic parameters, Bonyadi et al. (2015), Wang et al. (2019), and Talesara et al. (2020) provided the behavior model of the half bridge applying SiC MOSFETs, and the simulation and experiment results show that the overshoots and oscillations are mainly caused by the parasitic inductance in the loop, which should be reduced as much as possible. The analytical model is proposed in Stark et al. (2021) to characterize the switching behaviors of the SiC MOSFET. Riccio et al. (2018) confirmed that the gate driving resistor can damp the oscillation of the SiC MOSFET. However, comprehensive research about the influence of driving parameters and parasitic parameters on the switching behaviors of the SiC MOSFET is lacking among the existing studies, and there is no conductive guidance about designing the gate driver.

In this study, comprehensive research about the influence of driving parameters and parasitic parameters on the switching behaviors of the SiC MOSFET is carried out, which includes the gate resistance R_g, the gate–source capacitance C_{gs}, the gate–drain capacitance C_{gd}, the drain–source C_{ds}, the gate inductance L_g, the source inductance L_s, and the loop inductance L_{loop}. The measured results show that the switching behavior of the SiC MOSFET is controlled by these parameters from different aspects and should be given special attention during the designing period.

This paper is organized as follows. In Section 2, the switching behavior of the SiC MOSFET is studied. The dynamic characteristics of the SiC MOSFET with different driving and parasitic parameters are explained in Section 3. Finally, the conclusion is drawn in Section 4.

2 Switching behavior

2.1 Comparison between SiC and Si devices

The SiC MOSFET is considered a good substitute for the Si IGBT because better static and dynamic characteristics can be

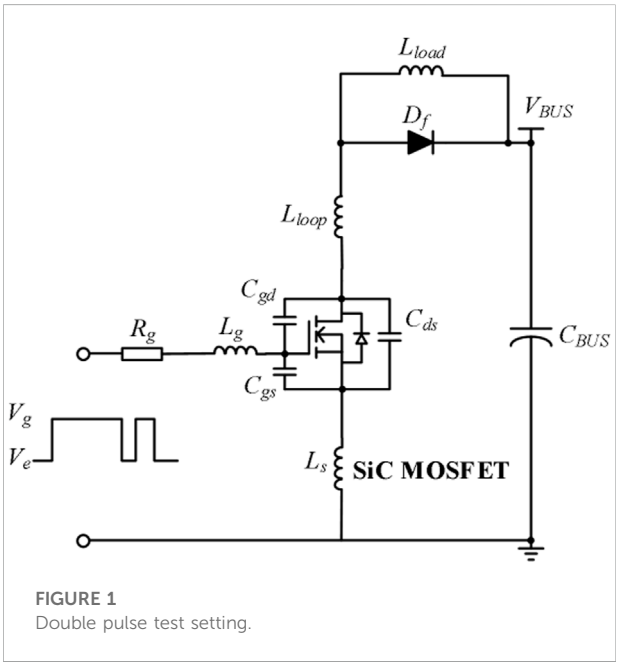

FIGURE 1
Double pulse test setting.

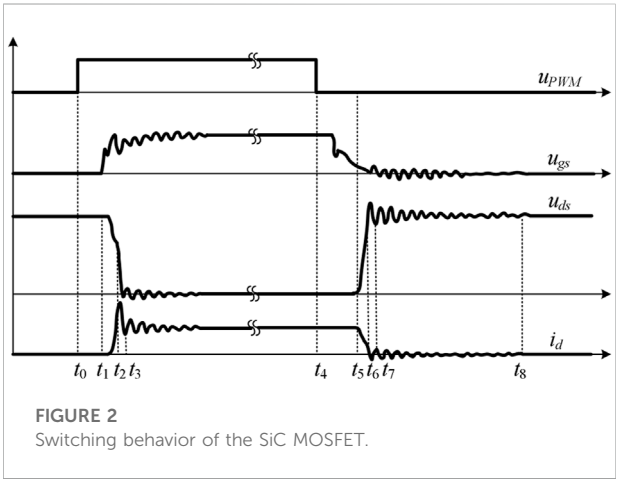

FIGURE 2
Switching behavior of the SiC MOSFET.

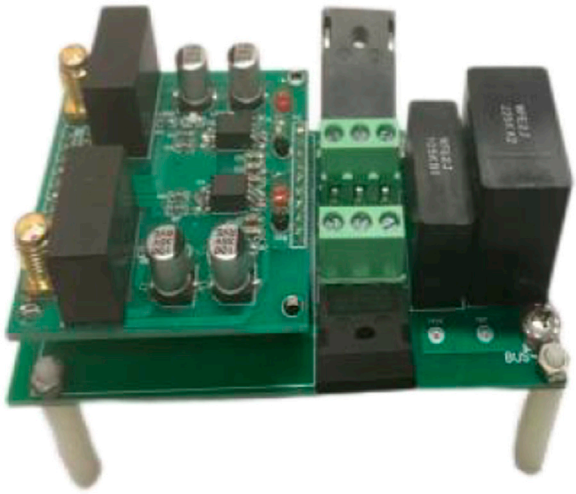

FIGURE 3
DPT prototype.

achieved in the SiC MOSFET. Table 1 shows the comparison of the key parameters between the SiC MOSFET and the Si IGBT. The Si IGBT (IXGH20N120B) and SiC MOSFET (C2M0080120D) are selected in the comparison because the power levels of the two devices are similar. In terms of the static characteristic, the on-state resistance of the SiC MOSFET is 80 mΩ, while the on-state voltage drop of the Si IGBT is 2.9 V, so the conduction loss of the SiC MOSFET is lower than that of the Si IGBT when the continuous conducting current is lower than 36.25 A. In terms of the dynamic characteristic, the gate charge and input capacitance of the SiC MOSFET are 62 nC and 950 pF, respectively, while those parameters of the Si IGBT are 72 nC and 1,700 pF, respectively. The lower gate charge and input capacitance of the SiC MOSFET mean that the SiC MOSFET can switch at a higher speed and frequency than those of the Si IGBT. It can be seen in Table 1 that the turn-on and turn-off switching losses of the SiC MOSFET are lower than those of the Si IGBT due to the high switching speed of the SiC MOSFET.

The high switching speed of the SiC MOSFET will cause overshoots, oscillations, and EMI during the ns-level switching transient. The driving parameters will influence the charging speed of the input capacitance, and the parasitic parameters will form resonant networks. In order to investigate the dynamic characteristics of the SiC MOSFET in detail, the double pulse test is carried out as follows.

2.2 Double pulse test

The dynamic characteristics of the power device are usually tested on the double pulse test (DPT) platform, which is built into PSpice software. The DPT setting is shown in Figure 1, where V_{BUS} is the bus voltage, C_{BUS} is the bus capacitor, L_{load} is the load inductor, D_f is the body diode of the SiC MOSFET, L_{loop} is the parasitic inductance in the loop, L_g is the inductance in the gate loop, L_s is the source inductance of the device, C_{gs} is the gate–source capacitance,

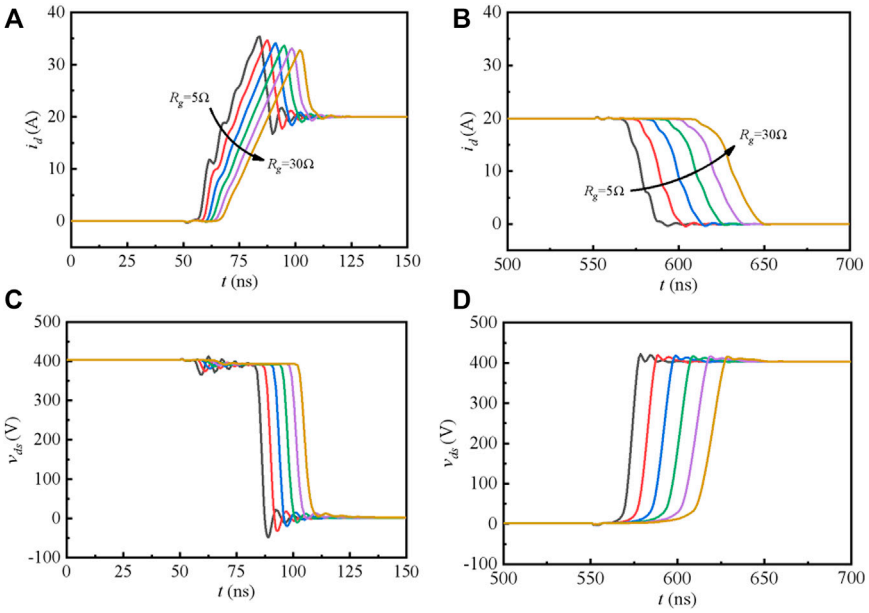

FIGURE 4
Influence of R_g on the switching behavior of the SiC MOSFET. **(A)** Turn-on i_d. **(B)** Turn-off i_d. **(C)** Turn-on u_{ds}. **(D)** Turn-off u_{ds}.

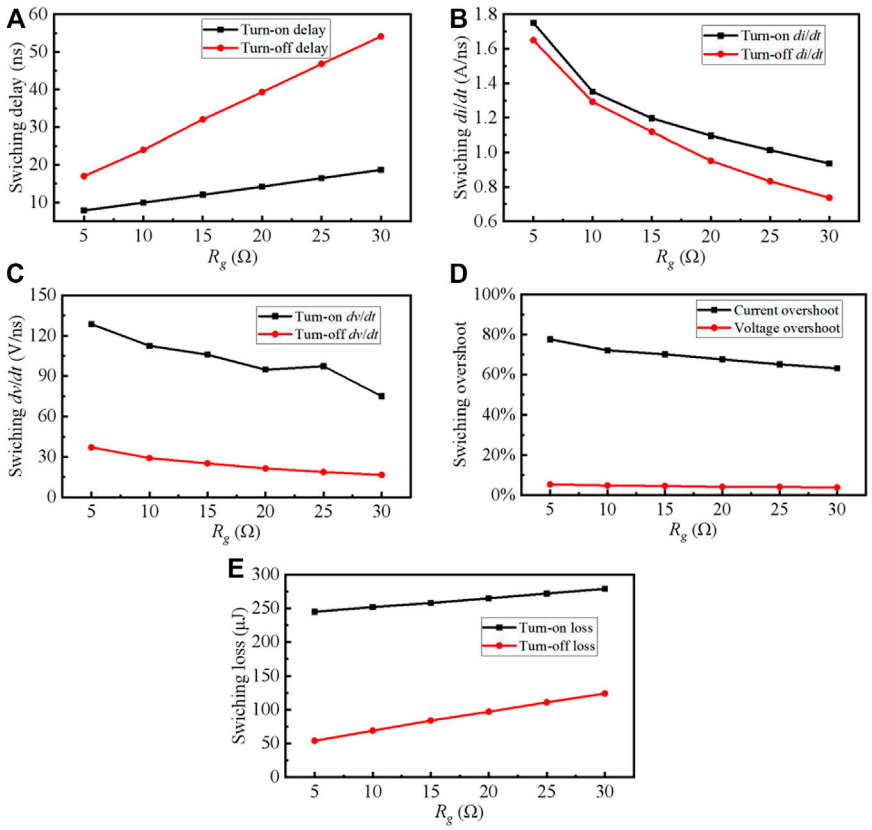

FIGURE 5
Dynamic characteristics of the SiC MOSFET with different R_g. **(A)** Switching delay. **(B)** Switching *di/dt*. **(C)** Switching *du/dt*. **(D)** Switching overshoot. **(E)** Switching loss.

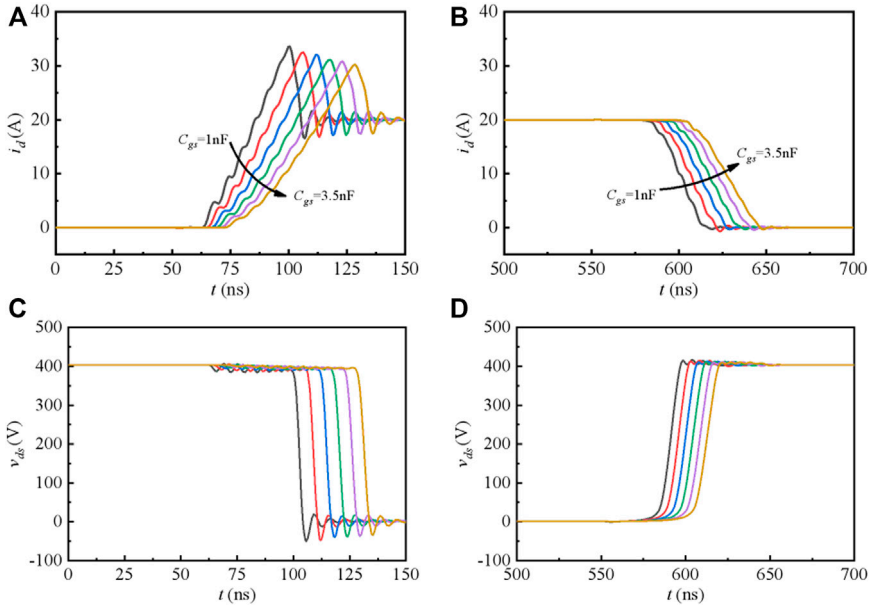

FIGURE 6
Influence of C_{gs} on the switching behavior of the SiC MOSFET. **(A)** Turn-on i_d. **(B)** Turn-off i_d. **(C)** Turn-on u_{ds}. **(D)** Turn-off u_{ds}.

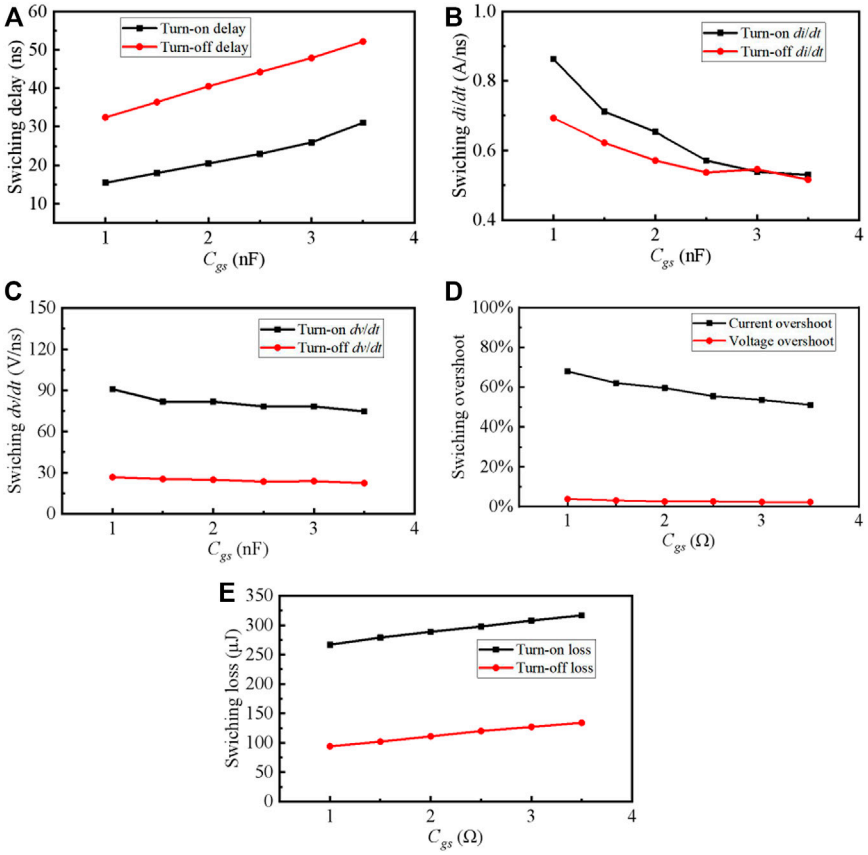

FIGURE 7
Dynamic characteristics of the SiC MOSFET with different C_{gs}. **(A)** Switching delay. **(B)** Switching di/dt. **(C)** Switching du/dt. **(D)** Switching overshoot. **(E)** Switching loss.

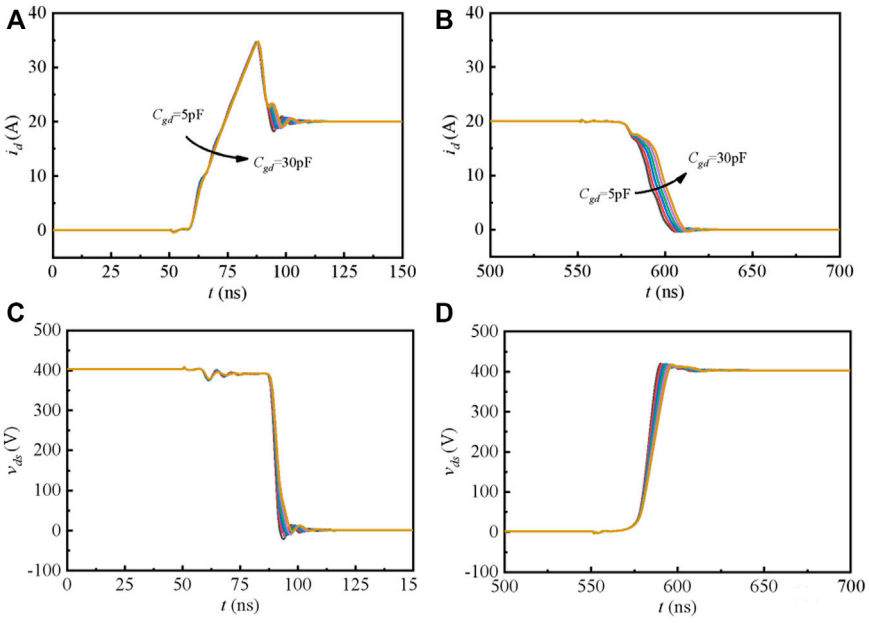

FIGURE 8
Influence of C_{gd} on the switching behavior of the SiC MOSFET. **(A)** Turn-on i_d. **(B)** Turn-off i_d. **(C)** Turn-on u_{ds}. **(D)** Turn-off u_{ds}.

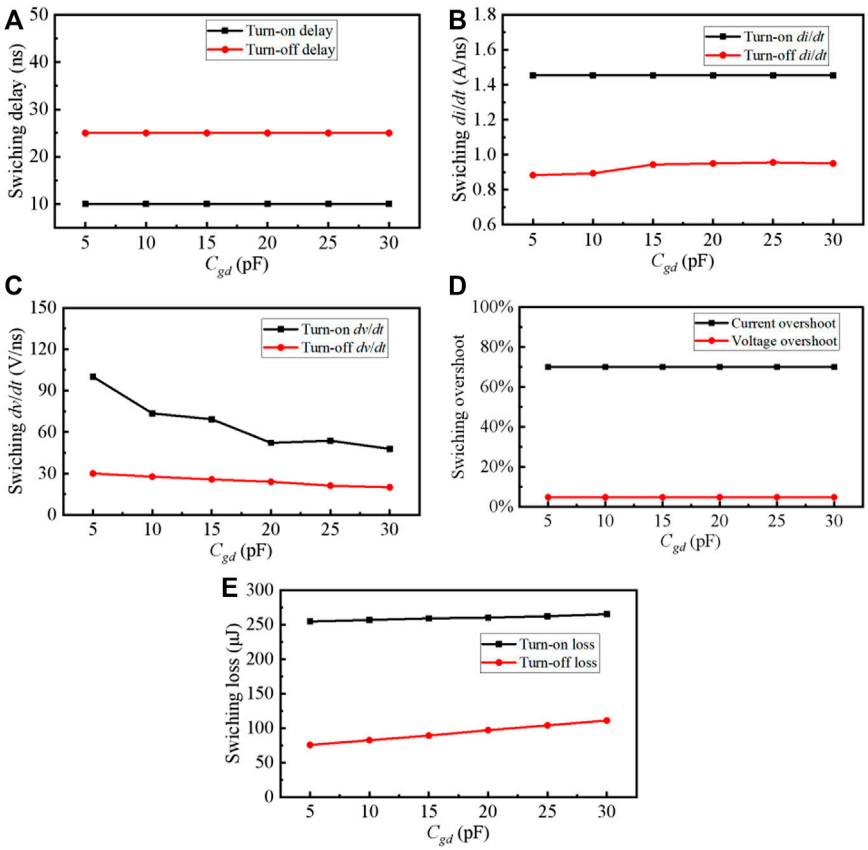

FIGURE 9
Dynamic characteristics of the SiC MOSFET with different C_{gd}. **(A)** Switching delay. **(B)** Switching *di*/*dt*. **(C)** Switching *du*/*dt*. **(D)** Switching overshoot. **(E)** Switching loss.

C_{gd} is the gate–drain capacitance, C_{ds} is the drain–source capacitance, R_g is the driving resistance, V_g is the positive driving voltage, and V_e is the negative driving voltage (Duan et al., 2018; Qin et al., 2018). The first driving pulse is used to establish the load current by turning on the SiC MOSFET, and the second pulse is used to observe the dynamic characteristics of the SiC MOSFET. It should be noted that R_g, C_{gs}, C_{gd}, and C_{ds} are changeable, and the parasitic inductances L_{loop}, L_g, and L_s are controllable during the design period.

2.3 Switching behaviors

The switching behavior of the SiC MOSFET can be represented by the waveforms of the gate–source voltage u_{gs}, the drain–source voltage u_{ds}, and the drain current i_d (Li et al., 2017; Huang et al., 2021; Xiong et al., 2022a). The key waveforms of the SiC MOSFET are shown in Figure 2.

It can be seen from Figure 2 that the turn-on behavior and turn-off behavior of the SiC MOSFET have the similar and symmetrical relationship. Both the turn-on and turn-off periods have five typical transients, namely, the delay period, the *di*/*dt* period, the *du*/*dt* period, the overshoot and oscillation period, and the state period (As detailed in Appendix A). The slew rate of the drain current is the cause of the overshoot for i_d and u_{ds}. In the turn-on transient, the reverse recovery of the body diode will cause the current overshoot, and it has

$$I_{peak} = \sqrt{\frac{2Q_{rr}\frac{di_d}{dt}}{S+1}}, \tag{1}$$

where I_{peak} is the peak value of i_d, Q_{rr} is the reverse recovery charge of the body diode, and S is the snappiness factor of the body diode. In the turn-off transient, the parasitic inductance in the loop will cause an obvious overshoot in u_{ds} (Wu et al., 2020; Zhao et al., 2020a; Qi et al., 2021), and it has

$$V_{peak} = L_{loop}\frac{di_d}{dt} + V_{BUS}. \tag{2}$$

The slew rate of the drain–source voltage u_{ds} is the cause for the crosstalk phenomena. When the SiC MOSFET switches at

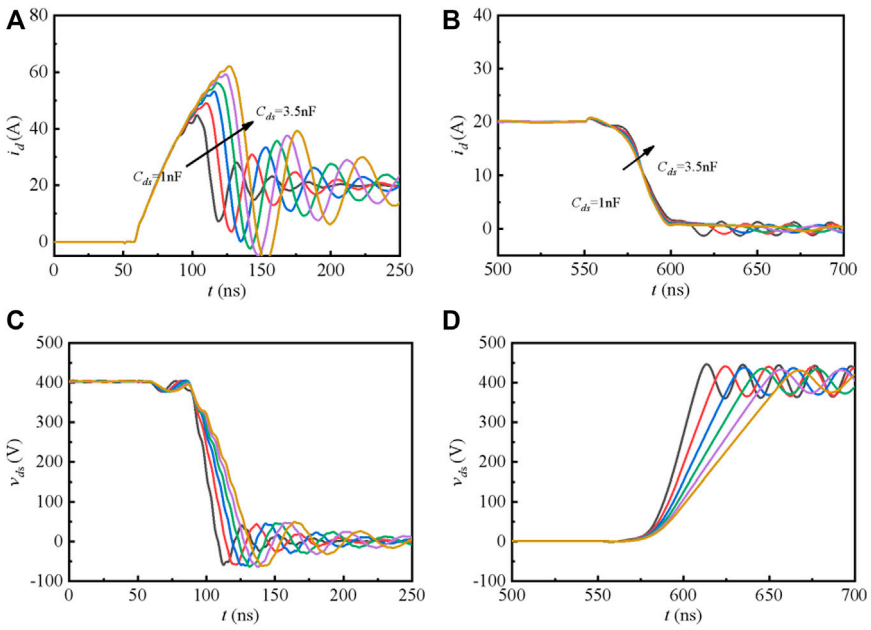

FIGURE 10
Influence of C_{ds} on the switching behavior of the SiC MOSFET. **(A)** Turn-on i_d. **(B)** Turn-off i_d. **(C)** Turn-on u_{ds}. **(D)** Turn-off u_{ds}.

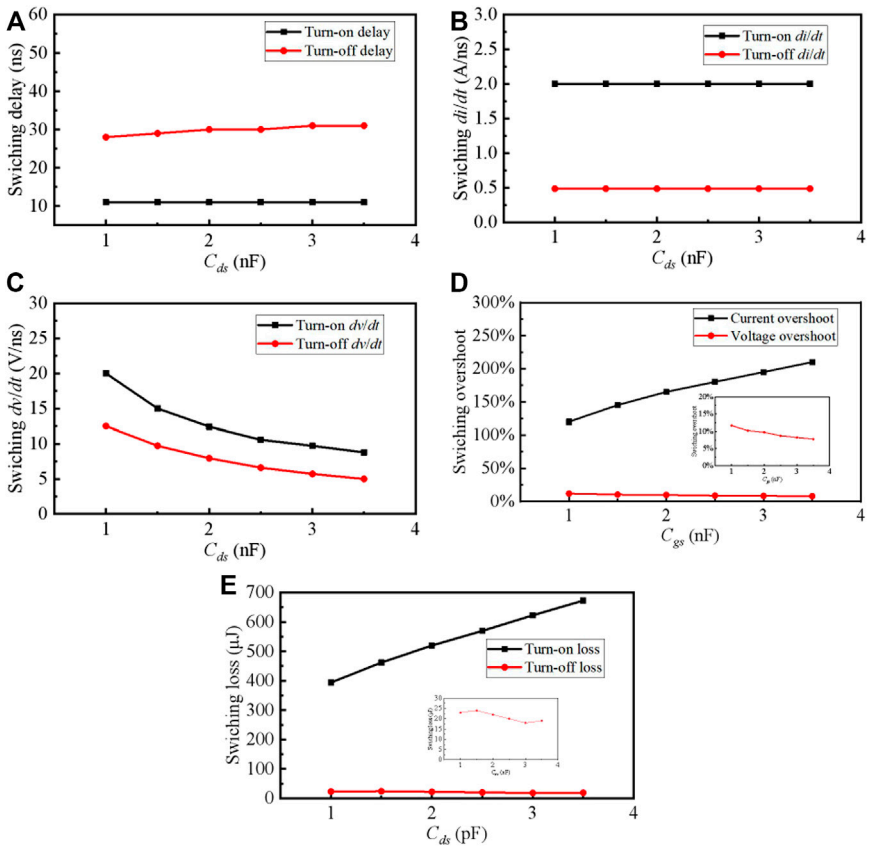

FIGURE 11
Dynamic characteristics of the SiC MOSFET with different C_{ds}. **(A)** Switching delay. **(B)** Switching *di*/*dt*. **(C)** Switching *du*/*dt*. **(D)** Switching overshoot. **(E)** Switching loss.

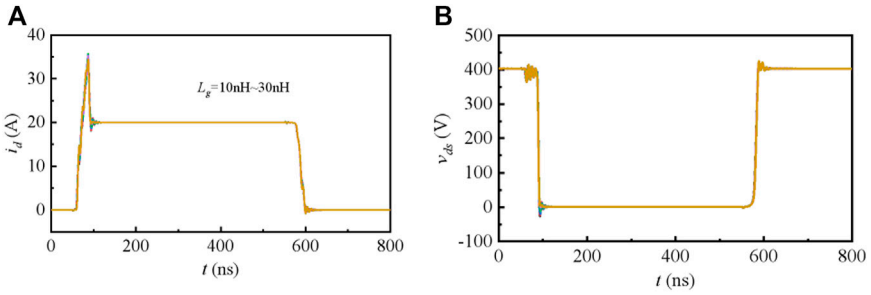

FIGURE 12
Influence of L_g on the switching behavior of the SiC MOSFET. **(A)** Turn-on and Turn-off of i_d. **(B)** Turn-off u_{ds}.

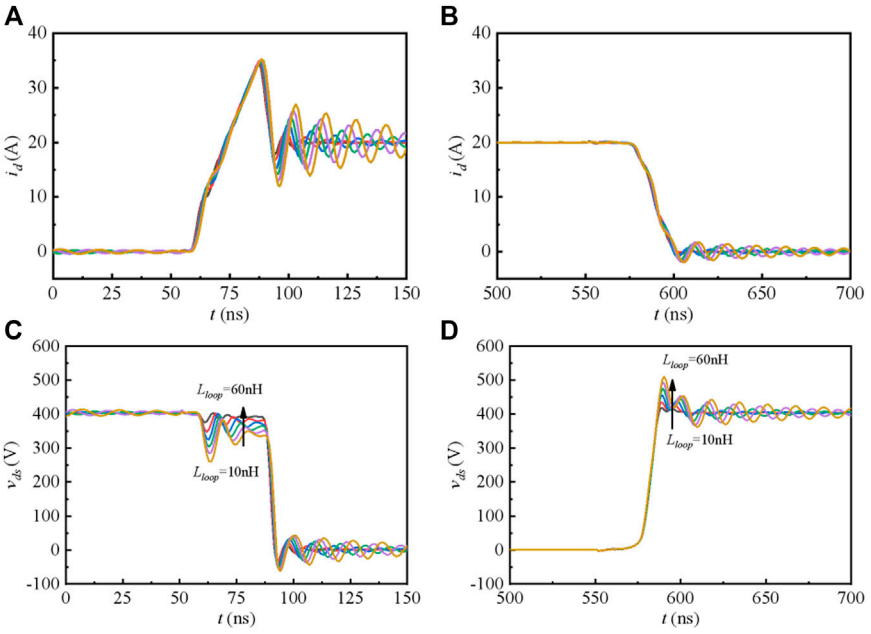

FIGURE 13
Influence of L_{loop} on the switching behavior of the SiC MOSFET. **(A)** Turn-on i_d. **(B)** Turn-off i_d. **(C)** Turn-on u_{ds}. **(D)** Turn-off u_{ds}.

high switch, the displacement current through C_{gd} will cause the false turn-on of the synchronization device (Roy and Basu, 2021), and the displacement current i_{gd} can be expressed as follows:

$$i_{gd} = C_{gd}\frac{du_{ds}}{dt}. \tag{3}$$

The switching behavior of the SiC MOSFET is directly related to the reliability of the device (Chen et al., 2021; Rashid et al., 2021). Therefore, it is important to carry out the comprehensive research about the influence of driving parameters and parasitic parameters on the switching behaviors of the SiC MOSFET.

3 Experiment results

The DPT prototype is applied to investigate the dynamic characteristics of the SiC MOSFET, as shown in Figure 3. The load inductance L_{load} is equal to 200 μH, the tested device is C2M0080120D of CREE, the bus voltage is equal to 400 V, and the load current is 20 A. The oscilloscope is DPO3054 (500 MHz), the current probe is TCP305 A (30 MHz), and the voltage probe is P6139 A (500 MHz). The bandwidth of the probe is enough for measuring the transients of u_{ds} and i_d.

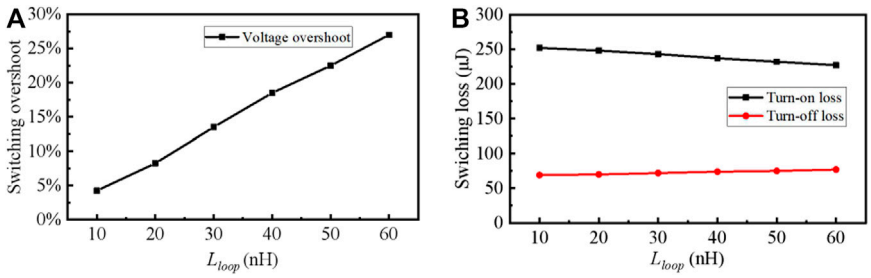

FIGURE 14
Dynamic characteristics of the SiC MOSFET with different L_{loop}. **(A)** Switching overshoot. **(B)** Switching loss.

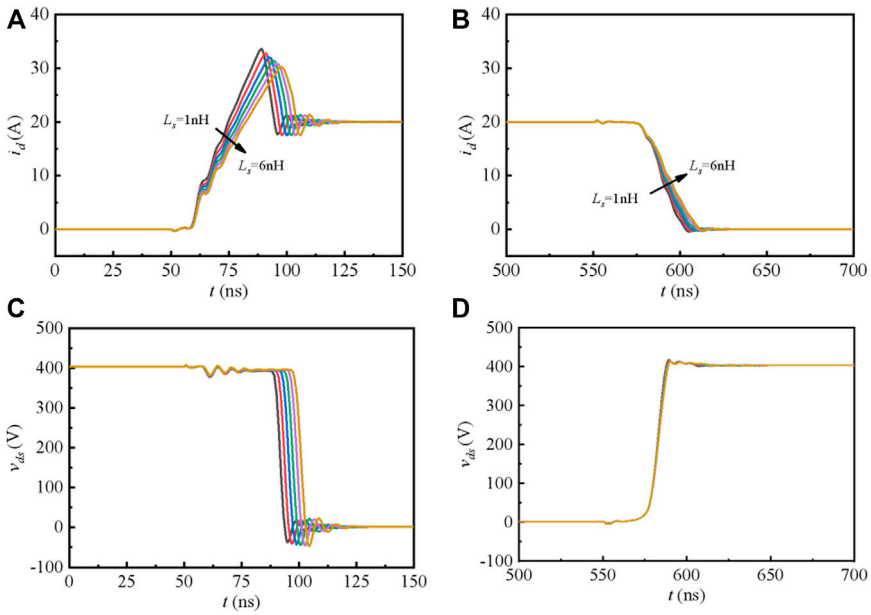

FIGURE 15
Influence of L_s on the switching behavior of the SiC MOSFET. **(A)** Turn-on i_d. **(B)** Turn-off i_d. **(C)** Turn-on u_{ds}. **(D)** Turn-off u_{ds}.

3.1 Influence of R_g

The gate driving R_g can be selected during the designing period. Figure 4 shows the waveforms of i_d and u_{ds} with different R_g, and Figure 5 presents the dynamic characteristics of the SiC MOSFET with different R_g. It is obvious that with the increase in R_g, the turn-on and turn-off delay of the device will increase because the charging time of the input capacitance increases. The slew rate of i_d and u_{ds} decreases with the increase of R_g, so the overshoot decreases and the device can operate at a slower speed. It is evident that both turn-on and turn-off losses increase with a larger R_g. Therefore, the worst efficiency of the converter occurs when a relatively large R_g is selected.

3.2 Influence of C_{gs}

The gate–source capacitance C_{gs} determines the delay time and the value of di/dt. As shown in Figure 6 and Figure 7, the influence of C_{gs} on the dynamic characteristics of the SiC MOSFET is similar to that of R_g. The switching speed will decrease if a larger C_{gs} is selected. It should be noted that the value of C_{gs} has no significant influence on the slew rate of u_{ds}.

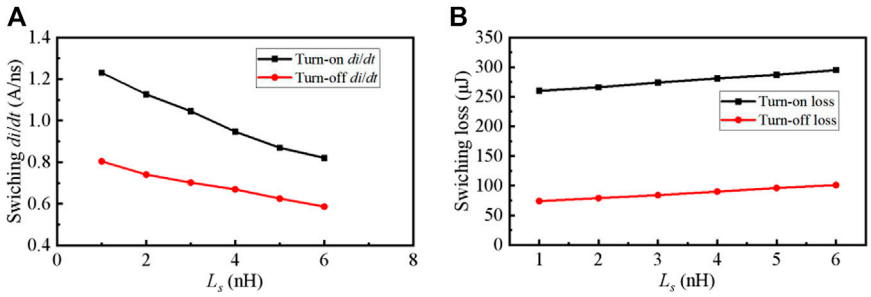

FIGURE 16
Dynamic characteristics of the SiC MOSFET with different L_s. **(A)** Switching *di*/*dt*. **(B)** Switching loss.

3.3 Influence of C_{gd}

The gate–drain capacitance C_{gd} determines the value of *du*/*dt*, which is also called the "Miller capacitance." The value of C_{gd} is far lower than the value of C_{gs} and C_{ds}, and a little change in C_{gd} will cause a significant change in the value of *du*/*dt*. Figure 8 shows the waveforms of i_d and u_{ds} with different C_{gd}, and Figure 9 presents the dynamic characteristics of the SiC MOSFET with different C_{gd}. It can be seen that delay and *di*/*dt* have no obvious relationship with the value of C_{gd}. However, *du*/*dt* will decrease with the increase of C_{gd}, which will cause an increase in switching losses in turn. It should be noted that though the value of *du*/*dt* decreases with a larger C_{gd}, no significant optimization of overshoot occurs, and the risk of false turn-on will increase.

3.4 Influence of C_{ds}

The drain–source capacitance C_{ds} can influence the value of *du*/*dt*, and there is no necessary relationship between C_{ds}, delay, and *di*/*dt*. The additional C_{ds} is applied to achieve the soft turn-off by increasing C_{ds}. As shown in Figure 10 and Figure 11, both turn-on and turn-off *du*/*dt* will decrease with the increase of C_{ds}, and the turn-off loss and turn-off voltage overshoot will decrease as a result. However, the energy stored in C_{ds} during the turn-off period will cause a significant current overshoot during the turn-on period, which means an obvious increase in the turn-on loss.

3.5 Influence of L_g

The gate inductance L_g is caused by the PCB trace of the gate loop. As shown in Figure 12, the value of L_g has a minor influence on the dynamic characteristics of the SiC MOSFET. However, L_g should be reduced as much as possible because L_g will result in the overshoot of u_{gs}, which risks the reliability of the gate.

3.6 Influence of L_{loop}

The gate inductance L_{loop} is caused by the PCB trace of the power loop. It is different to cancel the L_{loop}, even though the relatively short PCB trace is designed. The most significant drawback brought by L_{loop} is the larger voltage overshoot, which will cause the device to breakdown. As shown in Figure 13 and Figure 14, the value of L_{loop} only influences the oscillation frequency and the voltage overshoot. In order to enhance the reliability of the SiC MOSFET, L_{loop} should be reduced as much as possible. It should be noted that a larger L_{loop} will result in lower turn-on loss because the drain–source voltage will drop during the *di*/*dt* period. At the same time, the turn-off loss will increase with the larger L_{loop} due to the additional loss from the voltage overshoot.

3.7 Influence of L_s

The source inductance L_s exists in the gate loop and the power loop. As shown in Figure 15 and Figure 16, when the drain current i_d changes sharply, the induced voltage on L_s will slow down the switching speed as a negative feedback effect. Therefore, the larger L_s will cause lower *di*/*dt* during the switching transients. In order to reduce the switching losses, new type packages are provided by manufacturers, such as TO-247-4 and TO-263-7.

4 Conclusion

The SiC MOSFET is widely used in high-frequency and high-temperature applications, which helps to improve the efficiency and power density of the converter. However, the parasitic parameters will inevitably cause overshoot and oscillation of i_d and u_{ds}, which reduce the reliability of the SiC MOSFET. In this study, comprehensive research about the influence of driving parameters and parasitic parameters on the switching behaviors of the SiC MOSFET is carried out, and some valuable conclusions drawn are as follows:

1) The parasitic inductance should be reduced as much as possible by optimizing PCB traces and applying advanced packages
2) Different driving parameters will cause different dynamic responses of the SiC MOSFET, which should be considered according to special applications, respectively
3) The increase in C_{gd} is not recommended due to the higher risk of crosstalk

The influences of circuit parameters on the switching behaviors of the SiC MOSFET are listed as shown in Table 2.

Data availability statement

The original contributions presented in the study are included in the article/Supplementary Material; further inquiries can be directed to the corresponding author.

Author contributions

SZ: conceptualization, formal analysis, data curation, writing—original draft, visualization, and funding acquisition.

Funding

This work was supported by the Education Department Project of Shaanxi Province, China (20JK0614), and the Science and Technology Bureau Project of Shangluo City, China (2021-Z-0016).

Conflict of interest

The author declares that the research was conducted in the absence of any commercial or financial relationships that could be construed as a potential conflict of interest.

Publisher's note

All claims expressed in this article are solely those of the authors and do not necessarily represent those of their affiliated organizations, or those of the publisher, the editors, and the reviewers. Any product that may be evaluated in this article, or claim that may be made by its manufacturer, is not guaranteed or endorsed by the publisher.

References

Bonyadi, R., Alatise, O., Jahdi, S., Hu, J., Ortiz Gonzalez, J. A., Ran, L., et al. (2015). Compact electrothermal reliability modeling and experimental characte- rization of bipolar latchup in SiC and CoolMOS power MOSFETs. *IEEE Trans. Power Electron.* 30 (12), 6978–6992. doi:10.1109/tpel.2015.2388512

Camacho, A. P., Sala, V., Ghorbani, H., and Romeral, L. (2017). A novel active gate driver for improving SiC MOSFET switching trajectory. *IEEE Trans. Ind. Electron.* 11, 9032–9042. doi:10.1109/TIE.2017.2719603

Chen, X., Chen, W., Yang, X., Ren, Y., and Qiao, L. (2021). Common-mode EMI mathematical modeling based on inductive coupling theory in a power module with parallel-connected SiC MOSFETs. *IEEE Trans. Power Electron.* 36 (6), 6644–6661. doi:10.1109/TPEL.2020.3046658

Duan, Z., Fan, T., Wen, X., and Zhang, D. (2018). Improved SiC power MOSFET model considering nonlinear junction capacitances. *IEEE Trans. Power Electron.* 33 (3), 2509–2517. doi:10.1109/tpel.2017.2692274

Huang, H., Wang, N., Wu, J., and Lu, T. (2021). Radiated disturbance characteristics of SiC MOSFET module. *J. Power Electron.* 21 (2), 494–504. doi:10.1007/s43236.020-00187-4

Li, H., Munk-Nielsen, S., Beczkowski, S., and Wang, X. (2016). A novel DBC layout for current imbalance mitigation in SiC MOSFET multichip power modules. *IEEE Trans. Power Electron.* 31 (12), 8042–8045. doi:10.1109/tpel.2016.2562030

Li, X., Jiang, J., Huang, A. Q., Guo, S., Deng, X., Zhang, B., et al. (2017). A SiC power MOSFET loss model suitable for high-frequency applications. *IEEE Trans. Ind. Electron.* 64 (10), 8268–8276. doi:10.1109/tie.2017.2703910

Li, X., Lu, Y., Ni, X., Wang, S., Zhang, Y., and Tang, X. (2020). Novel driver circuit for switching performance improvements in SiC MOSFETs. *J. Power Electron.* 20 (6), 1583–1591. doi:10.1007/s43236-020-00132-5

Liu, T., Ning, R., Wong, T., and Shen, Z. J. (2016). Modeling and analysis of SiC MOSFET switching oscillations. *IEEE J. Emerg. Sel. Top. Power Electron.* 4 (3), 1–756. doi:10.1109/jestpe.2016.2587358

Mukunoki, Y., Konno, K., Matsuo, T., Horiguchi, T., Nishizawa, A., Kuzumoto, M., et al. (2018). An improved compact model for a silicon-carbide MOSFET and its application to accurate circuit simulation. *IEEE Trans. Power Electron.* 33 (11), 9834–9842. doi:10.1109/tpel.2018.2796583

Qi, J., Yang, X., Li, X., Chen, W., Long, T., Tian, K., et al. (2021). Comprehensive assessment of avalanche operating boundary of SiC planar/trench MOSFET in cryogenic applications. *IEEE Trans. Power Electron.* 36 (6), 6954–6966. doi:10.1109/tpel.2020.3034902

Qin, H., Ma, C., Zhu, Z., and Yan, Y. (2018). Influence of parasitic parameters on switching characteristics and layout design considerations of SiC MOSFETs. *J. Power Electron.* 18 (4), 1255–1267.

Rashid, A. U., Hossain, M. M., Emon, A. I., and Mantooth, H. A. (2021). Datasheet-driven compact model of silicon carbide power MOSFET including third-quadrant behavior. *IEEE Trans. Power Electron.* 36 (10), 11748–11762. doi:10.1109/tpel.2021.3062737

Riccio, M., Alessandro, V., Romano, G., Maresca, L., Breglio, G., and Irace, A. (2018). A temperature-dependent SPICE model of SiC power MOSFETs for within and out-of-SOA simulations. *IEEE Trans. Power Electron.* 33 (9), 8020–8029. doi:10.1109/TPEL.2017.2774764

Roy, S. K., and Basu, K. (2021). Analytical model to study turn-OFF soft switching dynamics of SiC MOSFET in a half-bridge configuration. *IEEE Trans. Power Electron.* 36 (11), 13039–13056. doi:10.1109/tpel.2021.3072329

Stark, R., Tsibizov, A., Nain, N., Grossner, U., and Kovacevic-Badstuebner, I. (2021). Accuracy of three interterminal capacitance models for SiC power MOSFETs under fast switching. *IEEE Trans. Power Electron.* 36 (8), 9398–9410. doi:10.1109/tpel.2021.3053330

Sun, J., Yuan, L., Duan, R., Lu, Z., and Zhao, Z. (2021). A semiphysical semibehavioral analytical model for switching transient process of SiC MOSFET module. *IEEE J. Emerg. Sel. Top. Power Electron.* 9 (2), 2258–2270. doi:10.1109/jestpe.2020.2992775

Talesara, V., Xing, D., Fang, X., Fu, L., Shao, Y., Wang, J., et al. (2020). Dynamic switching of SiC power MOSFETs based on analytical subcircuit model. *IEEE Trans. Power Electron.* 35 (9), 9680–9689. doi:10.1109/tpel.2020.2972453

Wang, X., Zhao, Z., Li, K., Zhu, Y., and Chen, K. (2019). Analytical methodology for loss calculation of SiC MOSFETs. *IEEE J. Emerg. Sel. Top. Power Electron.* 7 (1), 71–83. doi:10.1109/jestpe.2018.2863731

Wu, Y., Yin, S., Li, H., and Ma, W. (2020). Impact of RC snubber on switching oscillation damping of SiC MOSFET with analytical model. *IEEE J. Emerg. Sel. Top. Power Electron.* 8 (1), 163–178. doi:10.1109/jestpe.2019.2953272

Xie, Y., Chen, C., Yan, Y., Huang, Z., and Kang, Y. (2021). Investigation on ultralow turn-off losses phenomenon for SiC MOSFETs with improved switching model. *IEEE Trans. Power Electron.* 36 (8), 9382–9397. doi:10.1109/tpel.2021.3050544

Xiong, L. S., Liu, X. K., Liu, H. Q., and Liu, Y. (2022a). Performance comparison of typical frequency response strategies for power systems with high penetration of renewable energy sources. *IEEE J. Emerg. Sel. Top. Circuits Syst.* 12 (1), 41–47. doi:10.1109/jetcas.2022.3141691

Xiong, L. S., Liu, X. K., Liu, L., and Liu, Y. H. (2022b). Amplitude-phase detection for power converters tied to unbalanced grids with large X/R ratios. *IEEE Trans. Power Electron.* 37 (2), 1–2112. doi:10.1109/tpel.2021.3104591

Yang, P., Ming, W., Liang, J., Lüdtke, I., Berry, S., and Floros, K. (2022). Hybrid data-driven modeling metho- dology for fast and accurate transient simulation of SiC MOSFETs. *IEEE Trans. Power Electron.* 37 (1), 440–451. doi:10.1109/tpel.2021.3101713

Zeng, Z., and Li, X. (2018). Comparative study on multiple degrees of freedom of gate drivers for transient behavior regulation of SiC MOSFET. *IEEE Trans. Power Electron.* 33 (10), 8754–8763. doi:10.1109/tpel.2017.2775665

Zhao, C., Wang, L., and Zhang, F. (2020a). Effect of asymmetric layout and unequal junction temperature on current sharing of paralleled SiC MOSFETs with kelvin-source connection. *IEEE Trans. Power Electron.* 35 (7), 7392–7404. doi:10.1109/TPEL.2019.29547.16

Zhao, S., Dearien, A., Wu, Y., Farnell, C., Rashid, A. U., Luo, F., et al. (2020b). Adaptive multi-level active gate drivers for SiC power devices. *IEEE Trans. Power Electron.* 35 (2), 1882–1898. doi:10.1109/tpel.2019.2922112

Appendix A:

The turn-on current oscillation and the turn-off voltage oscillation are two critical phenomena when describing the switching behaviors of the SiC MOSFET (Li et al., 2020). The turn-on current resonance angle frequency and the resonance damping of the SiC MOSFET can be expressed as follows:

$$\omega_{on} = \frac{1}{\sqrt{L_{loop}\left(C_{oss} + C_L\right)}}, \tag{4}$$

$$\xi_{on} = \frac{R_{ds\_on}\left(C_{oss} + C_L\right)}{2\omega_{on}}. \tag{5}$$

The turn-off voltage resonance angle frequency and the resonance damping of the SiC MOSFET can be expressed as follows (Liu et al., 2016; Mukunoki et al., 2018):

$$\omega_{off} = \frac{1}{\sqrt{L_{loop}\left(C_{oss} + C_L\right)}}, \tag{6}$$

$$\xi_{off} = \frac{R_F}{2}\frac{1}{\omega_{off}L_{loop}} = \frac{R_F}{2}\sqrt{\frac{C_F + C_L}{L_{loop}}}, \tag{7}$$

where C_L is the output capacitance of the freewheeling diode and R_L is the equivalent on-state resistance of the freewheeling diode.

frontiers | Frontiers in Energy Research

TYPE Original Research
PUBLISHED 16 February 2023
DOI 10.3389/fenrg.2023.1112210

OPEN ACCESS

EDITED BY
Liansong Xiong,
Xi'an Jiaotong University, China

REVIEWED BY
Haitao Li,
Shandong University of Technology, China
Xiangbo Shu,
Nanjing University of Science and Technology, China

*CORRESPONDENCE
Jing Lu,
lujing@ipp.ac.cn

SPECIALTY SECTION
This article was submitted to Process and Energy Systems Engineering, a section of the journal Frontiers in Energy Research

RECEIVED 30 November 2022
ACCEPTED 16 January 2023
PUBLISHED 16 February 2023

CITATION
He R, Wu Y, Lu J, Li J, Zhang J, Tian Y and Wang P (2023), Harmonic analysis on direct-current side of tokamak power supply under asymmetrical triggering. *Front. Energy Res.* 11:1112210. doi: 10.3389/fenrg.2023.1112210

Harmonic analysis on direct-current side of tokamak power supply under asymmetrical triggering

Rui He[1,2], Yanan Wu[1], Jing Lu[1]*, Jun Li[1], Junmin Zhang[3], Yunxiang Tian[1,2] and Pengfei Wang[1,2]

[1]Institute of Plasma Physics, Chinese Academy of Sciences, Hefei, China, [2]University of Science and Technology of China, Hefei, China, [3]South-central University For Nationalities, Wuhan, China

Tokamak is a promising device for using nuclear fusion energy, and the triggering of Tokamak power supply has the characteristics of extreme asymmetry and drastic instantaneous change, which bring spectrum-rich harmonics to the DC side of the power supply, threatening the operational safety of the device. Although the harmonic analysis method of the DC side already exists, however, it still has the problem of cumbersome and inaccurate calculation when it is oriented to fusion power systems with complex operation modes. Based on the three-phase unified switching function, this paper introduces delay factor, and establishes a non-linear function model of converter suitable for the case of asymmetrical triggering. According to the principle of the switching function method, the frequency domain equation of the proposed model is obtained, then combined with power grid parameters, the harmonic analysis of the DC side can be derived. The correctness of the theoretical analysis is verified by comparing the calculation results with the harmonic frequency spectrum data obtained by direct Fourier decomposition of the DC side voltage.

KEYWORDS

fusion energy, tokamak, power supply, harmonic analysis, asymmetrical triggering

1 Introduction

Fusion energy could be the ultimate solution to the world energy crisis. Tokamak is the most promising magnetic confinement fusion device that has been adopted worldwide. Superconducting magnet is one of the most complex and important core components of the Tokamak device, and quench phenomenon can easily lead to the burning of the magnet, resulting in tens of millions of economic losses (Wang K et al., 2020; Lopes et al., 2021; Gorit et al., 2022). Accurate and effective quench detection is an important prerequisite for quench protection, which is crucial to the long-term safe and stable operation of the Tokamak device (Wang et al., 2018; Risse et al., 2019). To respond to the requirements of plasma millisecond-level fast control and variable magnetic field, the trigger control mode of converter of the Tokamak power supply exhibits the characteristic of extreme asymmetry and drastic instantaneous change (Xiong et al., 2021; Liu et al., 2022). This will bring a large number of sidelobe-rich, fast-changing non-characteristic harmonics on the superconducting magnet, which will drown the real quench signal, increase the risk of false alarms in quench detection, and affect the safe and stable operation of the Tokamak device (Lu et al., 2018; Wang Z M et al., 2020). In addition, the resonance phenomenon of

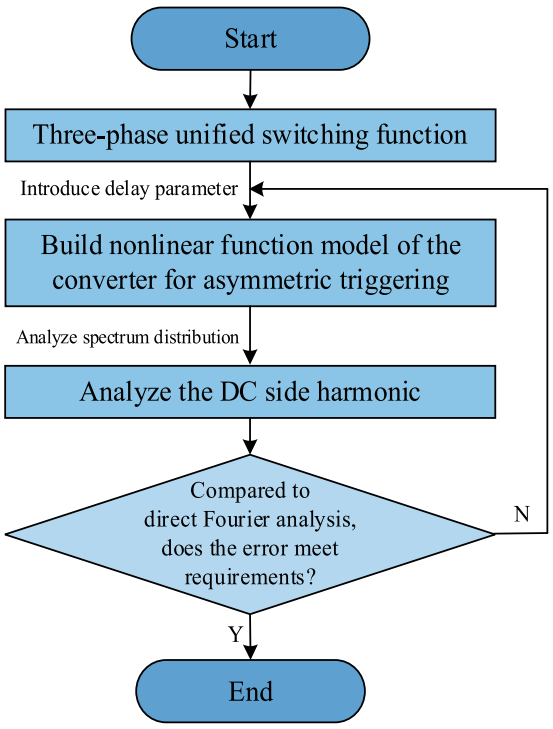

FIGURE 1
Flow chart of harmonic analysis on DC side.

the harmonics on the DC side will induce an inhomogeneous voltage distribution. It might even produce voltages high enough to damage the insulation between the superconducting magnet (Meguro et al., 2020; Sonoda et al., 2022).

At present, the generation and distribution of voltage harmonics in DC side of the Tokamak power supply are rarely studied. Hu and Yacamini (2016) first established the switching function, and analyzed the generation and conversion principle of 6*k*th harmonics on the DC side based on Fourier decomposition of the switching function, but did not analyze the non-characteristic subharmonics in the case of the asymmetrical triggering; Yang et al. (2009) uses the switching function method to analyze the voltage harmonics of DC side in the case of the asymmetrical triggering, but the function model used is relatively ideal, and the commutation overlap angle is not taken into account; Chen et al. (2022) improved the switching function, considered the commutation process, and proposed a more accurate three-phase unified switching function, but lacked further research on the trigger offset. Compared with direct Fourier decomposition of DC side voltage, the switching function method used in the above paper can simplify the harmonic analysis process and reduce the calculation amount because it uses a simple triangular transformation to replace the piecewise integration, and is more suitable for the working condition of rapid harmonic change of fusion power supply (Hu and Morrison, 1997). However, none of the models used in the switching function method can accurately describe the commutation process of the converter under an asymmetrical triggering, so it is also difficult to complete the analysis of voltage harmonics on the DC side.

This paper is organized as follows. Section 2 describes the composition of the poloidal field power supply of the EAST (Experimental Advanced Superconducting Tokamak) and analyzes the relationship between its output and the three-phase full-bridge controlled rectifier circuit. Based on the three-phase unified switching function, section 3 considers the influence of the asymmetrical triggering, introduces the delay factor, and establishes the non-linear function model of the converter suitable for the case of the asymmetrical triggering. In section 4, the frequency domain equation of the non-linear function model of the converter is obtained, then combined with power grid parameters, the DC side harmonic under asymmetrical triggering is analyzed and the calculation formula is derived. In section 5, the correctness of the theoretical analysis of section 4 is verified by comparing the calculation results with the harmonic frequency spectrum data obtained by direct Fourier decomposition of the DC side voltage. Finally, some discussions and conclusions are summarized in sections 6 and 7. The flow chart of harmonic analysis on DC side is shown in Figure 1.

2 The tokamak power supply

This paper takes the Tokamak power supply as the research object. In the EAST device, the four-quadrant thyristor converter is used as the poloidal field power supply to provide ±15 kA DC current to the magnet (Chen et al., 2016), as shown in Figure 2.

Its basic unit is a three-phase full-bridge controlled rectifier circuit, as shown in Figure 3, in the figure: u_a, u_b, u_c are three-phase voltages; i_a, i_b, i_c are three-phase currents; u_d and i_d are the voltage and current of the DC side. R is the equivalent resistance and L is the equivalent inductance.

In an ideal situation, the AC(Alternating Current) power supply can be considered as a three-phase symmetrical industrial frequency sine wave voltage, and the harmonics of the power supply itself are ignored (Liu et al., 2020; Liu et al., 2022). When the device is in a stable working state, the three-phase phase voltage is expressed as in Equation 1.

$$\begin{cases} u_a = U_m \sin \omega t \\ u_b = U_m \sin\left(\omega t - \dfrac{2\pi}{3}\right) \\ u_c = U_m \sin\left(\omega t + \dfrac{2\pi}{3}\right) \end{cases} \tag{1}$$

where U_m is the voltage amplitude, $\omega = 2\pi/T$ is the angular frequency, and T is the period.

In the EAST poloidal field four-quadrant thyristor converter, except PS(Power Supply)7, PS8 power supply, the difference between the two windings on the valve side of PS1, 2, 3, 4, 5, 6, 9, 10 and 11, 12 power supply is π rad. The forward converter is composed of TC(Thyristor Converter)11 and TC12 two groups of three-phase full-bridge controlled rectifier circuit, and the reverse converter is composed of TC21 and TC22, which are connected to the two valve side windings of the transformer respectively. The in-phase anti-parallel structure is formed during high current operation, and the DC side output of the superconducting magnet power supply for Tokamak is equivalent to the

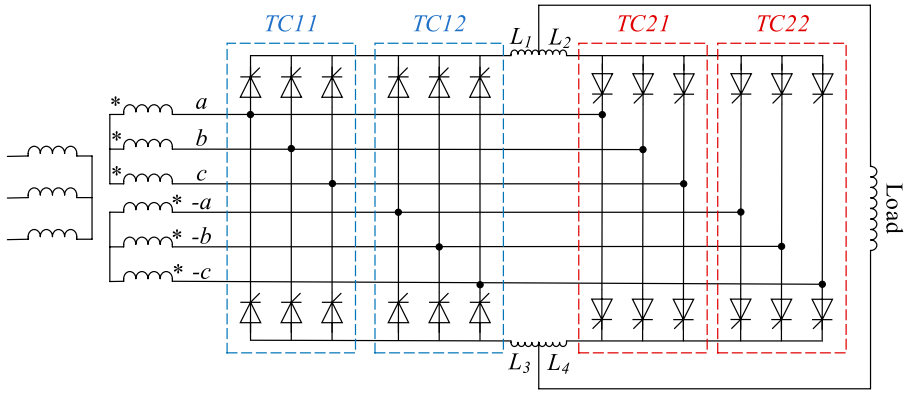

FIGURE 2
The four-quadrant thyristor converter in the EAST poloidal field.

superposition of the outputs of two three-phase full-bridge controlled rectifier with a phase difference of π rad (Chen et al., 2016; Wang et al., 2019).

$$U_d = u_d(\omega t) + u_d(\omega t - \pi) \tag{2}$$

Next, we take the three-phase full-bridge controlled rectifier as an example to study, and then consider the phase relationship between the primary and secondary sides of the converter transformer and then superimpose it.

3 The non-linear function model of converter for asymmetrical triggering

Since the commutation process cannot be completed instantaneously in the actual situation, Chen et al. (2022) further considers the commutation overlap angle γ on the basis of the traditional switching function, and obtains a three-phase unified switching function. On this basis, the natural commutation point is used as the starting point for calculating the firing angle α of each thyristor, and the expression of the non-linear function model of the converter f_i (i = 1,2,3,4,5,6) of the rectifier circuit is obtained as Equation 3

$$f_i = \begin{cases} \frac{P_2}{P_1}\left(\alpha + \frac{(2i-1)\pi}{6} \le \omega t \le \alpha + \gamma + \frac{(2i-1)\pi}{6}\right) \\ 1\left(\alpha + \gamma + \frac{(2i-1)\pi}{6} \le \omega t \le \alpha + \frac{(2i+3)\pi}{6}\right) \\ \frac{P_3}{P_1}\left(\alpha + \frac{(2i+3)\pi}{6} \le \omega t \le \alpha + \gamma + \frac{(2i+3)\pi}{6}\right) \end{cases} \tag{3}$$

Where

$$P_1 = \cos\left(\alpha + \frac{\pi}{6}\right) - \cos\left(\alpha + \gamma + \frac{\pi}{6}\right)$$
$$P_2 = \cos\left(\alpha + \frac{\pi}{6}\right) - \cos\left(\omega t - \frac{(i-1)\pi}{3}\right)$$
$$P_3 = \cos\left(\omega t - \frac{(i+1)\pi}{3}\right) - \cos\left(\alpha + \gamma + \frac{\pi}{6}\right)$$

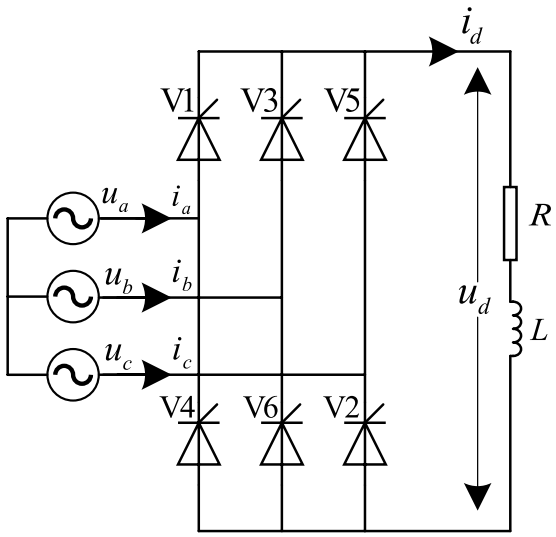

FIGURE 3
Three-phase full-bridge controlled rectifier circuit.

The time domain waveform diagram of the non-linear function model of the converter f_i (i = 1,2,3,4,5,6) in the case of the asymmetrical triggering is shown in Figure 4.

To meet the requirements of the current feedback control of the superconducting magnet, the fusion converter must be able to switch the angle quickly within the firing angle range, so the conduction time of each thyristor is different. When the firing angle of one of the six thyristors changes, only the non-linear function model of itself and its previous thyristor changes correspondingly, while the rest do not change. For example, the firing angle of a certain thyristor lags behind the normal firing angle of σ degrees. Affected by this, the non-linear function model of the previous thyristor will also change correspondingly, and its conduction time will be extended by the angle of σ. If the firing angle is ahead of the normal conduction angle, you can

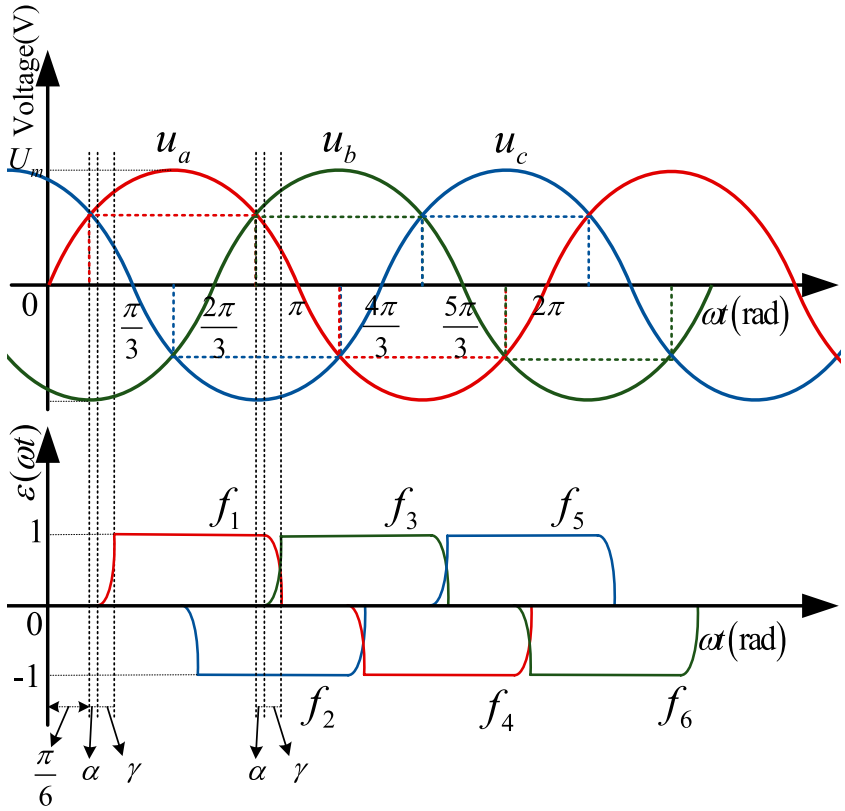

FIGURE 4
The time domain waveform diagram of three-phase voltage and the non-linear function model of converter under symmetrical triggering.

substitute -σ into the calculation, and other analysis procedures are the same.

Assuming that the conduction time of a thyristor will be shortened under the condition of the firing angle delay, the non-linear function model of the converter is f_i^-, and its expression is:

$$f_i^- = \begin{cases} \frac{P_5}{P_4}\left(\alpha+\sigma+\frac{(2i-1)\pi}{6} \le \omega t \le \alpha+\sigma+\gamma+\frac{(2i-1)\pi}{6}\right) \\ 1\left(\alpha+\sigma+\gamma+\frac{(2i-1)\pi}{6} \le \omega t \le \alpha+\frac{(2i+3)\pi}{6}\right) \\ \frac{P_3}{P_1}\left(\alpha+\frac{(2i+3)\pi}{6} \le \omega t \le \alpha+\gamma+\frac{(2i+3)\pi}{6}\right) \end{cases} \quad (4)$$

Where

$$P_4 = \cos\left(\alpha+\sigma+\frac{\pi}{6}\right) - \cos\left(\alpha+\sigma+\gamma+\frac{\pi}{6}\right)$$
$$P_5 = \cos\left(\alpha+\sigma+\frac{\pi}{6}\right) - \cos\left(\omega t - \frac{(i-1)\pi}{3}\right)$$

Because of the triggering delay of the latter thyristor, the conduction time of the former thyristor will inevitably become longer. Let the non-linear function model of this thyristor be f_i^+, and its expression is:

$$f_i^+ = \begin{cases} \frac{P_2}{P_1}\left(\alpha+\frac{(2i-1)\pi}{6} \le \omega t \le \alpha+\gamma+\frac{(2i-1)\pi}{6}\right) \\ 1\left(\alpha+\gamma+\frac{(2i-1)\pi}{6} \le \omega t \le \alpha+\sigma+\frac{(2i+3)\pi}{6}\right) \\ \frac{P_6}{P_4}\left(\alpha+\sigma+\frac{(2i+3)\pi}{6} \le \omega t \le \alpha+\sigma+\gamma+\frac{(2i+3)\pi}{6}\right) \end{cases} \quad (5)$$

Where

$$P_6 = -\cos\left(\alpha+\sigma+\gamma+\frac{\pi}{6}\right) + \cos\left(\omega t - \frac{(i+1)\pi}{3}\right)$$

The time domain waveform diagram of the non-linear function model of the converter f_i (i = 1,2,3,4,5,6) in the case of the asymmetrical triggering is shown in Figure 5.

4 Analysis of DC side harmonics

4.1 The principle of switching function method

The general method to analyze the harmonic characteristics of a non-sinusoidal periodic voltage (or current) is to directly perform Fourier decomposition on it. But to integrate the voltage or current in

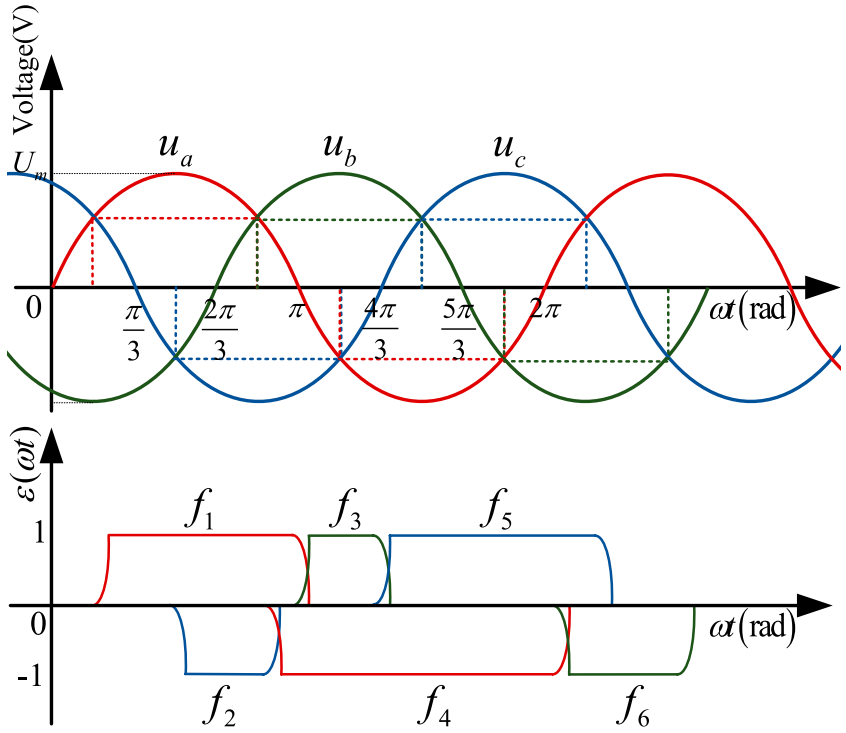

FIGURE 5
The time domain waveform diagram of three-phase voltage and the non-linear function model of converter under asymmetrical triggering.

a cycle to calculate the Fourier coefficient, the operation process is complicated and the amount of operation is large. Because the converter equipment has discrete sampling and modulation switching characteristics, the piecewise integration can be replaced by a simple triangular transformation, which can simplify the analysis process of the converter equipment related waveforms. This method of harmonic analysis for steady-state operation of converter equipment is called switching function method.

Fourier analysis of the non-linear function model of converter f_i (i = 1,2,3,4,5,6) is performed according to the definition:

$$f_i = a_0 + \sum_{n=1}^{\infty} (a_n \cos n\omega t + b_n \sin n\omega t) \tag{6}$$

Among them, a_0, a_n, b_n are Fourier coefficients, and using the orthogonality of trigonometric functions, the calculation formulas of a_0, a_n, b_n can be obtained as:

$$\begin{cases} a_0 = \frac{1}{T}\int_{-\frac{T}{2}}^{\frac{T}{2}} f_i(\omega t)d\omega t \\ a_n = \frac{2}{T}\int_{-\frac{T}{2}}^{\frac{T}{2}} f_i(\omega t)\cos n\omega t d\omega t \\ b_n = \frac{2}{T}\int_{-\frac{T}{2}}^{\frac{T}{2}} f_i(\omega t)\sin n\omega t d\omega t \end{cases} \tag{7}$$

The DC side voltage waveform of the converter is the result of modulating the AC voltage by the non-linear function model of the converter, During normal operation, each converter valve is triggered and turned on in turn at equal intervals, and the output DC voltage u_d is formed by modulating the input three-phase AC voltages u_a, u_b, u_c by the non-linear function models of converter f_1~f_6:

$$u_d = (f_1 - f_4)u_a + (f_3 - f_6)u_b + (f_5 - f_2)u_c \tag{8}$$

4.2 The frequency domain equation of the non-linear function model of converter

Fourier decomposition is performed on the proposed model f_i according to the principle of switching function method under the symmetrical triggering. a_0, a_n, b_n are calculated and substituted into Equation 6, and the sine and cosine terms of the same frequency are combined to obtain:

$$f_i = \frac{1}{3} + \sum_{n=1}^{\infty}\sum_{j=1}^{7} A_j \cos(n\omega t - \varphi_j) \tag{9}$$

In the equation, A_j and φ_j (j = 1,2,3,4,5,6,7) are as follows, where A_4 = -A_3, A_6 = -A_5. when n is 1 in Equation 9, the denominator of A_5 and A_6 will be zero, the equation will become meaningless. At this time, only limit operation needs to be done, that is, use $\lim_{n\to 1} A_5 = \frac{\gamma}{2\pi P_1}$ and $\lim_{n\to 1} A_6 = \frac{-\gamma}{2\pi P_1}$ to replace A_5 and A_6 for operation.

$$A_1 = \frac{2}{n\pi P_1}\sin\frac{n\gamma}{2}\cos\left(\alpha+\frac{\pi}{6}\right)\ \varphi_1 = n\left(\alpha+\frac{\gamma}{2}+\frac{2i-1}{6}\pi\right)$$

$$A_2 = -\frac{2}{n\pi P_1}\sin\frac{n\gamma}{2}\cos\left(\alpha+\gamma+\frac{\pi}{6}\right)\ \varphi_2 = n\left(\alpha+\frac{\gamma}{2}+\frac{2i+3}{6}\pi\right)$$

$$A_3 = -\frac{1}{(n+1)\pi P_1}\sin\frac{(n+1)\gamma}{2}\ \varphi_3 = (n+1)\left(\alpha+\frac{\gamma}{2}\right)+\frac{n(2i-1)+1}{6}\pi$$

$$A_5 = -\frac{1}{(n-1)\pi P_1}\sin\frac{(n-1)\gamma}{2}\varphi_4 = (n+1)\left(\alpha+\frac{\gamma}{2}\right)+\frac{n(2i+3)+1}{6}\pi$$

$$A_7 = \frac{2}{n\pi}\sin\frac{n(2\pi-3\gamma)}{6}\ \varphi_5 = (n-1)\left(\alpha+\frac{\gamma}{2}\right)+\frac{n(2i-1)-1}{6}\pi$$

$$\varphi_6 = (n-1)\left(\alpha+\frac{\gamma}{2}\right)+\frac{n(2i+3)-1}{6}\pi\ \varphi_7 = n\left(\alpha+\frac{\gamma}{2}+\frac{2i+1}{6}\pi\right)$$

Fourier decomposition is performed on f_i^- *and* f_i^+ in the same way under asymmetrical triggering.

$$f_i^- = -\frac{1}{2\pi}\left(\sigma+\gamma+\frac{Q_1}{P_1}-\frac{Q_2}{P_4}-\frac{2\pi}{3}\right)+\sum_{n=1}^{\infty}\sum_{j=1}^{7}B_j\cos\left(n\omega t-\theta_j\right) \tag{10}$$

$$f_i^+ = \frac{1}{2\pi}\left(\sigma-\gamma+\frac{Q_3}{P_1}-\frac{Q_4}{P_4}+\frac{2\pi}{3}\right)+\sum_{n=1}^{\infty}\sum_{j=1}^{7}C_j\cos\left(n\omega t-\eta_j\right) \tag{11}$$

Where Q_1, Q_2, Q_3, Q_4, B_j, C_j and θ_j, η_j (j = 1,2,3,4,5,6,7) are as follows, $B_2 = A_2$, $\theta_2 = \varphi_2$, $B_4 = A_4$, $\theta_4 = \varphi_4$, $B_6 = A_6$, $\theta_6 = \varphi_6$, $C_1 = A_1$, $\eta_1 = \theta_1$, $C_3 = A_3$, $\eta_3 = \theta_3$, $C_5 = A_5$, $\eta_5 = \theta_5$, $\eta_7 = \theta_7$:

$$B_1 = \frac{2}{n\pi P_4}\sin\frac{n\gamma}{2}\cos\left(\alpha+\sigma+\frac{\pi}{6}\right)\ \theta_1 = n\left(\alpha+\sigma+\frac{\gamma}{2}+\frac{2i-1}{6}\pi\right)$$

$$B_3 = -\frac{1}{(n+1)\pi P_4}\sin\frac{(n+1)\gamma}{2}\theta_3 = (n+1)\left(\alpha+\sigma+\frac{\gamma}{2}\right)+\frac{n(2i-1)+1}{6}\pi$$

$$B_5 = -\frac{1}{(n-1)\pi P_4}\sin\frac{(n-1)\gamma}{2}\theta_5 = (n-1)\left(\alpha+\sigma+\frac{\gamma}{2}\right)+\frac{n(2i-1)-1}{6}\pi$$

$$B_7 = \frac{2}{n\pi}\sin\frac{n(2\pi-3\gamma-3\sigma)}{6}\ \theta_7 = n\left(\alpha+\frac{\gamma+\sigma}{2}+\frac{2i+1}{6}\pi\right)$$

$$Q_1 = \gamma\cos\left(\alpha+\gamma+\frac{\pi}{6}\right)-2\cos\left(\alpha+\frac{\gamma}{2}+\frac{\pi}{6}\right)\sin\frac{\gamma}{2}$$

$$Q_2 = \gamma\cos\left(\alpha+\sigma+\frac{\pi}{6}\right)-2\cos\left(\alpha+\sigma+\frac{\gamma}{2}+\frac{\pi}{6}\right)\sin\frac{\gamma}{2}$$

When n is 1 in Equation 10, the denominator of B_5 and B_6 will be zero, the equation will become meaningless. At this time, only limit operation needs to be done, that is, use $\lim_{n\to1} B_5 = \frac{-\gamma}{2\pi P_4}$ and $\lim_{n\to1} B_6 = \frac{-\gamma}{2\pi P_1}$ to replace B_5 and B_6 for operation.

$$C_2 = -\frac{2}{n\pi P_4}\sin\frac{n\gamma}{2}\cos\left(\alpha+\sigma+\gamma+\frac{\pi}{6}\right)\quad \eta_2 = n\left(\alpha+\sigma+\frac{\gamma}{2}+\frac{2i+3}{6}\pi\right)$$

$$C_4 = \frac{1}{(n+1)\pi P_4}\sin\frac{(n+1)\gamma}{2}\quad \eta_4 = (n+1)\left(\alpha+\sigma+\frac{\gamma}{2}+\frac{n(2i+3)+1}{6}\pi\right)$$

$$C_6 = \frac{1}{(n-1)\pi P_4}\sin\frac{(n-1)\gamma}{2}\quad \eta_6 = (n-1)\left(\alpha+\sigma+\frac{\gamma}{2}+\frac{n(2i+3)-1}{6}\pi\right)$$

$$C_7 = \frac{2}{\pi P_4}\sin\frac{n(2\pi-3\gamma+3\alpha)}{2}\quad Q_3 = \gamma\cos\left(\alpha+\frac{\pi}{6}\right)-2\cos\left(\alpha+\frac{\gamma}{2}+\frac{\pi}{6}\right)\sin\frac{\gamma}{2}$$

$$Q_4 = \gamma\cos\left(\alpha+\sigma+\gamma+\frac{\pi}{6}\right)-2\cos\left(\alpha+\sigma+\frac{\gamma}{2}+\frac{\pi}{6}\right)\sin\frac{\gamma}{2}$$

When n is 1 in Equation 11, the denominator of C_5 and C_6 will be zero, the equation will become meaningless. At this time, only limit operation needs to be done, that is, use $\lim_{n\to1} C_5 = \frac{\gamma}{2\pi P_1}$ and $\lim_{n\to1} C_6 = \frac{\gamma}{2\pi P_4}$ to replace C_5 and C_6 for operation.

4.3 Harmonic analysis under asymmetrical triggering

First, according to Equation 7, calculate the values of a_0, a_1, b_1 when n is 1, and substitute them into Equation 6. Combined with Equation 8, it is found that the result of modulating the AC voltage by the fundamental component of the non-linear function model of the converter does not change with time, that is, the DC component in the output voltage, and its expression is Equation 12.

$$\begin{aligned}u_z = \frac{6U_m}{\pi}\Big[&\sin\frac{2\pi-3\gamma}{6}\ \cos\left(\alpha+\frac{\gamma}{2}\right)\\&+\frac{1}{P_1}\left(\sin\frac{\gamma}{2}\left(\cos\left(\alpha+\gamma+\frac{\pi}{6}\right)\cos\left(\alpha+\gamma+\frac{4\pi}{3}\right)\right.\right.\\&\left.-\cos\left(\alpha+\frac{\pi}{6}\right)\cos\left(\alpha+\frac{\gamma}{2}+\frac{2\pi}{3}\right)\right)\\&+\frac{\sqrt{3}}{4}\left(\sin\gamma\sin\left(2\alpha+\gamma+\frac{7\pi}{6}\right)+\frac{\gamma}{2}\right)\Big)\Big]\end{aligned} \tag{12}$$

When n is a positive integer that is not equal to 1, combine Equation 2 to obtain f_1-f_4, f_3-f_6, f_5-f_2 and substitute them into Equation 8 to obtain:

When the harmonic order n of the non-linear function model of the converter is 5, 11, 17... 6k-1 (k = 1, 2, 3...) times, the DC side will generate n+1st harmonics:

$$u_{n+1} = -\frac{3}{2}U_m\sum_{j=1}^{7}D_j\cos\left((n+1)\omega t+\phi_j\right) \tag{13}$$

When the harmonic order n of the non-linear function model of the converter is 7, 13, 19... 6k+1 (k = 1, 2, 3...) times, the DC side will generate n-1st harmonics:

$$u_{n-1} = \frac{3}{2}U_m\sum_{j=1}^{7}D_j\cos\left((n-1)\omega t+\phi_j\right) \tag{14}$$

In Equations (13) and (14) $D_j = A_j\ R_j$, where R_j, ϕ_j are as follows:

$$R_j = \sqrt{\left(\sin\varphi_{i=1,j}-\sin\varphi_{i=4,j}\right)^2+\left(\cos\varphi_{i=1,j}-\cos\varphi_{i=4,j}\right)^2}$$

$$\phi_j = \tan^{-1}\frac{\sin\varphi_{i=1,j}-\sin\varphi_{i=4,j}}{\cos\varphi_{i=1,j}-\cos\varphi_{i=4,j}}$$

From Eqs. 13, 14, it can be known that the n = 6k±1st harmonic of the non-linear function model of the converter modulates the AC voltage so that the DC side only contains the 6kth characteristic harmonic component in addition to the DC component. Therefore any 6kth harmonics on the DC side can be regarded as the superposition of u_{n+1} at n = 6k-1 and u_{n-1} at n = 6k+1.

If σ = 0 in Eqs. 4, 5, it can be seen the expression is the same as that when the trigger signal is symmetrical, so the symmetrical triggering operation is regarded as a special case of the asymmetrical triggering operation. In the case of asymmetrical triggering, the non-linear function model of converter has

10.3389/fenrg.2023.1112210

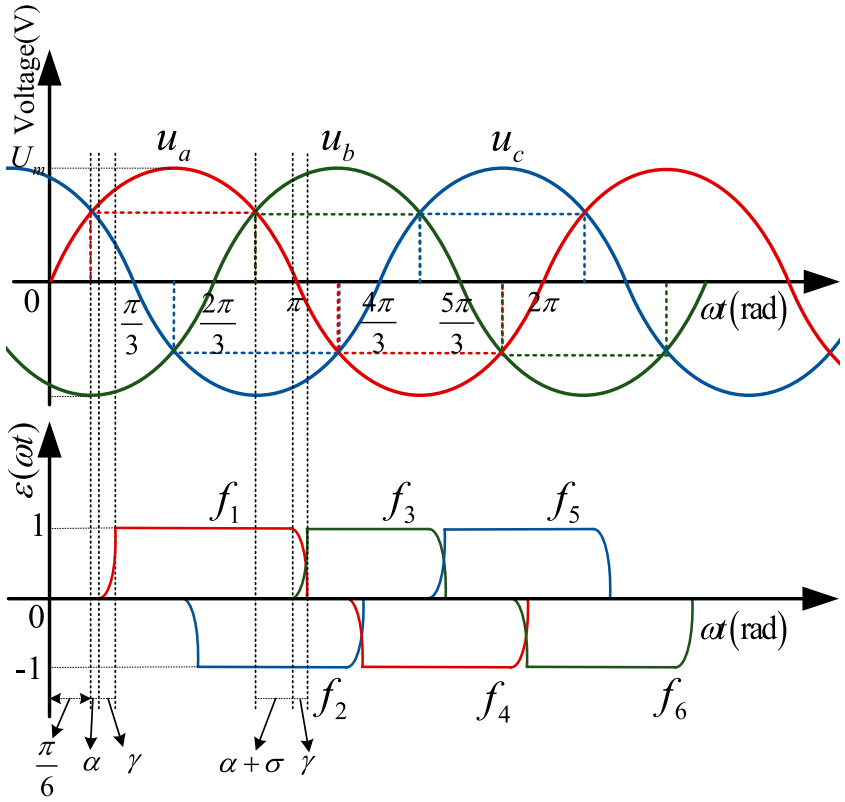

FIGURE 6
The time domain waveform diagram of three-phase voltage and the non-linear function model of converter under thyristor 3 lags behind σ degrees.

TABLE 1 Main parameters of the system.

Case	Firing angle	Commutation overlap angle	Deviation angle	Time
	α/rad	γ/rad	σ/rad	ωt/rad
Case 1	π/9	8π/180	0	3π/5
Case 2	57π/180	11π/180	0	5π/5
Case 3	94π/180	π/12	0	7π/5
Case 4	13π/18	π/10	0	9π/5
Case 5	π/9	8π/180	π/18	3π/5
Case 6	57π/180	11π/180	π/9	5π/5
Case 7	94π/180	π/12	π/6	7π/5
Case 8	13π/18	π/10	2π/9	9π/5

changed greatly, and various harmonic components have appeared. At this time, the voltage on the AC side may be affected by this, and various non-characteristic subharmonics will be generated on the DC side.

Randomly select one of the thyristors for discussion. For example, the firing angle of thyristor 3 lags behind the normal firing angle σ degrees. Affected by this, the conduction time of thyristor 1 will be extended by σ angle. The time domain waveform diagram of the non-linear function model of converter f_i (i = 1,2,3,4,5,6) in this case is shown in Figure 6.

According to the same principle of Equation 8, the expression of the output DC voltage $u_d^{'}$ during asymmetrical triggering is Equation 15:

$$u_d^{'} = (f_1^{+} - f_4)u_a + (f_3^{-} - f_6)u_b + (f_5 - f_2)u_c \tag{15}$$

TABLE 2 Calculation results under the conditions of Cases 1 to 4.

Order(n)		0	1	2	3	4	5	6	7	8	9	10	11	12	13	14	15	16	17	18
Case voltage(V)																				
Case1	Method A	553.3	0.0	0.0	0.0	0.0	0.0	75.1	0.0	0.0	0.0	0.0	0.0	37.76	0.0	0.0	0.0	0.0	0.0	18.4
	Method B	553.3	0.0	0.0	0.0	0.0	0.0	75.1	0.0	0.0	0.0	0.0	0.0	37.76	0.0	0.0	0.0	0.0	0.0	18.4
Case2	Method A	279.7	0.0	0.0	0.0	0.0	0.0	61.3	0.0	0.0	0.0	0.0	0.0	39.8	0.0	0.0	0.0	0.0	0.0	25.9
	Method B	279.7	0.0	0.0	0.0	0.0	0.0	61.3	0.0	0.0	0.0	0.0	0.0	39.8	0.0	0.0	0.0	0.0	0.0	25.9
Case3	Method A	117.6	0.0	0.0	0.0	0.0	0.0	22.8	0.0	0.0	0.0	0.0	0.0	13.4	0.0	0.0	0.0	0.0	0.0	7.4
	Method B	117.6	0.0	0.0	0.0	0.0	0.0	22.8	0.0	0.0	0.0	0.0	0.0	13.4	0.0	0.0	0.0	0.0	0.0	7.4
Case4	Method A	439.1	0.0	0.0	0.0	0.0	0.0	110.5	0.0	0.0	0.0	0.0	0.0	43.8	0.0	0.0	0.0	0.0	0.0	3.3
	Method B	439.1	0.0	0.0	0.0	0.0	0.0	110.5	0.0	0.0	0.0	0.0	0.0	43.8	0.0	0.0	0.0	0.0	0.0	3.3

u_d' can also be expressed as:

$$\boldsymbol{u_d^{'} = u_d + \Delta u_d} \tag{16}$$

Where:

$$\Delta u_d = (f_1^+ - f_1)u_a + (f_3^- - f_3)u_b$$

It can be seen that in the case of the asymmetrical triggering, the DC side voltage u_d' will still contain the harmonic components in the symmetrical case u_d. Since the output voltage in the case of the symmetrical triggering has been analyzed before, we will only analyze the non-characteristic harmonics of the DC side Δu_d caused by the asymmetrical moment. The harmonics of the final output voltage can be summed up by the u_d and Δu_d.

According to equation 9 and 11, f_1^+-f_1 is obtained by calculation:

$$\boldsymbol{f_1^+ - f_1 = E + \sum_{n=1}^{\infty}\sum_{j=1}^{7} S_j \sin\left(n\omega t + \zeta_j\right)} \tag{17}$$

Where E, S_j and ζ_j (j = 1,2,3,4,5,6,7)are as follows:

$$S_j = \sqrt{\left(C_j \sin\eta_{i=1,j} - A_j \sin\varphi_{i=1,j}\right)^2 + \left(C_j \cos\eta_{i=1,j} - A_j \cos\varphi_{i=1,j}\right)^2}$$

$$\zeta_j = \tan^{-1}\frac{C_j \sin\eta_{i=1,j} - A_j \sin\varphi_{i=1,j}}{C_j \cos\eta_{i=1,j} - A_j \cos\varphi_{i=1,j}}$$

$$E = \frac{1}{2\pi}\left(\sigma - \gamma + \frac{Q_3}{P_1} - \frac{Q_4}{P_4}\right)$$

According to equation 9 and 10, f_3^--f_3 is obtained by calculation:

$$\boldsymbol{f_3^- - f_3 = F + \sum_{n=1}^{\infty}\sum_{j=1}^{7} T_j \sin\left(n\omega t + \xi_j\right)} \tag{18}$$

Where F, T^j and ξ^j (j = 1,2,3,4,5,6,7) are as follows:

$$T_j = \sqrt{\left(B_j \sin\theta_{i=3,j} - A_j \sin\varphi_{i=3,j}\right)^2 + \left(B_j \cos\theta_{i=3,j} - A_j \cos\varphi_{i=3,j}\right)^2}$$

$$\xi_j = \tan^{-1}\frac{B_j \sin\theta_{i=3,j} - A_j \sin\varphi_{i=3,j}}{B_j \cos\theta_{i=3,j} - A_j \cos\varphi_{i=3,j}}$$

$$F = -\frac{1}{2\pi}\left(\sigma + \gamma + \frac{Q_1}{P_1} - \frac{Q_2}{P_4}\right)$$

Substitute f_1^+-f_1, f_3^--f_3 into Equation 16 to get:

$$\begin{aligned}\Delta u_d = {} & \boldsymbol{U_m G_1 \cos(\omega t - \psi_1) + U_m G_2 \sum_{n=1}^{\infty} \cos((n+1)\omega t - \psi_2)} \\ & \boldsymbol{+ U_m G_3 \sum_{n=1}^{\infty} \cos((n-1)\omega t - \psi_3)}\end{aligned} \tag{19}$$

Where

$$G_1 = \sqrt{E^2 - EF + F^2}$$

$$\psi_1 = -\tan^{-1}\frac{2E - F}{\sqrt{3}F}$$

$$G_2 = -\frac{1}{2}\sqrt{S_j^2 + T_j^2 + 2S_jT_j\left(\cos\zeta_j \cos\left(\xi_j + \frac{2\pi}{3}\right) + \sin\zeta_j \sin\left(\xi_j + \frac{2\pi}{3}\right)\right)}$$

$$\psi_2 = \tan^{-1}\frac{S_j \sin\zeta_j + T_j \sin\left(\xi_j + \frac{2\pi}{3}\right)}{S_j \cos\zeta_j + T_j \cos\left(\xi_j + \frac{2\pi}{3}\right)}$$

$$G_3 = \frac{1}{2}\sqrt{S_j^2 + T_j^2 + 2S_jT_j\left(\cos\zeta_j \cos\left(\xi_j - \frac{2\pi}{3}\right) + \sin\zeta_j \sin\left(\xi_j - \frac{2\pi}{3}\right)\right)}$$

$$\psi_3 = \tan^{-1}\frac{S_j \sin\zeta_j + T_j \sin\left(\xi_j - \frac{2\pi}{3}\right)}{S_j \cos\zeta_j + T_j \cos\left(\xi_j - \frac{2\pi}{3}\right)}$$

It can be seen from Equation 19 that when the harmonic order n of the non-linear function model of the converter is an even number of $2k$ (k = 1, 2, 3 . . .), the DC side will generate $2k$±1st odd order voltage harmonics; when n is an odd number of $2k$+1 (k = 1, 2, 3 . . .), the DC side will generate $2k$th and $2k$+2nd even order voltage harmonics. The calculation formula of DC side voltage harmonics can be derived as follows:`

$$\begin{cases} \boldsymbol{\Delta u_z = U_m G_3 \cos\psi_3} \\ \boldsymbol{\Delta u_1 = U_m\left[G_1 \cos(\omega t - \psi_1) + G_3 \cos(\omega t - \psi_3)\right]} \\ \boldsymbol{\Delta u_{2k} = U_m\left[G_2 \cos(2k\omega t - \psi_2) + G_3 \cos(2k\omega t - \psi_3)\right]} \\ \boldsymbol{\Delta u_{2k+1} = U_m\left[G_2 \cos((2k+1)\omega t - \psi_2) + G_3 \cos((2k+1)\omega t - \psi_3)\right]} \end{cases} \tag{20}$$

In Equation 20, Δu_z represents the DC component of the DC side voltage, which is formed by Δu_{d3} when n = 1; Δu_1 represents the fundamental component of the DC side voltage, which is formed by the superposition of Δu_{d1} and Δu_{d3} when n = 2; Δu_{2k} represents the even-order harmonic component of the DC side voltage, which is formed by the superposition of Δu_{d2} at n = $2k$-1 and Δu_{d3} at n = $2k$+1; Δu_{2k+1} represents the odd-order harmonic

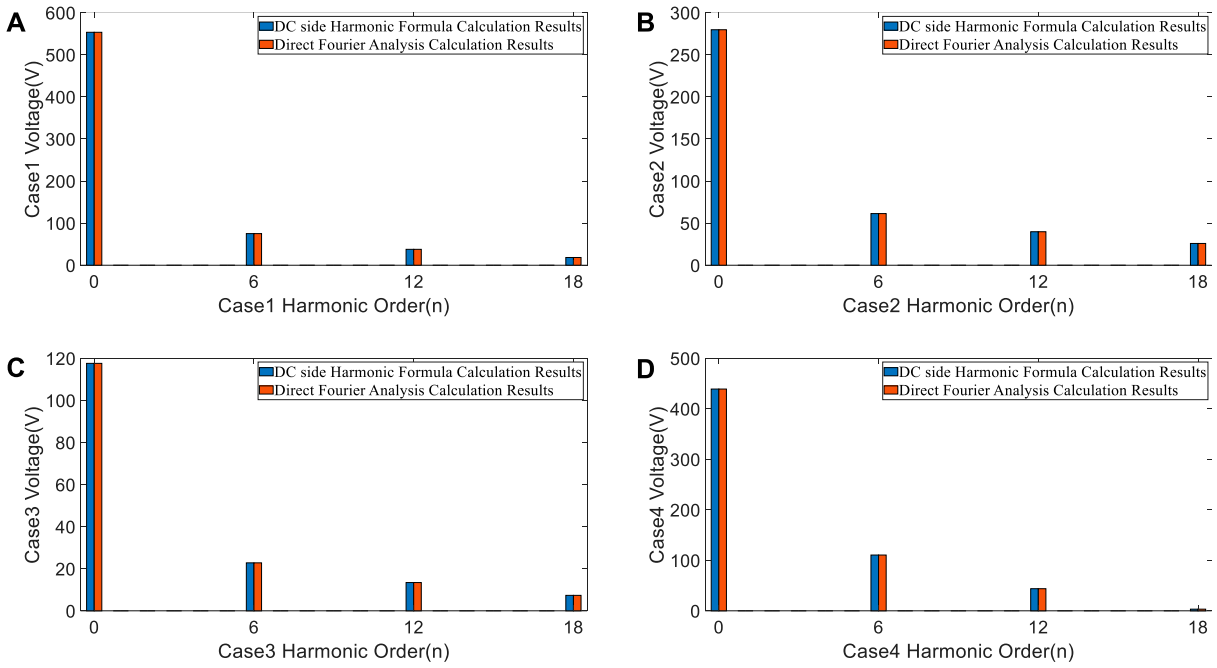

FIGURE 7
The comparison of calculation results of the DC side harmonic formula and the direct Fourier decomposition: **(A)** $\alpha = \pi/9$, $\gamma = 8\pi/180$, $\sigma = 0$, $\omega t = 3\pi/5$. **(B)** $\alpha = 57\pi/180$, $\gamma = 11\pi/180$, $\sigma = 0$, $\omega t = 5\pi/5$. **(C)** $\alpha = 94\pi/180$, $\gamma = \pi/12$, $\sigma = 0$, $\omega t = 7\pi/5$. **(D)** $\alpha = 13\pi/18$, $\gamma = \pi/10$, $\sigma = 0$, $\omega t = 9\pi/5$.

TABLE 3 Calculation results under the conditions of Cases 5 to 8.

Order(n)		0	1	2	3	4	5	6	7	8	9	10	11	12	13	14	15	16	17	18
Case voltage(V)																				
Case5	Method A	544.8	5.4	13.5	13.8	4.5	16.2	80.8	11.9	12.7	3.4	13.8	5.3	28.4	10.4	2.2	10.5	4.2	6.6	10.9
	Method B	544.8	5.4	13.5	13.8	4.5	16.2	80.8	11.9	12.7	3.4	13.8	5.3	28.4	10.4	2.2	10.5	4.2	6.6	10.9
Case6	Method A	246.4	48.7	5.2	38.8	59.2	47.1	73.7	23.2	40.7	34.2	12.4	9.5	19.8	16.9	6.6	2.3	5.1	2.8	26.1
	Method B	246.4	48.7	5.2	38.8	59.2	47.1	73.7	23.2	40.7	34.2	12.4	9.5	19.8	16.9	6.6	2.3	5.1	2.8	26.1
Case7	Method A	163.5	88.2	78.1	62.9	45.2	27.3	11.2	0.0	7.4	10.2	9.2	5.9	15.2	2.1	4.8	6.1	6.1	5.1	3.8
	Method B	163.5	88.2	78.1	62.9	45.2	27.3	11.2	0.0	7.4	10.2	9.2	5.9	15.2	2.1	4.8	6.1	6.1	5.1	3.8
Case8	Method A	466.6	49.6	34.8	15.1	4.1	17.9	86.8	21.5	13.7	4.3	3.4	7.1	37.2	3.4	0.0	3.3	3.9	2.6	2.9
	Method B	466.6	49.6	34.8	15.1	4.1	17.9	86.8	21.5	13.7	4.3	3.4	7.1	37.2	3.4	0.0	3.3	3.9	2.6	2.9

component of the DC side voltage, which is formed by the superposition of Δu_{d2} at $n = 2k$ and Δu_{d3} at $n = 2k+2$.

5 Comparison verification

Substitute the circuit parameters of the power grid and the converter into the DC side harmonic calculation formula, and calculate the theoretical value of the harmonic frequency spectrum data in MATLAB. It is compared with the frequency spectrum data obtained by direct Fourier decomposition of the DC side voltage data to verify the accuracy of the harmonic analysis in this paper.

5.1 Parameter selection

Taking the PS9 power supply of the poloidal field of the EAST device as an example, the effective value of the three-phase voltage input by the power grid is 259.3 V, the amplitude U_m is 366.7 V, and the frequency is industrial frequency 50 Hz. Taking the power supply system under rapidly rising and changing current demands still operating in steady state as a reference, when the converter works in the inverter state, if the firing angle delay is too large, it will easily lead to commutation failure. Therefore, the range of firing angle α is generally between $\pi/9$ rad to $13\pi/18$ rad. Correspondingly, the range of commutation overlap angle γ is

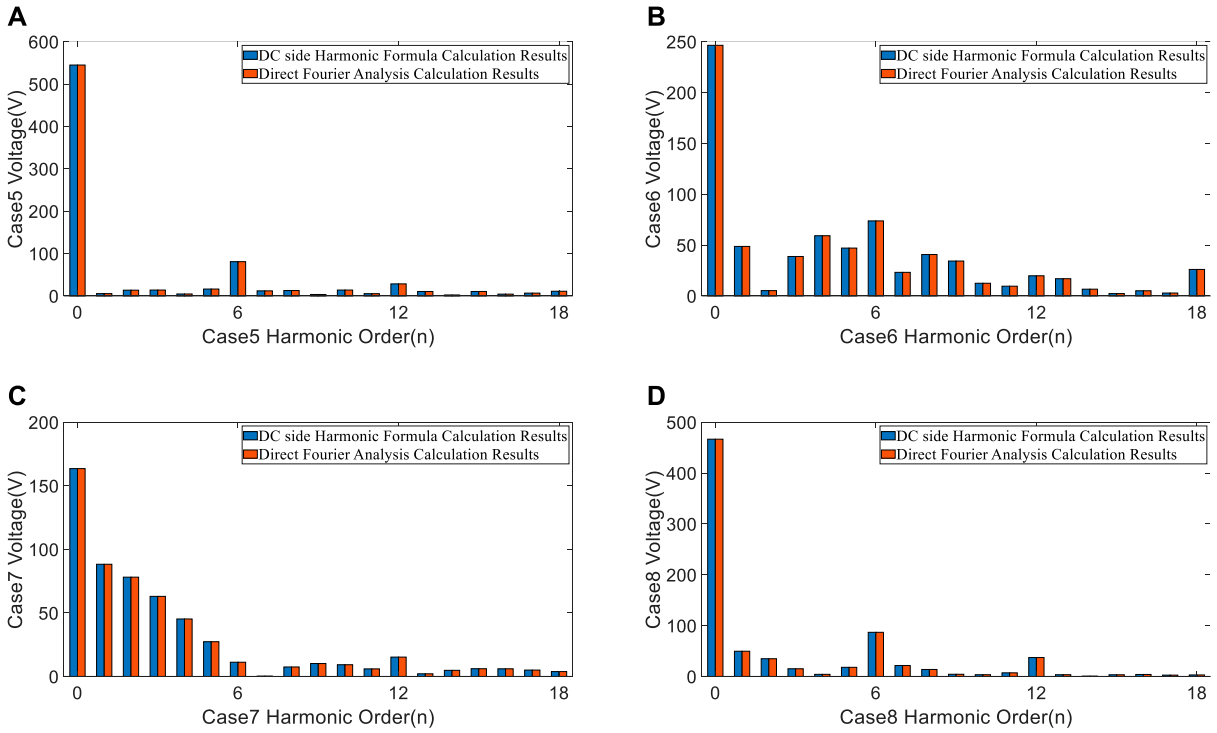

FIGURE 8
The comparison of calculation results of the DC side harmonic formula and the direct Fourier decomposition: **(A)** $\alpha = \pi/9$, $\gamma = 8\pi/180$, $\sigma = \pi/18$, $\omega t = 3\pi/5$. **(B)** $\alpha = 57\pi/180$, $\gamma = 11\pi/180$, $\sigma = \pi/9$, $\omega t = 5\pi/5$. **(C)** $\alpha = 94\pi/180$, $\gamma = \pi/12$, $\sigma = \pi/6$, $\omega t = 7\pi/5$. **(D)** $\alpha = 13\pi/18$, $\gamma = \pi/10$, $\sigma = 2\pi/9$, $\omega t = 9\pi/5$.

generally between $8\pi/180$ rad to $\pi/10$ rad, and the range of deviation angle σ is generally between 0 rad to $2\pi/9$ rad (Wang Z M et al., 2020). As shown in Tab.1, select operating parameters at equal intervals according to the above range, and 8 cases are set to verify the harmonic analysis in this paper.

5.2 Comparison of calculation results

Based on equations (13) and (14), the harmonic voltages on the DC side of the converter under symmetrical triggering conditions can be obtained. Table 2 and Figure 7 show the comparison of calculation results of the DC side harmonic formula (Method A) and the direct Fourier decomposition (Method B) under the conditions of Cases 1 to 4.

It can be seen from Table 2 and Figure 7 that the output voltage only contains 6*k*th characteristic harmonics under the symmetrical triggering condition, and the values of the voltage harmonics are equal.

Based on Equation 20, the harmonic voltages on the DC side of the converter under asymmetrical triggering conditions can be obtained. Table 3 and Figure 8 show the comparison of calculation results of the DC side harmonic formula (Method A) and the direct Fourier decomposition (Method B) under the conditions of Cases 5 to 8.

It can be seen from Table 3 and Figure 8 that the output voltage not only contains 6*k*th characteristic harmonics but also includes various non-characteristic harmonics under the asymmetrical triggering condition, and the values of the voltage harmonics are equal.

6 Discussion

Direct Fourier decomposition of the DC side voltage is a traditional and common method for analyzing the spectrum distribution of the DC side, its calculation results are an important reference for verifying the correctness of the analysis. Table 2 and Table 3 shows that the calculation results of the two methods are consistent with each other under the symmetrical trigger condition and asymmetrical trigger condition. So, the proposed method can accurately calculate the harmonic components of the DC side voltage, which verifies the accuracy of the analysis. This paper provides a simple and accurate method for the analysis and calculation of DC side harmonics. Analysis results can provide theoretical guidance for targeted harmonic suppression. It is conducive to reduce the risk of false alarm of quench detection and malfunction of quench protection, and to support the stable operation of the Tokamak.

7 Conclusion

In this paper, a non-linear function model of converter suitable for the asymmetrical triggering is established, so that the switching function method, which has the advantages of simplifying the analysis process and reducing the amount of calculation, can complete the DC side harmonic analysis and calculation under the asymmetrical triggering of Tokamak power supply.

1) The harmonic relationship between the DC side voltage and the non-linear function model of the converter is clarified: in the case

of the symmetrical triggering, the DC side only contains 6kth harmonics, which are superimposed by the 6*k*+1st and 6*k*-1st harmonics of the non-linear function model of converter. In the case of the asymmetrical triggering, the odd-order harmonics on the DC side are composed of the even-order harmonics of the non-linear function model of the converter, and the even-order harmonics on the DC side are composed of the odd-order harmonics of the non-linear function model of the converter;

2) The calculation formula of DC side voltage harmonics is deduced, and the quantitative relationship between each harmonic voltage value and AC side voltage value U_m, firing angle α, commutation overlap angle γ and deviation angle σ is clarified. The calculation results of this formula are compared with the harmonic frequency spectrum data obtained by direct Fourier decomposition of the DC side voltage data, which verifies the accuracy of the harmonic analysis in this paper.

Data availability statement

The original contributions presented in the study are included in the article/supplementary material, further inquiries can be directed to the corresponding author.

Author contributions

RH, project administration, formal analysis, validation, software, writing original draft. YW share first authorship: conceptualization, resources, methodology, funding acquisition. JLu is the corresponding author: investigation, formal analysis, data curation, funding acquisition. JLi, conceptualization, methodology, revision. JZ and YT and PW, software, revision, read. All authors agree to be accountable for the content of the work.

Funding

This work was supported by the NSFC (Natural Science Foundation of China) under Grant 52177165, NSFC under Grant 52007184, Youth Innovation Promotion Association of the Chinese Academy of Sciences under Grant 2020440, Natural Science Foundation of Anhui Province under Grant 2108085UD10, Comprehensive Research Facility for Fusion Technology Program of China under Contract No. 2018-000052-73-01-001228.

Conflict of interest

The authors declare that the research was conducted in the absence of any commercial or financial relationships that could be construed as a potential conflict of interest.

Publisher's note

All claims expressed in this article are solely those of the authors and do not necessarily represent those of their affiliated organizations, or those of the publisher, the editors and the reviewers. Any product that may be evaluated in this article, or claim that may be made by its manufacturer, is not guaranteed or endorsed by the publisher.

References

Chen, X. J., Fu, P., Huang, L. S., Gao, G., and He, S. Y. (2016). Hardware-in-the-loop simulation of the EAST PF converter for PF control system upgrade. *Fusion Eng. Des.* 112, 57–66. doi:10.1016/j.fusengdes.2016.07.020

Chen, X., Ma, J. P., Wang, S. L., Liu, T. Q., Liu, D., and Zhu, T. Y. (2022). An accurate impedance model of line commutated converter with variable commutation overlap. *Ieee Trans. Power Deliv.* 37 (1), 562–572. doi:10.1109/Tpwrd.2021.3064985

Gorit, Q., Nicollet, S., Lacroix, B., Louzguiti, A., Topin, F., Torre, A., et al. (2022). Thermal hydraulic analysis of JT-60sa TFC02 complementary quench tests in CTF. *Ieee Trans. Appl. Supercond.* 32 (6), 1–5. doi:10.1109/Tasc.2022.3171738

Hu, L. H., and Morrison, R. E. (1997). The use of modulation theory to calculate the harmonic distortion in HVDC systems operating on an unbalanced supply. *Ieee Trans. Power Syst.* 12 (2), 973–980. doi:10.1109/59.589796

Hu, L. H., and Yacamini, R. (1992). Harmonic transfer through converters and HVDC links. *Ieee Trans. Power Electron.* 32 (3), 514–525. doi:10.1109/63.145139

Liu, X. K., Grassi, F., Spadacini, G., and Pignari, S. A. (2020). Physically based modeling of hand-assembled wire bundles for accurate EMC prediction. *Ieee Trans. Electromagn. Compat.* 62 (3), 914–922. doi:10.1109/Temc.2019.2922455

Liu, X. K., Wu, B. B., and Xiu, L. C. (2022). A fast positive-sequence component extraction method with multiple disturbances in unbalanced conditions. *Ieee Trans. Power Electron.* 37 (8), 8820–8824. doi:10.1109/Tpel.2022.3161734

Liu, X. K., Xiong, L. S., Wu, B. B., Qian, Y., and Liu, Y. H. (2022). Phase locked-loop with decaying DC transient removal for three-phase grids. *Int. J. Electr. Power and Energy Syst.* 143, 108508. doi:10.1016/j.ijepes.2022.108508

Lopes, C. R., Zito, P., Zignani, C. F., Messina, G., Morici, L., Tomassetti, G., et al. (2021). Design optimization for the quench protection of DTT's superconducting toroidal field magnets. *Fusion Eng. Des.* 172, 112748. doi:10.1016/j.fusengdes.2021.112748

Lu, J., Fu, P., Li, J., Mao, H. F., Shen, X. S., Xu, L. W., et al. (2018). A new hybrid filter based on differential current control method for low-order harmonic suppression in Tokamak power system. *Int. J. Energy Res.* 42 (1), 82–90. doi:10.1002/er.3829

Meguro, H., Nakamura, K., Shogo, S., Nasu, K., Murakami, H., and Kizu, K. (2020). Effects of resonance phenomenon caused by power supply on JT-60sa CS. *Ieee Trans. Appl. Supercond.* 30 (4), 1–5. doi:10.1109/Tasc.2020.2970392

Risse, K., Rummel, T., Monnich, T., Ftillenbach, F., Bosch, H. S., and Team, W.-X. (2019). Updates on protection system for Wendelstein 7-X superconducting magnets. *Fusion Eng. Des.* 146, 910–913. doi:10.1016/j.fusengdes.2019.01.111

Sonoda, S., Nakamura, K., Hirose, Y., Yuinawa, K., Murakami, H., Hamada, K., et al. (2022). Investigation of transient response caused by power supply on JT-60sa central solenoid. *Ieee Trans. Appl. Supercond.* 32 (6), 1–4. doi:10.1109/Tasc.2022.3151038

Wang, J. J., Huang, Y. Y., Fu, P., Wu, Y. A., and Shen, X. S. (2019). Stability analysis for the voltage of EAST loads based on the short circuit capacity. *Fusion Eng. Des.* 149, 111355. doi:10.1016/j.fusengdes.2019.111355

Wang, K., Song, Z. Q., Fu, P., Li, H., Tong, W., Wang, S. S., et al. (2020a). Analysis and design of fast discharge resistor system based on forced-air cooling method. *Ieee Trans. Plasma Sci.* 48 (2), 542–553. doi:10.1109/Tps.2019.2961095

Wang, T., Hu, Y. L., Liu, H. J., Wu, Y., Shi, Y., Pan, C., et al. (2018). Quench detection design for CFETR CSMC. *Fusion Sci. Technol.* 74 (3), 229–237. doi:10.1080/15361055.2017.1415613

Wang, Z. M., Fu, P., Hang, L. S., Song, Z. Q., Zhang, X. Q., Deng, T. B., et al. (2020b). Preliminary design of high power magnet converter for CRAFT. *Plasma Sci. Technol.* 22 (4), 045604. doi:10.1088/2058-6272/ab7472

Xiong, L. S., Liu, L., Liu, X. K., and Liu, Y. H. (2021). Frequency trajectory planning based strategy for improving frequency stability of droop-controlled inverter based standalone power systems. *Ieee J. Emerg. Sel. Top. Circuits Syst.* 11 (1), 176–187. doi:10.1109/Jetcas.2021.3052006

Yang, W., Xu, L. W., Fu, P., Lu, H. W., and Sheng, Z. C. (2009). Non-characteristic harmonics analysis of the ITER pulsed power supply. *Plasma Sci. Technol.* 11 (4), 493–498. doi:10.1088/1009-0630/11/4/26

frontiers | Frontiers in Energy Research

TYPE Original Research
PUBLISHED 23 February 2023
DOI 10.3389/fenrg.2023.1148734

OPEN ACCESS

EDITED BY
Sayed Abulanwar,
Mansoura University, Egypt

REVIEWED BY
Abdelhady Ghanem,
Mansoura University, Egypt
Dejian Yang,
Northeast Electric Power University, China

*CORRESPONDENCE
Heling Dong,
435709576@qq.com

SPECIALTY SECTION
This article was submitted to Process and Energy Systems Engineering, a section of the journal Frontiers in Energy Research

RECEIVED 20 January 2023
ACCEPTED 15 February 2023
PUBLISHED 23 February 2023

CITATION
Dong H, Tang Z and Wei M (2023), Two-stage robust optimal operation of AC/DC distribution networks with power electronic transformers.
Front. Energy Res. 11:1148734.
doi: 10.3389/fenrg.2023.1148734

Two-stage robust optimal operation of AC/DC distribution networks with power electronic transformers

Heling Dong*, Zhong Tang and Minjie Wei

School of Electric Power Engineering, Shanghai University of Electric Power, Shanghai, China

Power electronic transformers (PET) are a new type of power electronic equipment with a multi-port flexible dispatch function, which can play the role of a power hub in a system composed of multiple AC-DC hybrid distribution grids for interactive sharing of power in multiple regions. In this study, a two-stage robust optimization operation model of a hybrid AC-DC distribution network with PET is proposed based on PET power transmission and transformation characteristics. The stochastic uncertainty of the distributed renewable energy output in the AC-DC grid is handled by a two-stage robust optimization method to determine the minimum total system operation cost under the worst case of distributed renewable energy output. Finally, a constrained column generation algorithm is used to solve the two-stage robust optimization model in the min-max-min form and verifies the validity of the model in this study.

KEYWORDS

optimal dispatching, power electronic transformer, AC/DC distribution network, two-stage robust optimization, renewable energy, distributed generation

1 Introduction

With the development of power technology, new energy sources represented by wind and photoelectricity are increasingly connected to power systems and generally belong to distributed generation (DG). The DC part of the AC/DC mixed current distribution is compatible with these DGs, and DC transmission can reduce the number of energy conversions and improve energy utilization, while the AC part is compatible with existing power equipment, saving costs. The AC-DC hybrid distribution grid also has advantages in terms of new energy consumption, peak shaving, and valley filling, and is a feasible solution to cope with future grid development.

A power electronic transformer (PET) consists of a power electronic converter and conventional high-frequency transformer, which allows for more flexible conversion of electrical energy through power electronics technology (Liu et al., 2017; Wang et al., 2017). Generally, power electronic transformers are classified into AC/AC- and AC/DC/AC-type PETs, depending on whether they contain a DC component (Li et al., 2018). PET plays the same role as a traditional voltage source converter (VSC) in an AC/DC distribution network, connecting the AC and DC components of the interactive distribution network. Compared with traditional VSC, PET has some unique advantages, such as its ability to contain multiple AC-DC converter ports, connect multiple AC and DC subgrids simultaneously, control the power and voltage of each port, and achieve power quality control, fault isolation, and energy interaction between ports

simultaneously. Therefore, PET can play the role of an energy hub in the AC-DC hybrid distribution network.

Pu et al. (2018) provided an overview of the technology and framework for the optimal operation of PET-based hybrid AC-DC systems, and illustrated the advantages of PET-based AC-DC distribution networks over other power conversion units, such as VSC-based AC-DC distribution networks. Yi and Wang, 2021 proposed a day-ahead economic operation strategy for multi-port PET-based AC-DC distribution networks, reflecting the flexible regulation capability of PET, and established a PET energy flow model. Guo et al. (2019) applied multi-port PET to AC-DC hybrid distributed energy systems, fully consuming renewable energy and reducing system operation cost by using the power regulation function of PET. However, most of the above models do not fully consider the uncertainty of the renewable energy power output, whose random uncertainty significantly affects the power interaction of PET and safe operation of the AC-DC distribution network with access to large-scale scenic power sources.

Owing to the access of a large number of distributed renewable energy sources such as photovoltaic (PV) and wind power, the power supply of the grid has more uncertainty and volatility, posing new challenges for optimal dispatching of the distribution network. The commonly used uncertainty optimization methods include stochastic and robust optimization.

The probability distribution of random variables must be set in stochastic optimization, but the assumed probability distribution model may not be able to accurately portray the variation pattern of the actual uncertainty factors when they are more complex. Zhang et al. (2022) proposed a stochastic optimization model for the impact of new energy uncertainty on the operation results of AC-DC distribution networks containing power electronic transformers. Xu et al. (2021) combined stochastic optimization and conditional value-at-risk theory to propose a stochastic operation optimization method for active distribution networks containing smart soft switches considering risk management. Robust optimization does not require prior knowledge of the specific probabilistic prediction information of uncertain quantities and uses uncertainty sets to model uncertainty and pursue the minimum total cost of system decision options under the worst-case scenario with uncertain variables. Liu et al. (2018) considered the uncertainty of new energy and load, developed a min-max-min two-stage robust optimization model, and regulated the model conservativeness by introducing uncertainty regulation parameters. Fu et al. (2019) proposed a reactive voltage control method for AC-DC distribution networks based on a two-stage robust optimization model and examined the results of the model under different prediction errors. Liao et al., 2020 proposed a two-stage robust optimization strategy for an AC-DC distribution network with an optical storage consortium and used a hierarchical approach to set two objectives to solve it. Zhang et al. (2022) proposed a two-stage robust optimization model incorporating both distribution network reconfiguration and reactive power optimization. Zhong et al. (2022) introduced game theory into the two-stage robust optimization model for AC-DC distribution networks and constructed a master-slave game optimization model. However, few of the above models apply the two-stage robust optimization method to the optimal operation of hybrid AC-DC distribution networks with PET, and further research is required to combine the robust modeling idea with the optimal operation of AC-DC distribution networks with PET.

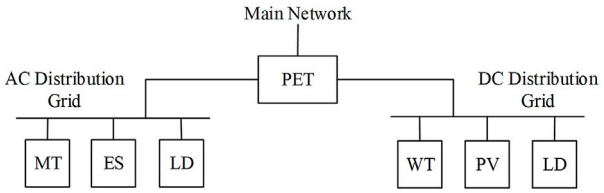

FIGURE 1
Schematic diagram of AC/DC distribution network with PET.

In this study, a two-stage robust optimal operation model of a hybrid AC-DC distribution network with PET is proposed. By connecting the AC-DC part of the distribution network and the super grid through PET, the utilization rate of distributed renewable energy is improved, and the safe and economic operation of the AC-DC distribution network is ensured. A two-stage robust optimization method is used to address the stochastic uncertainty of the renewable energy output and seek the minimum total system operation cost under the worst case scenario. Finally, a constrained column generation algorithm is used to solve the two-stage optimization model in the form of min-max-min.

Compared with the examples mentioned in the previous section, the two-stage robust optimization method used in this paper has the following advantages: first, compared with the traditional robust optimization method and the stochastic optimization method, the method used in this paper inherits the advantages of robust optimization such as strong accuracy and low out-of-bounds rate, and achieves the purpose of controlling the conservativeness of the model by adding uncertainty adjustment parameters. Secondly, compared with other two-stage robust optimization methods, the method used in this paper sets both spatial and temporal uncertainty adjustment parameters, which can control the number of bad scenarios taken in one cycle and the number of bad scenarios taken at the same time respectively, so that the conservativeness of the model can be controlled more flexibly and accurately to achieve better optimization results.

2 Two-stage robust operation model of AC/DC distribution network with power electronic transformers

2.1 Hybrid AC/DC distribution network structure with power electronic transformers

The hybrid AC-DC distribution network can be divided into three parts according to its composition: AC and DC distribution networks and VSC. The model in this paper used PET to replace the traditional VSC, which connects the DC, AC, and super grids and plays the role of power conversion. In the AC part, the micro turbine (MT), AC load, and energy storage (ES) are connected, and in the DC part, the PV, wind turbine (WT), DC load, and other parts are connected. The AC and DC parts are connected to the superior grid through PET. Figure 1 shows a schematic of the AC-DC hybrid distribution network. Compared with the traditional AC-DC distribution network, that with PET can directly

interact with the superior grid through PET, owing to the multi-port nature of PET, avoiding the loss caused by the interaction through the AC grid. Because the power can be freely interacted with in three ports, it improves the flexibility of power dispatching in the distribution network. Compared with traditional VSC, it improves the response speed and network flexibility and reduces the power conversion link, which is more suitable for distribution networks with uncertain DG (Pu et al., 2018; Li et al., 2021).

2.2 Equations

The optimization objective was to minimize the total operating cost during the dispatch cycle of the system. This entailed finding the operating solution with the lowest cost during the dispatch cycle by adjusting the purchased power from the higher grid, generation capacity of the micro turbine, and power of the energy storage equipment.

$$\min f = C^{M} + C^{MT} + C^{ES} + C^{PV} + C^{WT} \tag{1}$$

Among them,

$$C^{M} = \sum_{t\in T} c_t^{M} P_t^{M} \Delta t \tag{2}$$

$$C^{MT} = \sum_{t\in T} \sum_{i\in B^{MT}} \left(c_1^{MT} \left(P_{i,t}^{MT}\right)^2 + c_2^{MT} P_{i,t}^{MT} + c_3^{MT} \right) \Delta t \tag{3}$$

$$C^{ES} = \sum_{i\in B^{ES}} \sum_{t\in T} \left(c^{ES} (\eta P_{i,t}^{ch} - \frac{P_{i,t}^{dis}}{\eta}) \right) \Delta t \tag{4}$$

$$C^{WT} = \sum_{i\in B^{WT}} \sum_{t\in T} \left(c^{WT} (\tilde{P}_{i,t}^{WT} - P_{i,t}^{WT}) \right) \Delta t \tag{5}$$

$$C^{PV} = \sum_{i\in B^{PV}} \sum_{t\in T} \left(c^{PV} (\tilde{P}_{i,t}^{PV} - P_{i,t}^{PV}) \right) \Delta t \tag{6}$$

where f is the operation cost of the distribution network; C^{M} and C^{MT} are the costs of electricity purchased from the upper grid and generated by micro turbines, respectively; C^{ES} is the cost of energy storage; and C^{WT} and C^{PV} are the costs of abandoned wind and light, respectively. T is the operating period; B^{MT}, B^{ES}, B^{WT}, and B^{PV} are the sets of micro turbine nodes in the distribution network, energy storage nodes, wind turbine nodes, and photovoltaic nodes. c_t^{M} is the price of electricity purchased from the superior grid at time t; P_t^{M} is the power purchased from the superior grid by the distribution grid; and c_1^{MT}, c_2^{MT}, c_3^{MT} are the cost coefficients of micro turbine generation. $P_{i,t}^{MT}$ is the power output of micro turbine at node i at time t; c^{ES} is the cost coefficient of energy storage charging and discharging; η is the charging and discharging efficiency; $P_{i,t}^{ch}$ is the charging power of energy storage node i at time t; and $P_{i,t}^{dis}$ is the discharging power of energy storage node i at time t. C^{WT} and C^{PV} are the wind and light abandonment penalty coefficients, respectively; $\tilde{P}_{i,t}^{WT}$ and $\tilde{P}_{i,t}^{PV}$ are the predicted values of scenic output; and $P_{i,t}^{WT}$ and $\tilde{P}_{i,t}^{PV}$ are the actual scenic output values.

2.3 Constraints

2.3.1 Constraints of DistFlow branch currents in AC-DC distribution networks

The DistFlow tidal model was planned to be used for both the AC and DC parts of this model because part of this model contained non-linear terms that were not favorable for solving the model using software. To improve the solution speed, in this study, linearization and second-order cone relaxation were used to transform the model into a linear problem (Lavaei and Low, 2012), which was then solved by a commercial solver to achieve an easy solution and increase the solution speed as follows:

First, linearization transformation was performed through variable substitution:

$$\begin{cases} \left(V_i^{AC}\right)^2 = \tilde{V}_i^{AC} \\ \left(I_i^{AC}\right)^2 = \tilde{I}_i^{AC} \\ \left(V_i^{DC}\right)^2 = \tilde{V}_i^{DC} \\ \left(I_i^{DC}\right)^2 = \tilde{I}_i^{DC} \end{cases} \tag{7}$$

The results of the second-order cone relaxation of the DistFlow power flow model of the AC/DC hybrid distribution network were as follows.

AC part:

$$P_{j,t}^{AC} = \sum_{k\in\delta(j)} P_{jk,t}^{AC} - \sum_{i\in\pi(j)} \left(P_{ij,t}^{AC} + \tilde{I}_{ij,t}^{AC} r_{ij} \right) \tag{8}$$

$$Q_{j,t}^{AC} = \sum_{k\in\delta(j)} Q_{jk,t}^{AC} - \sum_{i\in\pi(j)} \left(Q_{ij,t}^{AC} + \tilde{I}_{ij,t}^{AC} x_{ij} \right) + b_i \tilde{V}_{i,t}^{AC} \tag{9}$$

$$\tilde{V}_{j,t}^{AC} = \tilde{V}_{i,t}^{AC} - 2\left(r_{ij} P_{ij,t}^{AC} + x_{ij} Q_{ij,t}^{AC} \right) + \left(r_{ij}^2 + x_{ij}^2 \right) \tilde{I}_{ij,t}^{AC} \tag{10}$$

$$\left\| \begin{matrix} 2P_{ij,t}^{AC} \\ 2Q_{ij,t}^{AC} \\ \tilde{I}_{ij,t}^{AC} - \tilde{V}_{j,t}^{AC} \end{matrix} \right\|_2 \le \tilde{I}_{ij,t}^{AC} - \tilde{V}_{j,t}^{AC}, \forall t \tag{11}$$

$$P_{j,t}^{AC} = P_{j,t}^{MT} + P_{j,t}^{ch} + P_{in,t}^{ACPET} - P_{out,t}^{ACPET} - P_{j,t}^{dis} - P_{j,t}^{ACLoad} \tag{12}$$

$$Q_{j,t}^{AC} = Q_{j,t}^{MT} + Q_{in,t}^{ACPET} - Q_{out,t}^{ACPET} - Q_{j,t}^{ACLoad} \tag{13}$$

where $\delta(j)$ is the set of end nodes with j as the first node, $\pi(j)$ is the set of first nodes with j as the end node, B^{AC} is the set of AC subnetwork nodes, and L^{AC} is the set of AC subnetwork branches. $P_{ij,t}^{AC}$, $Q_{ij,t}^{AC}$ are the active and reactive power flowing from node i to node j in the AC subnetwork, respectively; r_{ij}, x_{ij}, and b_i are the resistance and reactance of the branch ij and the shunt electrons at node i, while $P_{j,t}^{AC}$, $Q_{j,t}^{AC}$, $\tilde{V}_{t,j}^{AC}$, and $\tilde{I}_{ij,t}^{AC}$ are the active power, reactive power, voltage squared, and square of the current flowing through branch ij in the AC subgrid injected into node j at time t, respectively. $P_{in,t}^{ACPET}$, $P_{out,t}^{ACPET}$, $Q_{in,t}^{ACPET}$, $Q_{out,t}^{ACPET}$ are the active reactive power flowing into and out of the PET AC port.

DC part:

$$P_{j,t}^{DC} = \sum_{k\in\delta(j)} P_{jk,t}^{DC} - \sum_{i\in\pi(j)} \left(P_{ij,t}^{DC} + \tilde{I}_{ij,t}^{DC} r_{ij} \right) \tag{14}$$

$$\tilde{V}_{j,t}^{DC} = \tilde{V}_{i,t}^{DC} - 2 r_{ij} P_{ij,t}^{DC} + r_{ij}^2 \tilde{I}_{ij,t}^{DC} \tag{15}$$

$$\left\| \begin{matrix} 2P_{ij,t}^{DC} \\ \tilde{I}_{ij,t}^{DC} - \tilde{V}_{j,t}^{DC} \end{matrix} \right\|_2 \le \tilde{I}_{ij,t}^{DC} - \tilde{V}_{j,t}^{DC} \tag{16}$$

$$P_{j,t}^{DC} = P_{j,t}^{WT} + P_{j,t}^{PV} + P_{in,t}^{DCPET} - P_{out,t}^{DCPET} - P_{j,t}^{DCLoad} \tag{17}$$

where B^{DC} and L^{DC} are the sets of DC subnet nodes and branches, respectively, and $P_{j,t}^{DC}$ is the active power injected into node j at time t of the DC subnet. $P_{ij,t}^{DC}$ is the active power flowing from i to j on DC branch ij; $\tilde{I}_{ij,t}^{DC}$ and $\tilde{V}_{j,t}^{DC}$ are the square of the current flowing through the ij branch from i to j and the square of the voltage at i in the DC

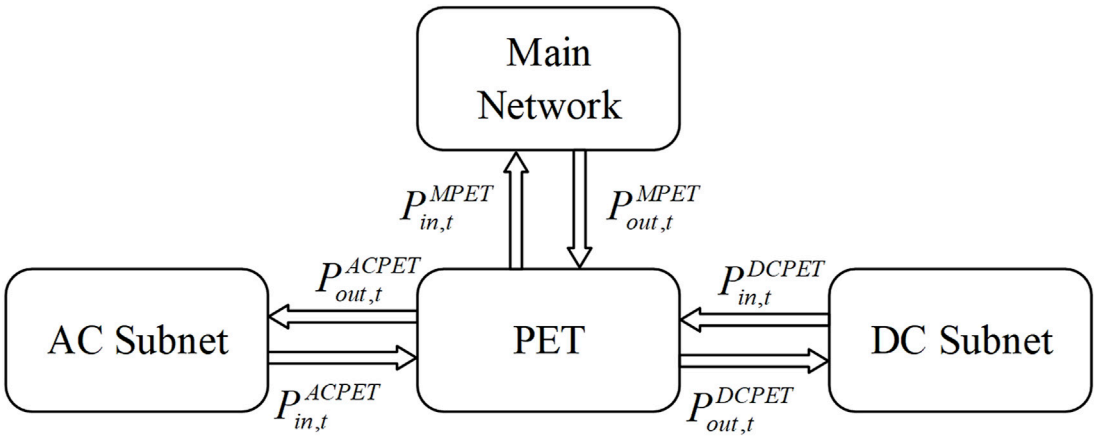

FIGURE 2
Schematic diagram of PET energy flow.

subnet, respectively; and $P_{in,t}^{DCPET}$ and $P_{out,t}^{DCPET}$ are the power flowing into and out of the PET DC port, respectively.

2.3.2 Operational constraints of distributed power generation

(1) Upper and lower limit constraints of micro turbine output:

$$\begin{cases} 0 \le P_{i,t}^{MT} \le P_i^{MTmax} \\ 0 \le Q_{i,t}^{MT} \le Q_i^{MTmax} \end{cases} \tag{18}$$

where P_i^{MTmax} and Q_i^{MTmax} are the maximum values of active and reactive power of the micro turbine, respectively. Because the step size selected in this model was 1 h, the regulation speed of the micro turbine was faster at this time scale, so the climbing constraint of the model was not considered.

(2) Wind turbine and photovoltaic output constraints:

$$0 \le P_{i,t}^{WT} \le \tilde{P}_{i,t}^{WT}, \forall t, \forall j \in B^{WTG} \tag{19}$$

$$0 \le P_{i,t}^{PV} \le \tilde{P}_{i,t}^{PV}, \forall t, \forall j \in B^{PV} \tag{20}$$

where $\tilde{P}_{i,t}^{WT}$ and $\tilde{P}_{i,t}^{PV}$ are the predicted wind turbine and PV outputs, respectively.

(3) Operational constraints of energy storage:

$$\begin{cases} 0 \le P_{i,t}^{ch} \le U_i(t) P^{ch}_{max} \\ 0 \le P_{i,t}^{dis} \le [1 - U_i(t)] P^{dis}_{max} \end{cases} \tag{21}$$

$$E_{i,t} = E_{i,t+1} - \eta P_{i,t}^{ch} + \frac{P_{i,t}^{dis}}{\eta} \tag{22}$$

$$E_i^{min} \le E_{i,t} \le E_i^{max} \tag{23}$$

where $P_{i,t}^{ch}$, $P_{i,t}^{dis}$ denote the charging and discharging power at node i at time t; P^{ch}_{max}, P^{dis}_{max} denote the maximum charging and discharging power of the energy storage device, respectively. $U_i(t)$ denotes the 0–1 correlation variable of the charging and discharging states at node i at time t, and 1 is charging and 0 is discharging. $E_{i,t}$, E_i^{max} denote the existing and maximum power stored in the energy storage device at node i at time t, respectively, and η denotes the charging and discharging efficiency of the energy storage device.

2.3.3 Operational constraints of power electronic transformers

In this study, we considered an AC/DC/AC-type PET with a DC section, which can be connected to multiple AC/DC distribution networks simultaneously because of its multi-port feature, and realize the power interaction function between each sub-network and the higher-level network through its AC/DC ports. Considering the limitations of PET, the amount of power interaction between each port was constrained.

Figure 2 shows a schematic diagram of the energy flow of the PET, where $P_{in,t}^{MPET}$ and $P_{out,t}^{MPET}$ are the active powers exchanged between the medium-voltage AC side port of the PET and the main network at moment t; $P_{in,t}^{ACPET}$ and $P_{out,t}^{ACPET}$ are the active powers exchanged between the low-voltage AC side of the PET and the AC distribution network at moment t; and $P_{in,t}^{DCPET}$ and $P_{out,t}^{DCPET}$ are the active powers exchanged between the low-voltage DC side of the PET and the DC distribution network at moment t (Zhang et al., 2017).

Letting the loss factor of PET be k_p and simplifying PET to a node (Li et al., 2018; Li et al., 2019; Li et al., 2021), we obtain:

$$P_{out,t}^{ACPET} + P_{out,t}^{DCPET} = k_p\left(P_{in,t}^{M} + P_{in,t}^{ACPET} + P_{in,t}^{DCPET}\right) \tag{24}$$

The capacity constraints of PET ports are:

$$\sqrt{\left(P_{in,t}^{MPET}\right)^2 + \left(Q_{in,t}^{MPET}\right)^2} \le S_{max}^{MPET} \tag{25}$$

$$\sqrt{\left(P_{out,t}^{MPET}\right)^2 + \left(Q_{out,t}^{MPET}\right)^2} \le S_{max}^{MPET} \tag{26}$$

$$\sqrt{\left(P_{out,t}^{ACPET}\right)^2 + \left(Q_{out,t}^{ACPET}\right)^2} \le S_{max}^{ACPET} \tag{27}$$

$$\sqrt{\left(P_{in,t}^{ACPET}\right)^2 + \left(Q_{in,t}^{ACPET}\right)^2} \le S_{max}^{ACPET} \tag{28}$$

$$P_{out,t}^{DCPET} \le P_{max}^{DCPET} \tag{29}$$

$$P_{in,t}^{DCPET} \le P_{max}^{DCPET} \tag{30}$$

Linearizing the non-linear term in the constraint so that it is transformed into a rotating cone constraint yields:

$$\left(P_{in,t}^{M}\right)^2+\left(Q_{in,t}^{M}\right)^2\le 2\frac{S_{max}^{MPET}}{\sqrt{2}}\frac{S_{max}^{MPET}}{\sqrt{2}} \tag{31}$$

$$\left(P_{out,t}^{M}\right)^2+\left(Q_{out,t}^{M}\right)^2\le 2\frac{S_{max}^{MPET}}{\sqrt{2}}\frac{S_{max}^{MPET}}{\sqrt{2}} \tag{32}$$

$$\left(P_{out,t}^{ACPET}\right)^2+\left(Q_{out,t}^{ACPET}\right)^2\le 2\frac{S_{max}^{ACPET}}{\sqrt{2}}\frac{S_{max}^{ACPET}}{\sqrt{2}} \tag{33}$$

$$\left(P_{in,t}^{ACPET}\right)^2+\left(Q_{in,t}^{ACPET}\right)^2\le 2\frac{S_{max}^{ACPET}}{\sqrt{2}}\frac{S_{max}^{ACPET}}{\sqrt{2}} \tag{34}$$

where S_{max}^{MPET}, S_{max}^{ACPET}, and P_{max}^{DCPET} are the power limits of the low-voltage AC and DC ports in the PET, respectively.

2.3.4 Uncertainty set of wind turbine, photovoltaic power output

Owing to the stochastic uncertainty of wind power and PV output, we considered the uncertainty set to characterize the uncertainty of the scenery output:

$$\begin{cases} u=\left[u_{i,t}^{WT},u_{i,t}^{PV}\right],t\in T \\ u_{i,t}^{WT}=\left[\hat{u}_{i,t}^{WT}-\Delta u_i^{WTmax},\hat{u}_{i,t}^{WT}+\Delta u_i^{WTmax}\right] \\ u_{i,t}^{PV}=\left[\hat{u}_{i,t}^{PV}-\Delta u_i^{PVmax},\hat{u}_{i,t}^{PV}+\Delta u_i^{PVmax}\right] \end{cases} \tag{35}$$

where $u_{i,t}^{WT}$, $u_{i,t}^{PV}$ are the actual wind and PV power, which are uncertainties; $\hat{u}_{i,t}^{WT}$, $\hat{u}_{i,t}^{PV}$ are the predicted values of wind and PV power; and Δu_i^{WTmax}, Δu_i^{PVmax} are the maximum deviation values allowed for wind and PV power, respectively.

To regulate the uncertainty of the model to control the conservativeness of the model, the time regulation parameters Γ_{WT}^{T}, Γ_{PV}^{T} and spatial regulation parameters Γ_{WT}^{S}, Γ_{PV}^{S} were introduced to represent the number of worst-case scenarios and wind turbines and photovoltaic units in the worst case simultaneously in one operating cycle, respectively. The specific expressions are as follows:

$$\begin{cases} u_{i,t}^{WT}=\hat{u}_{i,t}^{WT}-B_{i,t}^{WT}\Delta u_i^{WTmax} \\ u_{i,t}^{PV}=\hat{u}_{i,t}^{PV}-B_{i,t}^{PV}\Delta u_i^{PVmax} \\ \sum_{i=1}^{n}B_{i,t}^{WT}\le\Gamma_{WT}^{S} \\ \sum_{i=1}^{n}B_{i,t}^{PV}\le\Gamma_{PV}^{S} \\ \sum_{t=1}^{T}\sum_{i=1}^{n}B_{i,t}^{WT}\le\Gamma_{WT}^{T} \\ \sum_{t=1}^{T}\sum_{i=1}^{n}B_{i,t}^{PV}\le\Gamma_{PV}^{T} \end{cases} \tag{36}$$

where $B_{i,t}^{WT}$, $B_{i,t}^{PV}$ indicate whether the ith wind power and PV unit take the worst case at time t and are 0–1 variables.

3 Two-stage robust optimization model

As mentioned above, the optimization objective of the proposed model in this study was to minimize the cost of running one cycle, and the objective function can be expressed in the form of Eq. 1. Without considering the uncertainty of the PV of the wind turbine, the compact form of the objective function can be expressed as:

$$\begin{cases} \min\limits_{x,y}\ c^T y \\ s.t.\boldsymbol{D}y\ge\boldsymbol{d}\#(a) \\ \boldsymbol{K}y=0\#(b) \\ \boldsymbol{F}x+\boldsymbol{G}y\ge\boldsymbol{h}\#(c) \\ \boldsymbol{I_u}y=\hat{\boldsymbol{u}}\#(d) \\ \left\|\boldsymbol{M}y\right\|_2\le\boldsymbol{g}^T y\#(e) \end{cases} \tag{37}$$

where c is the column vector of coefficients corresponding to the objective function; $\boldsymbol{D}$, $\boldsymbol{K}$, $\boldsymbol{F}$, $\boldsymbol{G}$, $\boldsymbol{I_u}$, and $\boldsymbol{M}$ are the coefficient matrices of the various constraint equations; and $\boldsymbol{d}$, $\boldsymbol{h}$, and $\boldsymbol{g}^T$ are the column vectors of constants in the constraints. Equation (a) is the set of all inequality constraints known to be associated with **y** in the previous section; Equation (b) is the set of all equation constraints known to be associated with **y** in the previous section; Equation (c) is the set of all inequality constraints containing both **x** and **y**; Equation (d) is the set of all uncertainty constraints, which are represented by the predicted values of each uncertain outflow in the deterministic model; and Equation (e) is the set of all second-order cone constraints.

Where **x** and **y** are optimization variables, and their expressions are:

$$\begin{cases} x=[U_i(t)]^T \\ y=\left[P_{i,t}^{MT},P_{i,t}^{WT},P_{i,t}^{PV},P_{i,t}^{ch},P_{i,t}^{dis},P_{in,t}^{MPET},\right. \\ \left.P_{in,t}^{ACPET},P_{out,t}^{ACPET},P_{in,t}^{DCPET},P_{out,t}^{DCPET}\right]^T \end{cases} \tag{38}$$

When the uncertain output of wind and light is considered, a two-stage robust optimization approach can be used to find the scenario with the lowest cost of operating one cycle when the uncertain value of the scenery output is taken to the worst operating scenario with a preset uncertainty concentration, which is mathematically represented as follows:

$$\begin{cases} \min\limits_{x}\left\{\max\limits_{u\in U}\ \min\limits_{y\in\Omega(x,u)}\boldsymbol{c}^T y\right\} \\ st.\quad x=(x_1,x_2\cdot\cdot,x_{2T})^T \\ x_i\in\{0,1\},\forall i\in(1,2,\cdots,2\mathrm{T}) \end{cases} \tag{39}$$

where the outer layer is the first stage of the minimization problem with **x** as the optimization variable, and the inner layer is the second stage of the maximum minimization problem with **u** and **y** as the optimization variables. The first layer of the minimization problem was the objective function of this study, that is, the cost of running a cycle was minimized, and $\Omega(x,u)$ represents the feasible domain for a given set of **x**, **u**, **y**, whose expressions are as follows:

$$\Omega(x,u)=\begin{cases} y \\ \boldsymbol{D}y\ge\boldsymbol{d},\rightarrow\boldsymbol{\alpha} \\ \boldsymbol{K}y=0\rightarrow\boldsymbol{\beta} \\ \boldsymbol{F}x+\boldsymbol{G}y\ge\boldsymbol{h}\rightarrow\boldsymbol{\gamma} \\ \boldsymbol{I_u}y=\hat{\boldsymbol{u}}\rightarrow\boldsymbol{\delta} \\ \left\|\boldsymbol{M}y\right\|_2\le\boldsymbol{g}^T y\rightarrow\boldsymbol{\lambda},\boldsymbol{\mu} \end{cases} \tag{40}$$

where $\boldsymbol{\alpha}$, $\boldsymbol{\beta}$, $\boldsymbol{\gamma}$, $\boldsymbol{\delta}$, $\boldsymbol{\lambda}$, and $\boldsymbol{\mu}$ are pairwise vectors corresponding to each constraint matrix.

4 Model solving

To facilitate the solution, the above optimization model must be transformed into the form of a standard two-stage robust optimization

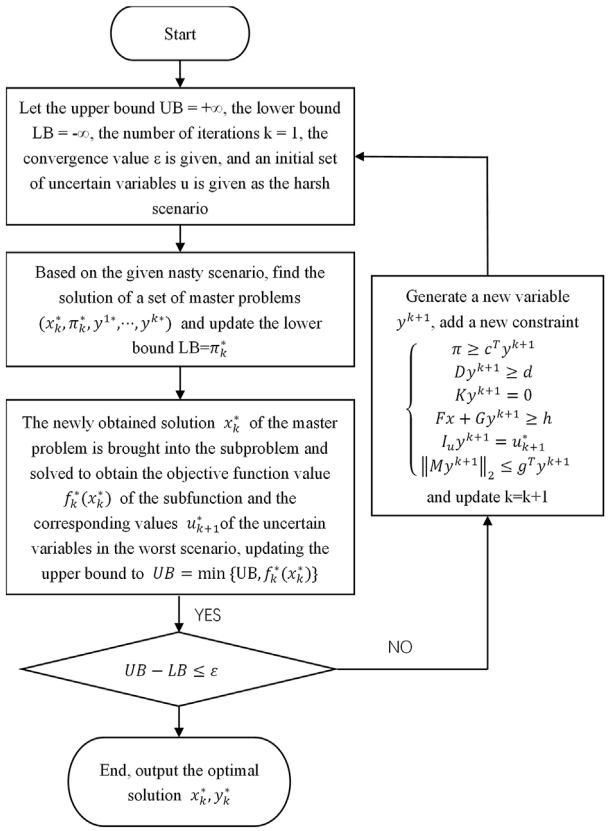

FIGURE 3
Algorithm flow chart.

model, which is a min-max-min multilayer optimization problem and is difficult to solve using general methods. In order to solve such problems, the commonly used methods are Benders decomposition method and Column and constraint generation (CCG) algorithm, and the CCG algorithm has the unique advantages of shorter computation time and fewer iterations compared with the Benders decomposition method, so the CCG algorithm is used to solve the two-stage robust optimization problem in this paper (Zeng and Zhao, 2013). The optimization problem was decomposed into a master problem and subproblem; the master problem min provided a lower bound for the subproblem max-min by calculation, whereas the subproblem provided a worst-case environment in the uncertainty set to provide an upper bound for the model, and then iterated the model several times so that the difference between the upper and lower bounds only decreased gradually. Finally, the result reached the preset convergence condition to obtain the desired optimization result. The specific process is as follows:

The main problem provides the lower bound for the model as:

$$\begin{cases} \min\limits_{x,y} \ \pi \\ st. \boldsymbol{\pi} \geq \boldsymbol{c}^T y_l \\ \boldsymbol{D} y_l \geq \boldsymbol{d} \# \\ \boldsymbol{K} y_l = 0 \# \\ \boldsymbol{F}x + \boldsymbol{G} y_l \geq \boldsymbol{h} \# \\ \boldsymbol{I_u} y_l = \boldsymbol{u_l^*} \# \\ \left\|\boldsymbol{M} y_l\right\|_2 \leq \boldsymbol{g}^T y_l \\ \forall \boldsymbol{l} \leq \boldsymbol{k} \end{cases} \tag{41}$$

where k is the number of current iterations, l is the number of historical iterations, y_l is the solution of the subproblem after l iterations, and $\boldsymbol{u_l^*}$ is the value of the uncertain variable u under the worst conditions obtained after the lth iteration.

The objective of the sub-problem was to derive the worst-case scenario with an objective function expressed as follows:

$$\max_{u \in U} \ \min_{y \in \Omega(x,u)} \boldsymbol{c}^T y \tag{42}$$

With (**x**,**u**) given, the subproblem can be viewed as a deterministic problem, and the equations of the subproblem are transformed into a dual form by the method mentioned above, thus transforming the min problem into a max problem for an easy solution, and the expression obtained is

$$\begin{cases} \max\limits_{u \in U, \alpha, \beta, \gamma, \delta, \varepsilon, \epsilon} \boldsymbol{d}^T \boldsymbol{\alpha} + (\boldsymbol{h} - \boldsymbol{F}x)^T \boldsymbol{\gamma} + u^T \boldsymbol{\delta} \\ \boldsymbol{D}^T \boldsymbol{\alpha} + K^T \boldsymbol{\beta} + \boldsymbol{G}^T \boldsymbol{\gamma} + \boldsymbol{I_u}^T \boldsymbol{\delta} \leq \boldsymbol{c} \\ \boldsymbol{\alpha} \geq 0, \boldsymbol{\gamma} \leq 0, \boldsymbol{\delta} \geq 0 \\ \|\boldsymbol{\lambda}\| \leq \boldsymbol{\mu} \end{cases} \tag{43}$$

The results obtained from the subproblem provide the upper bound for the whole model. The specific iteration process is shown in Figure 3.

5 Example analysis

5.1 Test platform and model parameters setting

To verify the correctness and effectiveness of this two-stage robust optimization method for hybrid AC-DC distribution networks with PET proposed in this study, the YALMIP toolbox and CPLEX and Gurobi solvers were used to solve the model. The hardware platform used was AMD Ryzen 7 4800 H 2.90 GHz; 16 GB RAM. The operating system used was Windows 10, and the software was R2017b. The structure of the algorithm used in this study is shown in Figure 4.

As shown in Figure 4, this study adopted a hybrid AC-DC distribution network model combined with two improved IEEE33 node models, where the red line indicates the AC part of the distribution network, and blue indicates the DC part. The PET connects the AC-DC part as well as the main network, and even plays the role of an energy hub. The voltage of the AC part was 12.66 kV and that of the DC part was 15 kV. The limitation range of the node voltage in the distribution network was $V_i \in [0.95, 1.05]$pu. The maximum value of the interaction power of the PET with the superior grid was $S_{max}^{MPET} = 12000\,kVA$, and the maximum value of the interaction power with the AC distribution network was $S_{max}^{ACPET} = 12000\,kVA$. The maximum value of the interactive power with the DC distribution network was $P_{max}^{DCPET} = 1000\,kV$, the loss coefficient of PET $k_p = 0.05$, and the iterative convergence accuracy of the CCG algorithm was set to $\varepsilon^c = 0.01$. The network was connected to energy storage devices ES and MT as controllable distributed power, and WT and PV as uncontrollable distributed power supplies; the specific distribution is shown in Figure 4. When the energy supply in the

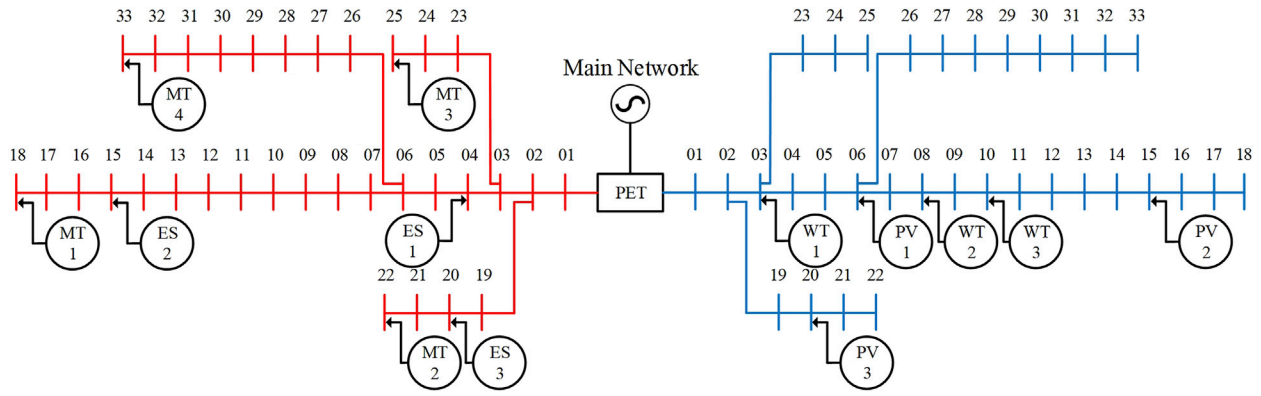

FIGURE 4
Structure diagram of AC/DC distribution network with PET.

TABLE 1 Output constraint of wind turbine.

No. Of wind turbine	Minimum output/kW	Maximum output power/kW
1	0	350
2	0	400
3	0	500

TABLE 2 Output constraint of photovoltaic.

No. Of wind photovoltaic	Minimum output/kW	Maximum output power/kW
1	0	300
2	0	350
3	0	500

TABLE 3 Parameters of micro turbine.

No. Of micro turbine	P_i^{MTmin}/kW	P_i^{MTmax}/kW	Q_i^{MTmin}/kW	Q_i^{MTmax}/kW	$c_1^{MT}/c_2^{MT}/c_3^{MT}$
1	125	350	75	210	0.10/30/0
2	80	300	48	180	0.12/29/0
3	150	375	90	225	0.14/22/0
4	50	250	30	150	0.11/25/0

AC or DC sub-network is insufficient, other sub-networks or higher-level grids can supply energy to them through PET. When there is a surplus of new energy in the DC sub-network, it can also be transmitted to the AC sub-network through PET, thus realizing peak reduction and valley filling in the distribution network to maximize economic benefits. The line parameters of the IEEE33 node system are detailed by (Kashem et al., 2000). The specific parameters of some devices are listed in the following Table 1, Table 2, Table 3, Table 4.

5.2 Analysis of simulation results

5.2.1 Results of running the two-stage robust optimization model

This example sets the spatial and temporal uncertainty regulation parameters $\Gamma_{WT}^{S} = \Gamma_{PV}^{S} = 2$ and $\Gamma_{WT}^{T} = \Gamma_{PV}^{T} = 12$. Figure 5 show the prediction curves for the wind turbine and photovoltaic outputs. The peak load was generally concentrated in the midday and evening hours, and the trough in the early

TABLE 4 Energy storage parameters.

No. Of energy storage	P_{min}^{ch} P_{min}^{dis}/kW	P_{max}^{ch} P_{max}^{dis}/kW	E_i^{min}/kW·h	E_i^{max}/kW·h	η
1	0	300	0	2000	0.95
2	0	300	0	2000	0.95
3	0	300	0	2000	0.95

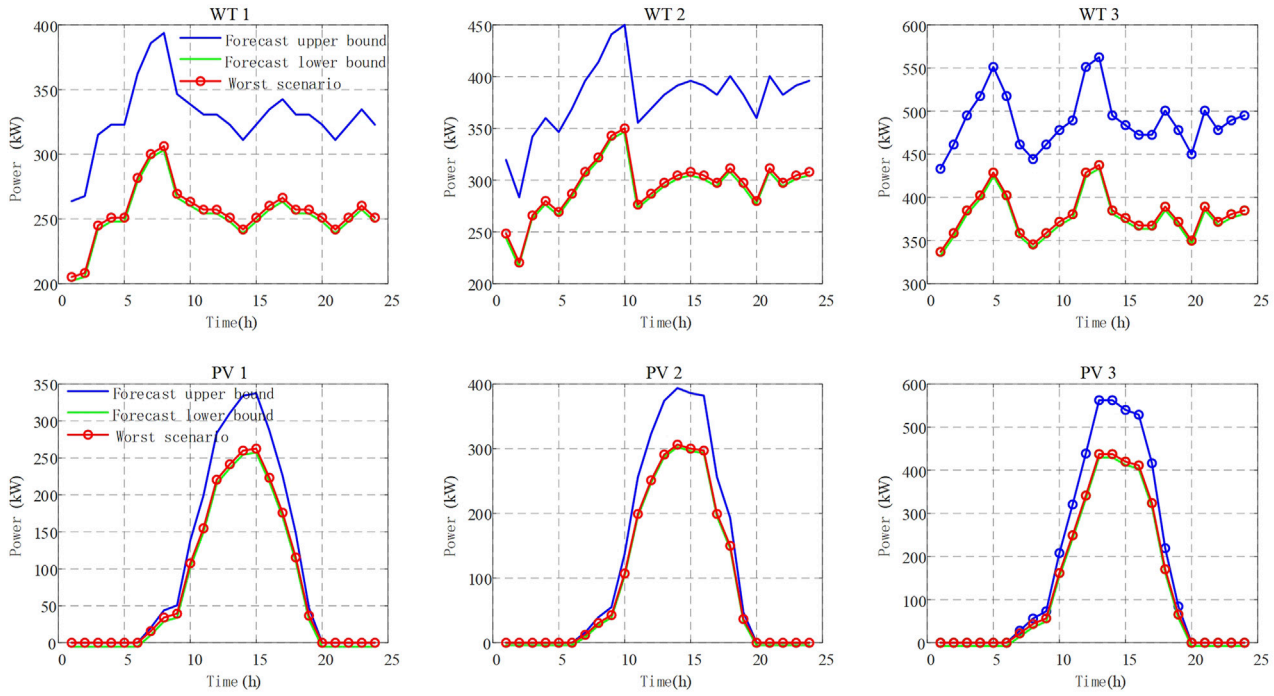

FIGURE 5
Output prediction curve of wind turbine and photovoltaic.

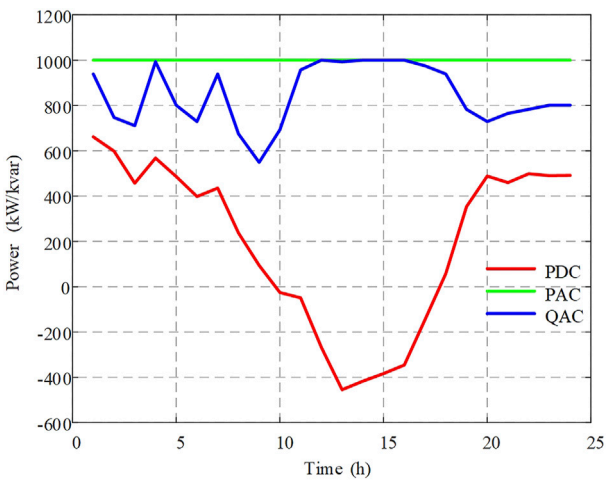

FIGURE 6
AC/DC port power of PET.

morning to morning hours. PV generated the most power at noon and hardly any at night, so wind power, PV, and MT must be combined to provide the power required by the load, with PET playing the role of energy router. Figure 6 and Figure 7 show the power output curves of the PET AC and DC ports and the power purchased by PET from the main grid, respectively. Figure 6 shows that during the time of high PV power generation around noon, the energy mainly flowed from the DC to the AC port, and the power purchased from the main grid during this time decreased. This reduced the costs of power purchase and abandonment penalty owing to the new energy consumption, thus achieving cost saving and new energy consumption. When there was no PV power at night, such as a DC subgrid power shortage, energy flowed from the AC to the DC port to ensure that the power was supplied to the load.

Comparing Figure 5 and Figure 8, the turbine generation was higher during the 5–10-h period, reducing the micro turbine generation at this time, thus reducing the system generation cost. Additionally, the dissipation of excess wind power reduced the

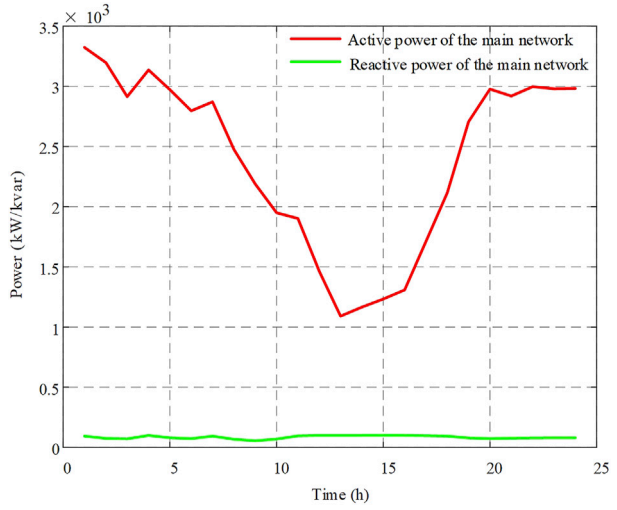

FIGURE 7
Purchased power to the main grid.

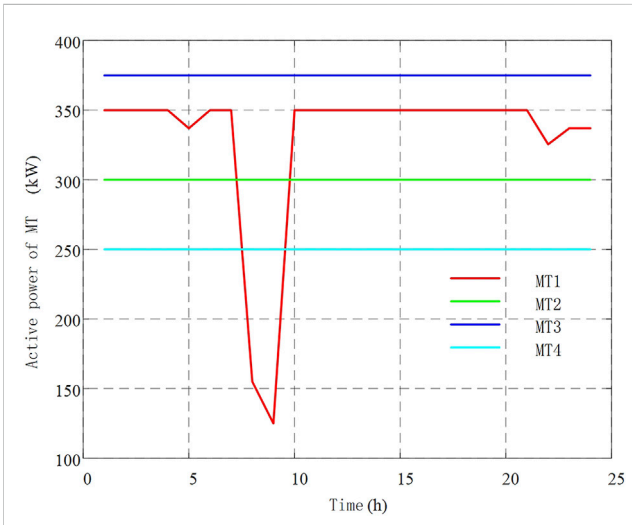

FIGURE 8
Power curve of micro turbine.

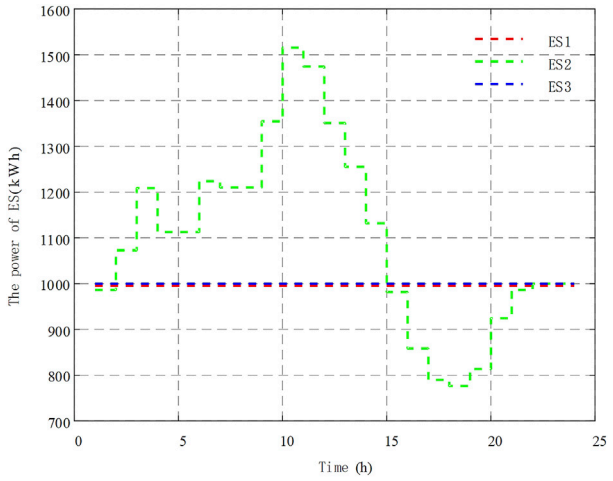

FIGURE 9
Energy storage curve.

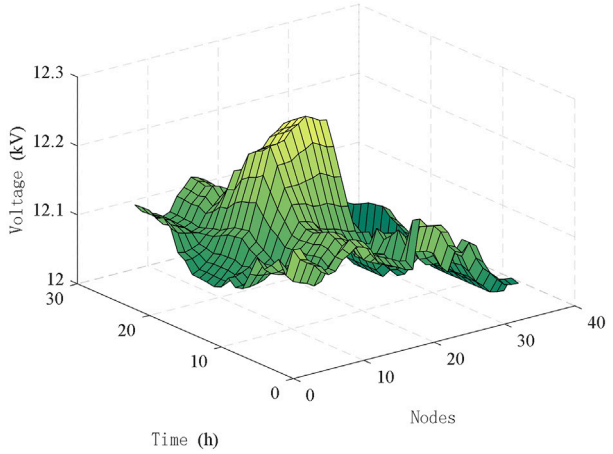

FIGURE 10
Voltage curve of DC section.

cost of the wind abandonment penalty. Figure 9 shows the energy storage power curves. When the overall new energy generation of the system was too large, energy could be stored to convert the power to the AC subnetwork through PET and store the excess energy in the storage device to reduce the cost of wind and light abandonment. In addition, when the overall system power was insufficient, it could also be discharged through energy storage to reduce power purchase and generation. When the system as a whole was short of power or when the cost of purchasing power from the higher grid was lower than the cost of generating power, power could be purchased from the higher grid through the PET interaction port with the higher grid to meet the system's power demand.

Figure 10 shows the voltage curve of the DC part of this model. Due the limitation of the number of graphs, we did not depict the nodal voltage curve of AC part as the AC part is similar to the DC part.

5.2.2 Comparison with deterministic and stochastic optimization models

The deterministic and stochastic optimization models were compared with the two-stage optimization model proposed in this study. By comparing the cost of operating the distribution network for one cycle under these conditions, the superiority of the models was verified. Furthermore, the impact of the uncertainty parameters on the conservative model was analyzed by comparing the cost of the models under different uncertainty parameters and number of iterations. The model

TABLE 5 Influence of uncertain parameters on results.

Optimization methods	Γ_{WT}^{T}、Γ_{PV}^{T}	Γ_{WT}^{S}、Γ_{PV}^{S}	Cost	Number of iterations
Two-stage robust optimization method	12	2	1518673.24	5
	12	3	1545173.23	5
	6	2	1429048.22	7
	6	1	1402673.23	8
	18	3	1624073.23	5
Deterministic optimization methods	0	0	842425	—
Stochastic optimization method	-	—	1269971.12	—

used in this study can be set with different uncertainty adjustment parameters for different DGs; however, for the convenience of presentation, the uncertainty adjustment parameters were the same for each DG in this study.

To verify the control effect of the uncertainty regulation parameter on the conservative type of model, several comparison tests were experimentally designed, as shown in Table 5, showing that the uncertain model was equivalent to the deterministic model when the uncertainty parameter was equal to 0. As the spatial and temporal uncertainty regulation parameters of the system increased, the number of units obtaining the worst case simultaneously and the total number of units that obtained the worst case in one operation cycle also increased. The uncertainty of the system also increased, increasing the cost of the model in one operation cycle, but the computation time and number of iterations decreased. This indicates that the more uncertainty the model considered, the worse the simulated operating conditions were, and the more conservative and costly the model was. Although the deterministic model had the lowest operating cost, it was not robust and, thus, could not cope with the uncertainty of new energy sources. The two-stage robust optimization model used in this study had a higher cost compared with the deterministic model, but it was robust because it considered the uncertainty of new energy. The larger the uncertainty parameter was, the more robust the model was, and the more it could cope with the uncertainty.

Compared with the stochastic optimization model commonly used in the literature mentioned previously, the cost of running one cycle of the stochastic optimization model was between that of the two-stage robust optimization and deterministic models. However, because the stochastic optimization model requires too many scenarios to be considered in the calculation, the calculation speed of the algorithm is slower, making its calculation time longer than that of the model used in this study. Additionally, the stochastic optimization model cannot guarantee the conservativeness of the calculation results, and the results have a certain probability of crossing the limit, which is not conducive to the safe power supply of the distribution network. The model used in this study can control the parameters of time and space uncertainty adjustment according to the actual situation to control the number of DGs of bad scenes in one cycle simultaneously, thus controlling the cost of running the model for one cycle. Therefore, the model used in this study is considered to have higher controllability and robustness when dealing with the actual problem.

5.2.3 Costs for different power supply configurations

The spatial uncertainty regulation parameter $\Gamma_{WT}^{S} = \Gamma_{PV}^{S} = 2$ and the temporal uncertainty regulation parameter $\Gamma_{WT}^{T} = \Gamma_{PV}^{T} = 12$. The cost is f = 1,518,673.24 when the power source in the optimization model contains both MT, ES and distributed new energy, which is used as a control group to compare and analyze the change of cost in other cases. When the model contains only MT and distributed new energy, the cost is f = 1759756.56. The reason for the increase in cost is that when there is no ES, it is not possible to reduce the peak and fill the valley, which makes the cost of wind and light abandonment penalty higher, and when the new energy output decreases, there is no energy storage to discharge, so we can only rely on MT power generation and purchase power from the upper grid, which increases the cost. When the model contains only MT, the overall power output of the system is too small to complete the power balance, resulting in the model cannot be iterated, and the cost results cannot be obtained.

6 Conclusion

This study established an optimal operation model of hybrid AC-DC distribution network with PET based on a two-stage robust optimization method, which considered the uncertainty of scenic power generation by using two-stage robust optimization. Based on ensuring the safety and reliability of the distribution network, the AC-DC part of the distribution network and super grid are connected by PET to improve the utilization rate of new energy and ensure the safe and economic operation of the distribution network. A comparison of the proposed model with deterministic and stochastic optimization models indicates that the model is more robust and can regulate the uncertainty of the system through the uncertainty parameters. However, the method used in this paper has the disadvantage of high cost, the next step will be to consider how to

model the uncertainty of renewable energy output in an AC-DC distribution network containing PET using a data-driven approach with a large amount of historical renewable energy data.

Data availability statement

The raw data supporting the conclusion of this article will be made available by the authors, without undue reservation.

Author contributions

The HD wrote the original draft. MW and ZT provided the supervision, review, and editing of the draft. All authors contributed to the article and approved the submitted version.

Funding

National Natural Science Foundation of China (61872230).

Acknowledgments

We would like to thank Editage (www.editage.cn) for English language editing.

Conflict of interest

The authors declare that the research was conducted in the absence of any commercial or financial relationships that could be construed as a potential conflict of interest.

Publisher's note

All claims expressed in this article are solely those of the authors and do not necessarily represent those of their affiliated organizations, or those of the publisher, the editors and the reviewers. Any product that may be evaluated in this article, or claim that may be made by its manufacturer, is not guaranteed or endorsed by the publisher.

References

Fu, Y., Zhang, Z. Q., and Li, Z. K. (2019). Research on reactive power voltage control strategy for hybrid AC/DC distribution network based on two-stage robust optimization model [J]. *Proc. CSEE* 39 (16), 4764–4774+4978. doi:10.13334/j.0258-8013.pcsee.180940

Guo, S. Q., Mu, Y. F., Chen, N. S., Pu, T. J., Yuan, X. D., and Li, Q. (2019). Day-ahead optimal scheduling of AC/DC hybrid distributed energy system with power electronic transformer [J]. *Adv. Technol. Electr. Eng. Energy* 38 (02), 44–51. doi:10.12067/ATEEE1806018

Kashem, M. A., Ganapathy, V., Jasmon, G. B., and Buhari, M. I. (2000). "A novel method for loss minimization in distribution networks. Electric Utility Deregulation and Restructuring and Power Technologies," in Proceedings. DRPT 2000. International Conference on. IEEE Xplore.

Lavaei, J., and Low, S. H. (2012). Zero duality gap in optimal power flow problem. *IEEE Trans. Power Syst. A Publ. Power Eng. Soc.* 27 (1), 92–107. doi:10.1109/TPWRS.2011.2160974

Li, K., Zhao, Z. M., Yuan, L. Q., Gao, C. Y., Wen, W. S., and You, X. J. (2021). Overview on research of multi-port power electronic transformer oriented for AC/DC hybrid distribution grid [J]. *High. Volt. Eng.* 47 (04), 1233–1250. doi:10.13336/j.1003-6520.hve.20201250

Li, S. C., Ling, Y. S., Pang, T. Y., and Zhang, H. Y. (2018). Research on power electronic transformer based on AC/DC and DC/AC two level structure [J]. *Electr. Energy Manag. Technol.* 543 (06), 7–10. doi:10.16628/j.cnki.2095-8188.2018.06.002,No.

Li, X. Y., Hu, Y., Zhu, B. T., and Geng, Q. (2019). Optimal configuration of hybrid AC/DC distribution network with power electronic transformer based on genetic algorithm. *J. Water Resour. Power* 37 (09), 192–196.

Liao, H. T., Huang, Y. H., Shi, Y. Z., and Chen, J. (2020). A Bi-level two-stage robust optimal operation strategy for AC and DC distribution network with photovoltaic and energy storage [J]. *Electr. Power Constr.* 41 (03), 110–118.

Liu, C., and Zhi, K. L. (2017). Hybrid cascaded power electronics transformer topology and control scheme [J]. *Power Syst. Technol.* 41 (02), 596–603. doi:10.13335/j.1000-3673.pst.2016.0942

Liu, Y. X., Guo, L., and Wang, C. S. (2018). Economic dispatch of microgrid based on two stage robust optimization [J]. *Proc. CSEE* 38 (14), 4013–4022+4307. doi:10.13334/j.0258-8013.pcsee.170500

Pu, T., J., Li, Y., Chen, N. S., Sun, Y. Y., Mu, Y. F., Dong, L., et al. (2018). Key technology and research framework for optimal operation control of hybrid AC/DC system based on power electronic transformer. *J. Power Syst. Technol.* 42 (09), 2752–2759. doi:10.13335/j.1000-3673.pst.2018.0730

Wang, Y., Zheng, Z. D., and Li, Y. D. (2017). Review of topology and control application of medium and high voltage power electronic transformer [J]. *Adv. Technol. Electr. Eng. Energy* 36 (05), 1–10.

Xu, C. B., Yang, X. D., Zhang, Y. B., Zhang, K. Y., Wang, X. Z., and Tang, M. (2021). Stochastic operation optimization method for active distribution networks with soft open point considering risk management and control [J]. *Automation Electr. Power Syst.* 45 (11), 68–76. doi:10.7500/AEPS20200331004

Yi, W. F., and Wang, X. (2021). Research on power electronic transformer based day-ahead economic operation strategy of AC/DC hybrid distribution network [J]. *Mod. Electr. Power* 38 (03), 339–345. doi:10.19725/j.cnki.1007-2322.2020.0393

Zeng, B., and Zhao, L. (2013). Solving two-stage robust optimization problems using a column-and-constraint generation method. *Operations Res. Lett.* 41 (5), 457–461. doi:10.1016/j.orl.2013.05.003

Zhang, T., Mu, Y. F., Jia, H. J., Wang, Y. X., and Pu, T. J. (2022). Stochastic operation optimization for AC/DC distribution network with power electronic transformer. *J. Power Syst. Technol.* 46 (03), 860–869. doi:10.13335/j.1000-3673.pst.2021.0536

Zhang, X. L., Zhou, H., Xiao, Z. H., Zhang, W., and Wu, D. (2017). Power electronic transformer applied to optimization of reactive power in active distribution system [J]. *Power Syst. Prot. Control* 45 (04), 80–85. doi:10.7667/PSPC160321

Zhang, X., Yao, L., Chen, C., Fang, R. S., and Lin, J. K. (2022). A novel two-stage robust model for Co-optimization of reconfiguration and reactive power in AC/DC hybrid distribution network [J]. *Power Syst. Technol.* 46 (03), 1149–1162. doi:10.13335/j.1000-3673.pst.2020.1870

Zhong, L., Gao, H. J., Yang, Y. H., Liu, Y. B., and Liu, J. Y. (2022). Load peak shaving operation management and control strategy of AC/DC hybrid distribution network based on two-stage robust game model [J]. *Proc. CSEE* 42 (15), 5550–5565. doi:10.13334/j.0258-8013.pcsee.210628

Frontiers in
Energy Research

Advances and innovation in sustainable, reliable and affordable energy

Explores sustainable and environmental developments in energy. It focuses on technological advances supporting Sustainable Development Goal 7: access to affordable, reliable, sustainable and modern energy for all.

Discover the latest Research Topics

See more →

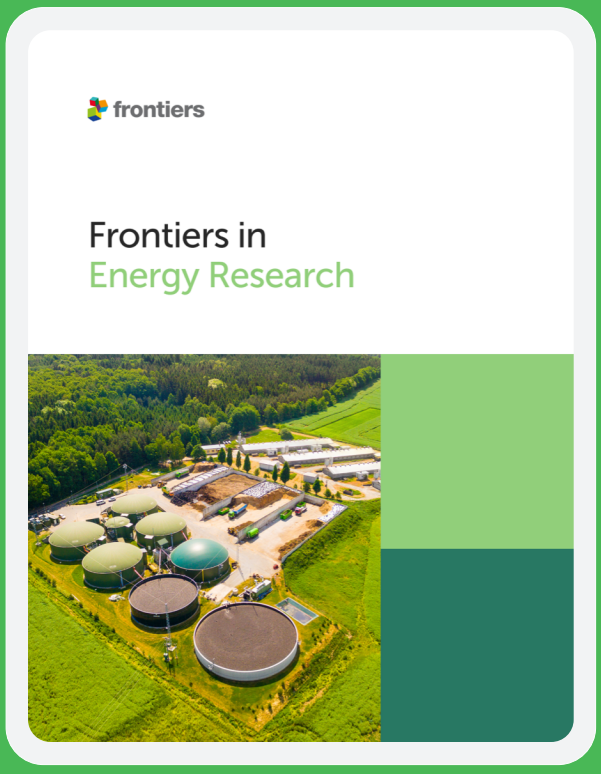

Frontiers

Avenue du Tribunal-Fédéral 34
1005 Lausanne, Switzerland
frontiersin.org

Contact us

+41 (0)21 510 17 00
frontiersin.org/about/contact